SAPIENZA
UNIVERSITÀ DI ROMA

Functional nanocomposites based on graphene/DNA interface: Towards a bio-inspired sensing of UV radiation effects

Ph.D. Course in Electrical, Materials and Nanotechnology Engineering

Curriculum B - Materials and Raw Materials Engineering

XXXII Cycle

Ph.D. Candidate:

Elisa Toto
ID number 1187221

Advisor:

Prof. Mariagabriella Santonicola

Co-Advisor:

Prof. Susanna Laurenzi

Thesis defended on 25 February 2020

Functional nanocomposites based on graphene/DNA interface: Towards a bio-inspired sensing of UV radiation effects
Ph.D. Thesis - Sapienza University of Rome

Author's email: elisa.toto@uniroma1.it

“He who fights, can lose. He who doesn't fight, has already lost.”

Bertolt Brecht

This Thesis is dedicated to my parents

Contents

List of Acronyms

AC: alternating currents
AFM: atomic force microscopy
CFRP: carbon-fiber reinforced polymer
CMC: ceramic matrix composite
CNT: carbon nanotube
CP: conductive polymer
CPD: cyclobutane pyrimidine dimer
DC: direct currents
DNA: deoxyribonucleic acid
DSC: differential scanning calorimetry
dsDNA: double-stranded deoxyribonucleic acid
EIS: electrical impedance spectroscopy
EIT: electrical impedance tomography
ERT: electrical resistance tomography
EUV: extreme ultraviolet radiation
EVA: extravehicular activities
GFRP: glass fiber-reinforced polymer
GNP: graphene nanoplatelet
GO: graphite oxide
HALS: hindered-amine light stabilizer
IPA: isopropyl alcohol
ISS: international space station
KAS: Kissinger–Akahira–Sunose (method)
LEO: low earth orbit
MMC: metal matrix composite
OCA: optical contact angle
OFW: Ozawa–Flynn–Wall (method)
PCR: polymerase chain reaction

PDMS: polydimethylsiloxane

PDMS-OH: hydroxyl-terminated polydimethylsiloxane

PEDOT:PSS: poly(3,4-ethylenedioxythiophene) polystyrene sulfonate

PEEK: poly(ether ether ketone)

PMC: polymer matrix composite

(6-4)PP: pyrimidine (6-4) pyrimidone (photoproduct)

PPS: poly(phenylene sulfide)

PTFE: polytetrafluoroethylene

PVC: poly(vinyl chloride)

PVP: polyvinylpyrrolidone

RNA: ribonucleic acid

RTM: resin transfer molding

SEM: scanning electron microscopy

SFE: surface free energy

TML: total mass loss

UV: ultraviolet (radiation)

VCM: volatile condensable material

WCA: water contact angle

WVR: water vapor regained

List of Figures

List of Tables

Chapter 1

Towards a bio-inspired sensing of UV radiation effects

1.1 Introduction

Ultraviolet (UV) radiation naturally characterizes the Earth environment and the outer space, representing one of the most hazardous agents for human health and for the useful lifetime of organic materials, such as plastics and rubber [1-4]. UV exposure on Earth is limited by several factors, among them the presence of the ozone layer that shields the most dangerous shorter wavelengths, such as those forming the UV-C band (100 nm to 280 nm). Differently, the space environment is characterized by a massive and non-filtered incoming UV radiation, which amounts to about 10% of the total amount of the electromagnetic radiation from the Sun. A strict monitoring of the effects of UV radiation becomes therefore necessary in order to protect biological systems and materials that are typically involved during a space mission.

The possibility to develop a UV-detecting system able to ensure a good sensitivity and stability during measurements, and possessing at the same time endearing characteristics, such as low weight and a real-time response, represents a fascinating challenge towards new technological advances in the field of radiation sensitive materials. In particular, the engineering of devices characterized by a sensitive component in the form of a thin film or a reduced-size 3D material would be desirable to overcome traditional problems that afflict space mission equipment, such as onboard encumbrance, or that can limit their use on Earth.

Specifically, miniaturized UV sensors can be employed to monitor hazardous exposures during working activities involving artificial sources of radiation, without interfering with normal activities. Some applications, such as sterilization processes, involve the use of the highly damaging UV-C light, making necessary the presence of a space-saving sensitive system that is able to detect and quantify any accidental exposure for the workers. In addition, an enhanced UV sensitive device could allow to detect

eventual small amounts of incoming UV-C radiation and to correlate these measurements with the phenomenon of depletion of the ozone layer, especially at the Earth regions that are most at risk, such as those near the equator.

A large number of studies have been focused on human diseases induced by hazardous UV exposure, from cataract to skin cancer, investigating the UV-promoted effects on the main biological molecules and the principal mechanisms of interaction [1, 5-8]. In particular, UV-induced damages on DNA represent the starting point of processes such as mutations, cell death, and development of tumors, which lead to the impairment of the health state of the overall biological system [9-12]. In light of this, several UV-detecting devices exploit biological molecules or simple biological systems, such as spores or bacteria, performing a biological-weighted monitoring of the UV exposure effects [13-17]. In particular, DNA exhibits its maximum sensitivity to short wavelengths, with a peak of absorption at 260 nm [1], which belongs to the UV-C radiation band causing the main direct alterations on the DNA structure. For this reason, this biomolecule can be considered a good candidate to integrate in the design of UV sensing materials.

A novel approach can be undertaken through the fusion of a bio-inspired UV sensing concept, based on the employment of UV-sensitive biological elements, and the field of advanced composite materials. Hence, the assembly of heterogeneous components can be opportunely tuned in order to obtain a functional material with tailored properties for an efficient UV detection. In this perspective, graphene represents a promising component of such sensitive materials, since it exhibits enhanced properties that make it one of the most used elements in the field of multifunctional sensors [18-20]. In addition, graphene nanostructures can be successfully combined with biological molecules using both covalent and non-covalent interactions [21, 22]. This represents the main starting point towards the engineering of a novel bio-inspired UV sensitive nanocomposite, possessing several attractive features, such as low weight, reduced size, and real-time response, which are useful for sensing applications in space and on Earth.

1.2 Concept of this Thesis

The concept of the research described in this Thesis is centered around the design, preparation and testing of bio-inspired UV sensitive nanocomposites based on graphene/DNA interface.

Chapter 2 provides the pathway from the heterogeneous field of composite materials towards the sensing of UV radiation, drawing from the literature background. In particular, the first part of the Chapter describes the fundamental characteristics of composite materials, starting from the concepts underlying their development and classification until their extensive application in sensing devices. Among the different types of composites, graphene-based nanofilled materials are discussed in detail, in order to elucidate their fabrication processes and the peculiar properties that make them good candidates for a bio-inspired approach to UV sensing. The second part of this Chapter contains a report of UV radiation as one of the constituent factors of the Earth and the outer space environments, highlighting sources and typical conditions of exposure. Moreover, UV-damaging effects on human health and materials are described, in order to underline the relevance of detecting and monitoring exposure to this type of radiation. At last, a background of the traditional equipment used for UV radiation monitoring is provided.

A first approach towards the development of UV sensitive nanocomposite materials is reported in **Chapter 3**. Graphene nanoplatelets were opportunely combined with DNA with the aim to obtain a sensitive filler and, at the same time, to improve their dispersibility in a polymer matrix [23]. GNP-DNA/poly(3,4-ethylenedioxythiophene) polystyrene sulfonate (PEDOT:PSS) films were fabricated and their properties analyzed before and after UV-C irradiation at different doses, in order to examine their UV response. Several techniques were used to characterize these films, including water contact angle measurements, electrical impedance spectroscopy, topography reconstruction from scanning electron microscopy (SEM). Moreover, Raman microscopy mapping was proved to be a useful technique to unveil the chemical modifications of the nanocomposite films induced by UV exposure.

The UV response of the GNP-DNA/PEDOT:PSS nanocomposites was further investigated using electrical resistance tomography (ERT). **Chapter 4** describes the application and the optimization of this technique in order to provide conductivity changes that can be directly related to the UV damage caused on the nanocomposite surfaces. In particular, these nanocomposites were applied as coatings onto carbon-fiber reinforced polymer (CFRP) plates, which are advanced materials typically employed in structural elements for space applications [24-26]. This experimental study proposes the

combination of GNP-DNA/PEDOT:PSS coatings and ERT as a possible method for the health monitoring of materials, such as CFRPs, and structures that are exposed to damaging levels of UV radiation. Moreover, other complementary techniques, including SEM and Raman microscopy, were used to validate the results.

The following experiments were focused on incorporating the graphene/DNA filler in a different polymer matrix, based on flexible polydimethylsiloxane (PDMS), with the aim to fabricate free-standing films or 3D materials with improved conformability and reduced size. Moreover, the specific optical properties of PDMS, such as its high transparency to UV radiation with a good transmittance in the UV-C band (above 240 nm) [27], allow for a major exposure of the incorporated filler during irradiation. Prior to testing the UV sensitivity of the PDMS-based nanocomposites with GNP-DNA filler, their curing reactions were fully investigated, and results are reported in **Chapter 5.** Starting from differential scanning calorimetry (DSC) measurements, the curing kinetics of different PDMS-based blends were examined, in order to add valuable information for the materials processing and highlights possible limitations due to the presence of the filler.

In the following experimental phase, the fabrication process of the GNP-DNA/PDMS films was optimized by the use of a suitable solvent, in order to reach a good level of dispersion of the filler into the PDMS matrix. The properties of these films were investigated before and after exposure to UV-C radiation, and the effect of different amounts of filler evaluated. Procedures and results are summarized and discussed in **Chapter 6.**

Finally, **Chapter 7** describes the realization of GNP-DNA/PDMS nanocomposites with increased thickness and their testing as free-standing 3D materials in simulated space environment. The properties of the nanocomposites, in particular their surface morphology and electrical conductivity, were examined before and after tests performed in a thermal vacuum-chamber, under simulated solar irradiation. The sensitivity to solar radiation was also evaluated for the GNP/PDMS nanocomposites without the DNA element in order to compare their response to that of the samples containing the UV sensitive GNP-DNA filler.

1.3 References

[1] W. Harm, Biological effects of ultraviolet radiation, Cambridge University Press Cambridge1980.

[2] W.H. Organization, IARC monograph on the evaluation of carcinogenic risks to humans, Human Papillomaviruses, (2000).

[3] A.L. Andrady, S. Hamid, X. Hu, et al., Effects of increased solar ultraviolet radiation on materials, Journal of Photochemistry and Photobiology B: Biology, 46 (1998) 96-103.

[4] A. Andrady, H. Hamid, A. Torikai, Effects of solar UV and climate change on materials, Photochemical & Photobiological Sciences, 10 (2011) 292-300.

[5] T. Schwarz, Mechanisms of UV-induced immunosuppression, The Keio Journal of Medicine, 54 (2005) 165-171.

[6] R.P. Rastogi, A. Kumar, M.B. Tyagi, et al., Molecular mechanisms of ultraviolet radiation-induced DNA damage and repair, Journal of Nucleic Acids, 2010 (2010).

[7] C.-H. Lee, S.-B. Wu, C.-H. Hong, et al., Molecular mechanisms of UV-induced apoptosis and its effects on skin residential cells: the implication in UV-based phototherapy, International Journal of Molecular Sciences, 14 (2013) 6414-6435.

[8] H. Nakazawa, D. English, P.L. Randell, et al., UV and skin cancer: specific p53 gene mutation in normal skin as a biologically relevant exposure measurement, Proceedings of the National Academy of Sciences, 91 (1994) 360-364.

[9] J.H. Miller, Mutagenic specificity of ultraviolet light, Journal of Molecular Biology, 182 (1985) 45-65.

[10] G.P. Pfeifer, Y.-H. You, A. Besaratinia, Mutations induced by ultraviolet light, Mutation Research/Fundamental and Molecular Mechanisms of Mutagenesis, 571 (2005) 19-31.

[11] S. Tornaletti, G.P. Pfeifer, Slow repair of pyrimidine dimers at p53 mutation hotspots in skin cancer, Science, 263 (1994) 1436-1438.

[12] S.J. Kuerbitz, B.S. Plunkett, W.V. Walsh, et al., Wild-type p53 is a cell cycle checkpoint determinant following irradiation, Proceedings of the National Academy of Sciences, 89 (1992) 7491-7495.

[13] G. Horneck, P. Rettberg, E. Rabbow, et al., Biological dosimetry of solar radiation for different simulated ozone column thicknesses, Journal of Photochemistry and Photobiology B: Biology, 32 (1996) 189-196.

[14] P. Rettberg, C.S. Cockell, Biological UV dosimetry using the DLR-biofilm, Photochemical & Photobiological Sciences, 3 (2004) 781-787.
[15] A.P. Schuch, R. da Silva Galhardo, K.M. de Lima-Bessa, et al., Development of a DNA-dosimeter system for monitoring the effects of solar-ultraviolet radiation, Photochemical & Photobiological Sciences, 8 (2009) 111-120.
[16] S.W. Wilhelm, W.H. Jeffrey, C.A. Suttle, et al., Estimation of Biologically Damaging UV Levels in Marine Surface Waters with DNA and Viral Dosimeters, Photochemistry and Photobiology, 76 (2002) 268-273.
[17] H. Yoshida, J.D. Regan, UVB DNA dosimeters analyzed by polymerase chain reactions, Photochemistry and Photobiology, 66 (1997) 82-88.
[18] H. Song, L. Zhang, C. He, et al., Graphene sheets decorated with SnO2 nanoparticles: in situ synthesis and highly efficient materials for cataluminescence gas sensors, Journal of Materials Chemistry, 21 (2011) 5972-5977.
[19] S.K. Hazra, S. Basu, Graphene-oxide nano composites for chemical sensor applications, C—Journal of Carbon Research, 2 (2016) 12.
[20] W. Zhang, J. Suhr, N. Koratkar, Carbon nanotube/polycarbonate composites as multifunctional strain sensors, Journal of Nanoscience and Nanotechnology, 6 (2006) 960-964.
[21] X. Zou, S. Wei, J. Jasensky, et al., Molecular interactions between graphene and biological molecules, Journal of the American Chemical Society, 139 (2017) 1928-1936.
[22] D. Li, W. Zhang, X. Yu, et al., When biomolecules meet graphene: From molecular level interactions to material design and applications, Nanoscale, 8 (2016) 19491-19509.
[23] A.J. Patil, J.L. Vickery, T.B. Scott, et al., Aqueous stabilization and self-assembly of graphene sheets into layered bio-nanocomposites using DNA, Advanced Materials, 21 (2009) 3159-3164.
[24] M. Martins, R. Gomes, L. Pina, et al., Highly Conductive Carbon Fiber-Reinforced Polymer Composite Electronic Box: Out-of-Autoclave Manufacturing for Space Applications, Fibers, 6 (2018) 92.
[25] A. Francesconi, C. Giacomuzzo, S. Kibe, et al., Effects of high-speed impacts on CFRP plates for space applications, Advances in Space Research, 50 (2012) 539-548.

[26] A.A. Abusafieh, D.R. Federico, S.J. Connell, et al., Dimensional stability of CFRP composites for space-based reflectors, Optomechanical Design and Engineering 2001, International Society for Optics and Photonics, 2001, pp. 9-16.
[27] M.D. Borysiak, K.S. Bielawski, N.J. Sniadecki, et al., Simple replica micromolding of biocompatible styrenic elastomers, Lab on a Chip, 13 (2013) 2773-2784.

Chapter 2

Composite materials: properties and applications in perspective of UV radiation sensing

2.1 Introduction to composite materials

In the last years, composite materials have been used in increasingly different fields due to their versatility and capability to be endowed with characteristic properties for a specific application. Their development has been promoted prevalently by the possibility to customize their properties depending on the environment of use and the required performances.Advances in leading technological areas, such as aerospace and biomedicine, have required enhanced properties not found in commonly used materials, such as metal alloys, ceramics and polymers. These needs have stimulated an increasing interest towards the engineering of composite materials with properties more and more corresponding to the expectations, leading to the concept of *advanced materials* [1]. This concept presupposes a high level of interaction between the identified materials and the specific environment of application, and typically it can be realized involving multiple phases in the composite arrangement, each contributing with different chemical, physical, mechanical and sometimes biological properties.

Composite materials base their nature on the combination of a matrix, typically made of a polymer, metal or ceramic, with one or more materials used as filler. The starting systems are opportunely mixed obtaining a material with more useful structural or functional properties, which are not shown by the components if considered singularly. As reported by Wang et al. [2], composites, according to their definition, should show the following characteristics:

- microscopically, a distinct interface between the components
- single components with sufficiently different properties
- improvement in performances with respect to the starting materials

In particular, the interface separating the different phases shows properties able to influence significantly the composite performances [3], especially their mechanical behavior [4-7]. These properties are mainly determined by the chemical/morphological nature and physical/thermodynamic compatibility between the constituents, influencing in particular toughness in transverse and interlaminar fractures [8, 9]. Therefore, the design and development of composites need to take into account the specific interactions at the interface, in order to assure an efficient stress transfer and a good damage tolerance [10].

Composites can be grouped in three main categories based on the nature of the matrix:

1. Polymer matrix composites (PMCs): they are developed employing thermoset plastics, such as nylon, polyethylene, polypropylene, or thermoplastics, such as epoxy, polyester, or phenolic resins. These matrices are typically filled with materials that are able to enhance their mechanical properties, so the resulting composites exhibit high strength and stiffness-to-weight ratio.
2. Metal matrix composites (MMCs): they are realized using a metal matrix reinforced with fillers able to confer stiffness and strength, resulting in superior performances at high temperatures if compared with PMCs. For MMCs, the matrices are generally made of: aluminum, magnesium, titanium, iron, copper, nickel. This category of composites is characterized by high strength, high stiffness, abrasion resistance, dimensional stability and toughness.
3. Ceramic matrix composites (CMCs): ceramic matrices, such as alumina, silicon carbide and silicon nitride, are employed and generally reinforced with continuous ceramic fibers. They are developed with the main aim to overcome the brittleness of the monolithic ceramics, obtaining tough materials, with a high strain to failure. Differently from PMCs or MMCs, the failure strain of the matrix is lower than the failure strain of the fibers, so they are also known as “inverse composites” [11].

Polymer-matrix composites are widely used for their room-temperature properties, good processability and reasonable production costs. In particular, the most employed and least expensive polymer resins are polyesters and vinyl esters, which are mainly used when glass fibers are selected as filler [12, 13]. Conversely, epoxies represent a more expensive choice, but largely used for applications requiring high moisture resistance or enhanced

mechanical properties, such as in the aerospace sector [14]. Moreover, a comparison among thermoplastic and thermoset composites can be made, taking into account some of the most relevant aspects. In particular, several thermoplastics exhibit properties that make them suitable for advanced applications, such as poly(ether ether ketone) (PEEK) and poly(phenylene sulfide) (PPS), with superior toughness and damage tolerance and, at the same time, they offer the potential for short processing times. Nevertheless, in the case of thermoplastics reinforced with continuous fibers, the thermoforming is complicated by the tendency of the fibers to wrinkle and buckle if not maintained under tension. For this reason, the use of continuous-fiber thermoplastic composites becomes advantageous in the case of a demand for a large quantity of parts, and when the process can be automated removing almost all manual operations. As a result, this type of composites is mainly employed in the automotive industry rather than in the aerospace field, where lot sizes are small and production rates cannot justify the investment for more automated equipment [15].

Depending on the type of filler selected, composites can be further classified into three main types: particle-reinforced, fiber-reinforced, and structural composites. Particle-reinforced materials can be further divided in large-particle and dispersion-strengthened composites. The first are characterized by particle–matrix interactions that cannot be treated at atomic or molecular level, and continuum mechanics is adopted. In this case, the system is generally composed by hard and stiff fillers that tend to restrain the movement of the matrix, which transfers a part of the applied stress to the particles [16]. The mechanical properties of this type of composites are strictly dependent on the volume fractions of the constituents and, in general, they can be enhanced by increasing the particles loading. Moreover, the size of the filler is approximately the same in all directions and higher than 0.1 mm. Cermets represent an example of large-particle reinforced composites, where strong and brittle ceramic particles are used as filler, with the effect to improve the toughness of a soft and ductile metal matrix. In particular, tungsten carbide or titanium carbide are typically dispersed in a matrix of cobalt or nickel. Differently, dispersion-strengthened composites involve smaller particles, with diameters between 0.01 and 0.1 mm, and they are characterized by particle–matrix interactions with strengthening at the atomic or molecular level [16]. In this type of system, the matrix typically bears the main load, whereas the particles hinder the motion of dislocations into

the matrix. This limits plastic deformations, and the yield and tensile strengths have the effect of enhancing the particle-matrix interactions.

Fiber-reinforced composites exhibit properties strictly depending on the nature, geometry and dimension of the dispersed fibers. A schematic representation of fiber-based dispersed phases with different geometrical and spatial characteristics is shown in Figure 2.1. In the case of PMCs, the most used fibers are based on aramids, glass and carbon.

Aramid fibers are prevalently employed for ballistic products, sporting goods and as replacement for asbestos in automotive brake and clutch linings [17]. They are selected mainly for their outstanding strength-to weight ratios, which are superior to metals [18]. Further, these fibers show advantages such as toughness, impact resistance, resistance to creep and fatigue failure, with a thermal stability up to 500 °C [19]. Chemically, they are susceptible to degradation by strong acids and bases, showing a good grade of stability in other solvents [20]. Glass fibers are typically chosen for properties such as good chemical, biological and thermal resistance, thermal and electric insulation, low costs of fabrication [21]. Depending on the type of glass fiber, the properties of the resulting composites can differ particularly in terms of mechanical strength and thermal stability. For these reasons, *S-glass* fibers, that are known for their extreme temperature resistance, high strength and stiffness, and corrosive resistance, are generally employed in aerospace and aeronautic industries [22, 23], whereas the other types, in particular *E-glass* fibers, are mainly used for automotive and marine bodies, pipes, storage containers and industrial floorings. Carbon-fiber reinforced polymers (CFRPs) can be considered the materials prevalently selected for advanced technological applications, due to the high performances of the carbon-fibers. In fact, this type of fiber exhibits the highest specific modulus and strength if compared with the other types of reinforcement [24]. Moreover, at room temperature, they are not affected by moisture and by most solvents, acids and bases [25]. Characteristics such as high electrical and thermal conductivity, high mechanical strength, stiffness and low weight make them suitable for aerospace applications, but also for automotive, sports and recreational equipment [26-28].

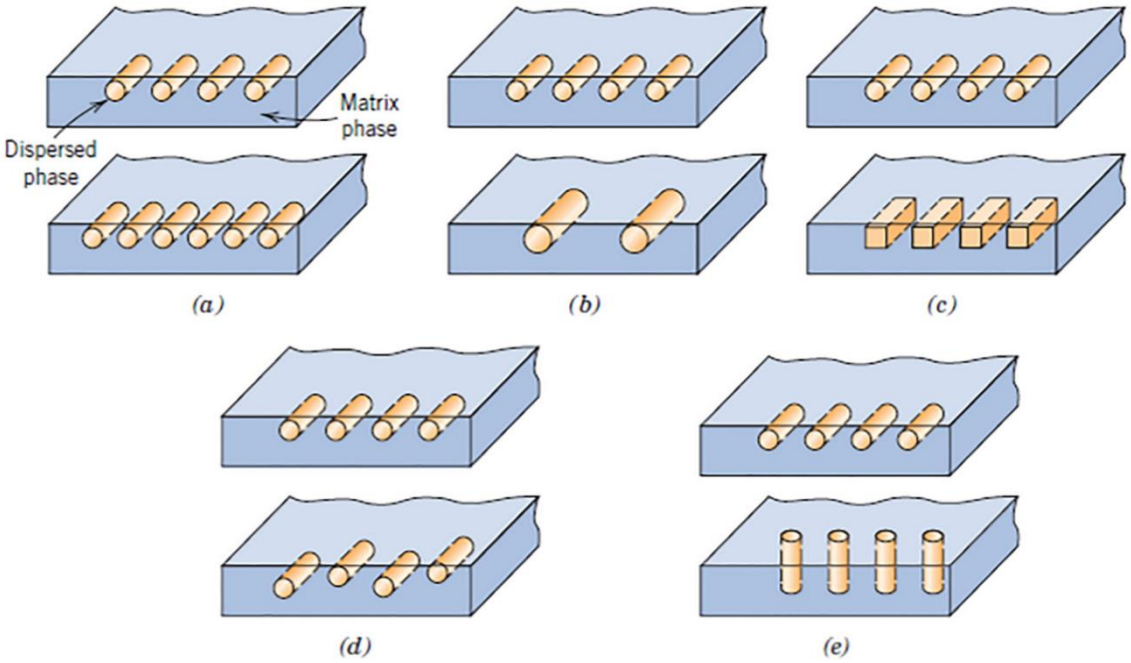

Figure 2.1. *Schematic representation of composites with different geometrical and spatial characteristics of the dispersed phase: (a) concentration, (b) size, (c) shape, (d) distribution, (e) orientation [29].*

Structural composites are typically assembled starting from composite and homogeneous materials, with properties strictly related to the geometry of the structural elements. Laminar composites and sandwich panels are the main types of structural composites that are used. In particular, laminated composites can be obtained piling layers or lamina of unidirectional composite materials, and the properties can be varied not only with the type of piled materials, but also adopting different ways of piling the layers on top of each other. Sandwich composites are realized using external strong layers, the face sheets, attached to a layer of less dense material, the core, with low stiffness and low strength. For instance, in Figure 2.2, a schematic representation of the assembly of a honeycomb core sandwich panel is reported. The main role of the face sheets is to withstand most of the plane loads and transversal bending stresses, whereas the core separates both face sheets and resists deformations perpendicular to the face plane. Sandwich panels are used in a wide variety of applications including roofs, floors, walls of buildings, aerospace and aircraft [30, 31].

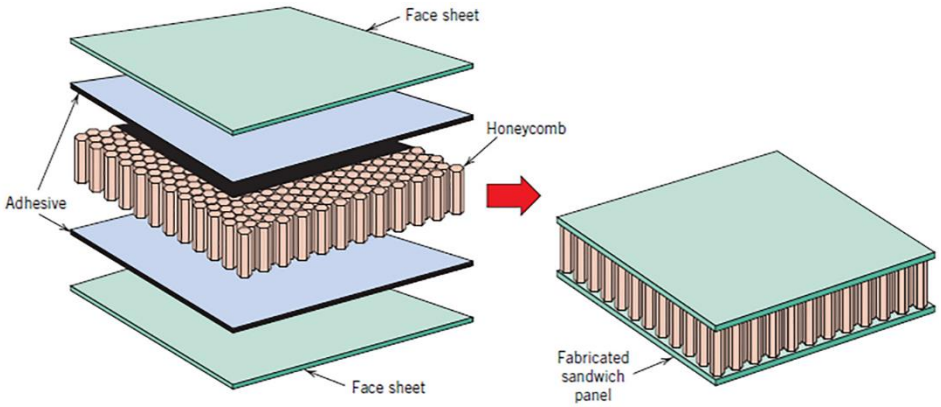

Figure 2.2. *Schematic representation of the assembly of a honeycomb core sandwich panel [32].*

2.2 Nanocomposite materials

A promising type of composites base the enhancement of their properties on the dimensions of the interacting parts, particularly in the case of *nanocomposites*. These composite materials are characterized by at least one of the phases with dimensions in the nanometer range [33]. They have been developed taking into account the effective influence of the phases size on the overall performances. In fact, changes in particle properties can be observed when their size is less than a particular level, called *critical size*. Dimensions in the range of nanometers can favor an improvement of the interactions at the interfaces between the phases, inducing an enhancement of the overall materials properties [34]. In particular, the surface area-to-volume ratio of the reinforcements plays a crucial role on the nanocomposites performances.

In recent years, the research and development of nanofilled polymers have greatly increased due to the possibility to preserve the advantages offered by the resins, such as mechanical properties and processability, and, at the same time, enhancing their performances without affecting significantly the final weight. In fact, due to the nanoscale size of the reinforcing phase, the interface-to-volume ratio is higher than in conventional composites [35]. Therefore, the volume fraction of the second phase can be reduced, without inducing a degradation of the properties.

Nanoscale-filled polymer composites are characterized by fillers with at least one dimension <100 nm and can be grouped in three categories [36]:

1. fiber or tube nanofillers, with a diameter and an aspect ratio of at least 100;
2. plate-like nanofillers, layered materials with a thickness of the order of 1 nm and an aspect ratio in the other two dimensions of at least 25;
3. three dimensional (3D) nanofillers, relatively equi-axed particles <100 nm in their largest dimension.

Nanometric dimensions and extreme aspect ratios of the tubes and plates used as filler determine peculiar properties, such as a low percolation threshold (0.1-2 vol%), a large number of particles per particle volume (10^6-10^8 particles/μm^3), extensive interfacial area per volume of particles (10^3-10^4 m^2/mL) and short distances between particles (10-50 nm at 1-8 vol%) [37].

Figure 2.3 offers a comparison between a macro-composite and a nanocomposite at the same volume fraction of filler, highlighting the dimensional differences at schematic level and by morphological investigations.

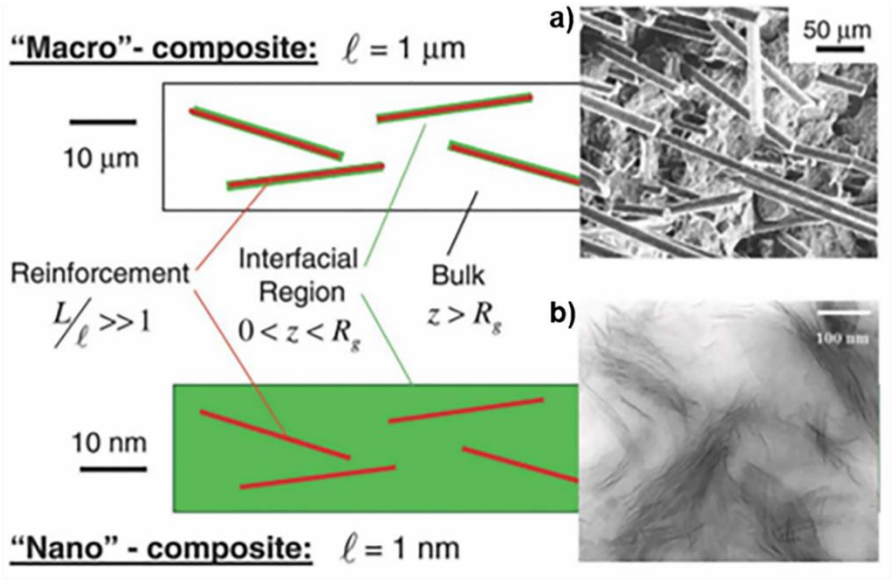

Figure 2.3. *Schematic comparison between a macro-composite and a nanocomposite at the same volume fraction of filler. The interfacial region (in green) extends into the matrix on the order of R_g, the radius of gyration of the polymer. a) Scanning electron micrograph shows E-glass reinforced polyolefin (15 μm fiber) and b) transmission electron micrograph shows montmorillonite-epoxy nanocomposite (1 nm thick layers) [37].*

From the mechanical point of view, the main advantage offered by nanoparticles is that their size is smaller than the critical crack length that typically initiates failure in traditional composites [38]. As a result, nanoparticles can provide an improvement in terms of toughness and strength. Generally, nanocomposites also offer enhancements in terms of electrical conductivity due to a better compactness of the polymer, leading to a better coupling among the nanoparticles through the grain boundaries [35]. Moreover, the use of active optical nanofillers, such as gold and silver nanoparticles, can allow to opportunely modulate the overall optical properties of the resulting nanocomposites, depending on the size, distribution and shape of the particles [39-41]. Transparent nanocomposites with enhanced mechanical and electrical properties have been developed, using nanofillers to regulate the index of refraction [42, 43]. In this case, the desired grade of transparency can be achieved by opportunely modulating the volume fraction of the nanoparticles.

A crucial aspect concerning nanocomposites regards the improvement of the nanofiller dispersion. This represents a not trivial task, and is a fundamental requirement in order to ensure homogeneous properties of the nanocomposites and to prevent losses in terms of fracture toughness typically due to nanofiller agglomeration [44-46].

2.2.1 Graphene-based nanocomposites: properties and fabrication

Graphene represents one of the most attractive materials currently employed to develop functional nanocomposites. It is one of the allotropes of carbon and is composed by a one-atom-thick planar sheets of sp^2 bonded carbon atoms that are densely packed in a honeycomb crystal lattice. This 2D structure can be wrapped up into 0D fullerenes, rolled into 1D nanotubes or stacked into 3D graphite, as shown in Figure 2.4 [47]. The exceptional properties shown by graphene justify its increasing use as functional filler, especially for polymer matrix-based nanocomposites. In particular, it possesses peculiar electrical characteristics, such as an anomalous quantum hall effect and a high electron mobility at room temperature (23×10^4 cm^2/Vs) [48, 49], and shows excellent mechanical performances [50]. Specifically, its high tensile strength, elasticity, Young's modulus (~1 TPa) and spring constant are mainly due to its hexagonal lattice structure, with the sp^2 bonds that confer stability and oppose in-plane deformations [51]. In addition, graphene shows a high thermal conductivity (~$4\text{-}5 \times 10^3$ $Wm^{-1}K^{-1}$) [52], and its field of application

is further extended by the possibility to functionalize it chemically. Several biological applications involving graphene highlighted its biocompatibility [53-56], even though this aspect is currently the subject of extensive investigations due to the possible toxicity of nanomaterials.

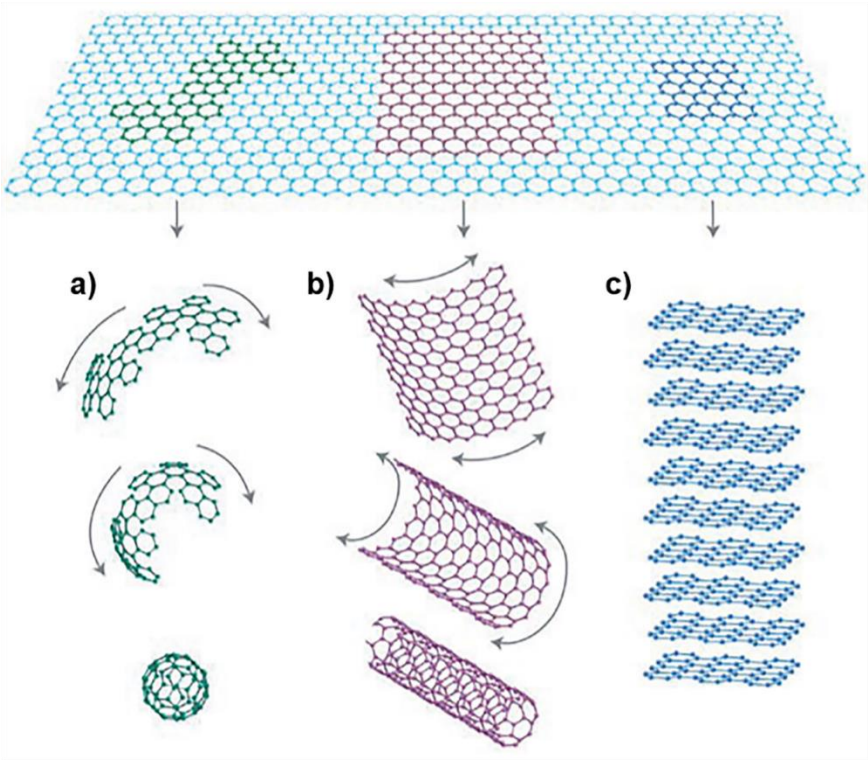

Figure 2.4. *Representation of 2D-structure of graphene that can be wrapped up into a) 0D fullerenes, rolled into b) 1D nanotubes or stacked into c) 3D graphite [57].*

Different approaches are currently used for the synthesis of graphene. These can be grouped in two main categories that are referred to as bottom-up and top-down methods. The bottom-up approaches allow, typically, a small-scale production, characterized by high quality and large size sheets, starting from compounds comprising carbon. These methods include techniques such as carbon vapor deposition (CVD), arc discharge, epitaxial growth on silicon carbide, self-assembly, and reduction of CO_2 [58], and allow to produce both monolayer and multiple-layer graphene. Conversely, the top-down methods allow a large-scale production of graphene with small size, pure or opportunely functionalized. Therefore, this approach is particularly suitable to synthetize graphene to be used as filler in polymer nanocomposites. It involves the separation of graphene

directly from graphite or graphite derivative, and includes several methods such as the exfoliation or super acid dissolution of graphite, the solvothermal reduction or chemical reduction of graphite oxide, and thermal exfoliation/reduction of graphite oxide.

In general, the commonly referred "graphite oxide" (GO) is made of graphene oxide sheets, stacked with an interlayer spacing between 6 and 10 Å depending on the water content [59]. According to the Lerf-Klinowski model [60-62], graphene oxide can be described as pristine aromatic "islands" separated from each other by aliphatic regions, containing epoxide and hydroxyl groups and carbon-carbon double bonds. Typically, hydroxyl and epoxy groups can be detected at higher concentrations on the basal plane of graphene oxide, whereas carbonyl and carboxylate acid groups at the sheet edges [62]. A representation of graphene, graphene oxide, and reduced graphene oxide structures is shown in Figure 2.5a.

The thermal exfoliation of GO allows to separate the graphene oxide sheets and reduce the oxygen content, generally leading to restore the attitude to conduct electricity [63]. In particular, GO can be reduced and exfoliated simultaneously upon a rapid heating, that induces the thermal decomposition of the oxygen-containing functional groups with the pressure of the gas products, in particular CO_2, that builds up instantaneously between the sheets [63-65]. The obtained graphene can be dispersed in polar organic solvents due to the polar oxygen-containing functional groups remained on it and to its wrinkled nature preventing the sheets from restacking [63, 64, 66]. The oxygen-to-carbon element ratio and the electrical conductivity of the resulting graphene can be modulated depending on the time and temperature adopted during the process [67]. For instance, high quality graphene with less structural and topological defects was obtained at lower process temperatures, under vacuum, or in presence of accelerating agent, such as H_2 or HCl, or with microwave or irradiation assistance [68, 69]. Figure 2.5b shows the possible steps leading from graphite to reduced graphene oxide during synthesis.

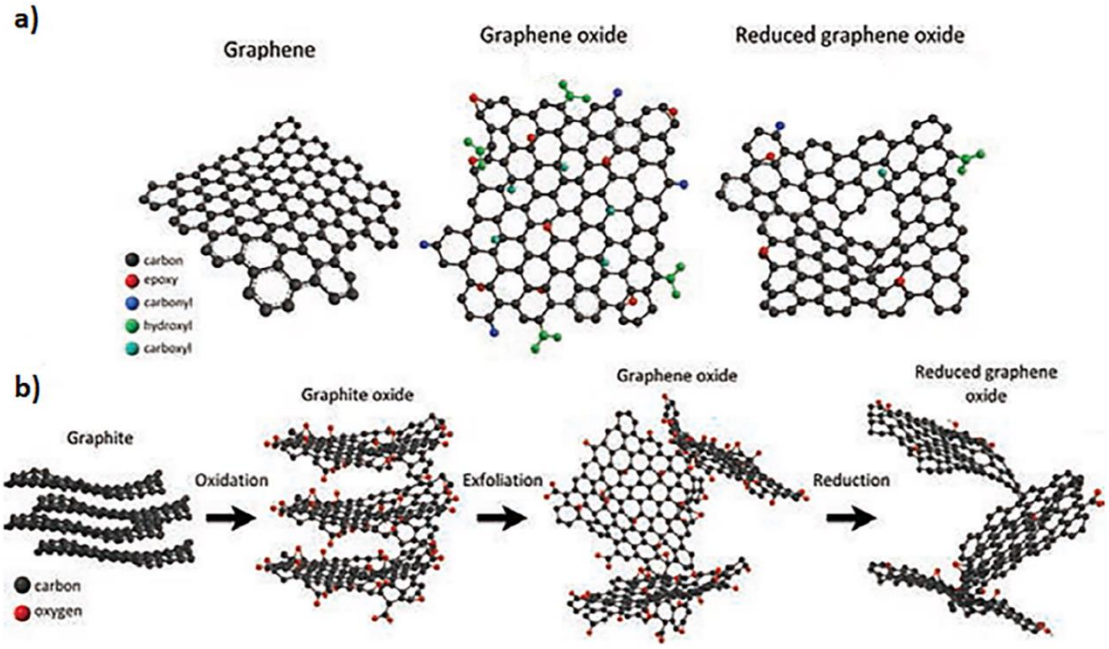

Figure 2.5. *a) Representation of graphene, graphene oxide, and reduced graphene oxide structures; b) Schematic steps from graphite to reduced graphene oxide [70].*

The chemical functionalization of graphene represents a valid aim approach in the perspective to improve the interaction between the filler and the polymer matrix, further increasing the solubility of the reinforcement [71-74]. The process involves functional groups that can be small molecules [75] or polymer chains [76], and both covalent and non-covalent functionalization can be carried out [77]. In particular, covalent functionalization can be performed at the end of the graphene sheets or on their surface and involves a rehybridization of one or more sp^2 carbon atoms into the sp^3 configuration by means of the mechanisms of nucleophilic substitution, electrophilic addition, condensation or addition [78]. Concerning the non-covalent functionalization, it allows the connection between the molecules without involving chemical bonds and, generally, requires the physical adsorption of suitable molecules on the graphene surface [79]. Specifically, these molecules wrap around graphene by means of van der Waals forces and can involve π–π interactions, electrostatic attraction, adsorption of surfactants and polymer wrapping [80-83].

After selection of the desired polymer and graphene nanofiller, taking into account their starting properties and the possibilities to maximize and optimize their interaction, three different methods can be commonly used to fabricate the related nanocomposites:

solution blending, in-situ polymerization and melt-mixing. In particular, solution blending, which can be considered the most known technique, involves the polymer solubilization in a suitable solvent and the mixing with graphene to form a dispersion. Generally, polymers such as polystyrene, polycarbonate, polyacrylamide, polyimides and poly(methyl methacrylate) are mixed with graphene oxide [84-87], that can be previously functionalized with isocyanates, alkylamine or alkyl-chlorosilanes in order to improve its dispersibility in organic solvents.

In-situ polymerization is based on the polymerization of the matrix in presence of the selected filler, starting from the monomer mixed with the reinforcement. Typically, this approach allows to obtain a good grade of dispersion of graphene-based nanofillers avoiding their previous exfoliation. Concerning melt mixing technique, it allows to disperse the filler in the polymer matrix exploiting high temperatures and shear forces. In particular, the high temperature liquefies the polymer phase facilitating the dispersion or intercalation of graphene oxide nanoplatelets avoiding the use of toxic solvents.

After fabrication, the properties of the resulting nanocomposites can be further related to interfacial adhesion, spatial distribution and alignment of the graphene nanofiller. In particular, polymer nanocomposites with low loadings of functionalized graphene sheets generally exhibit a shift in the glass transition temperature [84], if compared with the value of the uncharged polymer. This behavior can be ascribed to a reduced mobility of the polymer chains at the interfaces between the filler and the matrix [88, 89]. Therefore, the effect of constraint applied on the chains can directly induce an increase in glass transition temperature.

Performances in terms of thermal conductivity can be evaluated referring to the 2D geometry of the graphene fillers. They are characterized by a lower interfacial thermal resistance that provides a higher thermal conductivity to the host polymer matrix. Nevertheless, the 2D structure can be source of anisotropy in the nanocomposites arrangement, for which thermal conductivity in plane results as much as ten times higher than the cross-plane conductivity [90]. It is typically evaluated following the percolation theory, therefore considering phonons as the main mode for thermal conduction in polymers. Covalent bonding between filler and matrix can reduce phonon scattering at the interfaces leading to an overall enhancement of the thermal conductivity [91].

The behavior of nanocomposites in terms of electrical conductivity can be assessed considering the influence of different factors and their overall effect. In particular, the characteristics of the specific graphene-based filler, such as its aspect ratio and morphology, as well as its inter-sheet junction, can affect the electrical performances. In the same way, processing and dispersion, and the related state of aggregation and alignment of the nanoparticles concur to determine the electrical behavior of the resulting nanocomposites. Several theoretical models and experiments have focused, in particular, to effectively relate the effect of filler shape, geometry and state of dispersion to the percolation threshold [92, 93].

As mentioned above, the overall performance of nanocomposite materials can be related to the quality and stability of the polymer/filler interphase region. Typically, physical and mechanical properties and chemical composition of this region are different from the bulk polymer matrix [94, 95]. In the case of an interphase stiffer than the surrounding polymer, this can result in higher overall stiffness and strength of the composite, but with lower resistance to fracture [96]. The interphase properties can interfere with the mechanical behavior of the nanocomposites also depending on their morphology and size, therefore its thickness can be tailored with the aim to achieve both higher strength and improved toughness of the resulting nanocomposites. Generally, force modulation AFM and nanoindentation are used to investigate the interphase and its properties [94, 97]. In particular, AFM phase imaging is currently considered a useful tool to evaluate the thickness and the relative stiffness of the interphase, since it involves much lower interaction forces between the probe and the sample than force modulation or nanoindentation [96]. The arrangement of graphene-based fillers inside the matrix is also investigated in order to assess the state of dispersion at the microstructural level and its impact on the nanocomposites properties. Results reveal that graphene-based fillers, such as graphene oxide or graphene nanoplatelets (GNPs), can arrange differently in the host polymer, originating structural states that can be classified as stacked, intercalated or exfoliated, as shown in Figure 2.6.

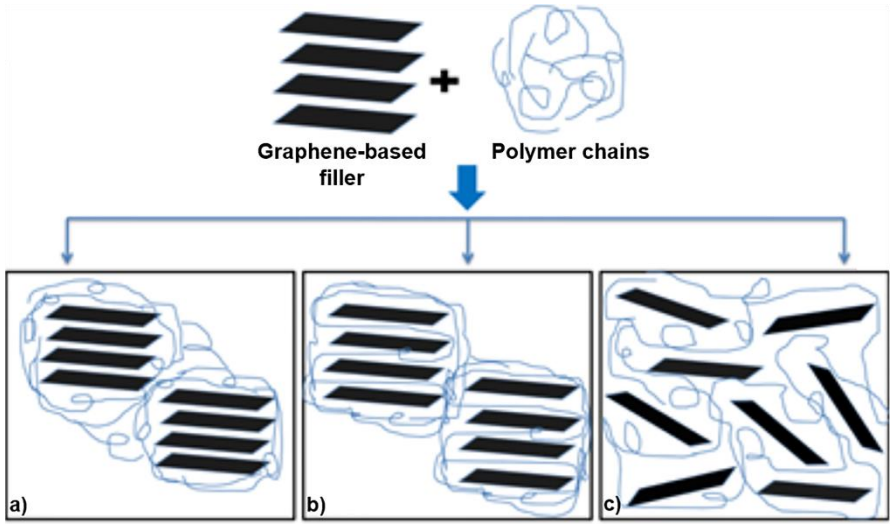

Figure 2.6. *Schematic representation of different filler arrangements in graphene-based nanocomposites: a) separated, b) intercalated and c) exfoliated state. Adapted from Ref. [98].*

The intercalated state can be considered a particular stacked structure characterized by a greater interlayer spacing, but within a few nanometers [99]. Generally, in the exfoliated structure, GNPs have the largest interfacial contact with the polymer matrix, and this allows to improve the performances of the composites in different ways. Due to the interactions with the matrix, the exfoliated phase can exhibit a curved shape. In this case, the rumpled shape assumed by the filler can result in a mechanical interlocking that represents a possible mechanism of strengthening. Therefore, the compatibility between the host polymer and the nanoplatelets is one of the factors that influence the filler arrangement encouraging it to adopt a more extended conformation in case of affinity or, conversely, a crumpled conformation when the affinity decreases [100]. Further, the technique used to fabricate the nanocomposites can affect the microstructure, as well as the characteristics of the filler prior to the process. Solution mixing or in-situ polymerization generally induce an exfoliated and randomly oriented status of the nanoplatelets, whereas the melt mixing technique originates a more oriented and intercalated or stacked structure [101].

2.3 Applications of composite materials in sensing devices

The enhanced properties of composite and nanocomposite materials and the possibility to tailor their performances towards more and more specific applications make them suitable materials for sensing. In this perspective, the ability to detect an external stimulus, having a chemical, physical or biological nature, and give information about it can be developed through an accurate selection and a successive engineering of the starting materials.

Graphene is one of the most promising materials for sensing applications, and its properties are widely employed singularly or functionally combined with other suitable materials. Metal oxide nanoparticles, for instance, are usually coupled with graphene (Figure 2.7a), graphene oxide or reduced graphene oxide for large-scale production of sensing devices in different fields, from environmental pollutions, safety and security to clinical and pharmacological detections. Another effective fusion has been realized coupling graphene and biological molecules, which results in hybrid nanomaterials with enhanced and functional properties that can be wisely employed for sensing applications [102, 103]. Figure 2.7b summarizes the main biomolecules that are typically combined with graphene and the possible interactions (covalent, electrostatic) between them.

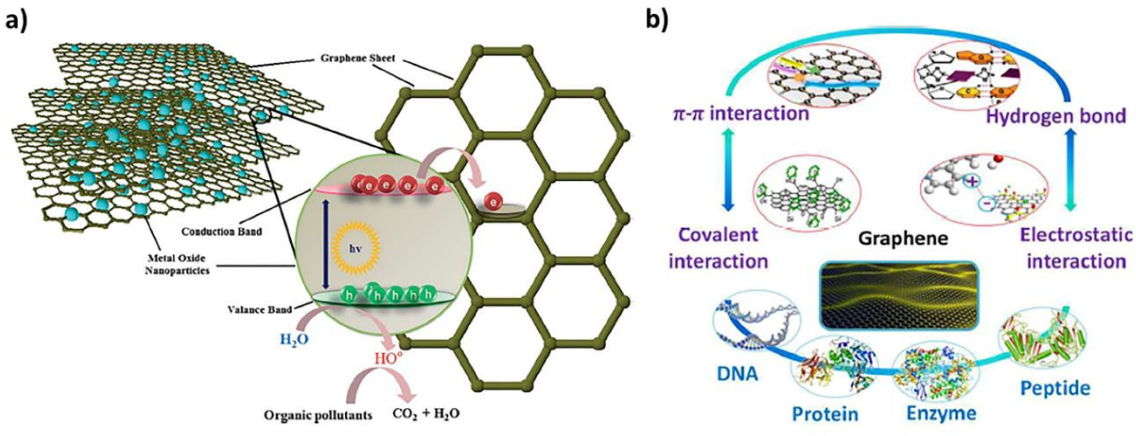

Figure 2.7. *a) Representation of graphene sheets decorated with metal oxide nanoparticles acting for pollutants detection [104]; b) Schematic representation of graphene coupled with biological molecules through different types of interaction [102].*

For instance, DNA molecules can be effectively immobilized onto graphene surface by physical adsorption or chemical binding, creating sensitive platforms where each binding event with the analyte can be detected through the changes of the electric or electrochemical properties of these platforms [105]. Noncovalent interactions can be promoted through the physical adsorption, involving π-π stacking interactions between the DNA nucleobases and the aromatic surface of graphene. In particular, in the case of single-stranded DNA (ssDNA), stable aqueous dispersions of graphene/DNA can be obtained, without traces of sedimentation for months [106]. Double-stranded DNA (dsDNA) is also used as dispersing agent for graphene nanoplatelets. However, in this case less stable aqueous solutions are obtained due to the weaker hydrophobic interactions arising from the base pairing of the nucleobases. Nevertheless, the graphene/dsDNA affinity can be significantly enhanced by further functionalizing graphene oxide with polar groups, which are able to establish electrostatic interactions with the DNA bases. The immobilization of DNA onto graphene through covalent bonds is generally carried out after functionalizing DNA with an amino group, which is able to interact with the graphene oxide surface via carbodiimide chemistry. In particular, amine-terminated ssDNA can be linked to the surface of graphene oxide directly or through the involvement of specific molecules that act as carriers. Zhang et al. developed a sensing surface based on graphene/DNA, where dopamine molecules were used for the reduction of graphene oxide and as carriers to link ssDNA that was previously treated with an alkylamino modifier. This graphene/DNA assembly was employed as a rapid and low-cost detection platform for mercury ions (Hg^{2+}), showing a detection limit of 5.0×10^{-9} M [107].

Graphene nanocomposites decorated with metals or metal oxides are widely used as gas sensors, such as in the case of copper oxide (Cu_2O) and zinc oxide (ZnO), respectively employed for detecting nitrogen dioxide (NO_2) and carbon monoxide (CO) [108, 109]. Graphene oxide and reduced graphene oxide can trap gas molecules causing a variation in the conducting properties, with a different effect promoted by oxidizing and reducing gases, which induce carrier generation or carrier annihilation, leading to a change in the device resistance or current. The cumulative contributions from metals and graphene oxide can enhance the response of the sensing nanocomposite, whereas the choice of the specific metal can be performed evaluating the best solid-gas interactions, depending on the nature of the analyte. In particular, palladium exhibits a significant

affinity for hydrogen, promoting the dissociation of its molecules into atoms [110], whereas nickel is more appropriate for the carbon monoxide detection, forming nickel carbonyl with a sufficiently low activation energy [111].

Gas detection is also accomplished by using composites that work as cataluminescence sensors. Their sensitivity is based on light emissions during a solid-gas interaction, and they can act as selective sensors due to the different luminescence signatures associated to the volatile organic compounds. Generally, they show a fast response, good reproducibility, long-term stability and they are able to detect very low concentrations (~1 ppm) of the analyte due to the reduced noise level [112]. For instance, composites based on tin dioxide (SnO_2)/graphene can be used for propanol detection [113], with a luminous output due to the catalytic oxidation of propanol molecules on the composite surface.

Functional groups exhibited by graphene oxide and reduced graphene oxide on their surfaces, such as carboxylic and hydroxyl ones, make them suitable fluorometric [104, 105] and voltammetric [106] probes for pH. Moreover, graphene oxide can be employed to detect biological analytes, such as uric acid and ascorbic acid [114], hydroquinone and catechol [115], and nucleic bases [116, 117]. The presence of functional groups on the surfaces is fundamental in order to create hydrogen bonds with the analytes, so the strength of these bonds and the distance between the interaction sites and the reaction center make possible the following discrimination of the analytes.

A large number of sensors based on the application of composite materials are involved in the monitoring of human health. In this perspective, the sensing materials need to be comfortable to wear, biocompatible, and lightweight. Recently, wearable sensors of temperature were developed using graphene oxide fibers that allow the integration into clothes and assure a real-time detection. In particular, they can offer a fast response time (7 s), good recovery time (20 s), high responsivity to temperature, and their sensitivity is not affected by eventual deformations [118]. Another wearable device was proposed by Park et al., consisting in contact lens that allowed a real-time and wireless detection of the glucose concentration in tears [119]. This device was based on a rectifier circuit, a glucose sensor and light-emitting diode fixed on a hybrid substrate, while a stretchable, transparent antenna and the interconnect electrodes made by silver nanofibers were placed on elastic regions. Specifically, the glucose sensing was realized

immobilizing glucose oxidase and catalase on a graphene surface. Electrolyte detection can be also realized by means of graphene-based structures, such as sheets and flakes, which are able to increase the hydrophobicity of the electrode surface involved in detection, due to their high surface area, excellent conductivity, electrocatalytic activity and promoting the electron transportation during the ion exchange between electrode and solution [120-122].

The development of new composite materials using biomolecules, such as enzymes, has allowed to extend even more the field of sensing applications in medical diagnosis, environmental and bioindustrial analysis. For instance, urease enzyme was successfully immobilized, and nanocomposite fibers of urease and polyvinylpyrrolidone (PVP) were fabricated [123] with the aim to detect low concentrations of urea and, at the same time, to offer a fast response time. Another sensing system for urea detection was developed through a co-immobilization of two different enzymes, as urease and glutamate dehydrogenase, onto superparamagnetic iron oxide nanoparticles-chitosan films [124]. In this case, an increased active surface area was obtained in order to carry out the immobilization of the enzymes, with an enhanced electron transfer and an increased shelf-life of the sensor. Figure 2.8 offers a representation of enzyme and antibody immobilizations on graphene surface for the realization of composite biosensors.

Biosensing also implies advances towards even more complex structures, able to enhance the overall sensitivity of the detecting surface. In this perspective, a sensing composite material was realized using fractal nanoplatinum with a cauliflower-like morphology, which was developed on a reduced graphene oxide paper [125]. As a result, a conductive composite paper with a high electroactive surface was obtained and then functionalized using glucose oxidase, via chitosan encapsulation, or RNA aptamer, via covalent linking. In this way, the material sensitivity towards glucose or Escherichia coli bacteria can be activated, depending on the type of the enzyme selected, and obtaining good performances in terms of sensitivity and response times.

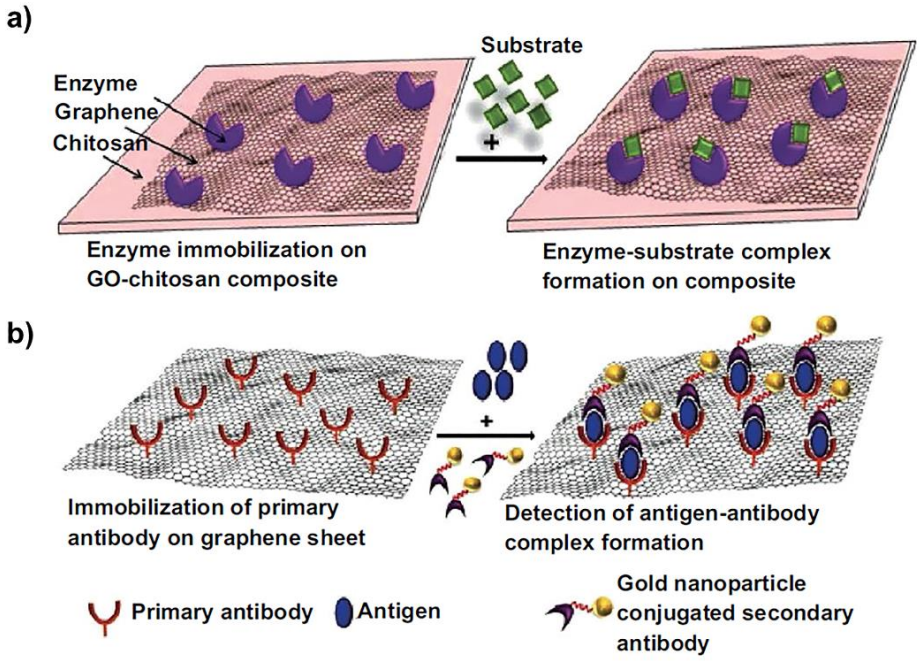

Figure 2.8. *a) Representation of graphene-chitosan composite biosensor for monitoring enzyme activity [126]; b) Representation of graphene bio-decorated sheet for antigen-antibody detection [126].*

The possibility to create devices based on composite materials comfortable to wear, encouraged advances in development of sensitive pressure, tactile and strain sensors. In recent years, piezoresistive pressure sensors based on composites with functional architectures have been realized, exhibiting high sensitivity and low power consumptions [124]. In particular, these materials are able to offer better performances if compared with the standard piezoresistive sensors having a planar structure, which are not suitable to ensure a good sensitivity or for detecting low pressures (< 10 kPa). Moreover, a sensor able to monitor wrist pulse and carotid artery pulse was developed starting from a millefeuille-like multilayer architecture of reduced graphene oxide, intercalated by covalently tethered molecular pillars [125]. This device showed good performances in terms of response time, durability and robustness.

Composite materials are also involved in the engineering of ultraviolet (UV) detectors, typically exploiting nanotechnologies comprising structures such as zinc oxide nanorods, gold and silver nanoparticles. In particular, gold nanoparticles were embedded into the pores of silicon matrix photodetectors with the aim to improve the rectification

properties of junction and so the overall device sensitivity (Figure 2.9a) [127]. Moreover, high-performance UV photodetectors were obtained assembling silver nanoparticles onto zinc oxide nanowires that resulted in sensing composite arrays (Figure 2.9b) [128].

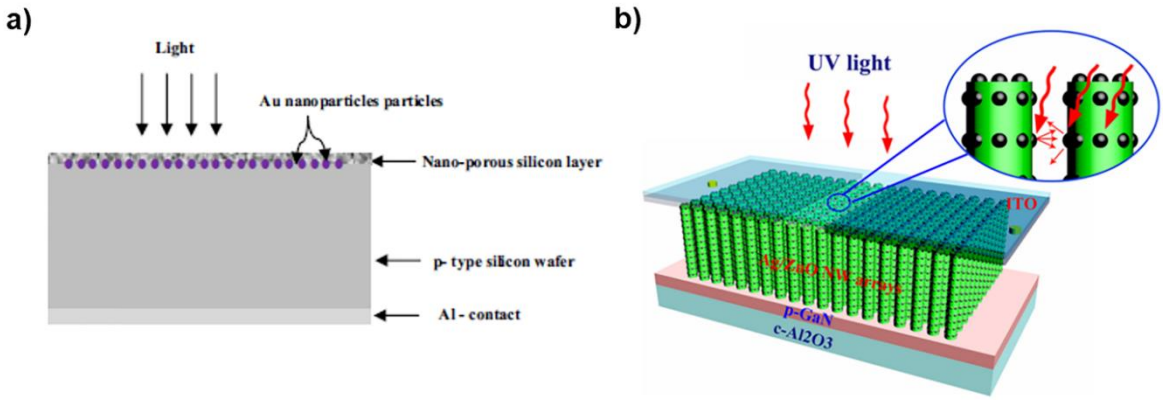

Figure 2.9. *a) Schematic representation of a photodetector based on a composite structure of gold nanoparticles embedded into silicon pores [127]; b) Schematic representation of sensing composite arrays based on silver nanoparticles onto zinc oxide nanowires [128].*

Graphene properties were exploited also for UV sensing, with the effect to improve the carrier transport, UV absorption and so the photoresponse. For instance, composites based on zinc oxide nanowires and reduced graphene oxide were fabricated [129, 130], showing enhanced performances if compared with the photodetectors based on nanowires made of pure zinc oxide. In particular, the graphene nanosheets allowed the development of conductive networks, and a photoresponse enhancement was favored by the large interface regions between graphene and zinc, which act preventing the carrier recombination and facilitating its transport [130]. Reduced graphene oxide was also combined with tungsten oxide nanodiscs [131], obtaining a UV-sensitive composite material. Tungsten oxide shows an indirect large energy band gap that makes it a good candidate for UV detection, nevertheless only a few studies [132, 133] focused on its employment for this purpose, probably due to its very slow response time. The coupling of tungsten oxide with reduced graphene oxide lead to a response time on the order of milliseconds [131], with an improvement that, also for this sensing composite, can be attributed to the carrier transport efficiency of graphene. Another kind of UV detecting

composite was developed exploiting colorimetric and fluorescence photochromism [134]. This sensor, based on polyoxometalate and viologen, showed different blue coloration states that were related to the UV irradiation intensities.

Novel sensing devices have been realized to monitor the health status of structures employing advanced composites. Current approaches include the use of sensors that can be applied into the structure that must be monitored or on its outside surface, detecting the damage as reaction to the involved changes. In general, strain sensing is implied in structural health monitoring, and this can be carried out exploiting nanocomposites typically filled with carbon nanotubes [135-138]. Among different CNT-based sensors, one type was developed by growing the CNTs on glass fibers ("fuzzy fibers") [139], exhibiting similar sensitivity to conventional strain gages, but with the advantage to be easily integrated into the structures to be monitored.

Nevertheless, the high cost of the CNTs has encouraged the development of new solutions, such as graphene–polyvinylidene fluoride nanocomposites [140]. These sensing materials were realized selecting polyvinylidene fluoride as matrix, due to its high chemical resistance and high temperature sustainability, and functionalizing the graphene-sheets filler in order to maximize their dispersibility into the matrix. In this case, a real-time response under tensile loads was obtained as a consequence of the variation of the composite electrical properties upon a mechanical deformation at the nanoscale. These materials can be used as strain sensors, exhibiting better performances if compared with the carbon nanotubes-based sensors, and assuring, at the same time, low cost, light weight and flexibility. Graphene-epoxy nanocomposites were also developed as suitable strain sensors and used for health structures detection [141], after deposition on the carbon fiber-reinforced composites to be monitored. In this case, a model able to predict the sensor piezoresistive behavior up to high deformation was also provided.

Another interesting field of application involving sensitive composites deals with the evaluation of the level of humidity, which is essential for several industrial applications as well as for human comfort. Typically, a quartz crystal microbalance is used, exploiting the principle that the mass change by mass loading on its piezoelectric crystal surface can be related to a shift in resonance frequency, where this shift can be measured as a function of the water vapor content [142-144]. The electrode of the quartz crystal microbalance is usually coated with a suitable film [145-147], in order to obtain

an improvement of the measurement of the trace water vapor content in the moist air. For instance, using a film of CNT/Nafion, the water molecules can easily have access to the hexagonal conformation of the CNTs, with an increase in the frequency response as the weight ratio of CNT-to-Nafion increases [148]. In this way, the composite coating allowed to enhance the sensitivity of the detecting system, especially at low humidity levels.

2.4 The space environment and UV radiation

The increasing interest in space exploration is accompanied by an increasing awareness of its characteristic environment, which is commonly referred as complex and harsh, according to the results from the experiments performed during the space missions.

The main factors that affect the Sun-Earth space are typically time-varying and include plasmas, high-energy charged particles, neutral gases, x-rays, meteoroids, orbital debris and the ultraviolet (UV) radiation. During a space mission, each of these factors can contribute to a different extent, interfering with the spacecraft system and inducing a degradation of materials as a consequence of thermal changes, contamination, radiation damage and background interference [149]. Differently from other factors, a part of UV radiation, depending on the wavelength, also affects the lower atmosphere and can reach the Earth's surface. Specifically, the solar UV radiation corresponds to a band of the electromagnetic spectrum characterized by wavelengths of about 100 to 400 nanometers, and typically classified as UV-A (315–400 nm), UV-B (280–315 nm) and UV–C (100–280 nm), following recommendation of the International Commission on Illumination ("*Commission Internationale de l'Éclairage"- CIE*) [150]. The wavelengths from 10 to 124 nm, partially overlapped with the UV-C band, were not included in this classification, but commonly referred as a subgroup of UV radiation, known as EUV (extreme ultraviolet) radiation.

The amount of UV radiation at the Earth's surface can be related to different agents and processes. In particular, atmospheric oxygen and ozone are responsible for absorbing most of the solar radiation at wavelengths less than 280 nm, so that UV-C cannot reach the troposphere. At increasing wavelengths, the ozone ability to UV absorption decreases, leading to the passage of a large amount of radiation at wavelengths greater than 320 nm (the UV-A region). Moreover, scattering processes can interfere with the UV radiation

path towards the Earth's surface. In particular, they can take place at molecular level (*Rayleigh scattering*) or interest large particles, such as cloud components and aerosols [151]. Figure 2.10 shows the UV spectral irradiance at the top of the atmosphere and at the Earth's surface detected for clear sky conditions.

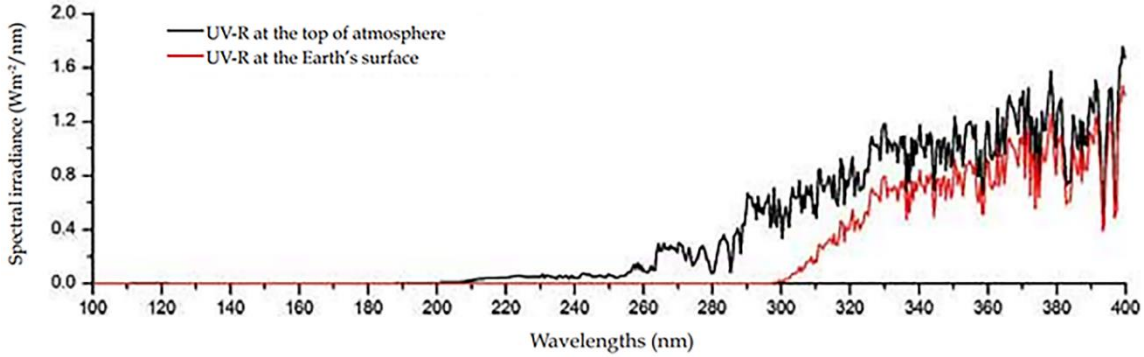

Figure 2.10. *UV spectral irradiance at the top of the atmosphere (black line) and at the Earth's surface (red line) for clear sky conditions [152].*

In a broader view, variations in the incident UV flux, referred to a generic planetary body, can be related not only to the atmosphere-radiation interactions, but also to the overall effect of manifold conditions, that can be firstly researched on the UV origin, the Sun. Specifically, the Sun is a G-type star with a radiant spectrum matching that of a 5500–6000 °C blackbody and able to emit photons ranging from ~1 nm (soft X-rays) to ~105 nm (radio waves). Most of the radiant energy involves infrared (~37%), visible (~43%), and UV (~7%) wavelengths [153]. Generally, in order to quantify the total amount of solar radiation that a planetary body can receive, the solar constant value (*S*) is considered, referred to an area that falls above the atmosphere at a vertical angle, and corresponding to 1371 W/m^2 at the mean Earth–Sun distance (1 astronomical unit or 1 a.u.). UV radiation is affected by a variability that is intrinsically related to the solar dynamics, and in particular that can be connected to the events on the upper photosphere, chromosphere and corona of the Sun, where this type of radiation originates [154]. Moreover, considering the planetary bodies which lack atmospheres, the incident UV flux on their surface is affected, at any point, by several conditions such as orbital position, Sun elevation angle, latitudinal changes, rotational periods, and radiation reflections off nearby surfaces [155]. Therefore, these bodies can receive a UV flux in a range from zero

to a value that can exceed the solar constant, especially due to the amount of radiation reflected off by other planetary surfaces or spacecrafts.

In general, for the planetary bodies with a proper atmosphere, the amount of UV absorption, reflection, and scattering can be expressed as a function of the atmospheric density. For instance, a comparison between Earth and Mars, which is nowadays one of the planets on which increasing investigation is focused, can be considered in order to highlight the influence of the atmospheric environment on the UV flux at the planet surface. In particular, this flux resulted more attenuated on the Earth's surface, where the atmospheric density is over 100 times the density of the average value reported for Mars [156]. Moreover, extremely cold surface temperatures induce significant pressure fluctuations on Mars, of ~40%, with values between ~6 and ~10 mbar, with the resulting effect to depress the shorter UV-C and UV-B spectral regions during the periods characterized by higher pressure [157, 158]. This phenomenon can be explained by the significant percentage of the Martian CO_2 that freezes into solid CO_2 at the poles during winter months, resublimating in the spring and summer, with the aforementioned results in terms of pressure and UV absorption. Figure 2.11a shows the atmospheric components of the Earth and the pressure values at different altitudes, whereas in Figure 2.11b the characteristics of Mars atmosphere at different altitudes and the temperature profiles retrieved from the entry probes of Mars landers are reported.

CO_2 can be considered the major UV-absorbing gas in the Martian atmosphere, especially in the case of solar UV radiation shorter than 190 nm [159], with the result that the UV environment on the Martian surface is much richer in UV-C and UV-B than on Earth's surface. The atmospheric gas composition of the Earth is mainly characterized by diatomic nitrogen (~78%) and oxygen (~21%), where a portion of the oxygen in the stratosphere interacts with sunlight and is converted to ozone, which strongly absorbs UV wavelengths shorter than ~300 nm [160]. Differently, the atmosphere of Mars, is mainly composed by carbon dioxide (~95%), with extremely low levels of oxygen (~0.13%), and ozone (~0.000004%) [161]. In addition, the amount of UV radiation striking the Martian surface is also influenced by severe variation in its axial tilt relative to the Sun [158], much more than in the case of Earth. In particular, the Mars axial tilt can vary between a low of nearly 10° to a high of 60°, over cycles lasting 10^5 years. Further, despite a greater distance from the Sun and the resulting solar constant that is 43% that of Earth's,

it was estimated that, under clear-sky conditions, the DNA-weighted UV irradiance on the Martian surface is approximately 3 orders of magnitude higher than that on Earth [158].

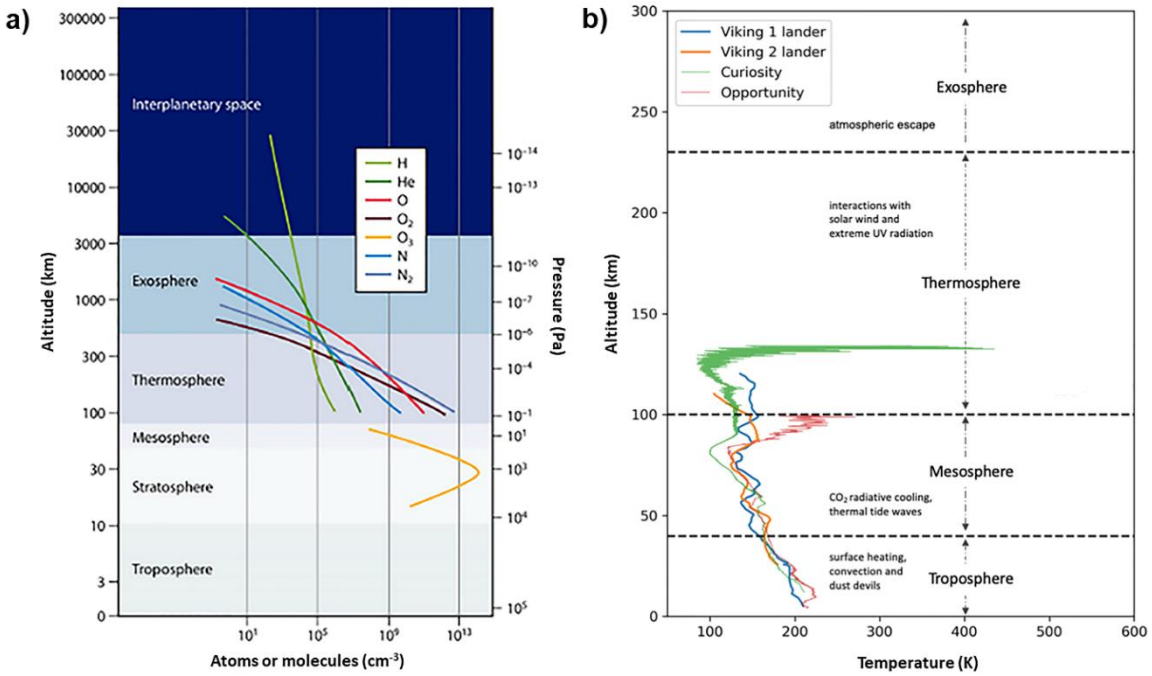

Figure 2.11. *a) Earth's atmospheric components and pressure at different altitudes [162]; b) Characteristics of Mars atmosphere at different altitudes and temperature profiles retrieved from the entry probes of Mars landers [163].*

Other atmospheric components such as vapor droplets, water ice and dust contribute actively to absorb, reflect, and scatter incident UV. In particular, in the case of Earth, solid particulates include the smoke from combustion and volcanism and airborne dust from windstorms, whereas, in the case of Mars, the impact of meteors and erosion on the surface, originate dust that moves into its atmosphere [164], interfering with the UV path. The overall impact of the atmospheric factors on the incoming solar radiation can be expressed by the *optical depth* [165]. On Mars, this value can reach 0.1 in a condition of a completely dust free atmosphere, corresponding to an atmospheric pressure of 7.1 mbar, which would produce an approximate 10% attenuation of UV irradiation [166]. Clear-sky conditions can induce an optical depth that ranges between 0.3 and 0.5, up to a value from

3.5 to 5 in global dust storm conditions [165, 167], which would cause a UV attenuation of about 25–97% [166].

The high number of factors that can influence the UV exposure suggests the necessity of a reliable system able to detect and quantify the level of irradiation, especially during the space missions, not less for the terrestrial necessities. UV damaging effects on human health and structures motivate the need to prevent harmful exposures, nevertheless the knowledge of the UV levels can allow to assess other UV-depending variables, as those concerning the state of the Earth's atmosphere and the Sun dynamics.

Sun is referred as the main natural source of UV radiation, but artificial UV sources have also been developed and they need to be opportunely monitored. According to the Health Physics Society, artificial UV sources include tanning booths, black lights, curing lamps, germicidal lamps, mercury vapor lamps, halogen lights, high-intensity discharge lamps, fluorescent and incandescent sources, and some types of lasers [168]. Light-emitting diodes (LEDs), lasers and arc lamps are generally used as UV sources, at different wavelengths, for industrial, medical and research applications. For instance, the emission spectrum of some models of commercially available UV lamps is reported (Figure 2.12). Specifically, disinfection and sterilization processes are typically carried out using UV-C radiation [169, 170], which is able to inactivate viruses and bacteria, and is generated by a low-pressure mercury discharge. The combination of UV-C and ozone can be effectively employed in reducing the undesired organic content of water, as in the case of the wash water for the fresh-cut vegetable industry [171]. Further, for the industrial processes that need a photochemical hardening, artificial UV-A sources are typically employed, as for glues, limiting the use of UV-B and UV-C sources only for the applications requiring highly energetic treatments.

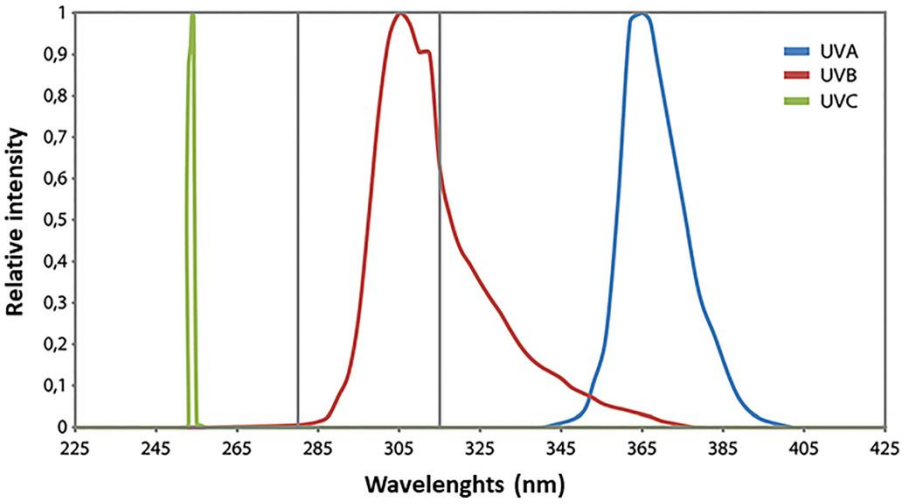

Figure 2.12. *Emission spectrum of different UV lamps. UV-A, UV-B and UV-C emissions referred to B100 (UVP), RPR-3000 (Southern New England Ultraviolet Co.) and BLE-8T254 (Spectronics Corporation) lamps, respectively [172].*

Sometimes, UV radiation is exploited to induce fluorescence, that is commonly employed for materials inspection. In this case, several lamps can be used based on different phosphors able to produce a wide range of spectral emissions in the range of the visible radiation, as well as in the UV-A and UV-B regions [173]. In the field of medical applications, xenon lamps are generally employed [174-176], especially for dermatological treatment, and they are opportunely filtered in order to prevent hazardous exposure to UV-A, UV-B and UV-C radiation.

2.4.1 UV radiation effects on human health and structures

UV radiation is able to actively interact with biological systems and structures causing, under certain conditions, significant alterations that can lead to damage and not-reversible effects. In particular, UV photons can interact with essential biological molecules, such as DNA or proteins, inducing photochemical absorptions [177]. The high energy of a short-wavelength UV photon (UV-C <280 nm, UV-B 280–315 nm) is directly absorbed by DNA bases, with a maximum at 260 nm [177]. Differently, at longer wavelengths as UV-A (315–400 nm), indirect mechanisms can be induced, such as the generation of reactive and damaging species as free radicals [178]. Figure 2.13a shows a

schematic representation of direct and indirect interactions between UV radiation and a biological system.

A large number of studies has been performed in order to evaluate a possible correlation between skin cancers and UV exposure, providing evidences that led the *International Agency for Research on Cancer* to establish this type of radiation as a human carcinogen [179]. It was demonstrated that mutations in cancer-relevant genes are produced by UV photoproducts that are not repaired before DNA replication [180]. Specifically, UV radiation at short wavelengths induces DNA damages in terms of chemical modifications, such as cyclobutane pyrimidine dimers (CPDs) and pyrimidine (6-4) pyrimidone photoproducts (6-4PPs) (Figure 2.13b) [181, 182], whereas DNA single-strand and double-strand breaks can occur as a consequence of failures during the DNA repair steps of CPDs and 6–4PPs [183-185]. Moreover, the indirect mechanisms promoted by UV-A involve typically reactive oxygen species, inducing damages that can be related to the oxidation of the DNA bases [186-188].

Several studies focused on the gene *p53*, which acts as human tumor suppressor and exhibits mutations in a high percentage of human skin cancers [180, 189, 190]. This gene is normally able to assure the genomic stability by enforcing the arrest of the G1 cell cycle or inducing the apoptosis in response to different types of cellular stress [191-193]. In particular, by promoting the arrest of the G1 cycle, the gene *p53* activates cellular pathways able to remove possible lesions involving DNA, before the processes of synthesis and mitosis, whereas, inducing the apoptosis, it allows to eliminate potential progenitors of malignant tumor cells [194-196]. Results show that the formation of CPDs and the DNA efficiency to repair them contribute to alter this gene, and, in particular, the sites of mutation coincide with sites where the DNA repair is particularly slow [197], where this can be quantified by removal of UV-induced CPDs.

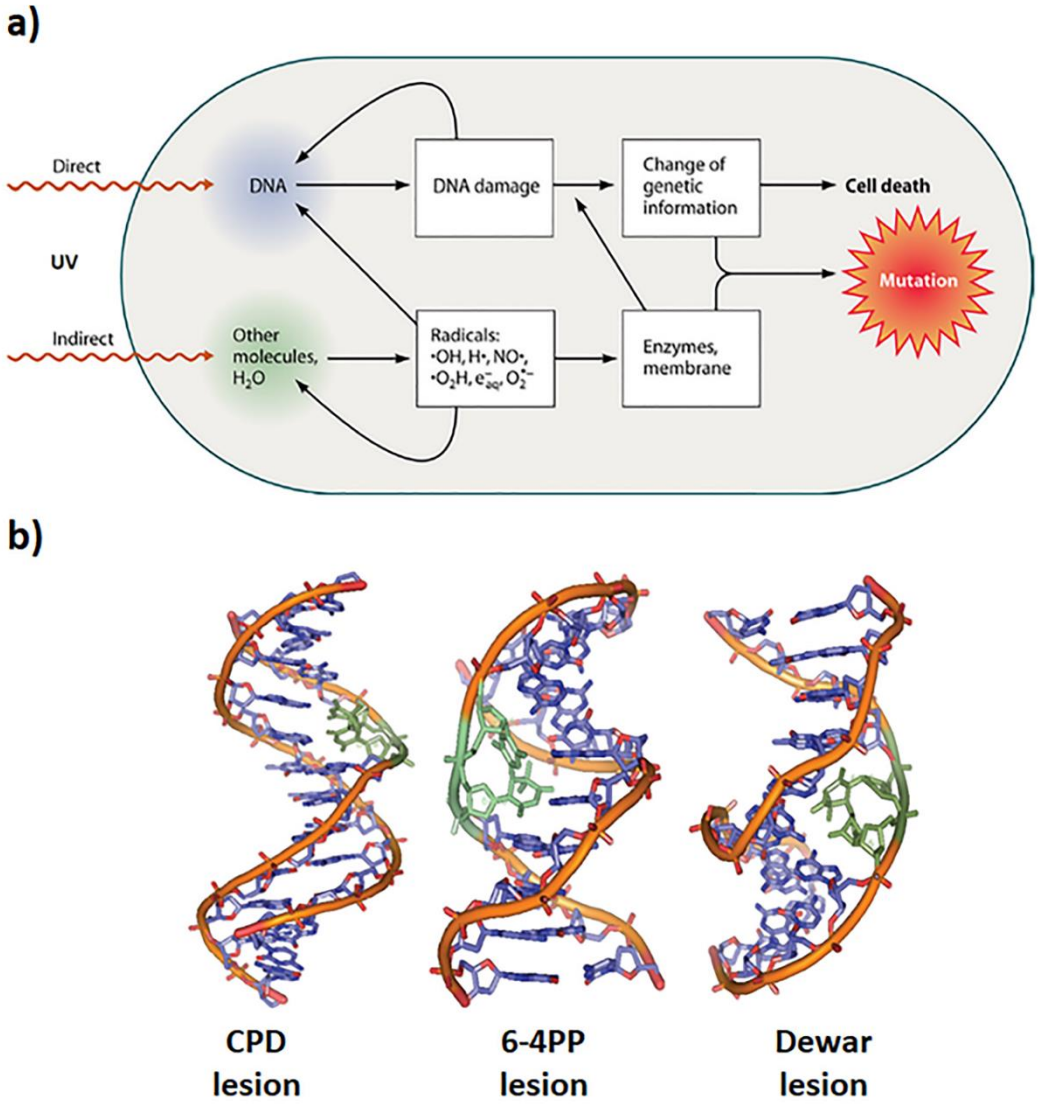

Figure 2.13. a) *Schematic representation of direct and indirect damages induced in a biological system by UV exposure. Adapted from Ref. [162]; b) Representation of typical UV-induced DNA lesions (in green). Adapted from Ref. [198].*

Skin cancer occurs prevalently as basal cell carcinoma, squamous cell carcinoma and melanoma, and each of these expressions can be related to the UV exposure, as reported by the *World Health Organization* [199]. Figure 2.14 shows the skin structure and the depth of UV penetration at different radiation wavelengths. Skin cancers are favored by a long-term, repeated UV radiation exposure. Moreover, an increasing incidence is detected at decreasing latitudes, since these are characterized by higher UV radiation levels. Specifically, the highest incidence was observed in Australia, where the annual rates are 10 and over 20 times the rates in Europe for women and men, respectively.

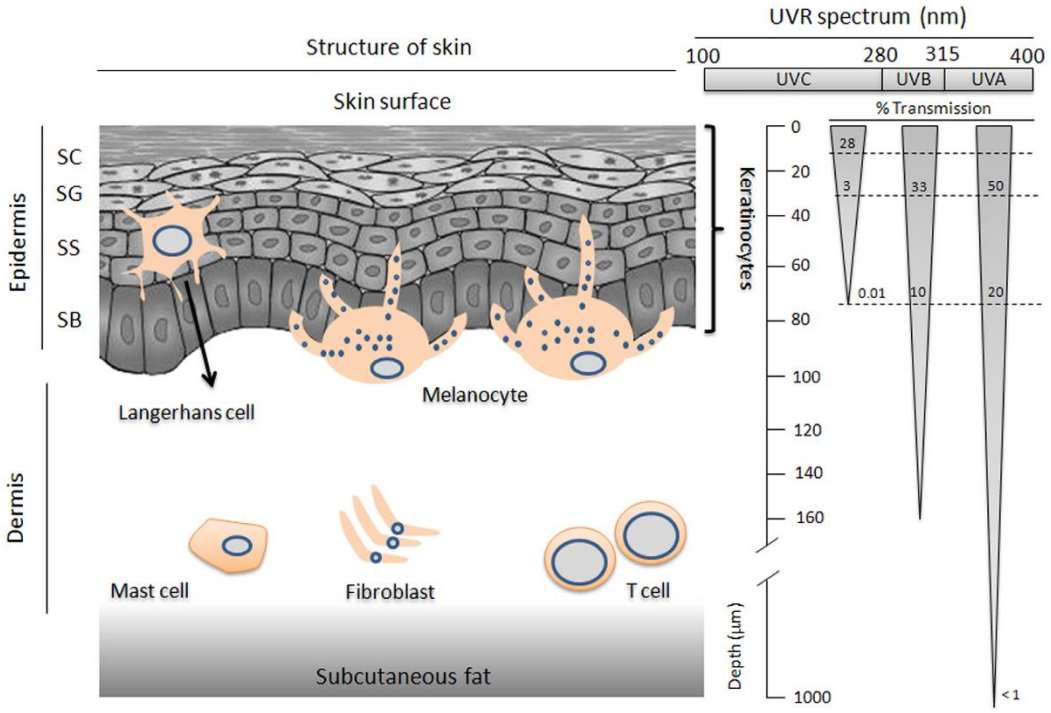

Figure 2.14. *Representation of skin structure and depth of UV penetration at different radiation wavelengths [200].*

Other relevant UV effects on human health are mainly referred to eye diseases, such as photokeratitis, photoconjunctivitis and cataracts [201, 202], and to the immune system [203]. Generally, light activates the constriction of the pupil and the squinting reflex in order to limit the access of the sun rays into the eye, acting as a natural defense. Nevertheless, in extreme conditions of UV exposure, this protection is not sufficient and inflammatory states can occur, comparable to sunburn of the eyeball and eyelids tissues.

UV exposures can induce a failure in the normal activities of the cells responsible for triggering immune responses, increasing the risk of infection due to viral, bacterial, parasitic or fungal agents. Further, radiation exposures can reduce the effectiveness of vaccines, as a consequence of a UV-induced reduction in the antigen-specific immune response [204].

UV effects on materials and structures, as well as on biological systems, have been widely investigated, with the main aim to forecast the materials durability and prevent eventual failures, especially in extreme conditions, such as during space missions. Also in this case, UV effects are evaluated taking into account the mechanisms of photon absorption, which originate from the interaction between radiation and material. The organic molecules involved in this interaction raise to an excited state and, if their energy level is sufficient, bond dissociation can occur, creating radical species. Depending on the physical properties and temperature of the material, these species can diffuse within several atomic distances from their origination point and can be involved in further reactions, altering the original properties of the material [205]. Moreover, after absorbing a photon, molecules can release their energy following other mechanisms, such as the emission of heat or light, or transferring electrons from a functional group to another one, before a relaxation event occurs.

The most common UV-induced effects in polymer materials are discoloration, ‘chalking’, loss of impact strength and reduction in tensile properties. Among the synthetic polymers, poly(vinyl chloride) (PVC) is best known for its tendency to undergo photoyellowing [206-208], and for this reason it is commonly treated with an opacifier, the titanium dioxide (TiO_2). TiO_2 is generally available as brookite, rutile and anatase, but only the rutile form can absorb efficiently UV radiation [209], acting as an effective protection. Results from solar-simulated irradiation of polypropylene and poly(methyl methacrylate) filled with TiO_2 (rutile) highlighted a better UV stability with respect to the neat polymers [210, 211]. From the point of view of the mechanical properties, the impact strength of PVC tends to decrease after UV interactions and, generally, the powder used as opacifier is gradually released, creating a surface layer loose enough to be rubbed off and leading to the chalking of the structure [208]. Other polymers, such as polyethylene, exhibit variations in their mechanical properties due to an extensive chain scission during

the UV-induced photodegradation, with a resultant decrease of molecular weight, extensibility and strength [212-214].

Generally, the rate of the photo-initiated oxidative degradation increases at increasing temperatures, and the magnitude of this acceleration can be related to the activation energy of the reactions and to the chemical nature of the material [215]. For instance, considering films based on polyethylene stabilized with conventional hindered-amine light stabilizers (HALS), an induced variation in terms of temperature, from 30 to 40 °C, produced a decrease in terms of tensile properties, equal to 40% [216]. Similarly, different rates of polypropylene degradation were detected in South India, comparing results referred to summer and winter periods, due to the high variation in terms of temperature [217].

During space missions performed in low earth orbit (LEO), materials degradation can be mainly ascribed to the synergistic effect of UV radiation and atomic oxygen. Atomic oxygen is the most prevalent chemical species present at altitudes between 300 and 500 km, and it results from the breakage of the O_2 molecular bond, promoted by solar photons at wavelengths below 243 nm [205]. Interactions between the atomic oxygen and organic polymer surfaces can lead to a fragmentation of the polymer chains and to a formation of a volatile condensable material (VCM), able to deposit and contaminate the nearby surfaces [218]. The concurrent actions of UV and atomic oxygen on the polymer structures can promote processes such as photo-oxidation, which leads to a discoloration and a reduction in terms of transparency, and to the formation of polar groups that are able to alter the original properties of the material.

Like plastics, wood is a commonly-used building material that is susceptible to UV-promoted degradation events. In particular, among the cell wall polymers, lignin can be identified as the most UV-sensitive component, due to the high number of chromophore groups in its chemical structure [219-222]. Also in this case, the main effects are a rapid discoloration and loss in mechanical properties. The photo-oxidation of lignin involves the formation of water-soluble carbonyl derivatives, resulting in yellowing of the wood surface [223, 224]. Moreover, the formation of singlet oxygen facilitates the degradation reactions and the formation of carbonyl moieties in UV-exposed wood [225], and determines an increase in terms of surface wettability, making the carbohydrate-rich degraded wood more susceptible to biological decay [226]. UV exposure can also induce

radial micro-cracks in the cell walls, the complete deterioration and thinning of the cell walls in young parenchyma tissue, and the degradation of pit membranes in parenchyma cells [227, 228].

2.4.2 Radiation monitoring systems

Traditional UV monitoring systems are commonly placed in one of the following categories: spectroradiometric monitoring equipment, narrowband/broadband measurement equipment, and personal dosimeters. Spectroradiometry allows to detect the spectral power distribution or the spectral irradiance of the UV source, and, typically, requires three basic components, that are input optics, monochromator and detector. Specifically, the task of the input optics is to collect the incoming radiation, with the main requirements of a 2π field of view and a cosine weighted angular response. These characteristics can assure that the radiation from different source configurations is depolarized and follows the same optical path through the system. For this reason, the optics commonly employed are the transmission diffuser or the integrating sphere [229]. The integrating sphere allows to obtain a cosine weighted-response, less approximately than in the case of a diffuser, and shows a small entrance aperture and an internal diffuse coating able to opportunely reflect the incident UV [230]. A second aperture in the sphere provides input for the UV via an entrance slit to a monochromator, which is at the focal point of a collimating mirror, where radiation is reflected as a parallel beam incident on a ruled diffraction grating. Radiation is separated into parallel beams, each with a wavelength dependent on angle. A second mirror collects UV from the grating at a fixed angle, corresponding to a specific wavelength, and focuses it onto the exit slit of the monochromator. Generally, the dispersion element is a blazed ruled diffraction grating, which shows better stray radiation characteristics with respect to a prismatic element. High performance can be achieved using a double grating monochromator with low stray radiation levels, in order to determinate also low UV irradiances at long wavelengths. At the exit slit of the monochromator, a detector is placed, such as a photomultiplier tube that incorporates a photocatode, with a suitable spectral response. At last, the signal from the detector is integrated and transferred to a microcomputer for storage and display. Figure 2.15 shows a schematic representation of a typical spectroradiometric equipment.

Narrowband measurement equipment is generally obtained combining a detector, which can be a vacuum phototube or a solid-state photodiode, with a wavelength-selective device, such as a color glass filter or interference filter, and input optics that can be typically a quartz hemispherical diffuser or polytetrafluoroethylene (PTFE) window [229]. This type of equipment is mainly used to measure the irradiance from extended UV sources, requiring the presence of a not collimated sensor able to receive from a not limited field of view and to return a cosine-weighted response.

Broadband measurements require the employment of a detector that is primarily able to react equally to all incoming UV wavelengths. Typically, thermal or photoelectrical detectors are used, where the UV energy absorption results in a measurable temperature change or involves a conversion into an electrical signal, respectively. Thermal detectors exhibit a uniform response within their region of operation, such as thermopiles and pyroelectric detectors. Specifically, thermopiles exploit the Seebeck effect, whereby a voltage is generated when heat is applied to the connection of two different metals. This type of detector is not suitable for UV irradiances greater than 2000 W/m^2, and, moreover, starting from values over 300 W/m^2, heat losses can cause not linear responses [230]. In the case of pyroelectric detectors, the temperature changes are related to the UV-induced variation in the polarization of a crystal, such as lithium tantalite, inducing a specific voltage at the detector. These devices are characterized by a fast response, with an operating range corresponding to UV irradiance values from 10^{-4} to 10^{6} W/m^2 [230].

Photoelectric detectors can be photomultiplier tubes, vacuum photodiodes, silicon photodiodes and GaAsP photodiodes, and they are mainly employed in direct reading radiometers, filtered UV meters and Robertson–Berger (R-B) meters. In particular, the direct reading radiometer involves the presence of a quartz wide-angle diffuser, an interference filter, a blocking filter and a ‘solar blind’ vacuum photodiode, whereas the filtered UV meter incorporates a diffuser and filters and is typically used for UV detection in the range of wavelengths from 306 nm to 360 nm [230].

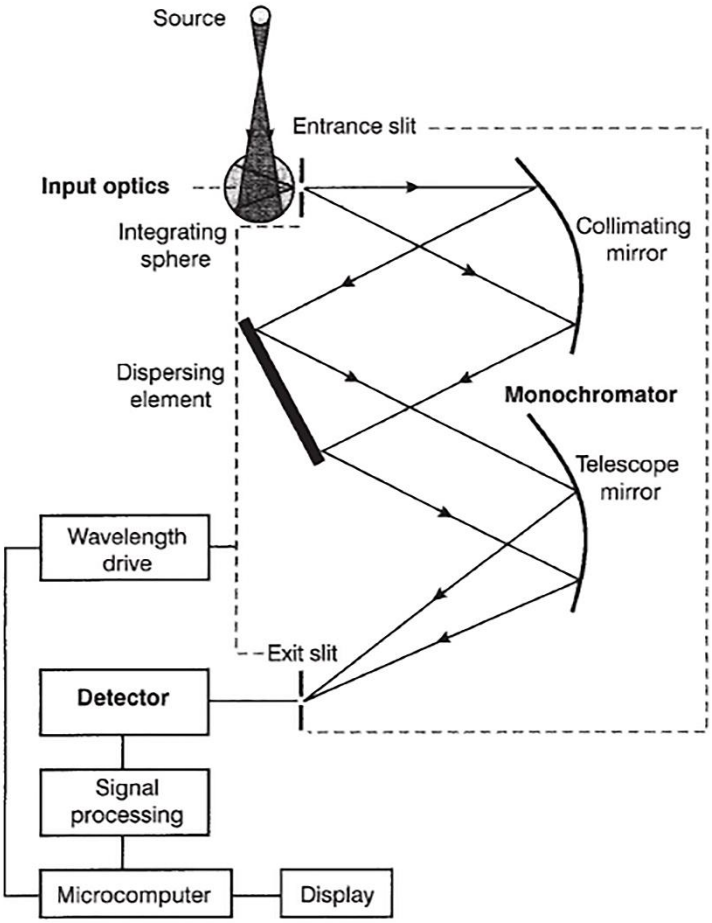

Figure 2.15. *Schematic representation of spectroradiometric equipment [230].*

Personal exposure to UV radiation is generally evaluated through the application of physical, chemical or biological dosimeters. Physical dosimeters are commonly realized electrically coupling the detector to a portable data logger, which can be held in a pocket. Chemical devices are more compact and cheaper, allowing to extend their application from personal to environmental monitoring, especially when bulky instrumentations cannot be applied. After UV exposure, these devices exhibit changes in terms of absorbance that can be opportunely related to the corresponding UV dose. For instance, films based on polysulphone show an increased absorbance when exposed to UV wavelengths less than 330 nm, which can be proportionally related to the radiation dose [231]. In the case of CR-39 (allyl diglycol carbonate) plastic films [232], after UV exposure, they need to be etched in a concentrated caustic solution at a temperature of 80°C, rinsed and dried, in order to evaluate the dose-related change in their absorbance.

In this system, the sensitivity varies with the concentration of the etching solution and with the wavelength at which the absorbance is measured.

Biological UV dosimetry is based on the correlation between the UV-induced biological effects and the radiation dose. Typical biological elements used for UV sensing are biomolecules (e.g. uracil, DNA, provitamin D) and bacteriophages (e.g. T7), bacteria (e.g. E. coli, B. subtilis), cultured eukaryotic cells. DNA, as aforementioned, represents the main target molecule for UV radiation, with the highest sensitivity at short UV wavelengths [177].

One of the DNA-based dosimeters was obtained starting from minidots of purified and dried bacteriophage λ DNA, placed on a UV-transparent biofilm [233, 234]. In this case, the UV-induced DNA damage was evaluated by stopping the DNA synthesis during the polymerase chain reaction (PCR) and reducing the amount of amplified product of UV-exposed DNA compared to control DNA. Moreover, UV-detecting systems based on naked DNA solutions were tested. For instance, a naked calf thymus DNA solution, stowed in cylindrical quartz tubes, was exposed to ambient UV radiation in Antarctica, for 3 h daily, corresponding to the UV-B radiation peak [235]. Results revealed the highest CPDs concentrations when ozone-mediated shifts favored the shorter wavelengths of UV-B radiation. Therefore, changes in solar spectral characteristics caused by ozone depletion could be detected with this biodosimeter. Further, this device was complemented with a phage dosimeter, consisting of intact bacteriophage PWH3a-P1, which revealed a strong correlation between dimer formation and the decay rates of viral infectivity, corresponding to an increasing penetration of UV-B radiation [236]. For instance, the UV response of a DNA dosimeter based on *Escherichia coli* plasmid is reported in Figure 2.16. In particular, UV absorption is evaluated by quantification of CPDs and 6-4PPs, starting from their antibodies.

Spore dosimeters are based on the measurement of spore inactivation, typically using the UV sensitive spores of a mutant strain of *Bacillus subtilis*, which is defective in both nucleotide excision repair and spore-photoproduct lyase [237, 238]. The mutated spores are irradiated, spotted and dried on membrane filters, and the spore inactivation dose is calculated starting from the average values of colony-formers recovered from exposed and control spots [239]. *Bacillus subtilis* spores are also employed to develop another type of dosimeter, the DLR-biofilm [240, 241]. For this system, the appropriate

strain of *Bacillus subtilis* is selected depending on the UV-exposure conditions. In particular, DNA-repair deficient strains are typically used for short-term measurements (≥10 min), whereas DNA-repair wildtype strains in the case of longer-term exposures (≤2 months) [240]. DLR-biofilms are usually placed in different types of exposure-boxes, and a non-exposed region of them is used as dark control.

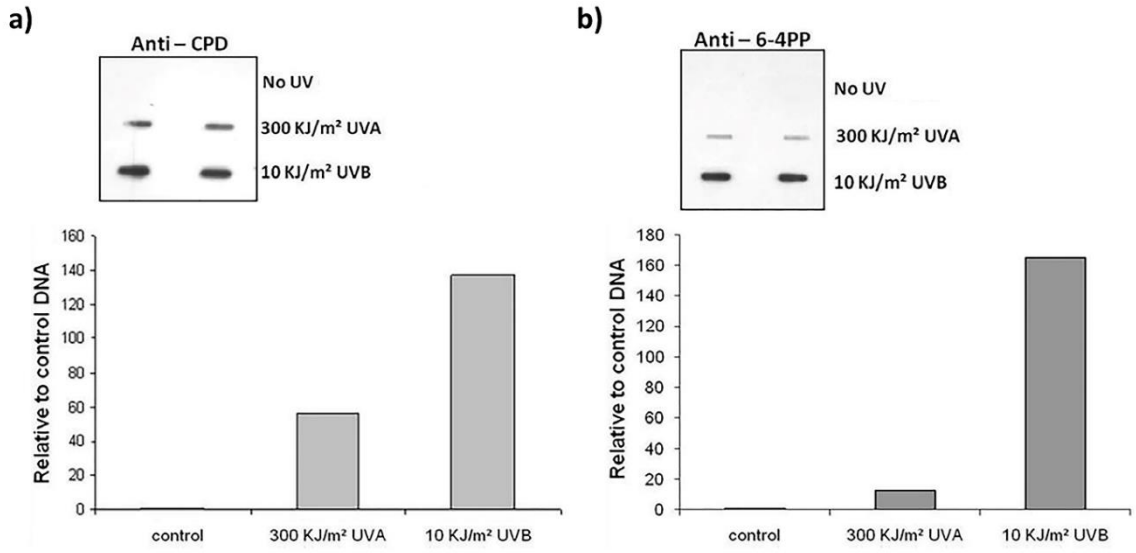

Figure 2.16. *UV response of a DNA dosimeter based on Escherichia coli plasmid. Quantification of a) CPD and b) 6-4PP UV-induction relative to DNA control samples using the antibodies anti-CPD and anti-6-4PP, respectively. Adapted from Ref. [242].*

Differently from the aforementioned devices, which exploit the UV-damaging effects on biological components, a dosimeter based on a UV favorable effect was developed, and that is the one involving the UV-promoted synthesis of vitamin D [243]. Specifically, the kinetics of previtamin D accumulation is related to the endpoint of the reaction in vitamin D synthesis, and represents the biological effect exploited in this type of UV-detecting system. This dosimeter uses a low-concentrated solution of vitamin D precursor, the provitamin D, diluted in ethanol and stored in quartz cuvettes for UV irradiation. The UV-induced photoconversion from provitamin D to previtamin D is accompanied by changes in the absorption spectrum of the solution. Therefore, using optical analysis, the UV exposure as a function of time can be evaluated, in order to determine the UV-biologically effective dose.

Biological dosimeters have also been tested under the harsh conditions of space environment. In particular, the DLR-biofilm dosimeters were exposed during the Spacelab mission D-2, in the experiment RD-UVRAD, for defined time intervals [244]. In this case, the UV radiation was filtered in order to simulate different ozone column thicknesses. Moreover, exploiting the EXPOSE facility, a DLR spore dosimeter was employed on the International Space Station (ISS) [245, 246], whereas the T7 phage was used in parallel to an uracil dosimeter in a vacuum-tight case [247]. In addition, a wide variety of other experiments involving biological samples has been performed, in order to test their response to the extraterrestrial conditions [248-251]. Among them, the Lithopanspermia experiments were carried out to evaluate the survival of different organisms, from bacteria and lichens to fungal spores, to outer space conditions. These organisms were partially covered with artificial meteorite material, with the final aim to demonstrate the possibility that early life forms could have arrived on Earth protected inside meteorites [252].

2.5 References

[1] I.A. Parinov, S.-H. Chang, V.Y. Topolov, Advanced Materials: Manufacturing, Physics, Mechanics and Applications, Springer2015.

[2] R.-M. Wang, S.-R. Zheng, Y.G. Zheng, Polymer matrix composites and technology, Elsevier2011.

[3] J.P. Jose, S. Thomas, J. Kuruvilla, et al., Advances in polymer composites: Macro- and microcomposites—State of the art, new challenges, and opportunities, Polymer Composites; Wiley: Weinheim, Germany, 1 (2012) 3-16.

[4] E. Van Hartingsveldt, J. Van Aartsen, Strain-rate dependence of interfacial adhesion in particle-reinforced polymers, Polymer, 32 (1991) 1482-1487.

[5] M.Z. Rong, M.Q. Zhang, S.L. Pan, et al., Analysis of the interfacial interactions in polypropylene/silica nanocomposites, Polymer International, 53 (2004) 176-183.

[6] Y. Thio, A. Argon, R. Cohen, Role of interfacial adhesion strength on toughening polypropylene with rigid particles, Polymer, 45 (2004) 3139-3147.

[7] M. Buggy, G. Bradley, A. Sullivan, Polymer–filler interactions in kaolin/nylon 6, 6 composites containing a silane coupling agent, Composites Part A: Applied Science and Manufacturing, 36 (2005) 437-442.

[8] J.-K. Kim, Y.-W. Mai, High strength, high fracture toughness fibre composites with interface control—a review, Composites Science and Technology, 41 (1991) 333-378.
[9] L. Drzal, M. Madhukar, Fibre-matrix adhesion and its relationship to composite mechanical properties, Journal of Materials Science, 28 (1993) 569-610.
[10] J.-K. Kim, Y.-W. Mai, Engineered interfaces in fiber reinforced composites, Elsevier1998.
[11] R. Naslain, M. Pomeroy, Ceramic matrix composites: Matrices and processing, (2016).
[12] H. Pıhtılı, N. Tosun, Investigation of the wear behaviour of a glass-fibre-reinforced composite and plain polyester resin, Composites Science and Technology, 62 (2002) 367-370.
[13] G. Lubin, Handbook of composites, Springer Science & Business Media2013.
[14] B. Cantor, H. Assender, P. Grant, Aerospace Materials, CRC Press2015.
[15] F. Campbell, Thermoplastic Composites: An Unfulfilled Promise, Manufacturing Processes for Advanced Composites, (2004) 357-397.
[16] G. Akovali, Handbook of composite fabrication, iSmithers Rapra Publishing2001.
[17] N. Bhatnagar, N. Asija, Durability of high-performance ballistic composites, Lightweight Ballistic Composites, Elsevier2016, pp. 231-283.
[18] S. Adanur, Wellington Sears handbook of industrial textiles, Routledge2017.
[19] R. Ash, Vehicle armor, Lightweight Ballistic Composites, Elsevier2016, pp. 285-309.
[20] F. Campbell, Fibers and Reinforcements: The String That Provides the Strength, Manufacturing Processes for Advanced Composites, (2004) 39-62.
[21] A. Shrivastava, Additives for Plastics, Plastics Design Library, Introduction to Plastics Engineering, (2018) 111-141.
[22] V. Giurgiutiu, Structural health monitoring of aerospace composites, Academic Press2015.
[23] I. Hamerton, L. Mooring, The use of thermosets in aerospace applications, Thermosets, Elsevier2012, pp. 189-227.
[24] P. Bhatt, A. Goe, Carbon Fibres: Production, Properties and Potential Use, Material Science Research India, 14 (2017) 52-57.

[25] N. Newhouse, Application of Composites in Natural Gas Vehicle Fuel Containers, Comprehensive Composite Materials, (2000) 581-597.
[26] L.N. Sun, Z. Deng, The carbon fiber composite materials application in sports equipment, Advanced Materials Research, Trans Tech Publ, 2012, pp. 173-176.
[27] Q. Zhang, The" Black Revolution" of Sports Equipment: Application of Carbon Fiber Reinforced Plastics (CFRP), Applied Mechanics and Materials, Trans Tech Publ, 2014, pp. 69-73.
[28] F.K. Michio Inagaki, Engineering and Applications of Carbon Materials, Materials Science and Engineering of Carbon: Fundamentals (Second Edition), (2014) 219-525.
[29] R.A. Flinn, P.K. Trojan, Engineering materials and their applications, Engineering Materials and Their Applications, 4th Edition, by Richard A. Flinn, Paul K. Trojan, pp. 1056. ISBN 0-471-12508-3. Wiley-VCH, December 1994., (1994) 1056.
[30] K.W. Ding, G. Wang, W.Y. Yin, Application of composite sandwich panels in construction engineering, Applied Mechanics and Materials, Trans Tech Publ, 2013, pp. 1172-1176.
[31] K. Ashida, K. Iwasaki, A. Landrock, Handbook of Plastic Foams, NOYES Publ, (1995).
[32] J. Weeton, Engineered Materials Handbook, Vol. 1: Composites, ASM International, Metals Park, OH, 1987.
[33] W. Work, K. Horie, M. Hess, et al., Definition of terms related to polymer blends, composites, and multiphase polymeric materials (IUPAC Recommendations 2004), Pure and Applied Chemistry, 76 (2004) 1985-2007.
[34] D. Pitsa, M.G. Danikas, Interfaces features in polymer nanocomposites: A review of proposed models, Nano, 6 (2011) 497-508.
[35] D.L. Schodek, P. Ferreira, M.F. Ashby, Nanomaterials, nanotechnologies and design: an introduction for engineers and architects, Butterworth-Heinemann2009.
[36] P.M. Ajayan, L.S. Schadler, P.V. Braun, Nanocomposite science and technology, John Wiley & Sons2006.
[37] R.A. Vaia, H.D. Wagner, Framework for nanocomposites, Materials Today, 7 (2004) 32-37.
[38] B. Lauke, On the effect of particle size on fracture toughness of polymer composites, Composites Science and Technology, 68 (2008) 3365-3372.

[39] S. Srivastava, M. Haridas, J. Basu, Optical properties of polymer nanocomposites, Bulletin of Materials Science, 31 (2008) 213-217.

[40] R. Jin, Y. Cao, C.A. Mirkin, et al., Photoinduced conversion of silver nanospheres to nanoprisms, Science, 294 (2001) 1901-1903.

[41] L. Armelao, D. Barreca, G. Bottaro, et al., Recent trends on nanocomposites based on Cu, Ag and Au clusters: A closer look, Coordination Chemistry Reviews, 250 (2006) 1294-1314.

[42] H. Althues, J. Henle, S. Kaskel, Functional inorganic nanofillers for transparent polymers, Chemical Society Reviews, 36 (2007) 1454-1465.

[43] J. Bohm, T. Hanemann, E. Ritzhaupt-Kleissl, et al., Polymer-Nanofiller Composites: Transparent Materials with a refractive index greater than 1.60, Lecture Notes in Computer Science, 1 (2005) 277-280.

[44] C. Ng, B. Ash, L. Schadler, et al., A study of the mechanical and permeability properties of nano-and micron-TiO2 filled epoxy composites, Advanced Composites Letters, 10 (2001) 096369350101000301.

[45] F. Vahedi, H. Shahverdi, M. Shokrieh, et al., Effects of carbon nanotube content on the mechanical and electrical properties of epoxy-based composites, New Carbon Materials, 29 (2014) 419-425.

[46] Y.S. Song, J.R. Youn, Influence of dispersion states of carbon nanotubes on physical properties of epoxy nanocomposites, Carbon, 43 (2005) 1378-1385.

[47] J. Slonczewski, P. Weiss, Band structure of graphite, Physical Review, 109 (1958) 272.

[48] Y. Zhang, Y.-W. Tan, H.L. Stormer, et al., Experimental observation of the quantum Hall effect and Berry's phase in graphene, Nature, 438 (2005) 201.

[49] K.S. Novoselov, Z. Jiang, Y. Zhang, et al., Room-temperature quantum Hall effect in graphene, Science, 315 (2007) 1379-1379.

[50] V. Singh, D. Joung, L. Zhai, et al., Graphene based materials: past, present and future, Progress in Materials Science, 56 (2011) 1178-1271.

[51] D.G. Papageorgiou, I.A. Kinloch, R.J. Young, Mechanical properties of graphene and graphene-based nanocomposites, Progress in Materials Science, 90 (2017) 75-127.

[52] A.A. Balandin, S. Ghosh, W. Bao, et al., Superior thermal conductivity of single-layer graphene, Nano Letters, 8 (2008) 902-907.

[53] N. Li, X. Zhang, Q. Song, et al., The promotion of neurite sprouting and outgrowth of mouse hippocampal cells in culture by graphene substrates, Biomaterials, 32 (2011) 9374-9382.

[54] A. Bendali, L.H. Hess, M. Seifert, et al., Purified Neurons can Survive on Peptide-Free Graphene Layers, Advanced Healthcare Materials, 2 (2013) 929-933.

[55] D. Sahni, A. Jea, J.A. Mata, et al., Biocompatibility of pristine graphene for neuronal interface, Journal of Neurosurgery: Pediatrics, 11 (2013) 575-583.

[56] Y. Liu, D. Yu, C. Zeng, et al., Biocompatible graphene oxide-based glucose biosensors, Langmuir, 26 (2010) 6158-6160.

[57] A.K. Geim, K.S. Novoselov, The rise of graphene, Nature Materials, 6 (2007) 183-191.

[58] H. Kim, A.A. Abdala, C.W. Macosko, Graphene/polymer nanocomposites, Macromolecules, 43 (2010) 6515-6530.

[59] S. Park, R.S. Ruoff, Chemical methods for the production of graphenes, Nature Nanotechnology, 4 (2009) 217.

[60] A. Lerf, H. He, M. Forster, et al., Structure of graphite oxide revisited, The Journal of Physical Chemistry B, 102 (1998) 4477-4482.

[61] H. He, J. Klinowski, M. Forster, et al., A new structural model for graphite oxide, Chemical Physics Letters, 287 (1998) 53-56.

[62] M. Chanda, Plastics technology handbook, CRC press2017.

[63] M.J. McAllister, J.-L. Li, D.H. Adamson, et al., Single sheet functionalized graphene by oxidation and thermal expansion of graphite, Chemistry of Materials, 19 (2007) 4396-4404.

[64] T.D. Dao, H.M. Jeong, Graphene prepared by thermal reduction–exfoliation of graphite oxide: Effect of raw graphite particle size on the properties of graphite oxide and graphene, Materials Research Bulletin, 70 (2015) 651-657.

[65] H.C. Schniepp, J.-L. Li, M.J. McAllister, et al., Functionalized single graphene sheets derived from splitting graphite oxide, The Journal of Physical Chemistry B, 110 (2006) 8535-8539.

[66] T.D. Dao, H.-i. Lee, H.M. Jeong, Alumina-coated graphene nanosheet and its composite of acrylic rubber, Journal of Colloid and Interface Science, 416 (2014) 38-43.

[67] C. Punckt, F. Muckel, S. Wolff, et al., The effect of degree of reduction on the electrical properties of functionalized graphene sheets, Applied Physics Letters, 102 (2013) 023114.

[68] C. Zhang, W. Lv, X. Xie, et al., Towards low temperature thermal exfoliation of graphite oxide for graphene production, Carbon, 62 (2013) 11-24.

[69] H.-B. Zhang, J.-W. Wang, Q. Yan, et al., Vacuum-assisted synthesis of graphene from thermal exfoliation and reduction of graphite oxide, Journal of Materials Chemistry, 21 (2011) 5392-5397.

[70] E.J.C. Amieva, J. López-Barroso, A.L. Martínez-Hernández, et al., Graphene-Based Materials Functionalization with Natural Polymeric Biomolecules, Recent Advances in Graphene Research, (2016) 257-298.

[71] J. Kim, B.-s. Yim, J.-m. Kim, et al., The effects of functionalized graphene nanosheets on the thermal and mechanical properties of epoxy composites for anisotropic conductive adhesives (ACAs), Microelectronics Reliability, 52 (2012) 595-602.

[72] J.K. Lee, S. Song, B. Kim, Functionalized graphene sheets-epoxy based nanocomposite for cryotank composite application, Polymer Composites, 33 (2012) 1263-1273.

[73] S. Qiu, C. Wang, Y. Wang, et al., Effects of graphene oxides on the cure behaviors of a tetrafunctional epoxy resin, Express Polymer Letters, 5 (2011).

[74] J. Kim, H. Im, J.-m. Kim, et al., Thermal and electrical conductivity of Al(OH)3 covered graphene oxide nanosheet/epoxy composites, Journal of Materials Science, 47 (2012) 1418-1426.

[75] T. Jiang, T. Kuila, N.H. Kim, et al., Enhanced mechanical properties of silanized silica nanoparticle attached graphene oxide/epoxy composites, Composites Science and Technology, 79 (2013) 115-125.

[76] R.K. Layek, A.K. Nandi, A review on synthesis and properties of polymer functionalized graphene, Polymer, 54 (2013) 5087-5103.

[77] K. Hu, D.D. Kulkarni, I. Choi, et al., Graphene-polymer nanocomposites for structural and functional applications, Progress in Polymer Science, 39 (2014) 1934-1972.

[78] T. Kuila, S. Bose, A.K. Mishra, et al., Chemical functionalization of graphene and its applications, Progress in Materials Science, 57 (2012) 1061-1105.

[79] C. Bao, Y. Guo, L. Song, et al., In situ preparation of functionalized graphene oxide/epoxy nanocomposites with effective reinforcements, Journal of Materials Chemistry, 21 (2011) 13290-13298.

[80] D. Cai, M. Song, Recent advance in functionalized graphene/polymer nanocomposites, Journal of Materials Chemistry, 20 (2010) 7906-7915.

[81] J. Fan, Z. Shi, J. Wang, et al., Glycidyl methacrylate-modified gum arabic mediated graphene exfoliation and its use for enhancing mechanical performance of hydrogel, Polymer, 54 (2013) 3921-3930.

[82] V. Muradyan, A. Arbuzov, E. Sokolov, et al., The effect of addition of functionalized graphene oxide on the dielectric properties of epoxy composite, Technical Physics Letters, 39 (2013) 798-800.

[83] X. Wang, W. Xing, X. Feng, et al., Functionalization of graphene with grafted polyphosphamide for flame retardant epoxy composites: synthesis, flammability and mechanism, Polymer Chemistry, 5 (2014) 1145-1154.

[84] T. Ramanathan, A. Abdala, S. Stankovich, et al., Functionalized graphene sheets for polymer nanocomposites, Nature Nanotechnology, 3 (2008) 327.

[85] D. Chen, H. Zhu, T. Liu, In situ thermal preparation of polyimide nanocomposite films containing functionalized graphene sheets, ACS Applied Materials & Interfaces, 2 (2010) 3702-3708.

[86] A.L. Higginbotham, J.R. Lomeda, A.B. Morgan, et al., Graphite oxide flame-retardant polymer nanocomposites, ACS Applied Materials & Interfaces, 1 (2009) 2256-2261.

[87] S. Stankovich, D.A. Dikin, G.H. Dommett, et al., Graphene-based composite materials, Nature, 442 (2006) 282.

[88] A. Bansal, H. Yang, C. Li, et al., Quantitative equivalence between polymer nanocomposites and thin polymer films, Nature Materials, 4 (2005) 693.

[89] R.D. Priestley, C.J. Ellison, L.J. Broadbelt, et al., Structural relaxation of polymer glasses at surfaces, interfaces, and in between, Science, 309 (2005) 456-459.

[90] L.M. Veca, M.J. Meziani, W. Wang, et al., Carbon nanosheets for polymeric nanocomposites with high thermal conductivity, Advanced Materials, 21 (2009) 2088-2092.

[91] S. Ganguli, A.K. Roy, D.P. Anderson, Improved thermal conductivity for chemically functionalized exfoliated graphite/epoxy composites, Carbon, 46 (2008) 806-817.
[92] Y. Wang, J.W. Shan, G.J. Weng, Percolation threshold and electrical conductivity of graphene-based nanocomposites with filler agglomeration and interfacial tunneling, Journal of Applied Physics, 118 (2015) 065101.
[93] E. Tkalya, M. Ghislandi, R. Otten, et al., Experimental and Theoretical Study of the Influence of the State of Dispersion of Graphene on the Percolation Threshold of Conductive Graphene/Polystyrene Nanocomposites, ACS Applied Materials & Interfaces, 6 (2014) 15113-15121.
[94] A.M. Díez-Pascual, M.n.A. Gómez-Fatou, F. Ania, et al., Nanoindentation assessment of the interphase in carbon nanotube-based hierarchical composites, The Journal of Physical Chemistry C, 116 (2012) 24193-24200.
[95] Y. Gu, M. Li, J. Wang, et al., Characterization of the interphase in carbon fiber/polymer composites using a nanoscale dynamic mechanical imaging technique, Carbon, 48 (2010) 3229-3235.
[96] T. Downing, R. Kumar, W. Cross, et al., Determining the interphase thickness and properties in polymer matrix composites using phase imaging atomic force microscopy and nanoindentation, Journal of Adhesion Science and Technology, 14 (2000) 1801-1812.
[97] L. Bokobza, B. Bresson, G. Garnaud, et al., Mechanical and AFM investigations of elastomers filled with multiwall carbon nanotubes, Composite Interfaces, 19 (2012) 285-295.
[98] M. Bera, P. Maji, Graphene-based polymer nanocomposites: materials for future revolution, MOJ Polymer Science, 1 (2017) 00013.
[99] W. Kai, Y. Hirota, L. Hua, et al., Thermal and mechanical properties of a poly (ϵ-caprolactone)/graphite oxide composite, Journal of Applied Polymer Science, 107 (2008) 1395-1400.
[100] M. Hirata, T. Gotou, S. Horiuchi, et al., Thin-film particles of graphite oxide 1: High-yield synthesis and flexibility of the particles, Carbon, 42 (2004) 2929-2937.
[101] H. Kim, Y. Miura, C.W. Macosko, Graphene/polyurethane nanocomposites for improved gas barrier and electrical conductivity, Chemistry of Materials, 22 (2010) 3441-3450.

[102] D. Li, W. Zhang, X. Yu, et al., When biomolecules meet graphene: From molecular level interactions to material design and applications, Nanoscale, 8 (2016) 19491-19509.
[103] X. Zou, S. Wei, J. Jasensky, et al., Molecular interactions between graphene and biological molecules, Journal of the American Chemical Society, 139 (2017) 1928-1936.
[104] R.K. Upadhyay, N. Soin, S.S. Roy, Role of graphene/metal oxide composites as photocatalysts, adsorbents and disinfectants in water treatment: a review, Rsc Advances, 4 (2014) 3823-3851.
[105] M.G. Santonicola, Label-Free Biosensing Platforms Based on Graphene/DNA Interfaces, Graphene Bioelectronics, Elsevier2018, pp. 177-191.
[106] A.J. Patil, J.L. Vickery, T.B. Scott, et al., Aqueous stabilization and self-assembly of graphene sheets into layered bio-nanocomposites using DNA, Advanced Materials, 21 (2009) 3159-3164.
[107] Y. Zhang, H. Zhao, Z. Wu, et al., A novel graphene-DNA biosensor for selective detection of mercury ions, Biosensors and Bioelectronics, 48 (2013) 180-187.
[108] S. Deng, V. Tjoa, H.M. Fan, et al., Reduced graphene oxide conjugated Cu2O nanowire mesocrystals for high-performance NO2 gas sensor, Journal of the American Chemical Society, 134 (2012) 4905-4917.
[109] G. Singh, A. Choudhary, D. Haranath, et al., ZnO decorated luminescent graphene as a potential gas sensor at room temperature, Carbon, 50 (2012) 385-394.
[110] B.G.S. Burkhanov, N.B. Gorina, N.B. Kolchugina, et al., Palladium-based alloy membranes for separation of high purity hydrogen from hydrogen-containing gas mixtures, Platinum Metals Review, 55 (2011) 3-12.
[111] N.B. Singh, B. Bhattacharya, U. Sarkar, Nickel decorated single-wall carbon nanotube as CO sensor, Soft Nanoscience Letters, 3 (2013) 9.
[112] S.K. Hazra, S. Basu, Graphene-oxide nano composites for chemical sensor applications, C—Journal of Carbon Research, 2 (2016) 12.
[113] H. Song, L. Zhang, C. He, et al., Graphene sheets decorated with SnO2 nanoparticles: in situ synthesis and highly efficient materials for cataluminescence gas sensors, Journal of Materials Chemistry, 21 (2011) 5972-5977.
[114] J.-L. Chang, K.-H. Chang, C.-C. Hu, et al., Improved voltammetric peak separation and sensitivity of uric acid and ascorbic acid at nanoplatelets of graphitic oxide, Electrochemistry Communications, 12 (2010) 596-599.

[115] H. Du, J. Ye, J. Zhang, et al., A voltammetric sensor based on graphene-modified electrode for simultaneous determination of catechol and hydroquinone, Journal of Electroanalytical Chemistry, 650 (2011) 209-213.
[116] M. Zhou, Y. Zhai, S. Dong, Electrochemical sensing and biosensing platform based on chemically reduced graphene oxide, Analytical chemistry, 81 (2009) 5603-5613.
[117] C.X. Lim, H.Y. Hoh, P.K. Ang, et al., Direct voltammetric detection of DNA and pH sensing on epitaxial graphene: an insight into the role of oxygenated defects, Analytical Chemistry, 82 (2010) 7387-7393.
[118] T.Q. Trung, H.S. Le, T.M.L. Dang, et al., Freestanding, Fiber-Based, Wearable Temperature Sensor with Tunable Thermal Index for Healthcare Monitoring, Advanced Healthcare Materials, 7 (2018).
[119] J. Park, J. Kim, S.-Y. Kim, et al., Soft, smart contact lenses with integrations of wireless circuits, glucose sensors, and displays, Science Advances, 4 (2018) eaap9841.
[120] Q. He, S.R. Das, N.T. Garland, et al., Enabling inkjet printed graphene for ion selective electrodes with postprint thermal annealing, ACS Applied Materials & Interfaces, 9 (2017) 12719-12727.
[121] S.-C. Tseng, T.-Y. Wu, J.-C. Chou, et al., Research of sensing characteristic and dynamic measurement of graphene oxides modified flexible arrayed RuO2 chlorine ion sensor, Materials Research Bulletin, 101 (2018) 155-161.
[122] Q. Yuan, S. Wu, C. Ye, et al., Sensitivity enhancement of potassium ion (K+) detection based on graphene field-effect transistors with surface plasma pretreatment, Sensors and Actuators B: Chemical, 285 (2019) 333-340.
[123] K. Sawicka, P. Gouma, S. Simon, Electrospun biocomposite nanofibers for urea biosensing, Sensors and Actuators B: Chemical, 108 (2005) 585-588.
[124] A. Kaushik, P.R. Solanki, A.A. Ansari, et al., Iron oxide-chitosan nanobiocomposite for urea sensor, Sensors and Actuators B: Chemical, 138 (2009) 572-580.
[125] S. Burrs, M. Bhargava, R. Sidhu, et al., A paper based graphene-nanocauliflower hybrid composite for point of care biosensing, Biosensors and Bioelectronics, 85 (2016) 479-487.
[126] S. Syama, P. Mohanan, Comprehensive application of graphene: emphasis on biomedical concerns, Nano-Micro Letters, 11 (2019) 6.

[127] R.A. Ismail, A.M. Alwan, A.S. Ahmed, Preparation and characteristics study of nano-porous silicon UV photodetector, Applied Nanoscience, 7 (2017) 9-15.
[128] Y. Liu, X. Zhang, J. Su, et al., Ag nanoparticles@ ZnO nanowire composite arrays: an absorption enhanced UV photodetector, Optics Express, 22 (2014) 30148-30155.
[129] M. Zare, S. Safa, R. Azimirad, et al., Graphene oxide incorporated ZnO nanostructures as a powerful ultraviolet composite detector, Journal of Materials Science: Materials in Electronics, 28 (2017) 6919-6927.
[130] C. Chen, P. Zhou, N. Wang, et al., UV-assisted photochemical synthesis of reduced graphene oxide/ZnO nanowires composite for photoresponse enhancement in UV photodetectors, Nanomaterials, 8 (2018) 26.
[131] D. Shao, M. Yu, J. Lian, et al., An ultraviolet photodetector fabricated from WO3 nanodiscs/reduced graphene oxide composite material, Nanotechnology, 24 (2013) 295701.
[132] K. Huang, Q. Zhang, F. Yang, et al., Ultraviolet photoconductance of a single hexagonal WO3 nanowire, Nano Research, 3 (2010) 281-287.
[133] L. Li, Y. Zhang, X. Fang, et al., WO3 nanowires on carbon papers: electronic transport, improved ultraviolet-light photodetectors and excellent field emitters, Journal of Materials Chemistry, 21 (2011) 6525-6530.
[134] H. Liu, Y. Lv, S. Li, et al., A solar ultraviolet sensor based on fluorescent polyoxometalate and viologen, Journal of Materials Chemistry C, 5 (2017) 9383-9388.
[135] F. Ubertini, S. Laflamme, H. Ceylan, et al., Novel nanocomposite technologies for dynamic monitoring of structures: a comparison between cement-based embeddable and soft elastomeric surface sensors, Smart Materials and Structures, 23 (2014) 045023.
[136] I. Kang, M.J. Schulz, J.H. Kim, et al., A carbon nanotube strain sensor for structural health monitoring, Smart Materials and Structures, 15 (2006) 737.
[137] H. Zhao, Y. Zhang, P.D. Bradford, et al., Carbon nanotube yarn strain sensors, Nanotechnology, 21 (2010) 305502.
[138] K.J. Loh, J.P. Lynch, N.A. Kotov, Conformable single-walled carbon nanotube thin film strain sensors for structural monitoring, Proceedings of the 5th International Workshop on Structural Health Monitoring, Stanford, CA, 2005, pp. 1-8.

[139] J. Sebastian, N. Schehl, M. Bouchard, et al., Health monitoring of structural composites with embedded carbon nanotube coated glass fiber sensors, Carbon, 66 (2014) 191-200.

[140] V. Eswaraiah, K. Balasubramaniam, S. Ramaprabhu, Functionalized graphene reinforced thermoplastic nanocomposites as strain sensors in structural health monitoring, Journal of Materials Chemistry, 21 (2011) 12626-12628.

[141] L.M. Chiacchiarelli, M. Rallini, M. Monti, et al., The role of irreversible and reversible phenomena in the piezoresistive behavior of graphene epoxy nanocomposites applied to structural health monitoring, Composites Science and Technology, 80 (2013) 73-79.

[142] F. Pascal-Delannoy, B. Sorli, A. Boyer, Quartz crystal microbalance (QCM) used as humidity sensor, Sensors and Actuators A: Physical, 84 (2000) 285-291.

[143] K. Galatsis, W. Qu, W. Wlodarski, Quartz crystal microbalance humidity sensor with porous electrodes, 1998 Conference on Optoelectronic and Microelectronic Materials and Devices. Proceedings (Cat. No. 98EX140), IEEE, 1998, pp. 373-375.

[144] M. Neshkova, R. Petrova, V. Petrov, Piezoelectric quartz crystal humidity sensor using chemically modified nitrated polystyrene as water sorbing coating, Analytica Chimica Acta, 332 (1996) 93-103.

[145] Y. Zhang, K. Yu, S. Ouyang, et al., Detection of humidity based on quartz crystal microbalance coated with ZnO nanostructure films, Physica B: Condensed Matter, 368 (2005) 94-99.

[146] P.-G. Su, Y.-P. Chang, Low-humidity sensor based on a quartz-crystal microbalance coated with polypyrrole/Ag/TiO2 nanoparticles composite thin films, Sensors and Actuators B: Chemical, 129 (2008) 915-920.

[147] Y. Zhang, K. Yu, R. Xu, et al., Quartz crystal microbalance coated with carbon nanotube films used as humidity sensor, Sensors and Actuators A: Physical, 120 (2005) 142-146.

[148] H.-W. Chen, R.-J. Wu, K.-H. Chan, et al., The application of CNT/Nafion composite material to low humidity sensing measurement, Sensors and Actuators B: Chemical, 104 (2005) 80-84.

[149] J.L. Barth, Space and atmospheric environments: from low earth orbits to deep space, Protection of Materials and Structures from Space Environment, Springer2004, pp. 7-29.
[150] R. McKenzie, M. Blumthaler, S. Diaz, et al., Rationalizing nomenclature for UV doses and effects on humans, (2014).
[151] S. Madronich, S. Flocke, Theoretical estimation of biologically effective UV radiation at the Earth's surface, Solar Ultraviolet Radiation, Springer1997, pp. 23-48.
[152] M.d.P. Corrêa, Solar ultraviolet radiation: properties, characteristics and amounts observed in Brazil and South America, Anais Brasileiros de Dermatologia, 90 (2015) 297-313.
[153] W.L. Nicholson, A.C. Schuerger, P. Setlow, The solar UV environment and bacterial spore UV resistance: considerations for Earth-to-Mars transport by natural processes and human spaceflight, Mutation Research/Fundamental and Molecular Mechanisms of Mutagenesis, 571 (2005) 249-264.
[154] J. Lean, Solar ultraviolet irradiance variations: A review, Journal of Geophysical Research: Atmospheres, 92 (1987) 839-868.
[155] B. Clark, A. Baker, A. Cheng, et al., Survival of life on asteroids, comets and other small bodies, Origins of Life and Evolution of the Biosphere, 29 (1999) 521-545.
[156] R.W. Zurek, J.R. Barnes, R.M. Haberle, et al., Dynamics of the atmosphere of Mars, Mars, (1992) 835-933.
[157] J. Appelbaum, D.J. Flood, Solar radiation on Mars, Solar Energy, 45 (1990) 353-363.
[158] C.S. Cockell, D.C. Catling, W.L. Davis, et al., The ultraviolet environment of Mars: biological implications past, present, and future, Icarus, 146 (2000) 343-359.
[159] W. Kuhn, S. Atreya, Solar radiation incident on the Martian surface, Journal of Molecular Evolution, 14 (1979) 57-64.
[160] P. Warneck, Chemistry of the natural atmosphere, Elsevier1999.
[161] T. Owen, K. Biemann, D. Rushneck, et al., The composition of the atmosphere at the surface of Mars, Journal of Geophysical Research, 82 (1977) 4635-4639.
[162] G. Horneck, D.M. Klaus, R.L. Mancinelli, Space microbiology, Microbiology and Molecular Biology Reviews, 74 (2010) 121-156.

[163] https://pds-atmospheres.nmsu.edu/data_and_services/atmospheres_data/MARS/mars_lander.html.
[164] M.G. Tomasko, L. Doose, M. Lemmon, et al., Properties of dust in the Martian atmosphere from the Imager on Mars Pathfinder, Journal of Geophysical Research: Planets, 104 (1999) 8987-9007.
[165] R. Kahn, S. Lee, T. Martin, et al., The Martian dust cycle, Bulletin of the American Astronomical Society, 1990, pp. 1076.
[166] A.C. Schuerger, R.L. Mancinelli, R.G. Kern, et al., Survival of endospores of Bacillus subtilis on spacecraft surfaces under simulated martian environments:: implications for the forward contamination of Mars, Icarus, 165 (2003) 253-276.
[167] D. Colburn, J. Pollack, R. Haberle, Diurnal variations in optical depth at Mars, Icarus, 79 (1989) 159-189.
[168] http://hps.org/hpspublications/articles/uv.html.
[169] M. Sisti, B. Pieretti, M. De Santi, et al., Inactivation of pathogenic dermatophytes by ultraviolet irradiation in swimming pool thermal water, International Journal of Environmental Health Research, 24 (2014) 412-417.
[170] J. Wyczarska-Kokot, Effect of disinfection methods on microbiological water quality in indoor swimming pools, Architecture Civil Engineering Environment, 4 (2009) 145-152.
[171] M.V. Selma, A. Allende, F. Lopez-Galvez, et al., Disinfection potential of ozone, ultraviolet-C and their combination in wash water for the fresh-cut vegetable industry, Food Microbiology, 25 (2008) 809-814.
[172] J.D. Mallet, P.J. Rochette, Wavelength-dependent ultraviolet induction of cyclobutane pyrimidine dimers in the human cornea, Photochemical & Photobiological Sciences, 12 (2013) 1310-1318.
[173] P. Vecchia, M. Hietanen, B.E. Stuck, et al., Protecting workers from ultraviolet radiation, Citeseer2007.
[174] A.-M. Wennberg, L.-E. Lindholm, M. Alpsten, et al., Treatment of superficial basal cell carcinomas using topically applied delta-aminolaevulinic acid and a filtered xenon lamp, Archives of Dermatological Research, 288 (1996) 561-564.
[175] R. Roelandts, Diagnosis and treatment of solar urticaria, Dermatologic Therapy, 16 (2003) 52-56.

[176] T. Kormeili, P. Yamauchi, N. Lowe, Topical photodynamic therapy in clinical dermatology, British Journal of Dermatology, 150 (2004) 1061-1069.
[177] W. Harm, Biological effects of ultraviolet radiation, Cambridge University Press Cambridge1980.
[178] P. Karran, R. Brem, Protein oxidation, UVA and human DNA repair, DNA Repair, 44 (2016) 178-185.
[179] W.H. Organization, IARC monograph on the evaluation of carcinogenic risks to humans, Human Papillomaviruses, (2000).
[180] G.P. Pfeifer, Y.-H. You, A. Besaratinia, Mutations induced by ultraviolet light, Mutation Research/Fundamental and Molecular Mechanisms of Mutagenesis, 571 (2005) 19-31.
[181] D.E. Brash, W.A. Haseltine, UV-induced mutation hotspots occur at DNA damage hotspots, Nature, 298 (1982) 189.
[182] J.H. Miller, Mutagenic specificity of ultraviolet light, Journal of Molecular Biology, 182 (1985) 45-65.
[183] T. Bonura, K.C. Smith, Enzymatic production of deoxyribonucleic acid double-strand breaks after ultraviolet irradiation of Escherichia coli K-12, Journal of Bacteriology, 121 (1975) 511-517.
[184] T. Bonura, K.C. Smith, Quantitative evidence for enzymatically-induced dna double-strand breaks as lethal lesions in uv irradiated pol+ and polal strains of e. coli K-12, Photochemistry and Photobiology, 22 (1975) 243-248.
[185] M.O. Bradley, Double-strand breaks in DNA caused by repair of damage due to ultraviolet light, Journal of Supramolecular Structure and Cellular Biochemistry, 16 (1981) 337-343.
[186] C. Kielbassa, L. Roza, B. Epe, Wavelength dependence of oxidative DNA damage induced by UV and visible light, Carcinogenesis, 18 (1997) 811-816.
[187] Z. Kuluncsics, D. Perdiz, E. Brulay, et al., Wavelength dependence of ultraviolet-induced DNA damage distribution: involvement of direct or indirect mechanisms and possible artefacts, Journal of Photochemistry and Photobiology B: Biology, 49 (1999) 71-80.

[188] X. Zhang, B.S. Rosenstein, Y. Wang, et al., Induction of 8-Oxo-7, 8-Dihydro-2'-Deoxyguanosine by Ultraviolet Radiation in Calf Thymus DNA and HeLa Cells, Photochemistry and Photobiology, 65 (1997) 119-124.

[189] D.E. Brash, J.A. Rudolph, J.A. Simon, et al., A role for sunlight in skin cancer: UV-induced p53 mutations in squamous cell carcinoma, Proceedings of the National Academy of Sciences, 88 (1991) 10124-10128.

[190] H. Nakazawa, D. English, P.L. Randell, et al., UV and skin cancer: specific p53 gene mutation in normal skin as a biologically relevant exposure measurement, Proceedings of the National Academy of Sciences, 91 (1994) 360-364.

[191] D. Eliyahu, D. Michalovitz, S. Eliyahu, et al., Wild-type p53 can inhibit oncogene-mediated focus formation, Proceedings of the National Academy of Sciences, 86 (1989) 8763-8767.

[192] A.J. Levine, J. Momand, C.A. Finlay, The p53 tumour suppressor gene, Nature, 351 (1991) 453.

[193] B. Vogelstein, K.W. Kinzler, p53 function and dysfunction, Cell, 70 (1992) 523-526.

[194] S.J. Kuerbitz, B.S. Plunkett, W.V. Walsh, et al., Wild-type p53 is a cell cycle checkpoint determinant following irradiation, Proceedings of the National Academy of Sciences, 89 (1992) 7491-7495.

[195] Q. Zhan, F. Carrier, A. Fornace, Induction of cellular p53 activity by DNA-damaging agents and growth arrest, Molecular and Cellular Biology, 13 (1993) 4242-4250.

[196] E. Yonish-Rouach, D. Resnftzky, J. Lotem, et al., Wild-type p53 induces apoptosis of myeloid leukaemic cells that is inhibited by interleukin-6, Nature, 352 (1991) 345.

[197] S. Tornaletti, G.P. Pfeifer, Slow repair of pyrimidine dimers at p53 mutation hotspots in skin cancer, Science, 263 (1994) 1436-1438.

[198] R.P. Rastogi, A. Kumar, M.B. Tyagi, et al., Molecular mechanisms of ultraviolet radiation-induced DNA damage and repair, Journal of Nucleic Acids, 2010 (2010).

[199] W.H. Organization, I.C.o.N.-I.R. Protection, Global solar UV index: a practical guide, World Health Organization, 2002.

[200] C.-H. Lee, S.-B. Wu, C.-H. Hong, et al., Molecular mechanisms of UV-induced apoptosis and its effects on skin residential cells: the implication in UV-based phototherapy, International Journal of Molecular Sciences, 14 (2013) 6414-6435.

[201] L.A. Moore, M. Hussey, J. Ferreira, et al., Review of photokeratitis: Corneal response to ultraviolet radiation (UVR) exposure, African Vision and Eye Health, 69 (2010) 123-131.

[202] H.R. Taylor, S.K. West, F.S. Rosenthal, et al., Effect of ultraviolet radiation on cataract formation, New England Journal of Medicine, 319 (1988) 1429-1433.

[203] T. Schwarz, Mechanisms of UV-induced immunosuppression, The Keio Journal of Medicine, 54 (2005) 165-171.

[204] C.Y. Wright, P.N. Albers, A. Mathee, et al., Sun protection to improve vaccine effectiveness in children in a high ambient ultraviolet radiation and rural environment: an intervention study, BMC Public Health, 17 (2017) 37.

[205] J.A. Dever, Low earth orbital atomic oxygen and ultraviolet radiation effects on polymers, (1991).

[206] A.L. Andrady, K. Fueki, A. Torikai, Photodegradation of rigid PVC formulations III. Wavelength sensitivity of the photo-yellowing reaction in processed PVC formulations, Journal of Applied Polymer Science, 39 (1990) 763-766.

[207] A.L. Andrady, Wavelength sensitivity in polymer photodegradation, Polymer Analysis Polymer Physics, Springer1997, pp. 47-94.

[208] A.L. Andrady, S. Hamid, X. Hu, et al., Effects of increased solar ultraviolet radiation on materials, Journal of Photochemistry and Photobiology B: Biology, 46 (1998) 96-103.

[209] X.D. Chen, Z. Wang, Z.F. Liao, et al., Roles of anatase and rutile TiO2 nanoparticles in photooxidation of polyurethane, Polymer Testing, 26 (2007) 202-208.

[210] C. Jianjun, G. Gang, W. Binhua, et al., Preparation of PP/TiO2 nano-composite and analysis for its mechanism of aging resistance, Engineering Plastics Application, (2004) 15.

[211] Z. Ling, L. Zhongshi, F. Wenjun, et al., A novel polymethyl methacrylate (PMMA)-TiO2 nanocomposite and its thermal and photic stability, Wuhan University Journal of Natural Sciences, 11 (2006) 415-418.

[212] S. Hamid, W. Prichard, Mathematical modeling of weather-induced degradation of polymer properties, Journal of Applied Polymer Science, 43 (1991) 651-678.

[213] M. Amin, H.S. Hamid, J.H. Khan, Photo-oxidative degradation of polyethylene greenhouse film in a harsh environment, Journal of Polymer Engineering, 14 (1995) 253-268.

[214] A. Andrady, J. Pegram, Y. Tropsha, Changes in carbonyl index and average molecular weight on embrittlement of enhanced-photodegradable polyethylenes, Journal of Environmental Polymer Degradation, 1 (1993) 171-179.

[215] A. Andrady, H. Hamid, A. Torikai, Effects of solar UV and climate change on materials, Photochemical & Photobiological Sciences, 10 (2011) 292-300.

[216] E. Espí, A. Salmerón, A. Fontecha, et al., The effect of different variables on the accelerated and natural weathering of agricultural films, Polymer Degradation and Stability, 92 (2007) 2150-2154.

[217] K. Rajakumar, V. Sarasvathy, A.T. Chelvan, et al., Natural weathering studies of polypropylene, Journal of Polymers and the Environment, 17 (2009) 191.

[218] Y. Haruvy, Risk Assessment of Atomic-Oxygen-Effected Surface Erosion and Induced Outgassing of Polymeric Materials in LEO Space Systems, ESA Journal-European Space Agency, 14 (1990) 109-119.

[219] J.S. Fabiyi, A.G. McDonald, M.P. Wolcott, et al., Wood plastic composites weathering: Visual appearance and chemical changes, Polymer Degradation and Stability, 93 (2008) 1405-1414.

[220] M. Azadfallah, S.A. Mirshokraei, A. Jahan Latibari, et al., Analysis of photodegraded lignin on cellulose matrix by means of FTIR spectroscopy and high pressure size exclusion chromatography, Iranian Polymer Journal, 17 (2008) 73.

[221] K.K. Pandey, Study of the effect of photo-irradiation on the surface chemistry of wood, Polymer Degradation and Stability, 90 (2005) 9-20.

[222] T.C.M. Pastore, C.C.K.d. Oliveira, J.C. Rubim, et al., Effect of artificial weathering on tropical woods monitored by infrared spectroscopy (DRIFT), Quimica Nova, 31 (2008) 2071-2075.

[223] G. Bonifazi, L. Calienno, G. Capobianco, et al., Modeling color and chemical changes on normal and red heart beech wood by reflectance spectrophotometry, Fourier

Transform Infrared spectroscopy and hyperspectral imaging, Polymer Degradation and Stability, 113 (2015) 10-21.

[224] M. Zborowska, A. Stachowiak-Wencek, M. Nowaczyk-Organista, et al., Analysis of photodegradation process of Pinus sylvestris L. wood after treatment with acid and alkaline buffers and light irradiation, BioResources, 10 (2015) 2057-2066.

[225] T.-C. Chang, S.-T. Chang, Multiple photostabilization actions of heartwood extract from Acacia confusa, Wood Science and Technology, 51 (2017) 1133-1153.

[226] A.L. Catto, L.S. Montagna, S.H. Almeida, et al., Wood plastic composites weathering: Effects of compatibilization on biodegradation in soil and fungal decay, International Biodeterioration & Biodegradation, 109 (2016) 11-22.

[227] Y. Ouadou, D. Aliouche, M.-F. Thevenon, et al., Characterization and photodegradation mechanism of three Algerian wood species, Journal of Wood Science, 63 (2017) 288-294.

[228] L. Reinprecht, M. Mamoňová, M. Pánek, et al., The impact of natural and artificial weathering on the visual, colour and structural changes of seven tropical woods, European Journal of Wood and Wood Products, 76 (2018) 175-190.

[229] B.L. Diffey, Sources and measurement of ultraviolet radiation, Methods, 28 (2002) 4-13.

[230] C. Driscoll, Dosimetry methods for UV radiation, Radiation Protection Dosimetry, 72 (1997) 217-222.

[231] B. Diffey, Ultraviolet radiation dosimetry with polysulphone film, Radiation Measurement in Photobiology, (1989) 136-159.

[232] C. Wong, R. Fleming, S. Carter, et al., Measurement of human exposure to ultraviolet-B solar radiation using a CR-39 dosimeter, Health Physics, 63 (1992) 457-461.

[233] H. Yoshida, J.D. Regan, Solar UVB dosimetry by amplification of short and long segments in phage LD DNA, Photochemistry and Photobiology, 66 (1997) 672-675.

[234] H. Yoshida, J.D. Regan, UVB DNA dosimeters analyzed by polymerase chain reactions, Photochemistry and Photobiology, 66 (1997) 82-88.

[235] A.L. George, H.J. Peat, A.G. Buma, Evaluation of DNA Dosimetry to Assess Ozone-Mediated Variability of Biologically Harmful Radiation in Antarctica, Photochemistry and Photobiology, 76 (2002) 274-280.

[236] S.W. Wilhelm, W.H. Jeffrey, C.A. Suttle, et al., Estimation of Biologically Damaging UV Levels in Marine Surface Waters with DNA and Viral Dosimeters, Photochemistry and Photobiology, 76 (2002) 268-273.

[237] N. Munakata, Killing and mutagenic action of sunlight upon Bacillus subtilis spores: a dosimetric system, Mutation Research/Fundamental and Molecular Mechanisms of Mutagenesis, 82 (1981) 263-268.

[238] N. Munakata, C.S. Rupert, Dark repair of DNA containing "spore photoproduct" in Bacillus subtilis, Molecular and General Genetics MGG, 130 (1974) 239-250.

[239] N. Munakata, S. Cornain, M. Kanoko, et al., Biological monitoring of solar UV radiation at 17 sites in Asia, Europe and South America from 1999 to 2004, Photochemistry and Photobiology, 82 (2006) 689-694.

[240] P. Rettberg, C.S. Cockell, Biological UV dosimetry using the DLR-biofilm, Photochemical & Photobiological Sciences, 3 (2004) 781-787.

[241] L. Quintern, G. Horneck, U. Eschweiler, et al., A biofilm used as ultraviolet-dosimeter, Photochemistry and Photobiology, 55 (1992) 389-395.

[242] A.P. Schuch, R. da Silva Galhardo, K.M. de Lima-Bessa, et al., Development of a DNA-dosimeter system for monitoring the effects of solar-ultraviolet radiation, Photochemical & Photobiological Sciences, 8 (2009) 111-120.

[243] O.N. Galkin, I.P. Terenetskaya, 'Vitamin D'biodosimeter: basic characteristics and potential applications, Journal of Photochemistry and Photobiology B: Biology, 53 (1999) 12-19.

[244] G. Horneck, P. Rettberg, E. Rabbow, et al., Biological dosimetry of solar radiation for different simulated ozone column thicknesses, Journal of Photochemistry and Photobiology B: Biology, 32 (1996) 189-196.

[245] G. Horneck, Biological monitoring of radiation exposure, Advances in Space Research, 22 (1998) 1631-1641.

[246] G. Horneck, D. Wynn-Williams, R. Mancinelli, et al., Biological experiments on the EXPOSE facility of the International Space Station, Utilisation of the International Space Station 2, 1999, pp. 459.

[247] A. Bérces, M. Egyeki, A. Fekete, et al., The PUR Experiment on the EXPOSE-R facility: biological dosimetry of solar extraterrestrial UV radiation, International Journal of Astrobiology, 14 (2015) 47-53.

[248] G. Horneck, H. Bücker, G. Reitz, Long-term survival of bacterial spores in space, Advances in Space Research, 14 (1994) 41-45.
[249] R. Saffary, R. Nandakumar, D. Spencer, et al., Microbial survival of space vacuum and extreme ultraviolet irradiation: strain isolation and analysis during a rocket flight, FEMS Microbiology Letters, 215 (2002) 163-168.
[250] J.-P.d. Vera, D. Möhlmann, F. Butina, et al., Survival potential and photosynthetic activity of lichens under Mars-like conditions: a laboratory study, Astrobiology, 10 (2010) 215-227.
[251] J.-P. De Vera, Lichens as survivors in space and on Mars, Fungal Ecology, 5 (2012) 472-479.
[252] R. De La Torre, L.G. Sancho, G. Horneck, et al., Survival of lichens and bacteria exposed to outer space conditions–results of the Lithopanspermia experiments, Icarus, 208 (2010) 735-748.

Chapter 3

UV-induced modification of PEDOT:PSS-based nanocomposite films investigated by Raman microscopy mapping*

Nanocomposite films with high electrical conductivity and UV sensitivity were prepared by integration of DNA-modified graphene nanoplatelets (GNPs) with a polymer matrix made of poly(3,4-ethylenedioxythio-phene):poly(styrenesulfonate) (PEDOT:PSS). The exceptional electrical properties and mechanical strength of graphene were used to enhance the PEDOT:PSS properties and stability, whereas DNA molecules are sensitive to UV and have an exfoliating effect on the GNPs in aqueous solution. GNP-DNA/PEDOT:PSS films were exposed to radiation in the energetic UV-C band (254 nm), and their properties investigated before and after irradiation. Several techniques, including scanning electron microscopy, optical contact angle, electrical impedance and Raman spectroscopies, were used to characterize the nanocomposites and to investigate their sensitivity to UV. In particular, Raman microscopy mapping was used to analyze the chemical structure of the films and its modification at molecular level upon exposure to UV-C radiation. Results reported in this Chapter are useful for the application of the GNP-DNA/PEDOT:PSS films in ultra-small and lightweight UV sensor devices for use in space environment, for example during extravehicular activities (EVA), or for industrial settings on Earth that are characterized by high levels of UV-C radiation.

---

*Parts of this Chapter have been published in: Toto E.; Botti S.; Laurenzi S.; Santonicola M.G. *Applied Surface Science* **2020**, 513, 145839

3.1 Introduction

Composite materials that are based on the conductive polymer poly(3,4-ethylenedioxythiophene):poly(styrenesulfonate) (PEDOT:PSS) are currently used for a wide range of applications in different fields [1, 2]. In fact, several attractive features of PEDOT:PSS, such as its high electrical conductivity, water solubility, and thermal stability, make it suitable for the development of thin-film transistors, solar cells, organic light-emitting diodes and sensors [3-5]. Recently, the combination of conductive polymers (CPs) with carbon fillers has led to a low-cost assembling of multifunctional composites with enhanced properties and, at the same time, with a good grade of processability as required for industrial manufacturing [6]. In particular, graphene nanoplatelets (GNPs), with their excellent mechanical strength and lightweight combined with high electrical and thermal conductivity [7], can be conjugated with a CP to obtain a sensitive nanocomposite [8, 9].

One of the most interesting applications of graphene-based nanocomposites is sensing and monitoring the effects of radiation in extreme environments, such as in space [10-12]. Here, radiation absorption is detrimental for both materials and biological systems, and the effects of radiation on human health needs to be monitored constantly [13, 14]. In particular, the exposure to UV radiations can degrade materials [15, 16] and biological components [17, 18] in irreversible ways. Many studies have focused on the potential negative consequences of UV exposure on human health, such as cancer and cataract [19-21], whereas a large number of authors have reported on the adverse effects of energetic UV radiation at the level of the DNA structure [22-24]. As a consequence, the interest to develop more efficient radiation monitoring devices and with a lower detection limit of the radiation negative effects is very high. To this end, materials properties such as lightweight, real-time detection capability and stability in harsh environments are crucial requirements to integrate in radiation monitoring systems. In fact, the development of UV-detecting devices that are easy to wear, due to small volume and weight, represents an ideal solution for comfortable monitoring systems for working activities in extreme environments, such as space. Such devices would also be beneficial in environments involving a daily use of UV radiations on Earth, such as in sterilization plants.

Currently used UV detectors are mainly based on wide-bandgap semiconductor materials, which offer high sensitivity and possess several advantages for space applications, such as chemical inertness and mechanical strength [25-27]. Nevertheless, these detectors are expensive and require sophisticated fabrication processes. Among the wide-bandgap materials, zinc oxide (ZnO) is largely employed for photosensor fabrication [28-30], and several UV detection devices based on zinc oxide nanowires have been reported [31, 32]. These materials are characterized by high sensitivity and fast response due to their large surface-to-volume ratio and Debye length comparable to the small size [33], but they remain limited by the complexity of fabrication and of the measurement procedures [34, 35]. Silicon-based photodetectors and photomultiplier tubes (PMTs), combined with suitable filters, have been proposed for UV radiation detection in harsh conditions, such as in space environment [36, 37]. PMTs represent one of the approaches offering higher sensitivity, yet they require a high-voltage power supply and a cooled photocathode, which lead to costly, large-size and heavy systems for UV sensing.

In this work, novel UV sensitive films are investigated with the aim to overcome the above-mentioned drawbacks that are common to most available sensors, specifically for space applications. In particular, inexpensive starting materials and low-cost fabrication processes are combined for the realization of PEDOT:PSS-based nanocomposite films, with greatly reduced size and mass, which can monitor the effects of UV radiation exposure efficiently and can be easily integrated with materials and structures used in spacecrafts and satellite systems. In particular, an electrically conductive polymer matrix made of PEDOT:PSS is used for embedding graphene nanoplatelets that are functionalized with DNA molecules. The sensitivity to UV of the nanocomposites is enhanced by the presence of the double-stranded DNA, which represents an effective UV target since it is largely affected by exposure to this radiation. In particular, it has been demonstrated that radiation in the UV-C band (wavelength range 100–280 nm) induce a breaking of the chemical bonds in the DNA nucleic acid sequence [38]. Further, new intramolecular bonds are created with a consequent denaturation of the DNA native structure [22]. DNA also acts as an exfoliating agent for the more hydrophobic GNPs, which can be readily dispersed in aqueous solutions [39, 40]. A good dispersion of the graphene filler in the PEDOT:PSS matrix is indeed crucial to ensure enhanced and homogeneous properties for the composites realized [41, 42]. In this case,

the high specific surface area of the nanoplatelets favors the formation of a large number of non-covalent interactions between the amines of the DNA biomolecule and the carboxyl groups of the nanoplatelets [39, 43]. GNP-DNA/PEDOT:PSS films were deposited onto carbon-fiber reinforced polymer (CFRP) plates, which were selected for their high performances in the harsh space environment [44-46]. Films were exposed to UV-C radiation and different techniques used to evaluate their response under UV exposure and so their ability to detect an absorbed dose. In particular, Raman microscopy mapping is used to investigate the chemical modifications induced by UV radiation and the role of each component of the films in the overall response of the nanocomposites.

3.2 Results and discussion

UV sensitive nanocomposite films were prepared by embedding DNA-modified graphene nanoplatelets into a PEDOT:PSS matrix. DNA macromolecules were used for the modification primarily because they are known to be sensitive to UV damage [22], and because they are also efficient solubilizing agents for the hydrophobic GNP filler. Graphene nanoplatelets were selected for their high electrical conductivity and their ability to confer stability and mechanical strength to the PEDOT:PSS matrix. Neat PEDOT:PSS films and nanocomposites containing pristine GNP, without DNA modification, were also prepared in order to compare their properties under UV irradiation with those containing the GNP-DNA modified filler.

3.2.1 SEM analysis of UV-C effects on PEDOT:PSS-based nanocomposites

A morphological analysis of the nanocomposite surfaces was conducted starting from SEM investigations performed before and after UV-C irradiation of the films for 6 days, which corresponds to a radiation exposure dose of 326.6 J/cm^2. Following SEM image acquisition at two different tilt angles (0° and 5°), a 3D reconstruction of the surface profiles was performed, giving information on the effect of the UV-C exposure at the top surface of the nanocomposite films. Results of the SEM analysis for the nanocomposites with pristine GNP (GNP/PEDOT:PSS films) and with the DNA-modified GNP (GNP-DNA/PEDOT:PSS films) are reported in Figure 3.1 and Figure 3.2, respectively.

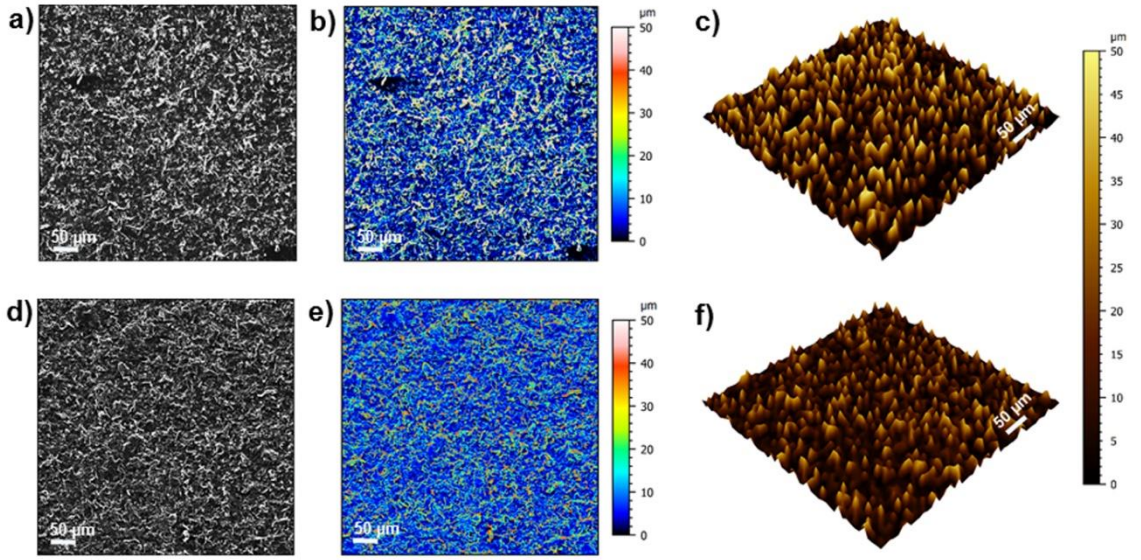

Figure 3.1. *Morphology investigation by SEM of GNP/PEDOT:PSS nanocomposite not irradiated (top) and after exposure to UV-C for 6 days (bottom): a), d) SEM images acquired with magnification of 500X; b), e) 2D view of the surface topography reconstructions; c), f) 3D view of the surface topography reconstructions.*

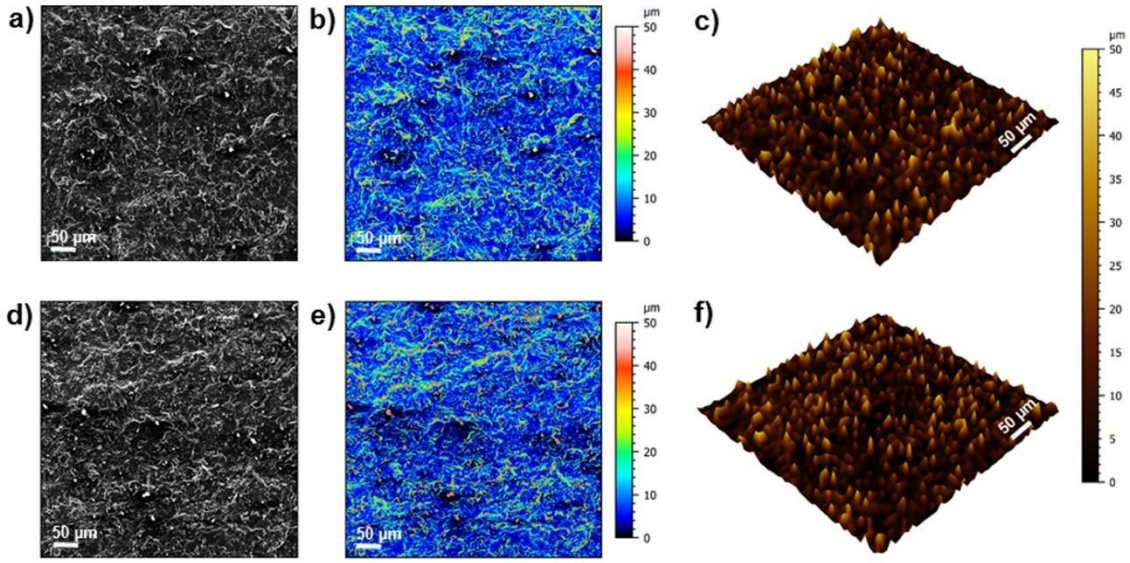

Figure 3.2. *Morphology investigation by SEM of GNP-DNA/PEDOT:PSS nanocomposite not irradiated (top) and after exposure to UV-C for 6 days (bottom): a), d) SEM images acquired with magnification of 500X; b), e) 2D view of the surface topography reconstructions; c), f) 3D view of the surface topography reconstructions.*

From the comparison of Figure 3.1a and Figure 3.2a, the presence of more agglomerates in the GNP/PEDOT:PSS nanocomposite film is evident, which contributes to an overall higher roughness of the surface with respect to the GNP-DNA/PEDOT:PSS film. This effect can be related to the absence of the DNA macromolecules in the filler, which act as exfoliating agent for the GNPs and lead to the formation of smaller aggregates in the aqueous dispersion containing PEDOT:PSS and the GNP-DNA filler. The 3D reconstructions performed with the MountainsMap® software allowed to extract the surface roughness values (R_a), which confirmed the different morphology in the absence or presence of DNA. In fact, the GNP-DNA/PEDOT:PSS films show a R_a value of 6.7 µm ± 1.2 µm, whereas a value of 11.7 µm ± 1.5 µm was determined for the films containing pristine GNP. After irradiation under UV-C light, a marked decrease (by 33%) of the roughness value was observed for the GNP/PEDOT:PSS nanocomposite, whereas the GNP-DNA/PEDOT:PSS type does not show a significant variation of roughness (4% decrease). The reason of this different response was further investigated by molecular level techniques, in particular by Raman microscopy mapping, whose results are reported further below.

3.2.2 Electrical properties and wettability of PEDOT:PSS-based nanocomposites under UV-C irradiation

Electrical impedance spectroscopy was used to evaluate the effects of UV-C exposure on the electrical properties of the PEDOT:PSS-based nanocomposites. EIS data were fitted to a RC-circuit model and then the surface conductivity values were calculated using Eq. (3.1), starting from the surface resistance values obtained by the fitting. In particular, five EIS measurements were performed for each sample and the average resistance values calculated (relative standard deviations less than 2%). Figure 3.3a shows the EIS spectra of the GNP-DNA/PEDOT:PSS and GNP/PEDOT:PSS nanocomposites obtained before and after a UV-C exposure of 24 h, corresponding to a dose of 54.4 J/cm^2.

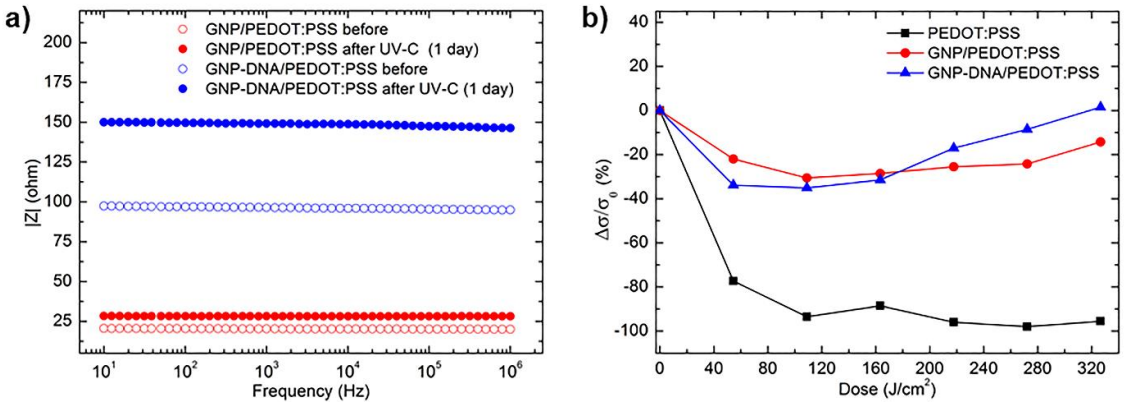

Figure 3.3. *Electrical properties of PEDOT:PSS-based nanocomposite films; a) Bode plot for EIS measurements of the films before and after exposure to UV-C for 24 h (radiation dose 54.4 J/cm^2); b) changes of the surface electrical conductivity of the films under UV-C irradiation up to 6 days.*

Both types of nanocomposite films, with GNP and GNP-DNA filler, exhibit an increase in their impedance values promoted by irradiation, but the largest variation was registered for the film containing the DNA-modified graphene filler. Further, the changes of the surface electrical conductivities were recorded daily and plotted against the absorbed UV-C dose after normalization by the initial conductivity value of each film (Figure 3.3b). Data were collected also for the neat PEDOT:PSS film, in order to separate the role of each component in the overall electrical response of the nanocomposite under UV-C radiation. Results in Figure 3.3b show that there is an initial significant variation of the surface conductivity after 1 day of exposure for all the films analyzed. Here, a decrease of the film capability to conduct electricity can be related to the damage caused by the radiation to the connections between filler and polymer matrix in the nanocomposites, and to the structure of the conductive PEDOT:PSS matrix [47]. However, differently than for the film made of only PEDOT:PSS, the nanocomposites exhibit a subsequent recovery in terms of conductivity, which can be ascribed to reactions/crosslinking in their chemical structure further promoted by UV-C exposure [48, 49]. In this sense, an interesting result was found for the GNP-DNA/PEDOT:PSS film, for which, starting from a dose of about 150 J/cm^2, the variation of the surface conductivity of the film is linearly proportional to the UV-C irradiation dose.

The surface wettability of the nanocomposites was investigated by static contact angle measurements in sessile drop configuration. The addition of GNP and GNP-DNA

to the hydrophilic PEDOT:PSS polymer matrix [50, 51] led to the formation of films with a good degree of hydrophobicity, with values of WCA larger than 100° in both cases (Table 3.1, non-irradiated samples).

Table 3.1. *Water contact angles (WCA) and surface free energies (SFE) with dispersive (γ^d) and polar (γ^p) components for PEDOT:PSS-based nanocomposite films with GNP and GNP-DNA filler, before and after exposure to UV-C for 6 days (radiation dose 326.6 J/cm^2).*

Sample	non-irradiated				after UV-C irradiation			
	WCA	**SFE**	**γ^d**	**γ^p**	**WCA**	**SFE**	**γ^d**	**γ^p**
	(degree)	**(mJ/m^2)**			**(degree)**	**(mJ/m^2)**		
GNP/ PEDOT:PSS	111.8 ± 1.5	49.4	48.1	1.3	120.2 ± 4.3	32.5	31.5	1.0
GNP-DNA/ PEDOT:PSS	106.5 ± 4.5	43.4	43.2	0.2	51.4 ± 2.7	48.5	19.8	28.7

For the non-irradiated samples, the lowest value of WCA was measured for the GNP-DNA/PEDOT:PSS nanocomposite films, as they contain the hydrophilic DNA component. After irradiation under UV-C light for 6 days, corresponding to an overall dose of 326.6 J/cm^2, both types of films exhibit a variation in surface wettability. In particular, the nanocomposite containing pristine GNP as filler shows an increase of the surface hydrophobicity, and this can be ascribed to PEDOT:PSS degradation in favor of the more hydrophobic GNP filler. On the other hand, the nanocomposite with GNP-DNA filler shows a significant decrease of its hydrophobicity (WCA from 106.5° to 51.4°), which is likely due to a prevalent oxidation of the DNA component caused by UV-C irradiation in air. In order to discriminate what nanocomposite element was more affected by the irradiation, the surface free energy (SFE) of the films, with its dispersive and polar components, was determined before and after irradiation. The SFE values determined by the Owens-Wendt method [52] confirm that the most significant variation occurs at the level of the polar component. In fact, after irradiation of the GNP-DNA/PEDOT:PSS

film, its polar component (γ^p) shows a notable increase from 0.2 to 28.7 mJ/m^2. This increase can be attributed to a UV-induced oxidation of the DNA molecules while irradiated. This was confirmed by the minimal variation of the SFE polar component in the case of GNP/PEDOT:PSS films, which do not contain DNA, under irradiation. In particular, the GNP/PEDOT:PSS films after irradiation show an overall decrease of the SFE, which is mainly due to its dispersive component (γ^d) varying from 48.1 to 31.5 mJ/m^2.

3.2.3 Raman microscopy investigations of PEDOT:PSS-based nanocomposites

Raman microscopy investigations were conducted to detect the chemical modifications in the PEDOT:PSS-based nanocomposite films caused by UV-C exposure. As illustrated in Figure 3.4a, the Raman spectrum of the PEDOT:PSS film before irradiation shows the presence of a main peak at 1426 cm^{-1}, ascribed to the symmetric stretching mode of the aromatic C=C bond in the PEDOT:PSS structure [53]. Other typical peaks for the PEDOT:PSS are detected at 1530 cm^{-1} (antisymmetric C_α–C_α stretching), at 1365 cm^{-1} (C_β–C_β stretching), and at 1261 cm^{-1} (C_α–C_α inter-ring stretching) [54, 55]. After a 6-day irradiation under UV-C (irradiance of 0.63 mW/cm^2), a stiffening of the PEDOT:PSS main peak is observed (Figure 3.4b). The blue shift from 1426 cm^{-1} to 1435 cm^{-1} was related, according to literature data, to a shortening of the conjugation length of the neutral parts promoted by UV-C irradiation [56].

Raman maps in Figure 3.4c and 3.4d were realized by using the position of PEDOT:PSS main peak as contrast parameter. The map reported in Figure 3.4c shows that in the pristine sample the peak position is in the 1420-1430 cm^{-1} range (green-blue color); differently, after UV-C irradiation, the peak position is the 1435-1440 cm^{-1} range (yellow-red color), indicating that the stiffening of PEDOT:PSS peak, which is caused by UV-C interaction with the polymer structure [47], occurs all over the area of the irradiated sample. As reported in Figure 3.5a, the Raman spectra of GNP/PEDOT:PSS film show the presence of the typical graphene peaks, the G peak at 1570 cm^{-1} and the 2D peak at 2700 cm^{-1} [57], in addition to the main PEDOT:PSS peak which is observed at 1437 cm^{-1}. Figure 3.5b reports a typical Raman spectrum of the irradiated GNP/PEDOT:PSS film, in which a shift of the main PEDOT:PSS peak and of the G peak of graphene are visible.

Specifically, the main PEDOT:PSS peak shifts to 1450 cm^{-1}, and the G peak to 1592 cm^{-1}. The I_G/I_{PEDOT} ratio was calculated before and after UV-C exposure, showing a variation from 0.3 to 0.5. Considering the I_G/I_{2D} value, no significant change was registered after irradiation, as it varies from 2.4 to 2.6 which are expected values for the GNP fillers [58].

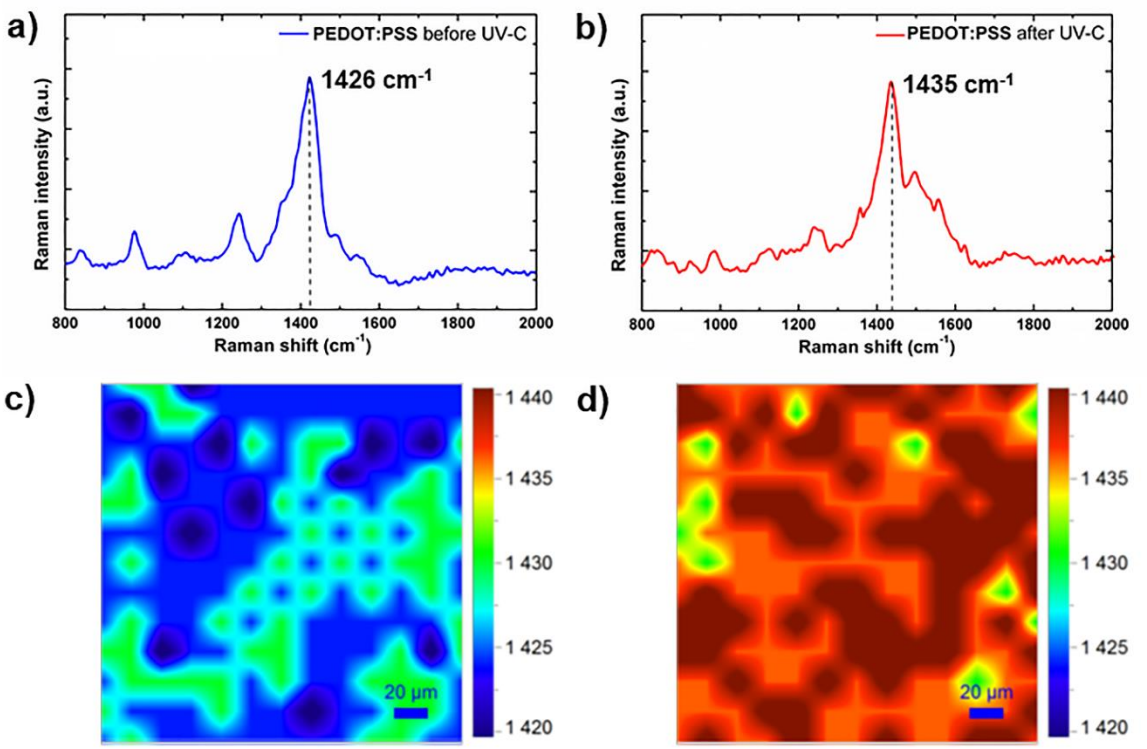

Figure 3.4. *Raman analysis of PEDOT:PSS film (a, c) non-irradiated and (b, d) after UV-C exposure for 6 days (irradiance of 0.63 mW/cm², total dose of 326.6 J/cm²). a), b) Raman spectra acquired with an excitation wavelength of 532 nm and a magnification of 10X; c), d) Raman maps obtained over an area of 200 µm × 200 µm using the position of the main PEDOT:PSS peak as contrast parameter. Color transition from blue to red indicates a shift of the PEDOT:PSS peak to higher wavenumbers after exposure to UV-C.*

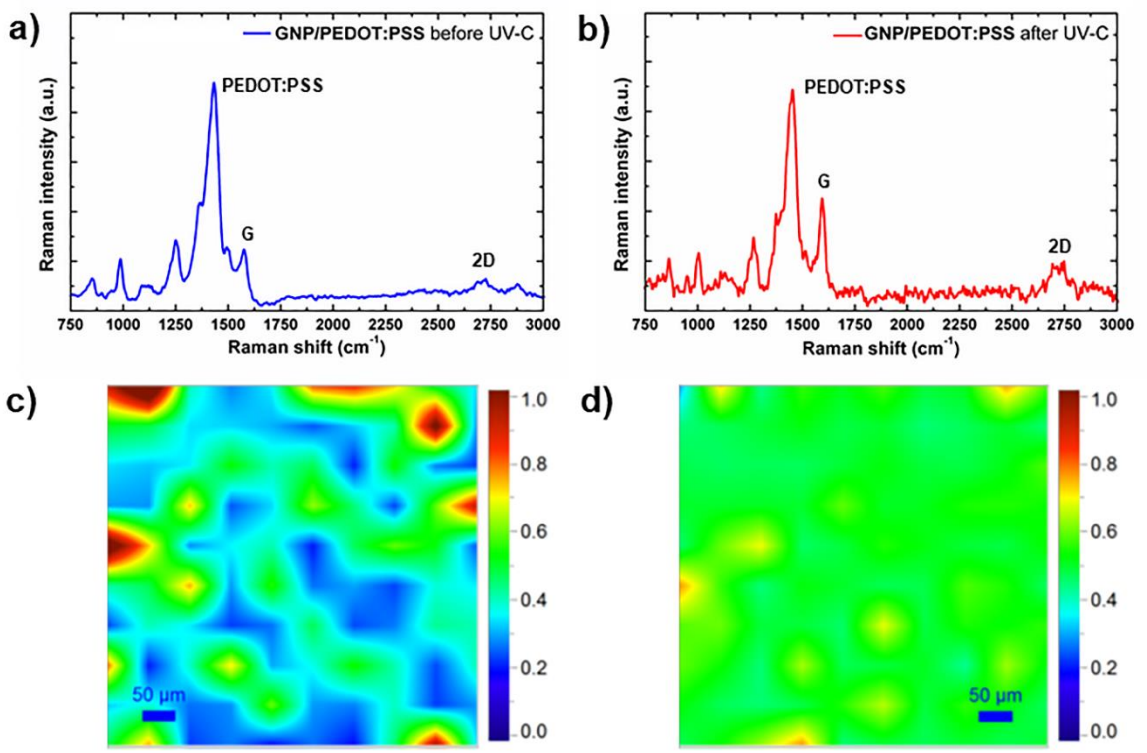

Figure 3.5. *Raman analysis of GNP/PEDOT:PSS film (a, c) non-irradiated and (b, d) after UV-C exposure for 6 days (irradiance of 0.63 mW/cm^2, total dose of 326.6 J/cm^2). a), b) Raman spectra acquired with an excitation wavelength of 532 nm and a magnification of 10X; c), d) Raman maps obtained over an area of 600 µm × 600 µm using the intensity of the G peak of graphene normalized to the intensity of the main PEDOT:PSS peak (I_G/I_{PEDOT}) as contrast parameter.*

The Raman maps of the I_G/I_{PEDOT} values before and after irradiation are presented in Figure 3.5c and 3.5d, respectively. In Figure 3.5d, the increase of this intensity ratio, uniform over all the irradiated area, can be explained by the PEDOT:PSS degradation promoted by UV-C exposure [47, 59]. The maps in Figure 3.6 show the shifts of the main PEDOT:PSS peak position in the films analyzed above. In particular, a first shift occurs upon the addition of the GNP filler to the polymer matrix (Figure 3.6b). Graphene nanoplatelets likely cause a compression of the PEDOT:PSS thiophene ring inducing a shift of its main peak from the value of 1426 cm^{-1} (Figure 3.6a) to 1437 cm^{-1} (Figure 3.6b). After irradiation of the GNP/PEDOT:PSS film, an additional shift to higher wavenumbers is observed as a result of the shortening of the conjugation length of the

neutral parts, which occurs under UV light [56]. In this case, the main PEDOT:PSS peak shifts from the value of 1437 cm^{-1} (Figure 3.6b) to 1450 cm^{-1} (Figure 3.6c).

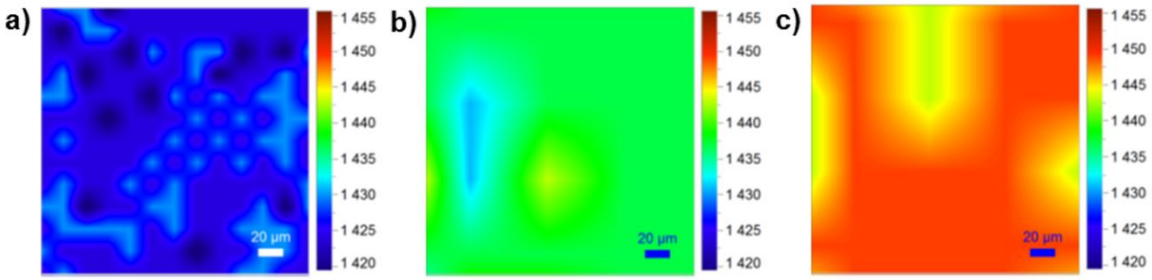

Figure 3.6. *Raman mapping of the position of the main PEDOT:PSS peak in (a) PEDOT:PSS film, (b) non-irradiated GNP/PEDOT:PSS film, and (c) irradiated GNP/PEDOT:PSS film after UV-C exposure for 6 days (irradiance of 0.63 mW/cm^2, total dose of 326.6 J/cm^2) using the position of the main PEDOT:PSS peak as contrast parameter (investigated area 200 µm × 200 µm). Color transition from blue to red indicates a shift of the peak position to higher wavenumbers.*

Additional Raman microscopy investigations of the GNP/PEDOT:PSS films were conducted at a magnification of 100X. The use of the 100X objective implies a larger value of the numerical aperture and a reduction in terms of working distance with respect to the values corresponding to the 10X objective. This means that, by using the 100X objective, a region closer to the top of the film is observed than through the 10X objective. Figure 3.7 shows the Raman map of the irradiated GNP/PEDOT:PSS film analyzed through the 100X objective, using the value of I_G/I_{PEDOT} as contrast parameter, and the corresponding Raman spectra for selected regions. For the irradiated sample and under the 100X objective, the G peak of the GNP component is always predominant with respect to the PEDOT:PSS peak, with an extended region for which the I_G/I_{PEDOT} ratio is equal to 10 (blue zone) and isolated regions for which the I_G/I_{PEDOT} ratio is much higher reaching values up to 70 (red zone). By comparing the Raman maps and spectra in Figure 3.7 (100X objective) with those in Figure 3.5 (10X objective), we can conclude that the PEDOT:PSS degradation promoted by UV-C is greater, with respect to that of graphene, at the outmost surface of the nanocomposite film. In fact, the I_{PEDOT} peak is lower than the I_G peak when using the 100X objective (smaller sampling depth), whereas it is higher with the 10X objective (larger sampling depth). This result is consistent with the fact that

the UV-C radiation has a very low penetration depth and prevalently degrades the outmost surface of materials. This phenomenon is more evident in the red zone of the sample surface, for which the corresponding Raman spectrum only shows the presence of GNPs and the PEDOT:PSS peak is negligible.

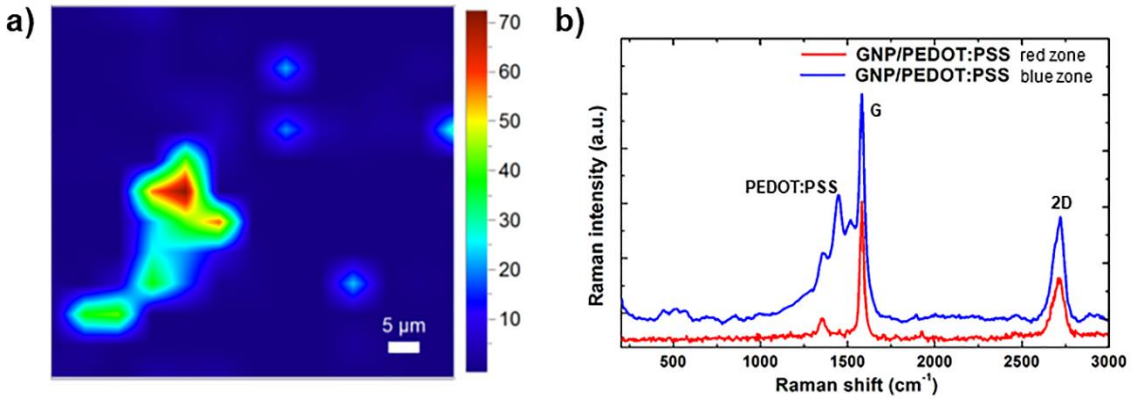

Figure 3.7. *Raman analysis of the GNP/PEDOT:PSS film after UV-C exposure for 6 days (total radiation dose of 326.6 J/cm^2) at magnification of 100X. a) Raman mapping over an area of 60 µm × 60 µm using the intensity of the G peak of graphene normalized to the intensity of the main PEDOT:PSS peak (I_G/I_{PEDOT}) as contrast parameter; b) Raman spectra corresponding to the blue and red regions of the map showing the higher intensity of the G peak with respect to PEDOT:PSS at the outermost surface.*

From the Raman mapping analysis, the PEDOT:PSS matrix emerges as the most sensitive component of the nanocomposite, whereas the GNP filler does not show damage induced by UV-C, as demonstrated by the invariance of the G peak width and slight change in the I_G/I_{2D} ratio (Figure 3.7). This result can be related to the different effects of UV-C exposure on the morphology of the films. The GNP/PEDOT:PSS surface exhibits a rougher profile as compared with the GNP-DNA/PEDOT:PSS films, which are more homogeneous and smoother because of the exfoliating effect of the DNA molecules. The asperities on surface constitute prominent regions of the GNP/PEDOT:PSS films that are more easily degraded under irradiation. This leads to a drastic reduction of the overall surface roughness (33% decrease) for the nanocomposite films containing pristine GNP

as filler, as opposed to the smoother GNP-DNA/PEDOT:PSS films for which the surface roughness does not vary significantly (4% decrease).

Regarding the Raman analysis of the GNP-DNA/PEDOT:PSS films, Figure 3.8a shows a typical spectrum obtained from the nanocomposites before any irradiation. The characteristic PEDOT:PSS peak is observed at 1432 cm^{-1}, whereas the DNA bands due to the vibrational modes of deoxyribose-phosphate (labeled as I) and of the cytosine and adenine rings (labeled as II) are centered at 1150 cm^{-1} and 1256 cm^{-1}, respectively [60-62].

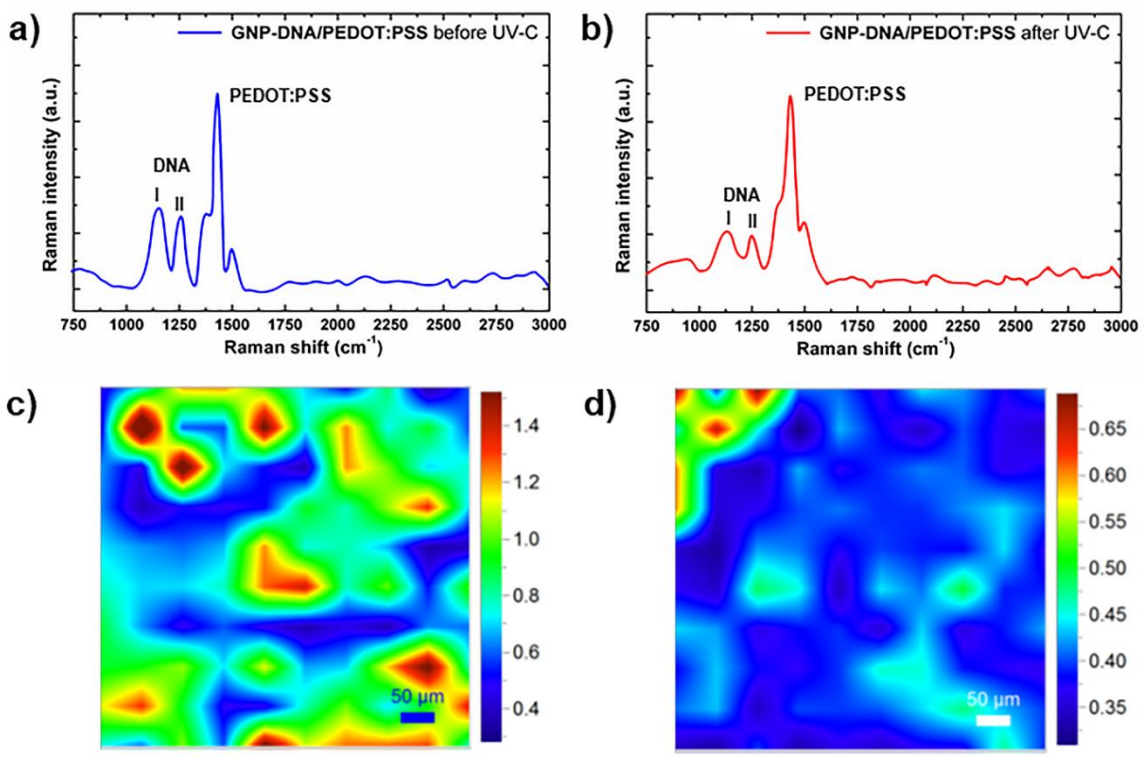

Figure 3.8. *Raman analysis of GNP-DNA/PEDOT:PSS film (a, c) non-irradiated and (b, d) after UV-C exposure for 6 days (irradiance of 0.63 mW/cm^2, total dose of 326.6 J/cm^2). a), b) Raman spectra acquired with an excitation wavelength of 532 nm and a magnification of 10X; c), d) Raman maps obtained using the intensity of the DNA I peak normalized to the intensity of the main PEDOT:PSS peak ($I_{DNA\ I}/I_{PEDOT}$) as contrast parameter, showing the decrease of the DNA I peak intensity after irradiation (investigated area 600 µm × 600 µm).*

In these spectra, the G peak of graphene (~1570 cm^{-1}) appears as a shoulder of the main PEDOT:PSS peak and the 2D peak (~2700 cm^{-1}) is undistinguishable. In fact, the use of DNA as modification of the graphene nanoplatelets makes the Raman analysis of the full GNP-DNA/PEDOT:PSS nanocomposites very challenging. For this reason, a detailed study of the PEDOT:PSS and GNP/PEDOT:PSS films, as provided above, was necessary. In particular, notable results were obtained by investigating the GNP/PEDOT:PSS samples under UV irradiation, for which the much higher radiation sensitivity of the PEDOT:PSS element with respect to graphene was determined. Therefore, in the case of the GNP-DNA/PEDOT:PSS films, we restricted the Raman analysis to the characteristic peaks of the DNA and PEDOT:PSS elements, which are the most affected under UV-C exposure. After irradiation (Figure 3.8b), both DNA bands (I and II) decrease in terms of intensity and shift to lower wavenumbers, in particular from 1150 to 1123 cm^{-1} and from 1256 to 1243 cm^{-1}. These changes can be related to the alterations of the DNA molecular conformation induced by harsh treatments, such as heating or irradiation, as reported by Ke et al. [62]. For the nanocomposite films investigated in this work, the ratio between the intensity of the peak corresponding to the vibrational modes of deoxyribose-phosphate (indicated as "DNA I") and the intensity of the main PEDOT:PSS peak was evaluated, before and after irradiation. The Raman maps of the $I_{DNA\ I}/I_{PEDOT}$ ratio were constructed and reported in Figure 3.8c and 3.8d for the non-irradiated and irradiated samples, respectively. By comparing these maps, a clear decrease of the $I_{DNA\ I}/I_{PEDOT}$ ratio upon irradiation is observed. This finding can be attributed to the damaging effects of UV-C radiation at the level of the DNA and PEDOT:PSS components of the film.

3.3 Conclusions

Nanocomposite films based on a PEDOT:PSS matrix filled with GNP-DNA particles were realized and their sensitivity to UV-C radiation investigated. In order to evaluate the role of each component, films made of neat PEDOT:PSS and nanocomposites containing pristine GNP were also tested. Different techniques were used to detect the radiation effects on the films and, in particular, Raman microscopy mapping proved to be useful to unveil the chemical modifications promoted by the UV-C radiation in the PEDOT:PSS-based nanocomposite materials. Results by EIS spectroscopy

revealed that there is a large variation of the surface electrical conductivity, for all the investigated films, after the first day of exposure. In addition, for the GNP-DNA/PEDOT:PSS film, after a cumulative radiation dose of 150 J/cm^2, a region can be detected in which the conductivity variation is linearly proportional to the UV-C dose. The surface wettability analysis showed a different sensitivity of the films to the UV-C radiation depending on the type of filler used. In particular, for the films containing the GNP-DNA filler, a decrease of the film hydrophobicity occurs, due to the oxidation of the DNA promoted by UV-C. On the other hand, the films containing pristine GNPs show an increase of hydrophobicity due to a degradation of the more hydrophilic PEDOT:PSS component in favor of the more hydrophobic graphene component. Raman investigations reveal that UV-C damages prevalently the PEDOT:PSS and DNA components of the films. This result was achieved through Raman microscopy investigations of the UV-C radiation effects on the single components of the films and exploiting this information to shed light on the more complex mechanisms acting in the overall nanocomposite films. Morphology investigations by SEM and the 3D topography reconstruction confirm a more homogeneous surface for the nanocomposites containing DNA which acts as exfoliating agent for the GNPs. The GNP-DNA/PEDOT:PSS films exhibit a good homogeneity and a significant degree of sensitivity to UV-C through the PEDOT:PSS and DNA components. After a UV-C dose of 150 J/cm^2, a region in which the surface electrical conductivity varies linearly with the absorbed dose was observed. This is a crucial point in the design of materials for radiation sensing applications, as in such regions any absorbed dose can be determined directly by monitoring the changes of the film electrical properties. Overall, the results reported in this Chapter are helpful for the design and fabrication of nanocomposite films that could be integrated in ultra-small and lightweight sensor, such as those needed to monitor human exposure to UV-C in radiation relevant environments in space and on Earth.

3.4 Experimental section

Materials: Graphene nanopowder (grade AO-4) was obtained from Graphene Supermarket (Graphene Laboratories, USA). According to the manufacturer datasheet, the AO-4 powder contains graphene nanoplatelets with average thickness of 60 nm and lateral size in the range 3-7 μm. Double-stranded DNA was purchased from Sigma-

Aldrich and used as received. Poly(3,4-ethylenedioxythiophene)-poly(styrenesulfonate) (PEDOT:PSS) was obtained in the form of dry re-dispersible pellet (Sigma-Aldrich) and used as polymer matrix for the nanocomposites. DNA solutions and GNP/DNA dispersions were prepared using ultrapure water (resistivity 18.2 MΩ·cm) from a Direct-Q3 UV water purification system (Millipore, France). The carbon-fiber reinforced polymer (CFRP) plates, which were used as substrates for the deposition of the nanocomposite films, were fabricated by resin transfer molding (RTM) using HexFlow RTM6 resin (Hexcel, UK). The fiber reinforcement was a 1K-T300 carbon plain weave with areal mass density of 120 g/m^2.

Preparation of PEDOT:PSS-based nanocomposite films: Nanocomposite films containing the GNP-DNA assembly dispersed in the PEDOT:PSS matrix were prepared by sonication in aqueous solution followed by deposition on CFRP plates and drying at 50 °C. This temperature value was chosen to prevent DNA denaturation caused by harsh heating [63], and to allow for a slow evaporation of water from the dispersion, thus avoiding the formation of cracks in the nanocomposite films during drying. For the deposition, the GNP grade AO-4 was added to an aqueous solution of DNA (10 mg/mL) at a GNP/DNA ratio of 1:1 (by weight), following previously established results [40, 64]. The dispersion was sonicated for 2 h in a cold bath to avoid thermal degradation of DNA [63]. Next, the PEDOT:PSS pellets were added to the GNP-DNA dispersion, while stirring, at a concentration of 0.7 wt%. This value was selected based on previous work in which the role of PEDOT:PSS on the electrical conductivity of the dried nanocomposite films was determined [10]. Films prepared from a dispersion with 0.7 wt% of PEDOT:PSS pellets show a purely resistive behavior (frequency range 10 – 10^6 Hz) with impedance values of about 100 Ω, which leads to a good level of electrical conductivity for sensing applications while ensuring a complete dissolution of the pellets in the GNP-DNA dispersion. Finally, a fixed volume (1.5 mL) of the GNP-DNA/PEDOT:PSS dispersion was deposited on the CFRP plates by drop casting and dried in oven at 50 °C overnight. The volume of 1.5 mL was determined as the minimum volume necessary to uniformly cover the surface of each CFRP plate (30 mm × 30 mm) by the drop casting technique. The average thickness of the nanocomposite films after drying was measured with a digital caliper (resolution 0.001 mm) and found to be of about 0.03 mm. The films were measured on the CFRP plate support at different points and the

uncovered plate thickness was subtracted. Before application of the GNP-DNA/PEDOT:PSS coating, the surface of the CFRP plates was modified with a thin layer of PEDOT:PSS, deposited from an aqueous solution at 0.7 wt% and dried at the same conditions, to improve the adhesion and stability of the nanocomposite film on the CFRP substrate.

UV-C irradiation experiments: The films deposited on the CFRP substrates were irradiated under a low-pressure UV lamp (3UV-38, 8 W from UVP LLC, USA) set at the wavelength of 254 nm. Experiments were performed in a closed chamber (50 cm × 17 cm × 20 cm) coated with aluminum foil and with the UV lamp at the top of the chamber [65]. The samples were located at a distance of 11 cm from the UV-C source, corresponding to an irradiance of 0.63 mW/cm^2. The irradiances inside the chamber were measured using a HD 2302.0 photo-radiometer (Delta Ohm, Italy) equipped with a LP 471 UV-C probe (spectral range 200–280 nm). The sample-to-source distance was selected to closely reproduce the maximum UV-C irradiation detected on the orbit of the International Space Station (ISS). In fact, according to the data provided by the Solar Radiation and Climate Experiment (SORCE) satellite (http://lasp.colorado.edu/sorce/data/data_product_summary.htm), the maximum value of UV-C irradiance is 0.64 mW/cm^2. The films were irradiated for several days at the above-mentioned conditions, corresponding to a daily dose of 54.4 J/cm^2.

Characterization methods: The morphology of the PEDOT:PSS-based films was investigated using a VEGA II LSH scanning electron microscope (TESCAN, Czech Republic) with an accelerating voltage of 5 kV and a magnification of 500X. SEM images were acquired before and after UV-C exposure. The MountainsMap software version 7 (Digital Surf, France) was used to perform a three-dimensional (3D) topography reconstruction of the investigated surfaces starting from pairs of SEM images from the same sample acquired at two different tilt angles [66]. For this reconstruction process, SEM images were first acquired in plane, corresponding to a tilt angle of the sample stage equal to 0 degree. Next, the specimen stage was tilted of 5 degrees and the corresponding image of the same sample was acquired. Surface roughness (R_a) values were extracted from the reconstructed maps averaging the R_a values obtained for each profile, typically 20 profiles for a surface area of 400 µm × 400 µm.

Electrical impedance spectroscopy (EIS) was performed using a Reference 600 Potentiostat/Galvanostat/ZRA instrument (Gamry Instruments, USA) controlled by Gamry Framework software (version 7.07). EIS measurements (10 replicates for each sample) were performed before and immediately after irradiation, considering exposure times in the range from 1 to 6 days. Samples were placed in a custom-made measurement cell made of acrylonitrile butadiene styrene (ABS) by 3D printing. The cell was designed with specific grooves to hold the electrodes (two parallel 1-cm-wide copper strips) in place over the coating surface. After positioning the sample, the top and bottom enclosures of the EIS measurement cell were tied with screws. The four probes of the Gamry potentiostat were connected to the cell in a two-electrode configuration, and the entire setup was placed inside a Faraday cage (Gamry Instruments) to avoid undesired noise during measurements. A sinusoidal voltage signal of 10 mV was applied, and impedance spectra were acquired in the frequency range 10 – 10^6 Hz with a sampling rate of 10 points per decade. The impedance data of the nanocomposite films were fitted to a parallel RC circuit model using the Gamry Echem Analyst software package. For each sample, the electrical resistance and capacitance were calculated by averaging the values obtained from the fitting of the ten replicate measurements, showing a relative standard deviation of less than 2%. The conductivity value was calculated from the average resistance value (R_s) using the following equation:

$$\sigma_s = \frac{1}{\rho_S} = \left(R_s \frac{D}{L}\right)^{-1} \tag{3.1}$$

where σ_s is the surface electrical conductivity, ρ_s is the surface resistivity, L is the distance between the two parallel electrodes, and D is the length of the electrodes in contact with the sample surface.

The surface wettability of the films was evaluated by measuring the contact angles (CA) at the top surface using a DataPhysics OCA15Pro analyzer (DataPhysics Instruments, Germany). Degassed ultrapure water and diiodomethane were selected as testing liquids. Measurements were conducted following the sessile drop method: a minimum of ten drops (volume 3 μl) on different areas of the substrate were analyzed for each nanocomposite film. The determination of the contact angle values was performed according to the Young-Laplace fitting method using the DataPhysics SCA20 image analysis software. The surface free energy (SFE) of the films was calculated from the

contact angle values measured with both water and diiodomethane. These values were implemented in the Owens-Wendt method [52]:

$$\gamma_l(1+\cos\theta) = 2\left[(\gamma_s^d\gamma_l^d)^{1/2} + (\gamma_s^p\gamma_l^p)^{1/2}\right] \quad (3.2)$$

where γ_s is the SFE of the solid that is analyzed, γ_l is the SFE of the measuring liquid, the apexes *d* and *p* indicate the dispersive and polar components respectively, and θ is the contact angle between the solid and the testing liquid.

Raman investigations were performed with a micro-Raman XploRA Plus system operated by LabSpec 6 software (Horiba Scientific, France). Measurements were carried out with a 532-nm excitation wavelength, 10X and 100X microscope objectives, and adopting a diffraction grating of 600 g/mm. Spectra were collected in the range 200 - 3000 cm^{-1} with an accumulation time of 5 s per spectrum. A filter of 10% was selected to prevent heating and damaging of the analyzed sample area. The Raman maps were recorded by scanning a sample surface up to 600 μm × 600 μm (10X objective) with step size of 7 μm in both X and Y axes. Selected samples were also investigated through a 100X objective (laser spot size of 800 nm) mapping an area up to 60 μm × 60 μm with step size of 5 μm. Raman maps were constructed by plotting the relative intensity or the position of the peaks that were selected in the acquired spectra for their relevance. Raman spectra and maps were processed using the Horiba LabSpec 6 software.

3.5 References

[1] H. Pang, L. Xu, D.-X. Yan, et al., Conductive polymer composites with segregated structures, Progress in Polymer Science, 39 (2014) 1908-1933.

[2] J.-K. Park, T.-G. Kang, B.-H. Kim, et al., Real-time humidity sensor based on microwave resonator coupled with PEDOT: PSS conducting polymer film, Scientific reports, 8 (2018) 439.

[3] D. Alemu, H.-Y. Wei, K.-C. Ho, et al., Highly conductive PEDOT: PSS electrode by simple film treatment with methanol for ITO-free polymer solar cells, Energy & environmental science, 5 (2012) 9662-9671.

[4] T. Lee, W. Kwon, M. Park, Highly conductive, transparent and metal-free electrodes with a PEDOT: PSS/SWNT bilayer for high-performance organic thin film transistors, Organic Electronics, 67 (2019) 26-33.

[5] X. Zhang, F. You, S. Liu, et al., Exceeding 4% external quantum efficiency in ultraviolet organic light-emitting diode using PEDOT: PSS/MoOx double-stacked hole injection layer, Applied Physics Letters, 110 (2017) 043301.

[6] M.H. Al-Saleh, W.H. Saadeh, U. Sundararaj, EMI shielding effectiveness of carbon based nanostructured polymeric materials: a comparative study, Carbon, 60 (2013) 146-156.

[7] M.-Y. Shen, T.-Y. Chang, T.-H. Hsieh, et al., Mechanical properties and tensile fatigue of graphene nanoplatelets reinforced polymer nanocomposites, Journal of Nanomaterials, 2013 (2013) 1.

[8] M. Clausi, E. Toto, S. Botti, et al., Direct effects of UV irradiation on graphene-based nanocomposite films revealed by electrical resistance tomography, Composites Science and Technology, 183 (2019) 107823.

[9] W. Lei, W. Si, Y. Xu, et al., Conducting polymer composites with graphene for use in chemical sensors and biosensors, Microchimica Acta, 181 (2014) 707-722.

[10] E. Toto, M.G. Santonicola, M.C. Mancini, et al., Ultraviolet-sensing surfaces based on hybrid nanocomposites for radiation monitoring systems, 2017 IEEE International Workshop on Metrology for AeroSpace (MetroAeroSpace), IEEE, 2017, pp. 369-373.

[11] E. Toto, M. Palombi, S. Laurenzi, et al., Functional nanocomposites with graphene-DNA hybrid fillers: Synthesis and surface properties under UV irradiation, Ceramics International, 45 (2019) 9631-9637.

[12] M. Santonicola, E. Toto, M. Palombi, et al., Experimental study of solar radiation effects on carbon nanocomposite sensors in simulated space environment, Proceedings of the International Astronautical Congress, IAC, 2018, pp. 1-8.

[13] M. Gussenhoven, E. Mullen, Space radiation effects program: An overview, IEEE Transactions on nuclear Science, 40 (1993) 221-227.

[14] M. Maalouf, M. Durante, N. Foray, Biological effects of space radiation on human cells: history, advances and outcomes, Journal of radiation research, 52 (2011) 126-146.

[15] A.L. Andrady, S. Hamid, X. Hu, et al., Effects of increased solar ultraviolet radiation on materials, Journal of Photochemistry and Photobiology B: Biology, 46 (1998) 96-103.

[16] A.J. Swallow, Radiation chemistry of organic compounds: international series of monographs on radiation effects in materials, Elsevier2016.
[17] B. Diffey, Solar ultraviolet radiation effects on biological systems, Physics in medicine & biology, 36 (1991) 299.
[18] W. Harm, Biological effects of ultraviolet radiation, Cambridge University Press Cambridge1980.
[19] F.A. Cucinotta, M. Durante, Cancer risk from exposure to galactic cosmic rays: implications for space exploration by human beings, The lancet oncology, 7 (2006) 431-435.
[20] F. Cucinotta, F. Manuel, J. Jones, et al., Space radiation and cataracts in astronauts, Radiation research, 156 (2001) 460-466.
[21] L.T. Chylack Jr, L.E. Peterson, A.H. Feiveson, et al., NASA study of cataract in astronauts (NASCA). Report 1: Cross-sectional study of the relationship of exposure to space radiation and risk of lens opacity, Radiation research, 172 (2009) 10-20.
[22] J.-L. Ravanat, T. Douki, J. Cadet, Direct and indirect effects of UV radiation on DNA and its components, Journal of Photochemistry and Photobiology B: Biology, 63 (2001) 88-102.
[23] J. Cadet, J.R. Wagner, DNA base damage by reactive oxygen species, oxidizing agents, and UV radiation, Cold Spring Harbor perspectives in biology, 5 (2013) a012559.
[24] M. Vorlíčková, E. Paleček, Changes in properties of DNA caused by gamma and ultraviolet radiation. Dependence of conformational changes on the chemical nature of the damage, Biochimica et Biophysica Acta (BBA)-Nucleic Acids and Protein Synthesis, 517 (1978) 308-318.
[25] F. Vigue, E. Tournié, J.-P. Faurie, et al., Visible-blind ultraviolet photodetectors based on ZnMgBeSe Schottky barrier diodes, Applied Physics Letters, 78 (2001) 4190-4192.
[26] S. Aslam, F. Yan, D. Pugel, et al., Development of ultra-high sensitivity wide-band gap UV-EUV detectors at NASA Goddard Space Flight Center, Solar Physics and Space Weather Instrumentation, International Society for Optics and Photonics, 2005, pp. 59011J.
[27] E. Monroy, F. Omnès, F. Calle, Wide-bandgap semiconductor ultraviolet photodetectors, Semiconductor science and technology, 18 (2003) R33.

[28] K. Liu, M. Sakurai, M. Aono, ZnO-based ultraviolet photodetectors, Sensors, 10 (2010) 8604-8634.

[29] J.H. Jun, H. Seong, K. Cho, et al., Ultraviolet photodetectors based on ZnO nanoparticles, Ceramics International, 35 (2009) 2797-2801.

[30] N. Nasiri, R. Bo, F. Wang, et al., Ultraporous Electron-Depleted ZnO Nanoparticle Networks for Highly Sensitive Portable Visible-Blind UV Photodetectors, Advanced Materials, 27 (2015) 4336-4343.

[31] S.N. Das, K.-J. Moon, J.P. Kar, et al., ZnO single nanowire-based UV detectors, Applied Physics Letters, 97 (2010) 022103.

[32] Y. Heo, B. Kang, L. Tien, et al., UV photoresponse of single ZnO nanowires, Applied Physics A, 80 (2005) 497-499.

[33] T. Zhai, L. Li, X. Wang, et al., Recent developments in one-dimensional inorganic nanostructures for photodetectors, Advanced Functional Materials, 20 (2010) 4233-4248.

[34] S. Bai, W. Wu, Y. Qin, et al., High-performance integrated ZnO nanowire UV sensors on rigid and flexible substrates, Advanced Functional Materials, 21 (2011) 4464-4469.

[35] L. Peng, L. Hu, X. Fang, Low-dimensional nanostructure ultraviolet photodetectors, Advanced Materials, 25 (2013) 5321-5328.

[36] L. Shi, S. Nihtianov, Comparative study of silicon-based ultraviolet photodetectors, IEEE Sensors Journal, 12 (2012) 2453-2459.

[37] G. Garipov, B. Khrenov, M. Panasyuk, et al., UV radiation from the atmosphere: Results of the MSU “Tatiana” satellite measurements, Astropart. Phys., 24 (2005) 400-408.

[38] D. Paunescu, C.A. Mora, M. Puddu, et al., DNA protection against ultraviolet irradiation by encapsulation in a multilayered SiO2/TiO2 assembly, Journal of Materials Chemistry B, 2 (2014) 8504-8509.

[39] A.J. Patil, J.L. Vickery, T.B. Scott, et al., Aqueous stabilization and self-assembly of graphene sheets into layered bio-nanocomposites using DNA, Advanced Materials, 21 (2009) 3159-3164.

[40] S. Botti, A. Rufoloni, S. Laurenzi, et al., DNA self-assembly on graphene surface studied by SERS mapping, Carbon, 109 (2016) 363-372.

[41] Y.S. Song, J.R. Youn, Influence of dispersion states of carbon nanotubes on physical properties of epoxy nanocomposites, Carbon, 43 (2005) 1378-1385.
[42] P. Martins, R. Gonçalves, S. Lanceros-Mendez, et al., Effect of filler dispersion and dispersion method on the piezoelectric and magnetoelectric response of CoFe2O4/P (VDF-TrFE) nanocomposites, Applied Surface Science, 313 (2014) 215-219.
[43] T.C. Hain, K. Kroeker, D.G. Stich, et al., Influence of DNA conformation on the dispersion of SWNTs: single-strand DNA vs. hairpin DNA, Soft Matter, 8 (2012) 2820-2823.
[44] R.A. Barnes, G.C. Mays, Fatigue performance of concrete beams strengthened with CFRP plates, Journal of composites for construction, 3 (1999) 63-72.
[45] A. Francesconi, C. Giacomuzzo, S. Kibe, et al., Effects of high-speed impacts on CFRP plates for space applications, Advances in Space Research, 50 (2012) 539-548.
[46] A. Hou, K. Gramoll, Design and fabrication of CFRP interstage attach fitting for launch vehicles, Journal of Aerospace engineering, 12 (1999) 83-91.
[47] T. Nagata, S. Oh, T. Chikyow, et al., Effect of UV–ozone treatment on electrical properties of PEDOT: PSS film, Organic Electronics, 12 (2011) 279-284.
[48] Z. Farhadinejad, M. Ehsani, I. Ahmadi-Joneidi, et al., Effects of UVC radiation on thermal, electrical and morphological behavior of silicone rubber insulators, IEEE Transactions on Dielectrics and Electrical Insulation, 19 (2012) 1740-1749.
[49] R. Verhaar, D.W. Dekkers, I.M. De Cuyper, et al., UV-C irradiation disrupts platelet surface disulfide bonds and activates the platelet integrin αIIbβ3, Blood, 112 (2008) 4935-4939.
[50] M.G. Tadesse, C. Loghin, Y. Chen, et al., Effect of liquid immersion of PEDOT: PSS-coated polyester fabric on surface resistance and wettability, Smart Materials and Structures, 26 (2017) 065016.
[51] C. Duc, A. Vlandas, G. Malliaras, et al., Wettability of PEDOT: PSS films, Soft Matter, 12 (2016) 5146-5153.
[52] D.K. Owens, R. Wendt, Estimation of the surface free energy of polymers, Journal of applied polymer science, 13 (1969) 1741-1747.
[53] S. Garreau, G. Louarn, J. Buisson, et al., In situ spectroelectrochemical Raman studies of poly (3, 4-ethylenedioxythiophene)(PEDT), Macromolecules, 32 (1999) 6807-6812.

[54] M. Łapkowski, A. Proń, Electrochemical oxidation of poly (3, 4-ethylenedioxythiophene)—"in situ" conductivity and spectroscopic investigations, Synthetic Metals, 110 (2000) 79-83.

[55] S. Garreau, J. Duvail, G. Louarn, Spectroelectrochemical studies of poly (3, 4-ethylenedioxythiophene) in aqueous medium, Synthetic metals, 125 (2001) 325-329.

[56] X. Crispin, S. Marciniak, W. Osikowicz, et al., Conductivity, morphology, interfacial chemistry, and stability of poly(3,4-ethylene dioxythiophene)–poly(styrene sulfonate): A photoelectron spectroscopy study, Journal of Polymer Science Part B: Polymer Physics, 41 (2003) 2561-2583.

[57] A.C. Ferrari, J. Meyer, V. Scardaci, et al., Raman spectrum of graphene and graphene layers, Physical review letters, 97 (2006) 187401.

[58] A. Reina, X. Jia, J. Ho, et al., Layer area, few-layer graphene films on arbitrary substrates by chemical vapor deposition, Nano letters, 9 (2009) 3087-3087.

[59] X. Ying-Jie, Q. Min-Fang, G. Deng-Zhu, et al., Increased work function in PEDOT: PSS film under ultraviolet irradiation, Chinese Physics B, 23 (2014) 038504.

[60] J.G. Duguid, V.A. Bloomfield, J.M. Benevides, et al., DNA melting investigated by differential scanning calorimetry and Raman spectroscopy, Biophysical journal, 71 (1996) 3350-3360.

[61] S.A. Overman, K.L. Aubrey, K.E. Reilly, et al., Conformation and interactions of the packaged double-stranded DNA genome of bacteriophage T7, Biospectroscopy, 4 (1998) S47-S56.

[62] W. Ke, D. Yu, J. Wu, Raman spectroscopic study of the influence on herring sperm DNA of heat treatment and ultraviolet radiation, Spectrochimica Acta Part A: Molecular and Biomolecular Spectroscopy, 55 (1999) 1081-1090.

[63] M. Karni, D. Zidon, P. Polak, et al., Thermal degradation of DNA, DNA and cell biology, 32 (2013) 298-301.

[64] M.G. Santonicola, M.G. Coscia, S. Botti, et al., Graphene/DNA nanostructured films for bioinspired sensing of UV radiation effects, Proceedings of the International Astronautical Congress, IAC, International Astronautical Federation, IAF, 2014, pp. 6313-6317.

[65] M.G. Santonicola, M.G. Coscia, M. Sirilli, et al., Nanomaterial-based biosensors for a real-time detection of biological damage by UV light, 2015 37th Annual International

Conference of the IEEE Engineering in Medicine and Biology Society (EMBC), IEEE, 2015, pp. 4391-4394.
[66] C. Mignot, Color (and 3D) for Scanning Electron Microscopy, Microscopy Today, 26 (2018) 12-17.

Chapter 4

Direct effects of UV irradiation on graphene-based nanocomposite films revealed by electrical resistance tomography*

The integration of surface sensing elements providing an *in situ* monitoring of the UV-induced degradation effects in composite materials and structures is crucial for their applications in hostile environments characterized by high levels of radiation, such as space. In this Chapter, the investigation of the electrical response of a UV-sensitive nanocomposite film using electrical resistance tomography (ERT) is reported. The conductivity changes measured at the irradiated surfaces were compared with results from morphology analysis by scanning electron microscopy (SEM) and surface analytical techniques, such as Raman microscopy. Highly conductive and UV-sensitive nanocomposite coatings were prepared by embedding the graphene and deoxyribonucleic acid (DNA) component in a poly(3,4-ethylene dioxythiophene):poly(styrene sulfonate) (PEDOT:PSS) matrix. The coatings were deposited onto carbon-reinforced laminated structures fabricated by resin transfer molding process using an aerospace-grade epoxy resin. Two different irradiation conditions were tested by exposing the nanocomposite surfaces to UV-C irradiances of 2.6 and 4.0 mW/cm^2. Results show that the ERT technique has great potential for the *in situ* health monitoring of carbon-based materials and structures for aerospace applications, which are subject to degradation by UV-C radiation: it allows mapping of the conductivity changes occurring at the surface of the graphene/DNA/PEDOT:PSS coatings during irradiation.

---

*Parts of this Chapter have been published in: Clausi M.†; Toto E.†; Botti S.; Laurenzi S.; La Saponara V.; Santonicola M.G. *Composites Science and Technology* **2019**, 183, 107823

†These authors contributed equally

4.1 Introduction

Carbon fiber-reinforced polymer composites are widely used in aerospace structures for their excellent strength-to-weight ratio and stiffness-to-weight ratio, improved corrosion resistance and property tailorability for specific applications [1, 2]. However, it is well known that hostile space conditions cause degrading effects on polymer composite laminates [3-5]. UV radiations, vacuum, atomic oxygen and large temperature gradients all lead to the degradation of polymer-based materials [4-8], affecting the structural integrity of spacecraft components, and reducing the life cycle of the structure. To solve these problems, researchers are investigating many solutions, one being the fabrication of sensor elements to integrate into the composite laminates, thus creating health monitoring systems for radiation-induced damage to aerospace structures [9-11]. In this contest, the use of electrical measurements for strain sensing and damage identification was recently proposed [12-19]. In particular, several groups are studying electrical conductivity-based health monitoring methods, in which the damaged areas in composite laminates are identified by monitoring the changes of electrical conductivity in such areas. To this end, electrical impedance tomography (EIT), based on alternating currents (AC), and electrical resistance tomography (ERT), based on direct currents (DC), are receiving great attention because they are low-cost and non-invasive techniques that allow to obtain electrical conductivity maps of the parts under exam. In their study, Schueler and colleagues demonstrated that, using EIT mapping, damaged areas in carbon fiber-reinforced composite materials correspond to areas with lower electrical conductivity [20]. Baltopoulos et al. investigated the effects of different types of damage (drilled hole, local indentation) on the electrical properties of composites reinforced with carbon fibers and nanotubes, using ERT [21, 22]. In both works, the authors were able to detect the presence of damage in terms of loss of conductivity in the same area where the damage occurred. Other studies investigated the use of electrically conductive nanocomposites and the possibility of identifying damage to the matrix by electrical measurements [23-25]. For example, by using carbon black filler and the EIT technique, Tallman et al. were able to locate the matrix damage in glass fiber/epoxy laminates [26].

Recently, the development of nanocomposite films is receiving great attention, where the films are applied on composite structures for damage monitoring purposes. Loh et al. fabricated nanocomposite films filled with carbon nanotubes as sensing skins on

different type of substrates [18]. They detected strain during applied load and spatial impact damage on the nanocomposite films by electrical impedance tomography. In another work, Loyola et al. studied the spatial distribution of conductivity changes in nanocomposite films that were spray-deposited on glass fiber-reinforced polymer (GFRP) composites upon damage from a drilling operation and from low-velocity impact [12]. Results showed that indeed, in the electrical resistance tomography maps, the damaged areas possess a lower conductivity. These trends were confirmed by Lestari et al. for uniaxial tensile loadings in glass fiber-reinforced polymer composites coated by nanocomposite films [27].

In this proof-of-concept work, the use of ERT to identify the damaging effects of UV-C radiation was investigated on nanocomposite coatings made of graphene nanoplatelets (GNP) functionalized with deoxyribonucleic acid (DNA) and embedded in a poly(3,4-ethylene dioxythiophene):poly(styrene sulfonate) (PEDOT:PSS) matrix. The DNA-functionalized GNPs were chosen based on previous work that demonstrated their sensitivity to UV radiation [9, 28], whereas the PEDOT:PSS matrix was selected to enhance the electrical conductivity of the overall nanocomposite [10]. The UV-sensitive coatings were applied to the surface of carbon fiber/epoxy laminates, which are composite structures that are typically used in the aeronautical and space fields. To our knowledge, this is the first report of the application of the ERT technique to the detection of surface conductivity changes induced by UV exposure. This technique in combination with the UV-sensitive coatings containing DNA-functionalized graphene can provide a health monitoring method for composite materials and structures that are exposed to damaging levels of UV radiation. A 16-electrode scheme was applied along the edges of the nanocomposite sensor coatings, and maps of conductivity changes were reconstructed after UV-C irradiation with two different intensities (2.6 and 4.0 mW/cm^2) for 24 h. The information from the ERT analysis is discussed and related to results from complementary techniques, such as scanning electron microscopy and Raman spectroscopy, which have previously proven to be a valuable tool for the characterization of carbon/DNA interfaces [29, 30].

4.2 Results and discussion

4.2.1 ERT sensitivity analysis

In the first part of the study, a sensitivity analysis on values and patterns of the injection currents was carried out, with the aim of identifying a combination which would be reasonably sensitive to surface defects in the as-manufactured samples, prior to UV-C irradiation. Direct current values of 10 mA, 20 mA, 30 mA, 40 mA, 50 mA, 80 mA, 100 mA and 150 mA were used. Previously, a 200 mA current was found to cause electrolysis damage to the electrodes [31], and therefore the selected currents for this study were lower. For each injection, 256 differential voltage data measurements were recorded at each load step ($m^2 = 256$, in which $m = 16$ is the number of electrodes). The number of independent measurements depends on the type of injection. Shi et al. have advocated the so-called pseudo-polar pattern as the best drive pattern for brain electrical impedance tomography: in this pattern, the driving current flows into one electrode and out of another electrode located almost at 180 degrees with respect to the injection electrode [32]. On the other hand, Kolehmainen et al. have found that the so-called adjacent injection pattern is more robust to modeling errors of contact impedance, electrode size, boundary in typical EIT biomedical problems [33]. Because of the nature of the samples in this work and the absence of earlier ERT studies on such samples, a reasonably broad set of injection patterns was investigated. Figure 4.1 shows the five different voltage measurement patterns that were investigated in combination with each injection current. In the adjacent pattern (Figure 4.1b), the current was injected through two neighboring electrodes, while the differential voltage data were recorded from all other electrodes. The sequence rotates for a new measurement until the pattern returns to the original position. In the opposite pattern (Figure 4.1c), the current was injected through the first and the ninth electrodes, and the procedure was repeated clockwise. In the 1-11 pattern (Figure 4.1d), the current was injected through the first and eleventh electrodes. In the 1-12 pattern (Figure 4.1e) and in the 1-13 pattern (Figure 4.1f), the current was injected through the first and twelfth electrodes, and from the first and the thirteenth electrodes, respectively.

The same procedure used for the adjacent and opposite patterns was applied to the 1-11, 1-12 and 1-13 patterns. For each injection, measurements at a specific current value and current pattern were repeated several times.

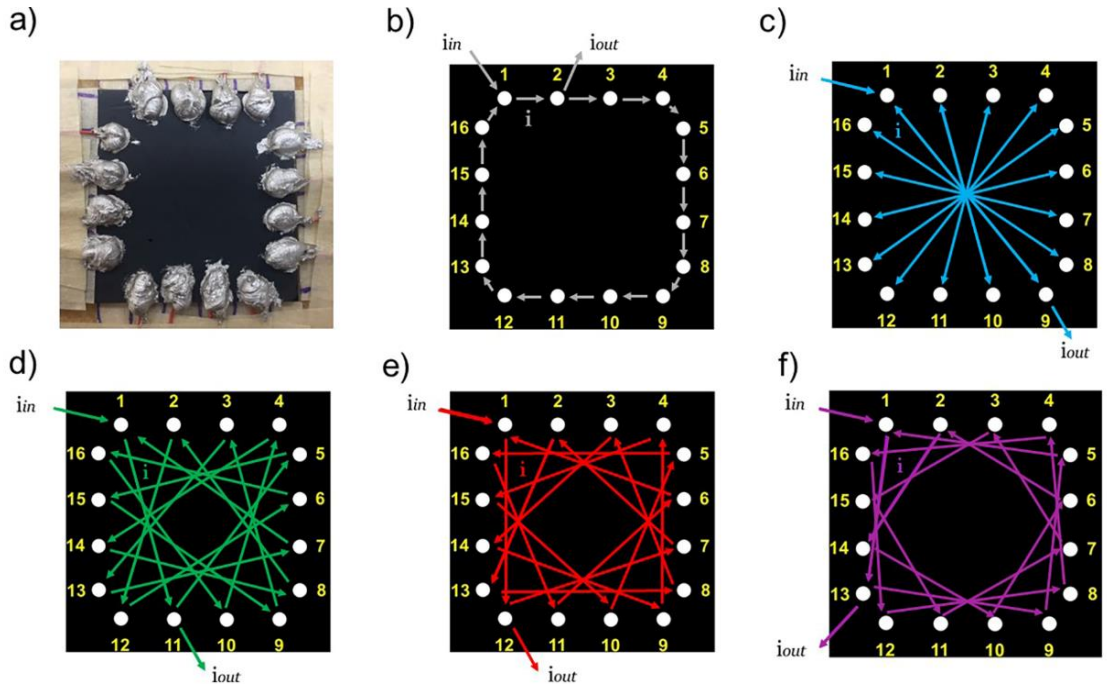

Figure 4.1. *(a) GNP-DNA/PEDOT:PSS nanocomposite film on CFRP laminated substrate (size 40 mm × 40 mm) with sixteen electrode elements fixed by conductive silver epoxy; schemes of applied current injection patterns: (b) adjacent pattern, (c) opposite pattern, (d) 1-11 pattern, (e) 1-12 pattern, and (f) 1-13 pattern.*

The results of the preliminary ERT sensitivity analysis for the nanocomposite coatings exposed to UV-C irradiances of 2.6 and 4.0 mW/cm^2 are reported in Figure 4.2 and Figure 4.3, respectively. The changes of voltage measurements due to UV-C irradiation, as recorded by the sixteen electrodes, are shown for different patterns and injection currents (range 10 – 50 mA).

In both cases of UV-C exposure, the opposite scheme resulted in the current pattern exhibiting the highest sensitivity to the changes induced by irradiation at all injection currents. For this reason, the opposite scheme was selected for the subsequent reconstruction of the conductivity change maps by the EIDORS toolbox. The optimal electric field density that is required for the reconstruction of meaningful conductivity change maps describing the changes of GNP-DNA/PEDOT:PSS surfaces under UV irradiation depends on the correct combination of injection pattern and current intensity. Results show that increasing the density of the injection pattern, for the same injection current, the absolute difference between the voltage measurements increases. From the optimization analysis of the ERT injection currents, in order to localize surface defects on the nanocomposite coatings under investigation, the best results were found using lower injection currents, up to 50 mA.

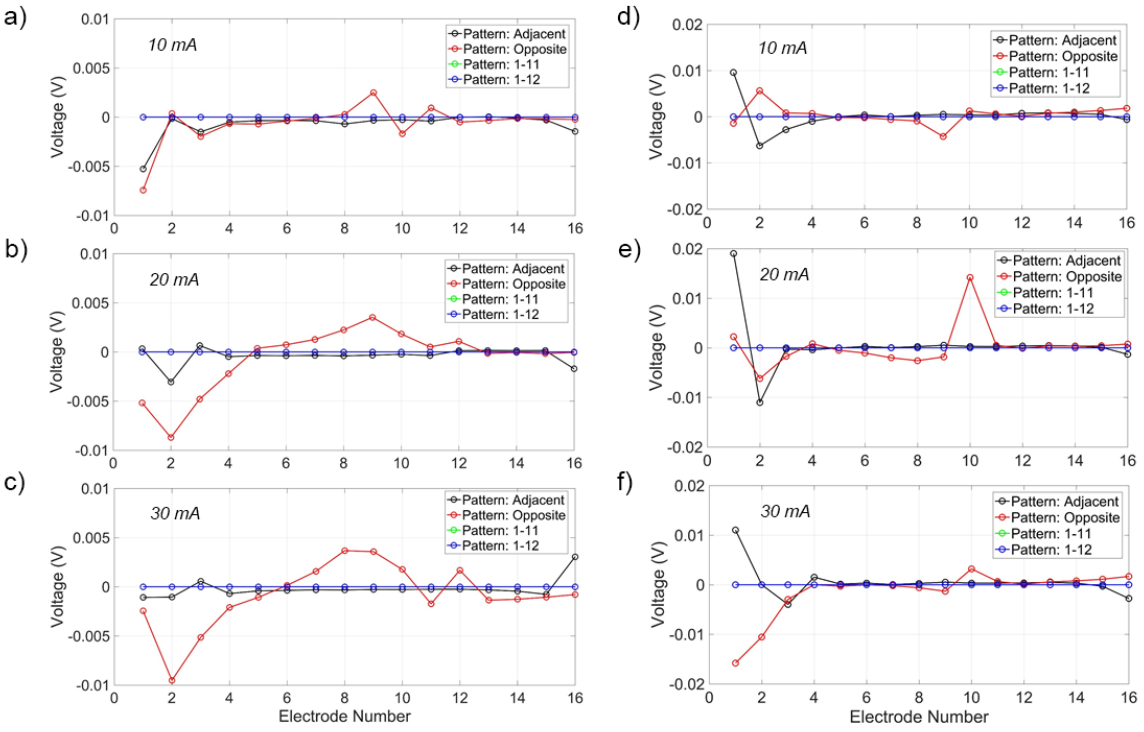

Figure 4.2. *Voltage changes of GNP-DNA/PEDOT:PSS surfaces due to UV-C irradiation recorded using the sixteen-electrode configuration with different injection patterns and currents of 10, 20 and 30 mA. UV-C exposure: (a, b, c) 2.6 mW/cm^2 for 24 h; (d, e, f) 4.0 mW/cm^2 for 24 h.*

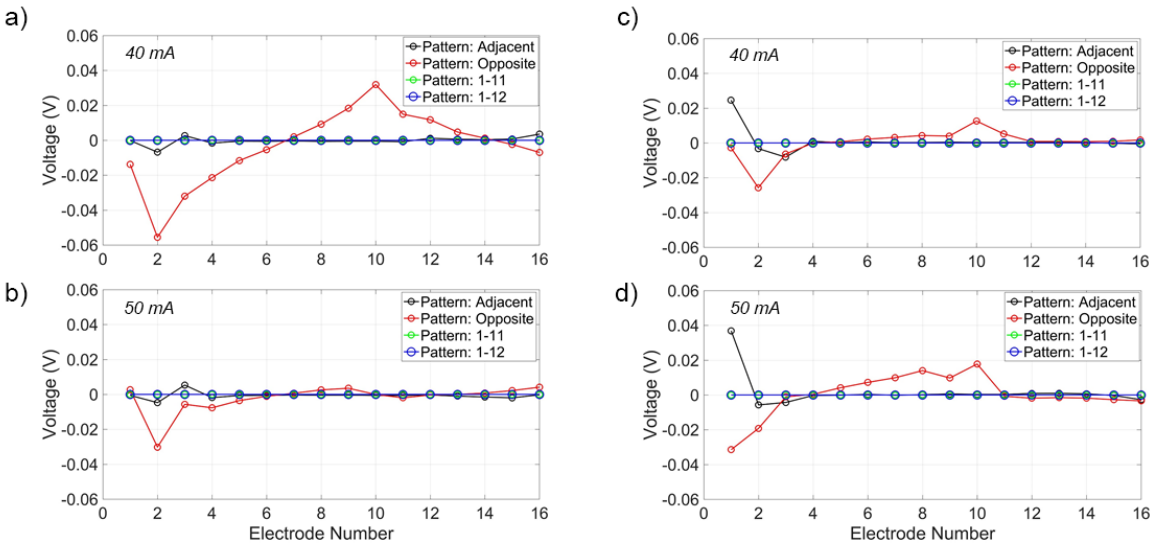

Figure 4.3. *Voltage changes of GNP-DNA/PEDOT:PSS surfaces due to UV-C irradiation recorded using the sixteen-electrode configuration with different injection patterns and currents of 40 and 50 mA. UV-C exposure: (a, b) 2.6 mW/cm^2 for 24 h; (c, d) 4.0 mW/cm^2 for 24 h.*

4.2.2 ERT mapping of UV damage on nanocomposite surfaces and further investigations on their properties

The ERT analysis was applied to investigate the effects of UV-C irradiation on the surface electrical conductivity of GNP-DNA/PEDOT:PSS surfaces. The normalized conductivity change maps reconstructed from the ERT data for the surfaces exposed to UV-C irradiance of 2.6 mW/cm^2 for 24 h are presented in Figure 4.4. Different injection currents in the range 10 – 50 mA were considered in combination with the opposite current injection pattern. The reconstruction was performed with the hyperparameter value *a* that yielded a noise factor NF = 1. In the maps, the yellow color indicates a negative change of the normalized electrical conductivity, indicating a local decrease of the sample electrical conductivity, whereas the blue color is associated with a positive conductivity change. A smaller area of the nanocomposite surface was radiated with the aim of evaluating the grade of accuracy of the ERT analysis in locating the surface electrical conductivity changes on the sample after UV-C exposure. The white dashed line denotes the central region (20 mm × 20 mm) that was exposed to UV-C, whereas the

edges of the sensor surface had been shielded to avoid damage to the electrodes. From the reconstruction of the voltage changes, it was noted that injection currents of 20 and 30 mA provided the best localization of the area exposed to UV, in which a significant loss of electrical conductivity seems to occur. This result was further investigated and confirmed by measurements of the average electrical impedance of the samples (see discussion below and Figure 4.7).

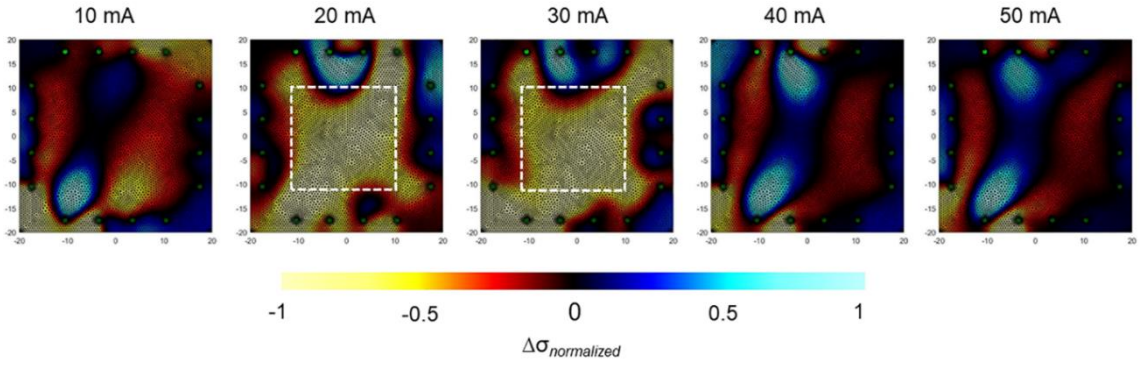

Figure 4.4. *ERT conductivity change maps of GNP-DNA/PEDOT:PSS film after UV-C irradiation (2.6 mW/cm^2, 24 h) reconstructed using EIDORS. Voltage data recorded with the opposite injection pattern and currents in the range 10-50 mA. The white dashed line denotes the UV-C irradiated area (20 mm × 20 mm).*

Researchers in the biomedical field (Kauppinen et al. [34]) have observed that the impedance obtained from a given current injection and a given voltage measurement could increase, decrease or just be unaffected by a conductivity change in the region of interest, undermining the sensitivity of the EIT approach. This observation may support why some combinations of current intensity and injection patterns were not successful in identifying the surface defects of the current study, and may have been possibly impacted by larger noise. In particular, for the dense opposite pattern, when considering the dimensions of the nanocomposite samples investigated in this study, the enhanced overlapping of the electric flux lines at higher injection currents causes a higher disturbance in the measurements. On the other hand, when using lower injection currents (20-30 mA), it was possible to localize the irradiated area on the samples, by observing the regions in which negative surface conductivity changes occur (in yellow color). Besides the opposite pattern, other injection schemes were also investigated, but did not

result in a meaningful correspondence between the irradiated area and the conductivity change maps.

Figure 4.5 shows a comparison of the ERT conductivity maps for the nanocomposites irradiated at two different intensities (2.6 and 4.0 mW/cm^2), which were reconstructed from data acquired using the opposite pattern and the injection current of 20 mA. For the surface irradiated at higher intensity, 4.0 mW/cm^2 corresponding to a UV-C dose of 346 J/cm^2 in 24 h, a different conductivity change pattern was observed (Figure 4.5b), with a prevalence of areas with positive conductivity changes (in blue color). For conductive composite materials that are fabricated by embedding a carbon-based filler in a polymer matrix, this result is not unexpected, and can be attributed to the large polymer degradation that is caused by exposure to a high dose of UV radiation [35, 36]. In fact, while the matrix is eroded, the conductive filler is progressively exposed causing an apparent increase of the coating electrical conductivity.

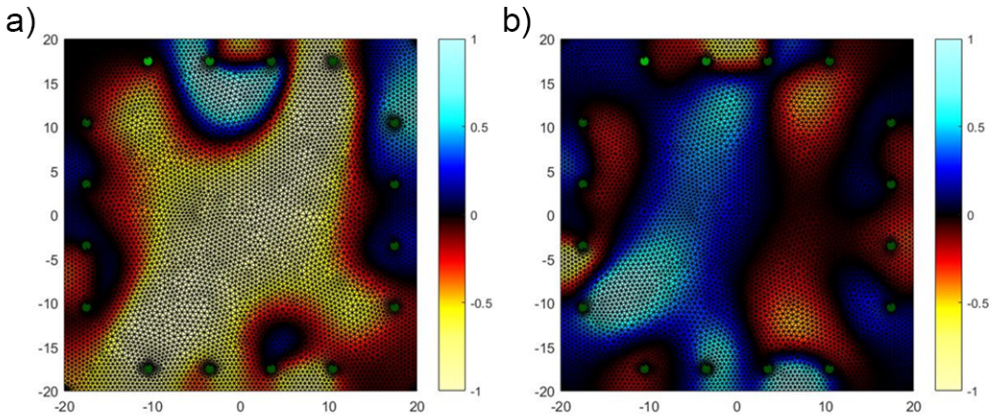

Figure 4.5. *Reconstructed conductivity change maps of irradiated GNP-DNA/PEDOT:PSS films after exposure to UV-C intensities of (a) 2.6 mW/cm^2 and (b) 4.0 mW/cm^2 (exposure time 24 h). Tests with 20 mA current, opposite injection pattern. The yellow and blue colors indicate negative and positive conductivity changes ($\Delta\sigma_{normalized}$), respectively.*

In this study, the morphology analysis of the GNP-DNA/PEDOT:PSS surfaces exposed to higher UV-C intensity (4.0 mW/cm^2) conducted by SEM revealed a marked difference between the irradiated and non-irradiated samples (Figure 4.6). A degradation of the non-conductive component of the nanocomposite coating can be observed after UV-C irradiation: the surface features are characterized by smoother edges than those of the non-irradiated sample, and this observation is more evident in the SEM images at higher magnification (Figure 4.6c and d). No changes were detected on the GNP-DNA/PEDOT:PSS sample exposed to lower values of irradiance (2.6 mW/cm^2).

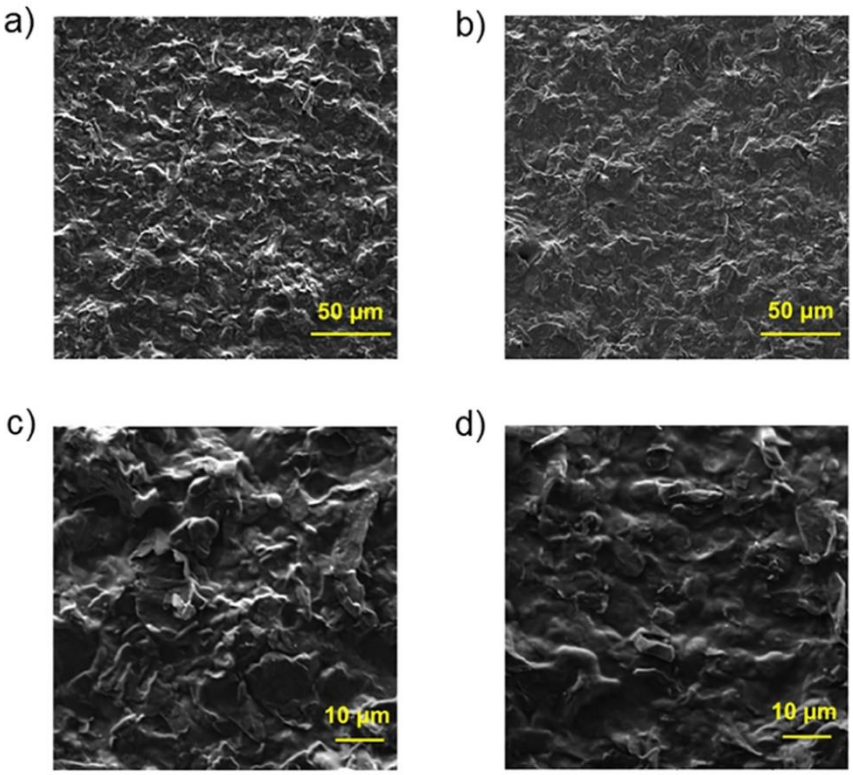

Figure 4.6. *SEM images of GNP-DNA/PEDOT:PSS nanocomposite surfaces (a, c) before irradiation and (b, d) after UV-C exposure (4.0 mW/cm^2, 24 h) showing local erosion effects on irradiated samples (right). Images acquired with accelerating voltage 10 kV and increasing magnification: (a, b) 1000 X, (c, d) 3000 X.*

In order to evaluate the accuracy of the results in the conductivity maps reconstructed from the ERT data, further investigations on the GNP-DNA/PEDOT:PSS surfaces under UV-C irradiation were performed. The positive or negative surface conductivity changes in the ERT reconstructed maps, localized in the areas exposed to different intensities of UV-C, were investigated by electrical impedance spectroscopy (EIS) in a traditional two-electrode cell. A lower irradiance (0.63 mW/cm^2) was used in order to obtain a trend of the surface conductivity change as a function of the UV-C dose within 7 days of irradiation tests. The normalized conductivity changes measured after each day of irradiation are reported in Figure 4.7. They show a non-linear behavior as a function of the dose. In particular, a significant drop of conductivity was measured after the first day of irradiation (dose of 50 J/cm^2). The conductivity remained approximately constant for the next 2 days, after which a linear increase as a function of the UV-C dose was observed. This result suggests that different levels of UV-C damage might be present at different radiation doses. Consequently, the electrical properties of the irradiated samples may vary significantly with the intensity of the UV-C radiation, leading to the results observed in the ERT conductivity change maps (Figure 4.5).

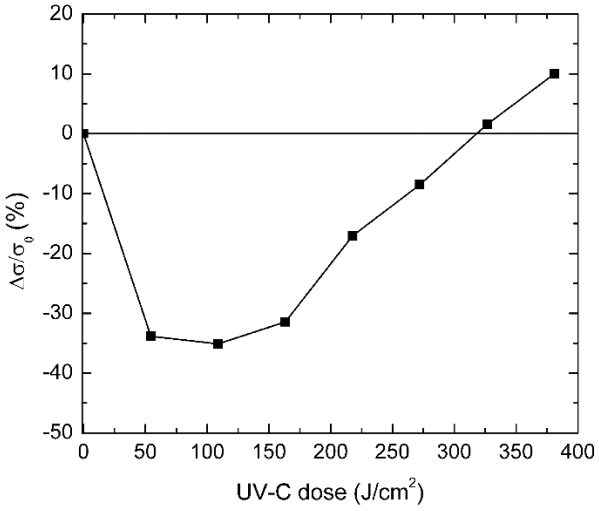

Figure 4.7. *Surface conductivity changes of irradiated GNP-DNA/PEDOT:PSS films as a function of the UV-C dose determined by electrical impedance spectroscopy in two-electrode measurement cell. Dose range corresponds to irradiation times from 0 to 7 days (UV-C irradiance of 0.63 mW/cm^2).*

The initial drop of conductivity of the irradiated GNP-DNA/PEDOT:PSS films in Figure 4.7 can be explained considering the degradation effect that UV radiation has on the conductive PEDOT:PSS matrix. Previous studies have demonstrated that irradiation under UV-C light determines a significant increase of the resistivity values of PEDOT:PSS films due to the decomposition of the polymer chemical bonds [37, 38]. This phenomenon is likely the initial phase of degradation of the GNP-DNA/PEDOT:PSS films, causing the marked conductivity drop during the first 3 days of exposure. This phase is followed by an almost linear increase of the conductivity, which can be related to a progressive exposure of the graphene nanoplatelets component.

Similarly to the analysis presented in the previous Chapter, Raman spectra were acquired on the GNP/PEDOT:PSS film before and after UV-C irradiation. In Figure 4.8a, the strong band observed at 1427 cm^{-1} can be assigned to the symmetric $C_\alpha=C_\beta$ stretching of PEDOT [39], whereas the peak at ~1580 cm^{-1} and the broad band at ~2700 cm^{-1} are the G and 2D peaks of graphene, respectively [40]. A significant decrease of the main PEDOT peak is evident in the spectrum of the irradiated samples. The analysis of the intensities of the PEDOT and GNP characteristic peaks reveals that the value of I_{PEDOT}/I_G changes from 4.0 to 2.1 upon irradiation, while the I_G/I_{2D} value stays approximately the same (from 2.4 to 2.6, typical values for multiple layers of graphene [41]). Similar results were obtained from analysis of the irradiated GNP-DNA/PEDOT:PSS films (Figure 4.8b), for which the I_{PEDOT}/I_G value varies from 4.6 to 2.8. For both types of films, the PEDOT component is more affected and degrades more quickly than graphene under UV-C irradiation. This is consistent with the initial conductivity drop measured by electrical impedance spectroscopy (Figure 4.7). In the Raman spectra of the GNP-DNA/PEDOT:PSS films, the characteristic peaks of DNA are visible in the 1100 – 1300 cm^{-1} region, with the bands near 1150 and 1256 cm^{-1} due to the vibrational modes of deoxyribose-phosphate and of cytosine and adenine rings, respectively [42, 43]. Both peaks exhibit a marked shift to lower frequency upon irradiation, from 1150 to 1123 cm^{-1} and from 1256 to 1243 cm^{-1}, which has been linked to alteration of the DNA structure [44]. The damage to DNA can be also inferred from the large drop of the Raman bands in the 1100 – 1300 cm^{-1} region after UV-C irradiation (Figure 4.8b). The intensity ratios I_{1150}/I_{1500} and I_{1256}/I_{1500} between the characteristic DNA peaks and the G band of graphene vary from 2.0 to 0.7 and from 1.8 to 0.7, respectively. Collectively, these results indicate

that the damage induced by UV-C is localized more on the PEDOT and DNA components of the nanocomposite films, and this is consistent with the conductivity increase observed after the initial degradation of the conductive polymer matrix, due to progressive exposure of the graphene nanoplatelets.

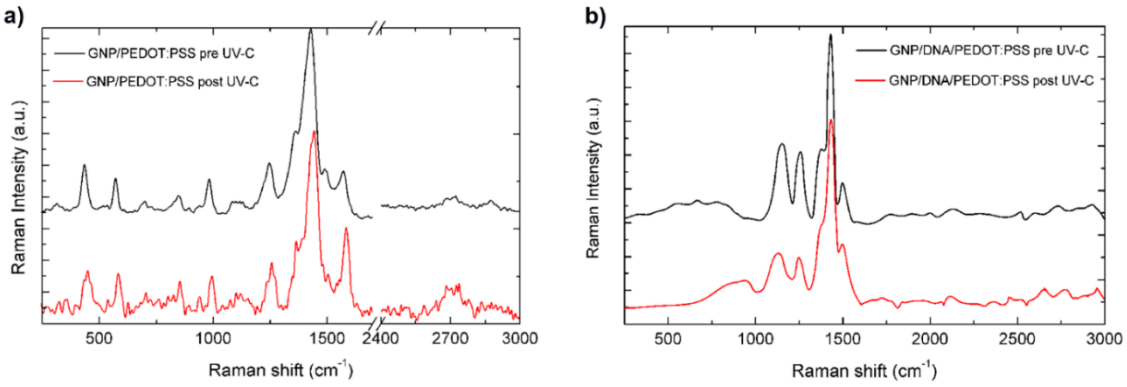

Figure 4.8. *Raman spectra of (a) GNP/PEDOT:PSS and (b) GNP-DNA/PEDOT:PSS films before and after UV-C irradiation (0.63 mW/cm^2 for 6 days corresponding to a dose of 327 J/cm^2) acquired with an excitation wavelength of 532 nm.*

4.3 Conclusions

Electrical resistance tomography was used to investigate the changes of the surface electrical properties of UV-sensitive nanocomposite films upon exposure to UV-C radiation. The nanocomposite coatings were fabricated by integration of DNA-functionalized graphene nanoplatelets into a conductive polymer matrix made of PEDOT:PSS. The ERT technique was optimized in terms of current patterns and injection values in order to detect damage induced by UV irradiation, with the opposite injection pattern and currents of the order of 20-30 mA giving the most reliable outcome. Maps of conductivity changes for the irradiated films were reconstructed from the acquired differential voltage changes with respect to a baseline sample. The nanocomposite area exposed and affected by the UV-C radiation was localized in the ERT maps with good agreement. Different levels of conductivity changes were detected by the technique when exposing the surfaces to different intensities of UV-C radiation. These conductivity changes were verified using 2-electrode impedance spectroscopy. The results were

supported by SEM morphology and Raman spectroscopy analyses. In particular, the GNP-DNA/PEDOT:PSS nanocomposite films face different stages of conductivity changes upon irradiation with UV-C light, with an initial drop of the electrical conductivity due to degradation of the conducting polymer matrix, and a subsequent increase related to DNA denaturation and progressive exposure of the GNP. Both situations were captured in the reconstructed conductivity maps, highlighting ERT as an effective technique, and a real-time health monitoring method for materials and structures subject to degradation by UV-C radiation.

4.4 Experimental section

Materials: Graphene nanoplatelets grade AO-4 with average thickness 60 nm and lateral size in the range 3-7 μm were purchased from Graphene Supermarket (Graphene Laboratories, USA). Double-stranded DNA and poly(3,4-ethylenedioxythiophene)-poly(styrenesulfonate) (PEDOT:PSS) in the form of dry re-dispersible pellets were purchased from Sigma-Aldrich and used as received. DNA solutions and GNP/DNA dispersions were prepared in Milli-Q deionized water (resistivity 18.2 MΩ·cm) from a Direct-Q3 UV water purification system (Millipore, France). Carbon fiber-reinforced polymer (CFRP) laminated plates were fabricated by resin transfer molding (RTM) as support for the nanocomposite sensors. The resin used was HexFlow RTM6, a space-grade mono-component epoxy resin purchased from Hexcel (Duxford, UK). The fiber reinforcement was a 1K-T300 carbon plain weave with areal mass density of 120 g/m^2. Silver paint (Ted Pella, USA) and silver epoxy conductive adhesive (Type 8331, MG Chemicals, Canada) were used to fabricate the electrodes on the top surface of the nanocomposite sensor.

Fabrication methods: Nanocomposite coatings containing GNP/DNA nanomaterial dispersed in the PEDOT:PSS matrix were prepared by sonication in aqueous solution followed by deposition on the CFRP laminated plates and drying at 50 °C. First, aqueous dispersions of GNP and double-stranded DNA (20 mg/ml) were prepared in ultrapure water and sonicated for 2 h in a cold bath to prevent DNA degradation. For an optimal dispersion of graphene in the DNA solution, the two components were mixed at a 1:1 weight ratio, following previously established results [30, 45]. Next, PEDOT:PSS pellets

were added to the GNP/DNA solution, while stirring, at a concentration of 0.7% by weight. The dispersion (4 mL) was deposited on the CFRP supports (size 40 mm x 40 mm) and dried in oven at 50 °C overnight. Prior to the deposition, the carbon fiber/epoxy supports were coated by a thin layer of PEDOT:PSS (from an aqueous solution at 0.7% by weight) using the same drying conditions. The interposed PEDOT:PSS layer allowed for enhanced adhesion between the support and the GNP-DNA/PEDOT:PSS coating. Nanocomposite coatings with a uniform thickness of 0.03 mm and reference conductivities of 0.08 - 0.09 S/mm were obtained at these conditions.

UV-C irradiation tests*:* Nanocomposite coatings were irradiated with monochromatic UV light at 254 nm from a 30 W low-pressure mercury lamp. Samples were placed in a closed irradiation chamber with the UV source fixed in the top lid. Only the central part (20 mm × 20 mm) of the sample was exposed to UV-C radiation for 24 h, while the edges of the sample (where the electrodes would be fixed) were protected using aluminum foil. In prior work, an irradiation period of 17 h was sufficient to observe changes of the electrical conductivity of GNP/DNA films (applied to a different fiber-reinforced polymer substrate) [9]. Here, an irradiation time of 24 h was used for testing convenience. Samples were placed at two different distances from the lamp in order to vary the radiation intensity on the surface. For the ERT investigation, irradiances of 2.6 and 4.0 mW/cm^2 were used, corresponding to sample-to-source distances of 93 mm and 55 mm, and to radiation doses of 225 and 346 J/cm^2 in 24 h, respectively. The UV-C irradiance levels were selected to be consistent with those in the Low Earth Orbit (LEO) environment, in which the International Space Station and most communication satellites are located. Here, approximately 0.8% of the solar irradiance value is in the UV-C region, in particular 1.30 mW/cm^2 at the wavelength of 254 nm [46]. In this work, higher levels of irradiances between two and four times those of the LEO environment were used in order to achieve radiation doses in the range 200-400 J/cm^2 within 24 h of exposure and due to the configuration of the available testing chamber.

Additional irradiation tests as a function of the UV-C dose were performed under a 8 W low-pressure lamp set at 254 nm (3UV-38, UVP LLC, USA) in a closed chamber. The irradiances were measured using a HD 2302.0 radiometer (Delta Ohm, Italy) fitted with a LP 471 UVC probe (spectral range 200–280 nm). Samples were exposed to an

irradiance of 0.63 mW/cm^2 and measured daily for up to 7 days, corresponding to a maximum dose of 380 J/cm^2.

ERT system, acquisition and post-processing*:* Electrical resistance tomography (ERT) is a technique that allows to obtain a distribution of electrical resistance values within the domain of interest [47]. The electrical resistance distribution in that domain is obtained by injecting a current into electrodes that are positioned around the boundary of the domain of interest on the sample surface. Then, the resulting voltages between two electrodes are measured along this boundary, as the output, which will be used in the image processing algorithm. The algorithm will eventually compute the conductivity map of the domain, in a two parts sequence: the solution of a forward problem, and the solution of an inverse problem, as discussed below.

The experimental ERT setup for the acquisition of differential voltage data from up to 16 electrodes was composed by the data acquisition system (DAQ) from National Instruments (NI-6216), connected to a 16-electrodes voltage buffer circuit used with the aim of reducing current leak from the voltage sensing electrodes [31]. Direct currents were injected using an Agilent DC current supply (Agilent E3610A), while an op-amp power supply was used to reduce the noise in the measurements. A digital multimeter (Tektronix DMM916) ensured that there was accuracy in the injection current amplitude during the tests. Differential voltage data were acquired using the LabVIEW software package (National Instruments, Inc.) at various injection currents, with the baselines consisting of the untreated coatings, i.e. before exposure to UV-C. Samples for the ERT investigations were of size 40 mm × 40 mm; 16 electrodes were fixed along the edge of the nanocomposite sensor surface, leaving a central area of 20 mm × 20 mm free for irradiation (Figure 4.1a). Four equidistant electrodes were applied to each side and in orderly sequence. To ensure a strong sensor-electrode contact, the electrodes were created with a layer of silver paint onto which the ends of electrical wires were placed and then fixed using silver epoxy conductive adhesive (cure in air at ambient conditions for 24 h). The size of the electrodes was mainly dictated by the challenge of bonding electrodes on the nanocomposite film. In the current study, the electrodes were manufactured at a nominal distance of 1-2 mm among each other. The electrode size could be construed as large with respect to the domain of interest. However, Gisser et al. [48] and Hua et al.

[49] used large electrodes in their study, achieving a more uniform internal current distribution, and leading to improvements in image reconstructions.

From the measured differential voltage data, ERT conductivity maps, describing the changes in the surface electrical conductivity of the nanocomposite samples after irradiation, were reconstructed by finite element method (FEM) approach using the open-source Electrical Impedance and Diffuse Optical Reconstruction Software (EIDORS) suite [50, 51], based on the commercial software MATLAB (Mathworks). The reconstruction problem was addressed by discretizing the sample in a finite number of elements, defining the dimension of the model, the position, the dimensions and the geometry of the electrodes on the sample surface, and describing all current injection patterns used (forward problem). Next, the reconstruction of the conductivity distribution on the sample surfaces was performed (inverse problem) [51, 52]. The relationship between the conductivity distribution σ and a vector of measured voltages v for a specific current injection and initial conductivity estimate σ_0 is approximated by a vector of analytically predicted boundary voltages $F(\sigma)$ expressed by the Taylor series (Eq. 4.2):

$$v = F(\sigma) \tag{4.1}$$

$$F(\sigma) = F(\sigma_0) + \sum_{n=1}^{\infty} \frac{1}{n!} \frac{\partial^n F(\sigma)}{\partial \sigma^n}\Big|_{\sigma_0} (\sigma - \sigma_0)^n \tag{4.2}$$

Recovering σ from experimental measurements v is an ill-posed inverse problem, which depends on several factors including the exact shape of the region of interest and electrode positions, variations in contact impedance, and estimation of the internal conductivity. Solving the non-linear inverse problem requires regularization techniques. In this work, the Tikhonov regularization was implemented [52], with the electrical conductivity changes of the sensor coatings ($\Delta\sigma$) related to the measured difference voltage data ($\Delta V_{\text{resultant}}$) as:

$$\Delta\sigma = (J^T J + aL^T L)^{-1} J^T \Delta V_{\text{resultant}} \tag{4.3}$$

Here, J is the Jacobian matrix for complex impedance, and a is the regularization hyperparameter, which governs the amount of smoothing in the reconstruction process in

conjunction with a discrete Laplacian filter L. In order to prevent over-smoothing and for an objective selection of the hyperparameter [53], the fixed noise figure (NF) method proposed by Adler and Guardo [54] was implemented. In this method, the hyperparameter α is chosen so that to the signal-to-noise ratio (SNR) for the voltage measurements (SNR_v) equals that of the reconstructed conductivity distribution (SNR_σ), which corresponds to a NF value of 1.

$$NF(\alpha) = \frac{SNR_v}{SNR_\sigma} \tag{4.4}$$

Several authors have selected the fixed NF method when implementing the ERT analysis in structural health monitoring applications using composite materials [12, 14, 27, 55]. In the reconstructed conductivity maps, the conductivity changes ($\Delta\sigma$) were normalized with respect to the maximum variation of the electrical conductivity occurring at the surface ($\Delta\sigma_{max}$) according to the following formula:

$$\Delta\sigma normalized = \Delta\sigma/\Delta\sigma_{max} = (J^T J + \alpha L^T L)^{-1} J^T (\Delta V_{\text{resultant}}/\Delta V_{\text{resultant}_{max}}) \tag{4.5}$$

Characterization methods*:* The morphology of the nanocomposite coatings was investigated by scanning electron microscopy (SEM) using a Tescan VEGA II LSH instrument with accelerating voltage of 10 kV and magnifications from 1000 X to 3000 X. The electrical resistance was determined by electrical impedance spectroscopy (EIS) using a Gamry Reference 600 potentiostat in a custom-made cell with two copper strips as electrodes [10]. Resistance values were converted to conductivity values using the following equation [55]:

$$\sigma = \frac{1}{\rho} = \left(R\frac{A}{l}\right)^{-1} \tag{4.6}$$

where σ is the electrical conductivity, ρ is the resistivity, R is the measured electrical resistance, l is the distance between the copper electrodes, and A is the cross-sectional area of the sensor coating. Raman experiments were performed with a Horiba XploRA PLUS Raman microscope with 532 nm laser excitation. The Raman signal was collected through a 10 X objective in the range 200 - 3000 cm^{-1} with accumulation time of 5 s per spectrum. Areas of the substrates up to 7 µm × 7 µm were scanned with diffraction grating

of 600 g/mm. All spectra were obtained with a 10% filter to avoid sample heating and damaging.

4.5 References

[1] C. Soutis, Fibre reinforced composites in aircraft construction, Progress in Aerospace Sciences, 41 (2005) 143-151.

[2] P.K. Mallick, Fiber-reinforced composites: materials, manufacturing, and design, CRC press 2007.

[3] J.A. Dever, S.K. Miller, E.A. Sechkar, et al., Space environment exposure of polymer films on the materials international space station experiment: results from MISSE 1 and MISSE 2, High Perform. Polym., 20 (2008) 371-387.

[4] J. Dever, B. Banks, K. de Groh, et al., Degradation of spacecraft materials, Handbook of environmental degradation of materials, (2005) 465-501.

[5] D. Hastings, H. Garrett, Spacecraft-environment interactions, Cambridge University Press 2004.

[6] T.K. Minton, D.J. Garton, Dynamics of atomic-oxygen-induced polymer degradation in low earth orbit, in: R.A. Dressler (Ed.) Chemical dynamics in extreme environments, World Scientific Publishing, Singapore, 2001, pp. 420-489.

[7] M. Clausi, M.G. Santonicola, L. Schirone, et al., Analysis of ultraviolet exposure effects on the surface properties of epoxy/graphene nanocomposite films on Mylar substrate, Acta Astronaut., 134 (2017) 307-313.

[8] X.F. Yang, J. Li, S. Croll, et al., Degradation of low gloss polyurethane aircraft coatings under UV and prohesion alternating exposures, Polym. Degrad. Stab., 80 (2003) 51-58.

[9] M. Clausi, S. Laurenzi, V. La Saponara, et al., Multifunctional sensors for UV and mechanical damage detection of aerospace structures, Proceedings of the International Astronautical Congress, IAC, 2016.

[10] E. Toto, M.G. Santonicola, M.C. Mancini, et al., Ultraviolet-sensing surfaces based on hybrid nanocomposites for radiation monitoring systems, IEEE International Workshop on Metrology for AeroSpace (MetroAeroSpace), 2017, pp. 369-373.

[11] N. Munakata, K. Makita, D. Bolsée, et al., Spore dosimetry of solar UV radiation: applications to monitoring of daily irradiance and personal exposure, Adv. Space Res., 26 (2000) 1995-2003.

[12] B.R. Loyola, T.M. Briggs, L. Arronche, et al., Detection of spatially distributed damage in fiber-reinforced polymer composites, Struct. Health Monit., 12 (2013) 225-239.

[13] B.R. Loyola, V. La Saponara, K.J. Loh, et al., Spatial sensing using electrical impedance tomography, IEEE Sens. J., 13 (2013) 2357-2367.

[14] G.J. Gallo, E.T. Thostenson, Spatial damage detection in electrically anisotropic fiber-reinforced composites using carbon nanotube networks, Compos. Struct., 141 (2016) 14-23.

[15] L. Zhao, J. Yang, K. Wang, et al., An application of impediography to the high sensitivity and high resolution identification of structural damage, Smart Mater. Struct., 24 (2015) 065044.

[16] T.N. Tallman, K. Wang, Damage and strain identification in multifunctional materials via electrical impedance tomography with constrained sine wave solutions, Struct. Health Monit., 15 (2016) 235-244.

[17] M. Hallaji, M. Pour-Ghaz, A new sensing skin for qualitative damage detection in concrete elements: Rapid difference imaging with electrical resistance tomography, NDT & E International, 68 (2014) 13-21.

[18] K.J. Loh, T.-C. Hou, J.P. Lynch, et al., Carbon nanotube sensing skins for spatial strain and impact damage identification, J. Nondestruct. Eval., 28 (2009) 9-25.

[19] T.-C. Hou, K.J. Loh, J.P. Lynch, Spatial conductivity mapping of carbon nanotube composite thin films by electrical impedance tomography for sensing applications, Nanotechnology, 18 (2007) 315501.

[20] R. Schueler, S.P. Joshi, K. Schulte, Damage detection in CFRP by electrical conductivity mapping, Compos. Sci. Technol., 61 (2001) 921-930.

[21] A. Baltopoulos, N. Polydorides, L. Pambaguian, et al., Damage identification in carbon fiber reinforced polymer plates using electrical resistance tomography mapping, J. Compos. Mater., 47 (2013) 3285-3301.

[22] A. Baltopoulos, N. Polydorides, L. Pambaguian, et al., Exploiting carbon nanotube networks for damage assessment of fiber reinforced composites, Composites Part B, 76 (2015) 149-158.

[23] D. Pedrazzoli, A. Dorigato, A. Pegoretti, Monitoring the mechanical behavior under ramp and creep conditions of electrically conductive polymer composites, Composites Part A, 43 (2012) 1285-1292.

[24] L. Böger, M.H. Wichmann, L.O. Meyer, et al., Load and health monitoring in glass fibre reinforced composites with an electrically conductive nanocomposite epoxy matrix, Compos. Sci. Technol., 68 (2008) 1886-1894.

[25] M. Nofar, S. Hoa, M. Pugh, Failure detection and monitoring in polymer matrix composites subjected to static and dynamic loads using carbon nanotube networks, Compos. Sci. Technol., 69 (2009) 1599-1606.

[26] T. Tallman, S. Gungor, K. Wang, et al., Tactile imaging and distributed strain sensing in highly flexible carbon nanofiber/polyurethane nanocomposites, Carbon, 95 (2015) 485-493.

[27] W. Lestari, B. Pinto, V. La Saponara, et al., Sensing uniaxial tensile damage in fiber-reinforced polymer composites using electrical resistance tomography, Smart Mater. Struct., 25 (2016) 085016.

[28] M.G. Santonicola, M.G. Coscia, M. Sirilli, et al., Nanomaterial-based biosensors for a real-time detection of biological damage by UV light, Proceedings of the Annual International Conference of the IEEE Engineering in Medicine and Biology Society, IEEE EMBS, Milan, Italy, 2015, pp. 4391-4394.

[29] S. Botti, S. Laurenzi, L. Mezi, et al., Surface-enhanced Raman spectroscopy characterisation of functionalised multi-walled carbon nanotubes, Phys. Chem. Chem. Phys., 17 (2015) 21373-21380.

[30] S. Botti, A. Rufoloni, S. Laurenzi, et al., DNA self-assembly on graphene surface studied by SERS mapping, Carbon, 109 (2016) 363-372.

[31] T.K. Gildner, Damage and Stress Concentration Identification in CFRP Composite Structures with Electrical Resistance Tomography and Digital Image Correlation, MS Thesis, University of California, Davis, 2017.

[32] X. Shi, X. Dong, W. Shuai, et al., Pseudo-polar drive patterns for brain electrical impedance tomography, Physiol. Meas., 27 (2006) 1071-1080.

[33] V. Kolehmainen, M. Vauhkonen, P.A. Karjalainen, et al., Assessment of errors in static electrical impedance tomography with adjacent and trigonometric current patterns, Physiol. Meas., 18 (1997) 289-303.

[34] P. Kauppinen, J. Hyttinen, J. Malmivuo, Sensitivity Distribution Visualizations of Impedance Tomography Measurement Strategies, Int. J. Bioelectromagnetism, 8 (2006) 63-71.

[35] E. Toto, M. Palombi, S. Laurenzi, et al., Functional nanocomposites with graphene-DNA hybrid fillers: Synthesis and surface properties under UV irradiation, Ceram. Int., (in press https://doi.org/10.1016/j.ceramint.2018.10.236).

[36] E.J. Petersen, T. Lam, J.M. Gorham, et al., Methods to assess the impact of UV irradiation on the surface chemistry and structure of multiwall carbon nanotube epoxy nanocomposites, Carbon, 69 (2014) 194-205.

[37] T. Nagata, S. Oh, T. Chikyow, et al., Effect of UV–ozone treatment on electrical properties of PEDOT:PSS film, Organic Electronics, 12 (2011) 279-284.

[38] A. Elschner, The spectral sensitivity of PEDOT:PSS films, Sol. Energy Mater. Sol. Cells, 95 (2011) 1333-1338.

[39] S. Garreau, G. Louarn, J.P. Buisson, et al., In Situ Spectroelectrochemical Raman Studies of Poly(3,4-ethylenedioxythiophene) (PEDT), Macromolecules, 32 (1999) 6807-6812.

[40] A.C. Ferrari, J.C. Meyer, V. Scardaci, et al., Raman Spectrum of Graphene and Graphene Layers, Phys. Rev. Lett., 97 (2006) 187401.

[41] A. Reina, X. Jia, J. Ho, et al., Large Area, Few-Layer Graphene Films on Arbitrary Substrates by Chemical Vapor Deposition, Nano Lett., 9 (2009) 30-35.

[42] J.G. Duguid, V.A. Bloomfield, J.M. Benevides, et al., DNA melting investigated by differential scanning calorimetry and Raman spectroscopy, Biophys. J., 71 (1996) 3350-3360.

[43] S.A. Overman, K.L. Aubrey, K.E. Reilly, et al., Conformation and interactions of the packaged double-stranded DNA genome of bacteriophage T7, Biospectroscopy, 4 (1998) S47-S56.

[44] W. Ke, D. Yu, J. Wu, Raman spectroscopic study of the influence on herring sperm DNA of heat treatment and ultraviolet radiation, Spectrochim. Acta Part A, 55 (1999) 1081-1090.

[45] M.G. Santonicola, M.G. Coscia, S. Botti, et al., Graphene/DNA nanostructured films for bioinspired sensing of UV radiation effects, Proceedings of the International Astronautical Congress, IAC, 2014, pp. 6313-6317.

[46] C.A. Gueymard, The sun's total and spectral irradiance for solar energy applications and solar radiation models, Solar Energy, 76 (2004) 423-453.

[47] D. Holder, T. Tidswell, Electrical Impedance Tomography: Methods, History and Applications, Bristol: Institute of Physics Publishing, 2006.

[48] D.G. Gisser, D. Isaacson, J.C. Newell, Current topics in impedance imaging, Clin. Phys. Physiol. Meas., 8 (1987) 39-46.

[49] P. Hua, E.J. Woo, J.G. Webster, et al., Iterative reconstruction methods using regularization and optimal current patterns in electrical impedance tomography, IEEE Transactions on Medical Imaging, 10 (1991) 621-628.

[50] M. Vauhkonen, W.R.B. Lionheart, L.M. Heikkinen, et al., A MATLAB package for the EIDORS project to reconstruct two-dimensional EIT images, Physiol. Meas., 22 (2001) 107-111.

[51] A. Adler, W.R. Lionheart, Uses and abuses of EIDORS: an extensible software base for EIT, Physiol. Meas., 27 (2006) 25-42.

[52] W. Lionheart, N. Polydorides, A. Borsic, The reconstruction problem, in: D.S. Holder (Ed.) Electrical Impedance Tomography: Methods, History and Applications, Institute of Physics Publishing, Bristol, 2005, pp. 3-64.

[53] B.M. Graham, A. Adler, Objective selection of hyperparameter for EIT, Physiol. Meas., 27 (2006) S65-S79.

[54] A. Adler, R. Guardo, Electrical impedance tomography: regularized imaging and contrast detection, IEEE Transactions on Medical Imaging, 15 (1996) 170-179.

[55] H. Dai, G.J. Gallo, T. Schumacher, et al., A Novel Methodology for Spatial Damage Detection and Imaging Using a Distributed Carbon Nanotube-Based Composite Sensor Combined with Electrical Impedance Tomography, J. Nondestruct. Eval., 35 (2016) 1-15.

Chapter 5

Curing reactions of elastomeric nanocomposites filled with DNA-modified graphene investigated by differential scanning calorimetry*

Soft polymer nanocomposites with elastomeric matrix and graphene nanoplatelets (GNP) can be endowed with multifunctional, mechanical and electrical, properties to address a wide range of applications from stretchable sensors to conductive and flexible substrates for cell-instructive materials. In this Chapter, differential scanning calorimetry (DSC) investigations are reported, and their applications in the kinetics study of the curing reactions of silicone-based nanocomposites are described. Prepolymer matrices with different viscosities were prepared from standard polydimethylsiloxane (PDMS, Sylgard 184) and its blend with hydroxyl-terminated PDMS (PDMS-OH). These matrices were loaded with a DNA-modified GNP filler (1-5 wt%), obtaining elastomeric composites with different mechanical behavior. The analysis of the nanocomposites curing behavior was performed from dynamic calorimetric measurements. The activation energies of the curing process were estimated using the Kissinger method and two model-free isoconversional approaches, the Ozawa–Flynn–Wall (OFW) and the Kissinger–Akahira–Sunose (KAS) methods. Results indicate how the presence of the DNA-modified graphene nanofiller affects the curing process of the elastomeric PDMS and PDMS/PDMS-OH matrices.

---

*Parts of this Chapter have been submitted for publication to *Composites Part A* by Toto E.; Laurenzi S.; Santonicola M.G.

5.1 Introduction

Composite materials consisting of carbon-based fillers embedded in an elastomeric polymer matrix are increasingly considered for stretchable and flexible electrodes in applications such as sensors, transducers and actuators in different fields, from aerospace technology to biomedicine and biotechnology [1, 2]. In particular, the interest in silicone nanocomposites with graphene filler is steadily growing as they can be endowed with a wide array of multifunctional properties by integrating the exceptional mechanical strength and the good thermal and electrical conductivities of graphene nanoplatelets (GNP) [3, 4] with the flexibility of a nontoxic polymer matrix, such as polydimethylsiloxane (PDMS), which is widely used in biocompatible materials and wearable devices [5, 6].

In the design of graphene nanocomposites with tailored properties, the modification of the filler surface is often useful to enhance the integration of the filler with the polymer matrix or to add a novel functionality to the overall nanocomposite. For example, modification of GNP with DNA enables the creation of a UV-sensitive nanofiller, which can be used in radiation monitoring devices [7, 8]. Due to its sensitivity to UV light, DNA can be used as a biological target [9, 10] for the detection of the UV-induced damage, and at the same time acts as a solubilizing and exfoliating agent for the graphene nanoplatelets in aqueous solutions. The DNA-modified graphene nanofiller was successfully embedded in a silicone (Sylgard 184 PDMS) matrix, which shows a good transmittance in the UV band (above 240 nm), thus creating a UV-sensitive stretchable nanocomposite [11]. In order to prevent alteration of their electrical properties, GNPs can be functionalized by DNA molecules through non-covalent interactions, involving DNA functional moieties and oxidized groups on the GNP edges or base-graphene π stacking [12, 13]. By varying the content of the DNA-modified graphene filler it is possible to obtain nanocomposites with different degrees of flexibility and electrical conductivity. In the biomedical field, this would allow for the use of such nanocomposites as soft elastic substrates for cell proliferation [14] or in devices that exploit their electro-mechanical properties, such as pressure sensors for artificial skin [15, 16]. DNA-functionalized graphene nanostructures with different electrical properties can be developed by changing the type of non-covalent functionalization [17]. Botti et al. have also shown that the electrical behavior of

GNP/DNA assemblies is affected by the DNA molecule orientation (tilted or flattened) with respect to the graphene surface, as revealed by surface-enhanced Raman spectroscopy mapping [18].

The curing process of polymer matrices and how it is affected by the presence of fillers (modified or not) is a crucial aspect in the design and fabrication of nanocomposite materials. In general, the specific properties of polymer-based composites are strictly related to the kinetics of the involved curing reactions [19-22]. In this perspective, differential scanning calorimetry (DSC) represents one of the most effective techniques to investigate the curing conditions of nanocomposites in order to choose the most suitable process parameters for their fabrication [23-26]. The possibility to assess the filler effects on the curing behavior of polymer matrices allows to avoid using nanoparticles that can negatively affect the polymerization (in terms of high activation energies, long times or high temperatures required), and, in some cases, detecting possible advantages as an accelerating effect on the process [27, 28]. A DSC analysis enables to determine the parameters that describe the curing phenomenon, which is denoted by a typical exothermic peak, such as enthalpy value, peak temperature and the corresponding cure time. Starting from DSC data, the curing kinetics can be examined by estimating the activation energy values using different methodologies. In particular, in the case of filled polymer matrices and other complex polymer systems, many authors have relied on isoconversional methods [23, 29-33] to have an assessment of the variation of the activation energy with the extent of cure. These methods, such as the Ozawa–Flynn–Wall (OFW) and Kissinger–Akahira–Sunose (KAS) ones, are based on the assumption that the reaction rate is only a function of the temperature. On the other hand, the Kissinger method represents a more simplistic method for estimation of the activation energy [34]. Nevertheless, this method can be applied, as done by most of the authors, with the purpose to compare and eventually validate its outcome with respect to more complex approaches.

The aim of this study is to investigate the curing behavior of silicone/GNP-DNA nanocomposites and the role of the DNA-modified GNP filler on the curing kinetics. In particular, this study focuses on determining the activation energy profiles of nanocomposites with PDMS-based matrix using differential scanning calorimetry under non-isothermal conditions. Different nanocomposite samples are investigated varying the type of matrix, PDMS (Sylgard 184) or its mixture with hydroxyl-terminated PDMS

(PDMS-OH), and the amount of GNP-DNA filler. The use of a PDMS/PDMS-OH matrix (ratio 75:25 w/w) allowed enhancing the filler dispersion, by lowering the prepolymer viscosity, and also affects the elasticity of the cured nanocomposite [35]. The overall goal is to determine the curing kinetics of these types of nanocomposites, which adds valuable information for the materials processing and highlights possible limitations due to the presence of the filler.

5.2 Results and discussion

Dynamic differential scanning calorimetry was used to analyze the curing kinetics of nanocomposite mixtures made of silicone-based matrices containing GNP nanofiller modified with DNA. First, the unfilled polymer matrices, Sylgard 184 PDMS and its blend with hydroxyl-terminated PDMS, were investigated. Figure 5.1a and Figure 5.2a show the non-isothermal scans for the neat PDMS and PDMS/PDMS-OH systems, respectively, at the four heating rates considered in this study (5, 10, 15, 20 °C/min). The typical exothermic peaks of the PDMS curing reactions occur in the range from 90 to 110 °C, and are slightly shifted to higher temperature (1-2 °C at most) for the PDMS/PDMS-OH blend. After addition of the GNP-DNA nanofiller to the PDMS matrix (Figure 5.1b and c), the position and depth of the exothermic peak do not vary significantly with respect to the neat matrix (Figure 5.1a). A different situation is noted for the nanocomposites with PDMS/PDMS-OH matrix, as a large shift of the peak combined with a decrease of the area under the curve can be observed (Figure 5.2b and c), in particular after addition of 5 wt% of GNP-DNA. This result is a first indication of the different compatibility of the DNA-modified GNP nanofiller with the PDMS and PDMS/PDMS-OH matrices, and will be investigated in more details later in terms of activation energy of the curing process using different kinetic models. From the analysis of the exothermic peaks of the DSC thermograms, the onset, peak and end temperatures, and the heat of reaction (ΔH) were determined. These parameters for the unloaded matrices and for the nanocomposites with the GNP-DNA filler are summarized in Table 5.1 and Table 5.2.

In general, for the standard PDMS (Sylgard 184) the characteristic temperatures of the exotherms show a relatively small increase, at fixed heating rate, upon addition of the GNP-DNA filler. On the other hand, the curing parameters of the nanocomposites with the PDMS/PDMS-OH (75:25 w/w) matrix vary significantly with the amount of GNP-DNA filler. In fact, a shift of the exotherms to higher temperatures and a marked decrease of the heat of reaction values at higher concentrations of GNP-DNA are observed. In particular, at the heating rate of 10 °C/min, there is an increase of 5.8-9.0% of the exotherm characteristic temperatures and a decrease of 25% of the heat of reaction, when comparing the unloaded PDMS/PDMS-OH matrix and the one filled with 5 wt% of GNP-DNA. It is interesting to note that, at each heating rate, the unloaded matrices show similar curing behavior in terms of peak temperature and heat of reaction values. However, the onset temperature of the exotherms of the PDMS/PDMS-OH blend always occurs at higher temperatures than that of the PDMS matrix.

When comparing the curing behavior of the nanocomposites with GNP-DNA filler, the situation is quite different depending on the type of silicone matrix. For the nanocomposites with PDMS matrix, the characteristic temperatures and ΔH values of the exothermic peaks do not vary significantly upon addition of the GNP-DNA filler. Samples containing 5 wt% of GNP-DNA show a difference of less than 1% in the exothermic peak temperature with respect to the empty PDMS matrix, and a difference of 5-7% in the ΔH values (Table 5.1). On the other hand, for the nanocomposites with PDMS/PDMS-OH (75:25 w/w) matrix, the curing behavior is strongly affected by the presence of the GNP-DNA filler. In particular, there is an increase of 7-8% in the peak temperatures and a decrease of 26-49% in the ΔH values (depending on the heating rate) for the nanocomposites with 5 wt% of GNP-DNA with respect to the unloaded PDMS/PDMS-OH blend (Table 5.2). These values indicate that the filler is more compatible with the neat PDMS matrix, whereas it affects negatively the curing kinetics of the nanocomposites with PDMS/PDMS-OH matrix.

Analysis of the trends of the characteristic temperatures (T_{onset}, T_{peak}, and T_{end}) of the exothermic peaks only provides a qualitative assessment of the nanocomposites curing process, and is not sufficient to thoroughly understand the dynamics of the curing reactions. The variation of enthalpy (ΔH), calculated as the area underneath the exothermic peak, adds important information to the analysis allowing to evaluate the extent of conversion (α) of the reaction. In fact, the value of α can be calculated as the ratio of ΔH_i, corresponding to a fixed degree of conversion *i*, and the overall variation of enthalpy of the curing reaction [36, 37]:

$$\alpha_i = \frac{\Delta H_i}{\Delta H} \tag{5.1}$$

For each sample made of neat silicone matrix or nanocomposite, the extent of conversion was plotted as a function of temperature at each fixed scan rate, obtaining the sigmoidal curves showed in Figure 5.3. Here, the sigmoidal shape is typical of an autocatalytic reaction mechanism, and its invariance upon addition of the filler indicates that the kinetics of the curing process are not altered by the presence of the filler. This is more evident for the samples with PDMS matrix (Figure 5.3a, b, c), whereas for the nanocomposites with PDMS/PDMS-OH matrix a shift of the sigmoidal towards higher temperatures is observed when increasing the content of the GNP-DNA filler (Figure 5.3d, e, f), suggesting a delay in the curing reaction caused by the filler addition.

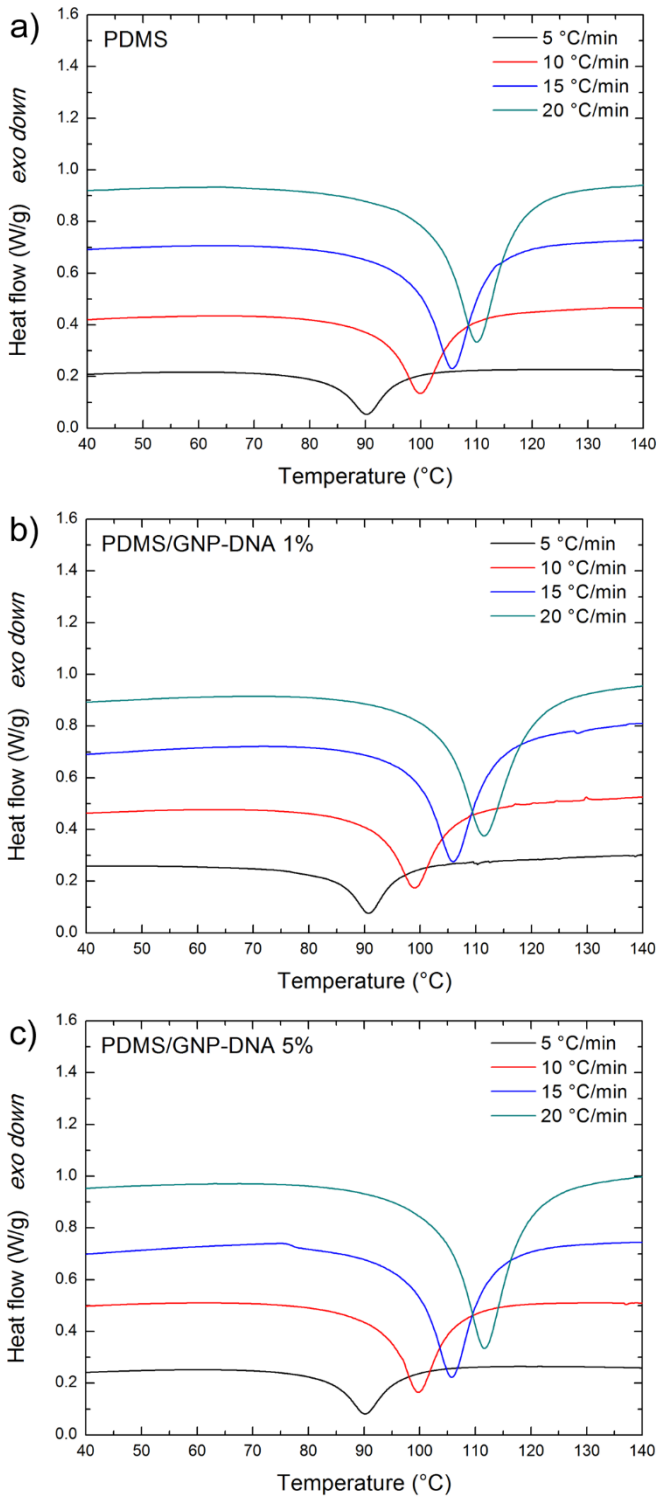

Figure 5.1. *DSC thermograms of (a) PDMS (Sylgard 184), (b) PDMS/GNP-DNA 1 wt% and (c) PDMS/GNP-DNA 5 wt% nanocomposite mixtures at different heating rates.*

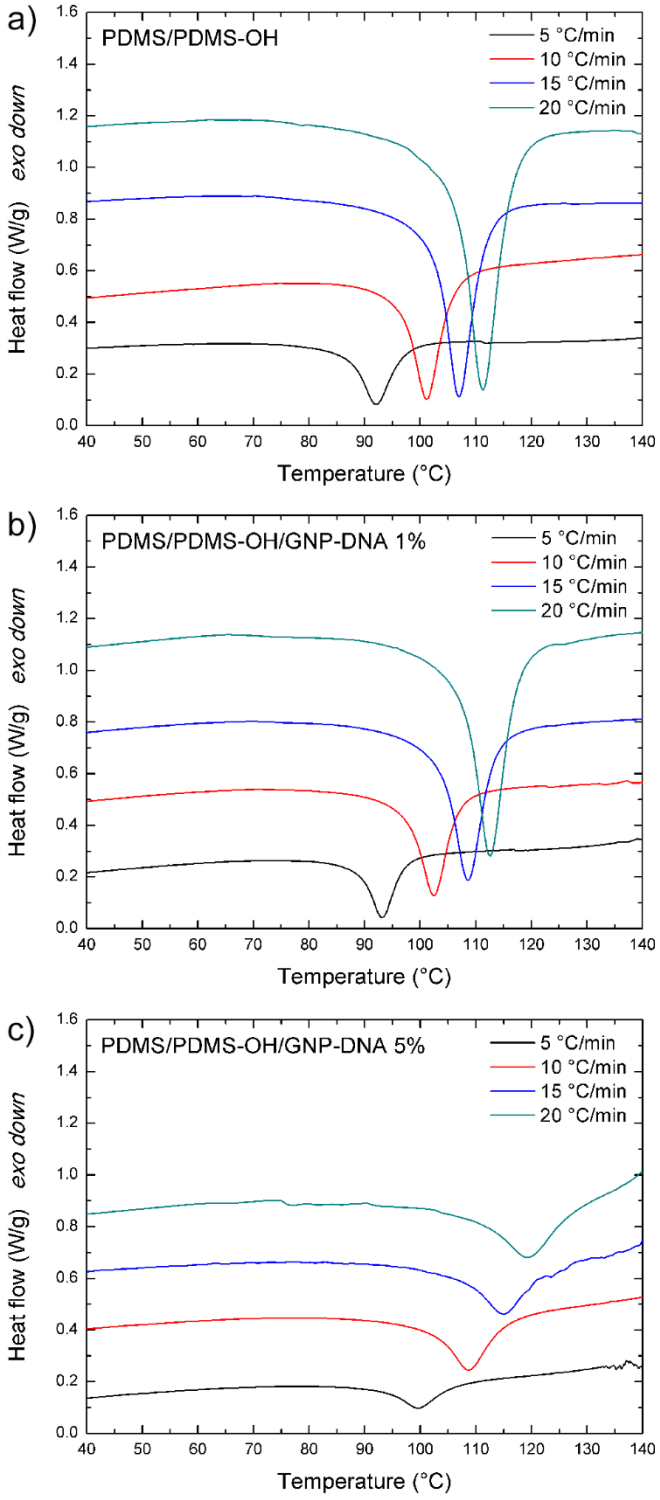

Figure 5.2. *DSC thermograms of (a) PDMS/PDMS-OH (75:25 w/w), (b) PDMS/PDMS-OH/GNP-DNA 1 wt% and (c) PDMS/PDMS-OH/GNP-DNA 5 wt% nanocomposite mixtures at different heating rates.*

Table 5.1. *Curing process parameters for PDMS (Sylgard 184) and PDMS/GNP-DNA nanocomposites from DSC dynamic scans at different heating rates.*

Sample	β (°C/min)	T_{onset}(°C)	T_{peak}(°C)	T_{end}(°C)	ΔH (J/g)
PDMS	5	83.3	90.2	96.4	22.0
	10	91.9	99.3	106.7	22.6
	15	98.0	105.7	112.6	24.1
	20	101.8	110.2	117.8	25.2
PDMS/ GNP-DNA 1 wt%	5	83.9	90.7	96.8	23.9
	10	92.0	99.0	106.0	21.6
	15	98.2	105.9	113.4	22.9
	20	103.0	111.5	120.7	24.3
PDMS/ GNP-DNA 5 wt%	5	83.5	90.2	96.6	23.7
	10	93.4	99.8	106.4	24.3
	15	98.2	105.7	112.7	24.5
	20	103.7	111.5	119.6	26.6

Table 5.2. *Curing process parameters for PDMS/PDMS-OH (75:25 w/w) blend and PDMS/PDMS-OH/GNP-DNA nanocomposites from DSC dynamic scans at different heating rates.*

Sample	β (°C/min)	T_{onset}(°C)	T_{peak}(°C)	T_{end}(°C)	ΔH (J/g)
PDMS/PDMS-OH	5	86.9	92.0	97.2	22.5
	10	96.1	101.1	105.9	23.6
	15	102.2	107.1	112.0	24.6
	20	106.1	111.3	116.8	24.5
PDMS/PDMS-OH/ GNP-DNA 1 wt%	5	89.2	93.2	97.1	20.6
	10	97.4	102.5	107	20.4
	15	103.4	108.6	113.5	20.7
	20	107.4	112.7	117.6	22.6
PDMS/PDMS-OH/ GNP-DNA 5 wt%	5	92.2	99.7	107.1	16.6
	10	101.7	108.7	115.5	17.7
	15	106.0	115.1	112.9	13.4
	20	109.0	119.3	128.3	12.4

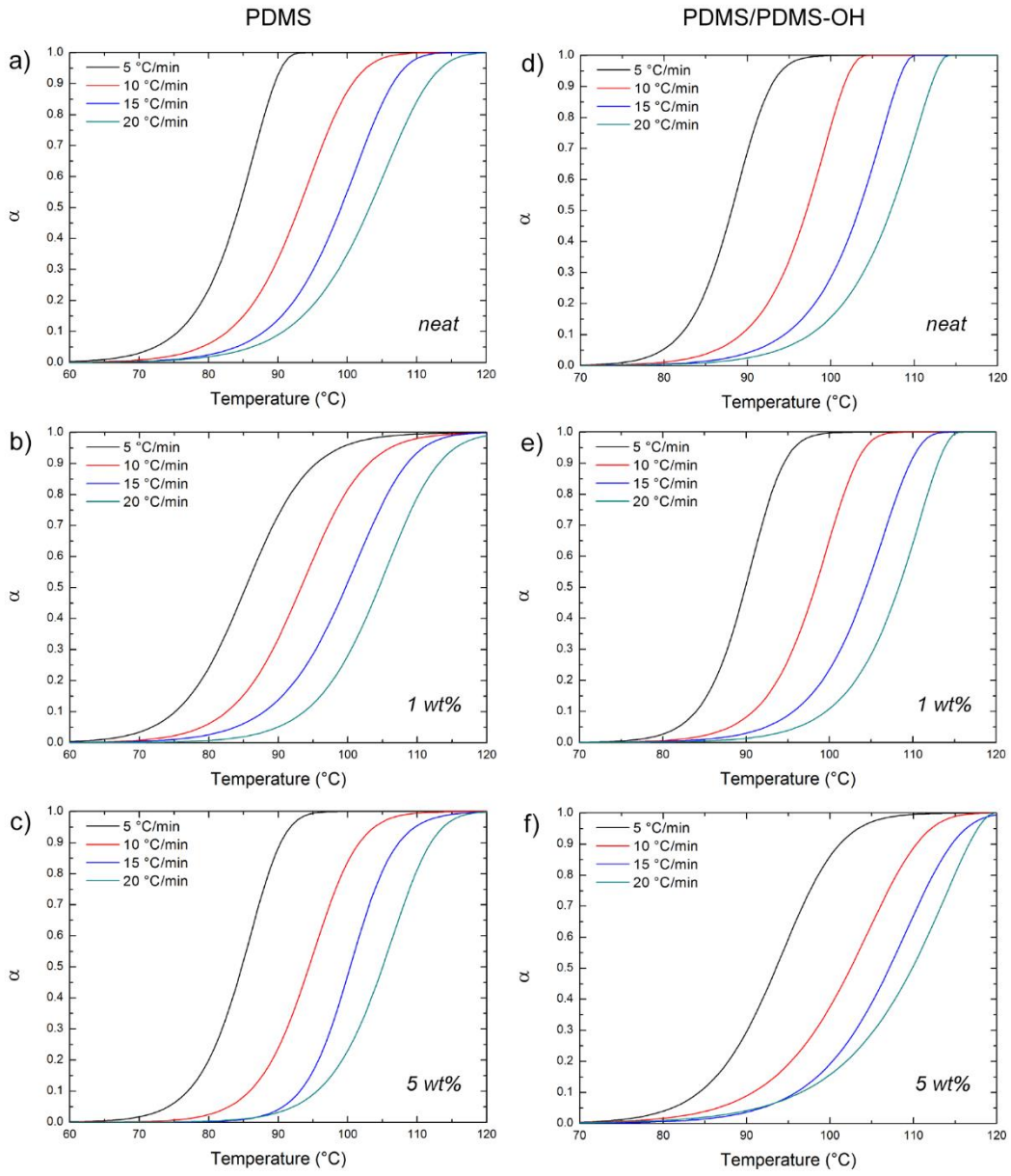

Figure 5.3. *Extent of conversion (α) as a function of temperature for nanocomposites with PDMS (Sylgard 184) and PDMS/PDMS-OH (75:25 w/w) matrix at different heating rates: (a, d) neat matrix; (b, e) matrix filled with 1 wt% GNP-DNA; (c, f) matrix filled with 5 wt% GNP-DNA.*

5.2.1 Modeling of the curing reactions of silicone-based nanocomposites filled with DNA-modified GNP

Starting from the data collected in the dynamic calorimetric experiments, different kinetic models were implemented with the aim to estimate and compare the activation energy values of the curing reactions. First, the Kissinger method was applied by plotting $\ln(\beta/T_p^2)$ versus $1/T_p$, using the values of peak temperature extracted from the thermograms at different heating rates (Table 5.1 and Table 5.2). For all cases of nanocomposite systems (with PDMS and PDMS/PDMS-OH matrix), the Kissinger equation gave a linear relationship with a high correlation factor (R-squared > 0.9884) and the curing activation energy (E) was determined confidently from the slope (Eq. (5.2)). Results from the linear regression are reported in Table 5.3. By comparing the curing activation energies of the PDMS and PDMS/PDMS-OH neat matrices, it is observed that the value of E is slightly higher for the mixed silicone system. This can be explained by the presence of the hydroxyl-terminated PDMS, which slows down the curing reaction of PDMS (Sylgard 184) occurring by cross-linking at the vinyl groups of the base component. Nevertheless, nanocomposites with PDMS/PDMS-OH matrix at the ratio of 75:25 w/w can be successfully cured also at low temperatures (50 °C for 24 h), whereas mixed matrices with higher content of hydroxyl-terminated PDMS (50:50 w/w) are only partially cured at the same conditions [35].

When considering the nanocomposite systems with GNP-DNA nanofiller at increasing concentrations, an opposite trend for the curing activation energy depending on the type of silicone matrix was observed. For the nanocomposites with PDMS (Sylgard 184) matrix, the presence of the filler contributes to lower the curing activation energy of the neat silicone, whereas when the matrix is made of the PDMS/PDMS-OH blend, the presence of the filler increases the activation energy. In particular, for nanocomposites with 5 wt% of GNP-DNA, the curing activation energy of the PDMS/PDMS-OH system is 13.2% higher than the nanocomposite with PDMS matrix. This result points to the different interaction of the filler with the PDMS-based matrices, suggesting that the GNP-DNA assembly is less compatible with the hydroxyl-terminated PDMS component of the mixed silicone matrix, than with the neat PDMS (Sylgard 184).

Table 5.3. *Activation energies for the curing process of PDMS (Sylgard 184) and PDMS/PDMS-OH (75:25 w/w) nanocomposite systems estimated by Kissinger method (R-squared values from linear regression in parentheses), and isoconversional methods Ozawa–Flynn–Wall (OFW) and Kissinger–Akahira–Sunose (KAS).*

Sample	E (kJ/mol)		
	Kissinger	**OFW**	**KAS**
PDMS	74.2 (0.9987)	78.6 ± 6.3	76.6 ± 6.7
PDMS/ GNP-DNA 1 wt%	71.2 (0.9884)	79.1 ± 4.0	77.1 ± 4.1
PDMS/ GNP-DNA 5 wt%	70.4 (0.9956)	72.6 ± 1.4	70.3 ± 1.5
PDMS/PDMS-OH	77.5 (0.9996)	81.4 ± 5.7	78.9 ± 4.6
PDMS/PDMS-OH/ GNP-DNA 1 wt%	77.0 (0.9997)	84.0 ± 3.9	82.2 ± 4.1
PDMS/PDMS-OH/ GNP-DNA 5 wt%	79.7 (0.9989)	96.8 ± 5.5	95.6 ± 5.8

After a first assessment of the activation energy by the Kissinger method, the curing process of the elastomeric nanocomposites was analyzed using the OFW and KAS isoconversional methods, following Eq. (5.3) and Eq. (5.4), respectively, and using the experimental data on the extent of conversion (α) as a function of temperature that are reported in Figure 5.3. Plots of ln(β) versus 1/T (Figure 5.4) and of $\ln(\beta/T^2)$ versus 1/T (Figure 5.5) were generated for the implementation of the OFW and KAS methods, respectively. Each data set was plotted at a fixed extent of conversion (α) ranging from 0.1 to 0.9, and the value of the activation energy (E_α) was estimated from the slop of the linear fit.

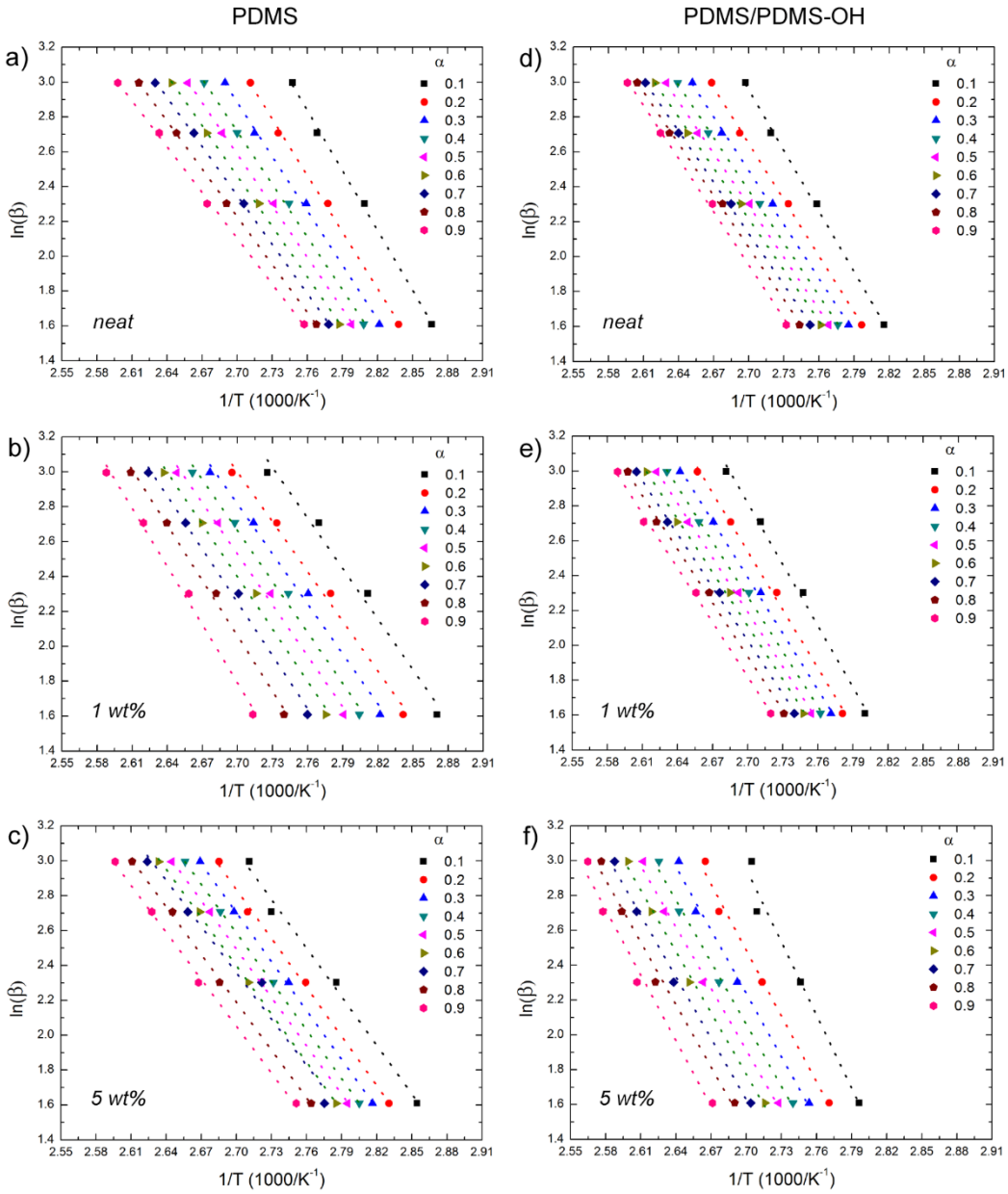

Figure 5.4. *Plots of ln(β) versus 1/T at different extents of conversion (α), according to Ozawa–Flynn–Wall model, for nanocomposites with PDMS and PDMS/PDMS-OH (75:25 w/w) matrix: (a, d) neat matrix; (b, e) matrix filled with 1 wt% GNP-DNA; (c, f) matrix filled with 5 wt% GNP-DNA.*

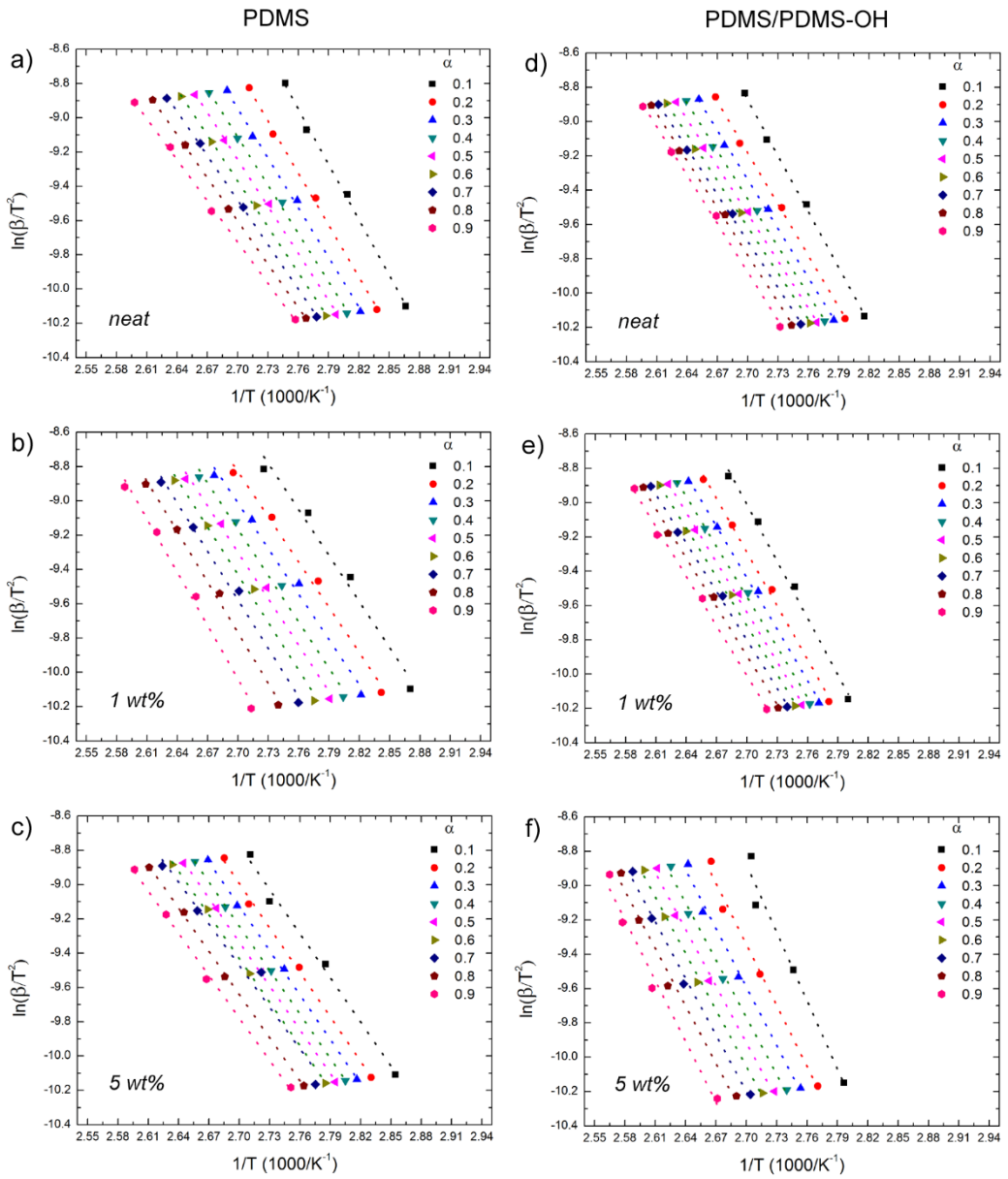

Figure 5.5. *Plots of ln(β/T²) versus 1/T at different extent of conversion (α), according to Kissinger–Akahira–Sunose model, for nanocomposites with PDMS and PDMS/PDMS-OH (75:25 w/w) matrix: (a, d) neat matrix; (b, e) matrix filled with 1 wt% GNP-DNA; (c, f) matrix filled with 5 wt% GNP-DNA.*

Results from the OFW and KAS analyses, in terms of activation energy of the curing process as a function of the extent of conversion α, are reported in Figure 5.6 and Figure 5.7, respectively.

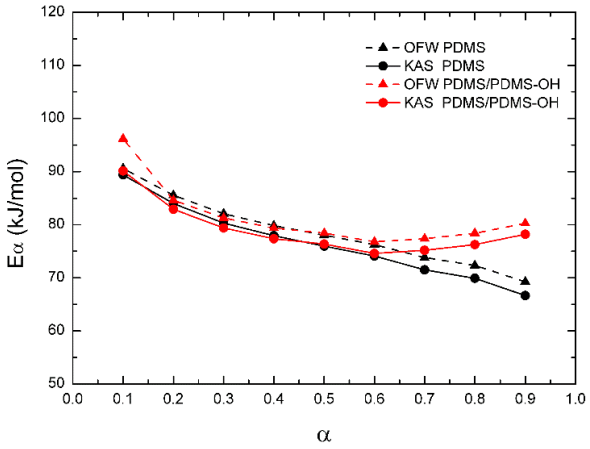

Figure 5.6. *Activation energy (E_α) for the curing process of unfilled PDMS matrix and PDMS/PDMS-OH (75:25 w/w) blend as a function of the extent of conversion estimated by Ozawa–Flynn–Wall (OFW) and Kissinger–Akahira–Sunose (KAS) methods.*

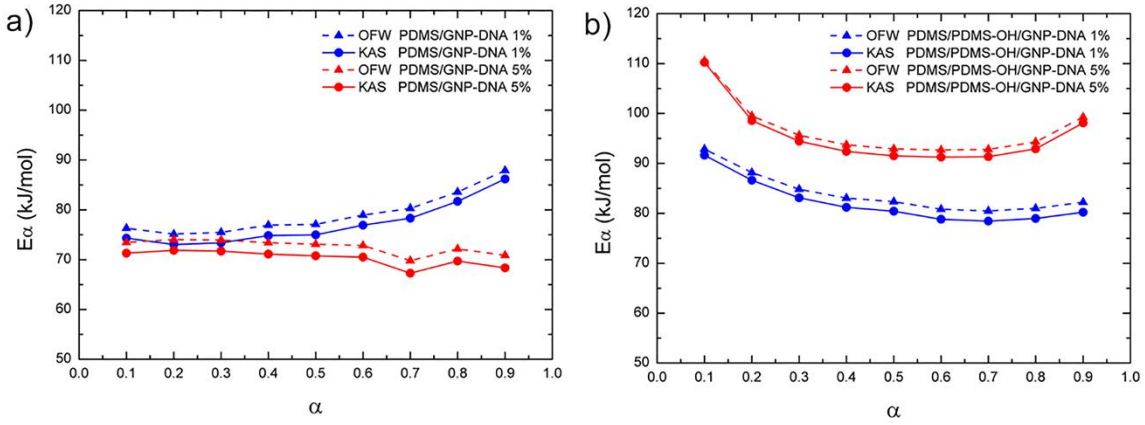

Figure 5.7. *Activation energies (E_α) as a function of the conversion degree estimated by Ozawa–Flynn–Wall (OFW) and Kissinger–Akahira–Sunose (KAS) methods for (a) PDMS-based nanocomposites filled with GNP-DNA (1 wt%, 5 wt%) and (b) PDMS/PDMS-OH based nanocomposites filled with GNP-DNA (1 wt%, 5 wt%).*

Since the difference between the maximum and minimum values of E_α across the range of the conversion degree does not exceed 20-30% of its average [38], from the OFW and KAS approach a mean value of E_α was calculated by averaging the values at each extent of conversion. Results are summarized in Table 5.3, where it can be noted that there is a small difference between the mean values of E_α obtained from the two methods. Such small difference has been reported by several authors [39-43], and is due to the different degree of accuracy of the two mathematical approaches. All methods are in good agreement as far as the curing behavior of the unfilled matrices is analyzed, and they all correctly indicate that the activation energy of the PDMS/PDMS-OH blend is higher than that of the neat PDMS matrix due to the presence of the silicone oil component. In general, the E_α values determined by the OFW and KAS methods are higher than those obtained by the Kissinger method, and most notably they show a larger variation for the nanocomposite samples with respect to the unfilled matrices. In fact, results by the Kissinger method do not show significant differences between the unfilled matrix and the nanocomposites, unlike what can be observed experimentally after the curing cycle, thus underestimating the effect of the nanofiller on the curing behavior of the PDMS-based matrices. In addition, the OFW and KAS approaches both confirm the opposite trend that the GNP-DNA nanofiller has on the curing kinetics of the two different matrices. In the case of the PDMS matrix, the presence of the nanofiller causes a decrease of the activation energies, reaching 8% decrease upon addition of 5 wt% of GNP-DNA (Table 5.3). This can be explained by the high thermal conductivity of the graphene nanoplatelets [44-47], which enhances the cure kinetics of the PDMS when a sufficient amount of GNP is added. On the other hand, for the PDMS/PDMS-OH blend, a progressive and significant increase of the E_α values is observed upon addition of the GNP-DNA filler, with an increase of about 20% at 5 wt% of filler (Table 3). This result is in agreement with the experimental values of enthalpies determined by the DSC thermograms and reported in Table 5.2, indicating a lower degree of curing for the PDMS/PDMS-OH blend upon addition of the nanofiller, and is due to the incompatibility of the hydrophobic GNP with the hydroxyl-terminated component (PDMS-OH) of the matrix.

Overall, the results above indicate that the Kissinger method underestimates the presence of the filler in the elastomeric matrices, whereas the OFW and KAS isoconversional methods are more suitable for the analysis of the curing kinetics of these nanocomposite samples.

5.2.2 Mechanical properties and surface wettability of silicone-based GNP-DNA nanocomposites

Following the calorimetric analysis of the cure behavior, the mechanical properties of the elastomeric nanocomposites prepared using the two silicone matrices (neat Sylgard 184 PDMS and PDMS/PDMS-OH 75:25 w/w blend) were determined after curing the samples for 24 h at 50 °C. These parameters were selected based on the thermal sensitivity of DNA, which undergoes degradation if exposed to temperatures higher than 90 °C for long times, and they still ensure a complete cure of the nanocomposite mixtures as determined by post-cure calorimetric measurements. In addition, it is known that PDMS substrates with different mechanical properties can be prepared by varying the cure temperature in the range from ambient temperature to 200 °C [48]. The mean values of the hardness and reduced elastic modulus obtained by nanoindentation method for all the investigated samples are shown in Table 5.4. Results clearly indicate that the elastic behavior and the hardness of the two nanocomposite systems, with neat PDMS and PDMS/PDMS-OH matrices, are quite different. The mixed PDMS/PDMS-OH matrix results in nanocomposites that are much softer and with reduced elastic modulus which varies significantly as a function of the nanofiller concentration. On the opposite, the nanocomposite samples with PDMS matrix show quite similar elastic modulus, up to 5 wt% of GNP-DNA. In both cases, the material hardness tends to increase upon addition of the modified graphene nanofiller.

Table 5.4. *Hardnesses and reduced elastic moduli of nanocomposites with GNP-DNA nanofiller and silicone-based matrices, PDMS (Sylgard 184) and PDMS/PDMS-OH blend (75:25 w/w), from nanoindentation tests (applied load of 0.5 mN). Curing process at 50 °C for 24 h. Standard deviations of the measurements are in the range 5-8%.*

Sample	Hardness (MPa)	Reduced elastic modulus (MPa)
PDMS	5.94	17.10
PDMS/GNP-DNA 1 wt%	6.21	18.11
PDMS/GNP-DNA 5 wt%	7.27	15.26
PDMS/PDMS-OH	1.10	3.13
PDMS/PDMS-OH/GNP-DNA 1 wt%	1.29	3.86
PDMS/PDMS-OH/GNP-DNA 5 wt%	2.40	10.62

Finally, the surface wettability of the elastomeric nanocomposites containing the GNP-DNA filler was assessed by contact angle measurements at room temperature using ultrapure water. Figure 5.8 shows optical images of water droplets on the nanocomposite samples and polymer matrix consisting of pure PDMS or the mixture PDMS/PDMS-OH (75:25 w/w). Addition of the less viscous PDMS-OH component to the silicone matrix significantly lowers its hydrophobicity due to the presence of the hydroxyl functional groups, with mean values of the water contact angle (WCA) decreasing from 113.8 ± 1.6 for the standard PDMS substrate to 89.6 ± 0.9 for the softer PDMS/PDMS-OH sample. No statistically relevant variation can be detected in the nanocomposites, up to 5 wt% of the DNA-modified graphene filler, with respect to the unfilled matrices (Table 5.5).

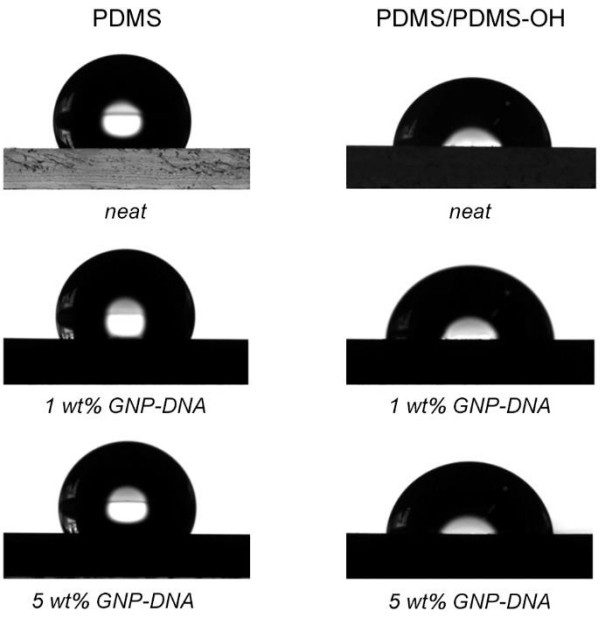

Figure 5.8. *Comparison of surface hydrophobicity of standard PDMS Sylgard 184 (left) and PDMS/PDMS-OH blend (75:25 w/w) (right), neat and after addition of 1 wt% and 5 wt% of GNP-DNA, as determined by sessile drop method.*

Table 5.5. *Mean values of the water contact angle (WCA) determined by sessile drop method for nanocomposites with PDMS and PDMS/PDMS-OH blend (75:25 w/w) and GNP-DNA filler.*

Sample	**Water contact angle (degree)**
PDMS	113.8 ± 1.6
PDMS/GNP-DNA 1 wt%	111.1 ± 1.9
PDMS/GNP-DNA 5 wt%	114.2 ± 1.5
PDMS/PDMS-OH	89.6 ± 1.2
PDMS/PDMS-OH/GNP-DNA 1 wt%	89.7 ± 1.0
PDMS/PDMS-OH/GNP-DNA 5 wt%	90.0 ± 1.5

5.3 Conclusions

Soft polymer nanocomposites with silicone matrices filled with DNA-functionalized graphene were investigated by DSC in order to determine their curing reaction kinetics. Dynamic calorimetric measurements were performed on the prepolymer mixtures prepared using two types of matrix, standard PDMS (Sylgard 184) and a PDMS/PDMS-OH blend (75:25 w/w), and loaded with different amounts of GNP-DNA filler. The different curing behavior and the effect of the filler on the silicone matrices were analyzed using the Kissinger method and two isoconversional models (OFW and KAS), showing that the first method underestimates the presence of the filler in the elastomeric matrices, whereas the OFW and KAS models are able to follow the complex trend of the curing behavior of the nanocomposites as a function of the filler content. In particular, the nanocomposites with standard PDMS are characterized by lower activation energies for the polymerization than those with the PDMS/PDMS-OH blend, as the hydroxylated component acts to hinder the crosslinking process. Further, the PDMS curing reaction appears to be favored by the presence of the GNP-DNA filler, at sufficiently high content (5 wt%), whereas the PDMS/PDMS-OH matrix is negatively affected by the modified graphene filler. Analysis of the mechanical properties by nanoindentation revealed that the nanocomposites with the PDMS/PDMS-OH matrix generate much softer materials after cure than those with standard PDMS, and their hardness and reduced elastic modulus can be tuned by varying the amount of the filler. The flexibility of the cured materials and the reduced viscosity of the prepolymer mixtures, which is often useful in the filler dispersion process, represent advantages of the nanocomposites with PDMS/PDMS-OH matrix with respect to those with standard PDMS, and may be used to extend the functional properties of elastomeric PDMS-based materials.

5.4 Experimental section

Materials: Graphene nanoplatelets were purchased from XG Sciences (Lansing, MI, USA) and they were of grade C750, consisting of aggregates of platelets with diameter of less than 2 μm, thickness of a few nm, and average surface area of 750 m^2/g according to the manufacturer datasheet. Two-component polydimethylsiloxane (PDMS, Sylgard

184) was obtained from Dow Corning (Midland, MI, USA). Double-stranded DNA and hydroxyl-terminated polydimethylsiloxane (PDMS-OH, average Mn ~550) were purchased from Sigma-Aldrich (Milan, Italy). Sterile deionized water (resistivity 18.2 MΩ·cm) was produced by a Direct-Q3 UV water purification system (Millipore, Molsheim, France) and used to prepare DNA solutions and DNA/graphene dispersions.

Preparation of nanocomposite mixtures: Nanocomposite mixtures were obtained by adding the DNA-modified graphene filler to the silicone prepolymer made of neat PDMS or PDMS/PDMS-OH (75:25 w/w) blend. The GNP-DNA filler was previously prepared by dispersing the GNP powder (grade C750) in an aqueous solution of DNA (2.5 mg/mL) and sonicating for 1 h in ultrasonic bath (Elmasonic P30H, Elma, Singen, Germany) with cold water. Graphene and DNA were mixed in a ratio of 1:1 (w/w) assuring a good degree of dispersion of the nanoplatelets in the DNA solution, as demonstrated in previous work [35]. The dispersion was completely evaporated by slow stirring at 50 °C and the desired amount of dried GNP-DNA weighed and added to the PDMS base or PDMS/PDMS-OH blend. The mixture was sonicated for 1-2 h and then the curing agent was added in a ratio of base to curing agent of 10:1 (w/w) and gently mixed mechanically. Different nanocomposite samples were realized varying the amount of GNP-DNA filler (1 wt% and 5 wt%) for each of the two types of silicone matrix. The PDMS/PDMS-OH matrix was prepared by mixing the two components in the ratio of 75:25 (w/w), resulting in a less viscous matrix than neat PDMS due to the lower molecular weight of hydroxyl-terminated PDMS (M_n ~550). The ratio 75:25 was selected as optimal ratio following previous work on the dispersion of graphene nanofillers in silicone-based matrices, where it was demonstrated that mixed PDMS matrices with higher amounts of hydroxyl-terminated PDMS could not be successfully cured at the conditions used in this study [35].

Dynamic DSC experiments: The curing process of the nanocomposites was investigated by differential scanning calorimetry under non-isothermal conditions at heating rates of 5, 10, 15 and 20 °C/min. A Pyris 1 DSC instrument (Perkin-Elmer, Waltham, MA, USA) calibrated with high purity indium and tin materials was used. DSC samples were prepared starting from each mixture immediately after the addition of the curing agent. Samples (~20 mg) were sealed in aluminum pans with lids and measured in the

temperature range from 30 °C to 150 °C under a constant flow of nitrogen (20 mL/min). An identical empty cell was taken as reference. A baseline was measured at the same experimental conditions using an empty cell and subtracted from the sample data. The exothermic peaks were analyzed using the thermal analysis software provided with the instrument. The heat flow data were processed to obtain the extent of conversion (α) as a function of temperature using the Perkin-Elmer Kinetics Software package.

Kinetic models for DSC analysis: Data collected in non-isothermal calorimetric experiments were implemented into different dynamic kinetic models, with the aim to estimate and compare the activation energy values related to the curing reactions. The first approach consisted in the application of the Kissinger method [34], which is based on the following equation:

$$\ln\left(\frac{\beta}{T_P^2}\right) = \ln\left(\frac{AR}{E}\right) - \frac{E}{RT_P} \tag{5.2}$$

where β is the linear heating rate, T_p is the peak temperature, A and E are the pre-exponential factor and activation energy, respectively, and R is the universal gas constant. By plotting $\ln(\beta/Tp^2)$ versus $1/T_p$ it is possible to estimate the values of A and E. This method assumes that the maximum reaction rate occurs at peak temperature, corresponding to the exothermal peak position in the dynamic scan, and it exploits the correlation between this temperature value and the heating rate. One of the main limitations of the Kissinger method is the assignment of a single activation energy value to the entire process, which means the assumption of a simple kinetic of reaction based on a single step. In general, the Kissinger method fails when multiple reaction mechanisms are present or when the activation energy depends on the extent of conversion (α). For these cases, isoconversional methods have been developed [49, 50], which require to determine the temperature (T_α) associated with a certain extent of conversion for a fixed heating rate. These methods are based on the subdivision of the entire kinetic process into multiple single-steps, where each step is characterized by a single value of the extent of conversion in a restricted range of temperature. Small variations of the activation energy values with the extent of conversion can legitimate the application of these methods, but without excluding other effects that can influence their use, as recommended by the Kinetics Committee of the International Confederation for

Thermal Analysis and Calorimetry (ICTAC) [38]. The Ozawa–Flynn–Wall (OFW) method [51, 52] is based on the equation:

$$\ln(\beta_i) = \text{const} - 1.052\left(\frac{E_\alpha}{RT_\alpha}\right) \tag{5.3}$$

whereas the Kissinger–Akahira–Sunose (KAS) method [53] relies on the equation:

$$\ln\left(\frac{\beta_i}{T_{\alpha,i}^2}\right) = \text{const} - \left(\frac{E_\alpha}{RT_\alpha}\right) \tag{5.4}$$

Here, the subscript α indicates isoconversional values, i.e. the values related to a given extent of conversion, and the index *i* identifies an individual heating rate (for non-isothermal programs). After studying the relation between the temperature values of the dynamic scan and the related extents of conversion, at each heating rate, the OFW and KAS methods were applied plotting $\ln(\beta_i)$ versus $1/T_\alpha$ and $\ln(\beta_i/T_\alpha^2)$ versus $1/T_\alpha$, respectively. By comparing the results from the Kissinger and isoconversional approaches it is possible to evaluate the consistency of the estimated activation energies. Since they are based on the same assumptions, results from the two isoconversional methods (OFW and KAS) only differ in the degree of accuracy. In fact, the OFW and KAS equations were derived by the same linear equation, in the following general form [38]:

$$\ln\left(\frac{\beta_i}{T_{\alpha,i}^B}\right) = \text{const} - C\left(\frac{E_\alpha}{RT_\alpha}\right) \tag{5.5}$$

The parameters B and C were approximated to 0 and 1, respectively, by Doyle [54] obtaining the OFW equation (Eq. (5.3)). Murray and White gave a more accurate approximation by setting B = 2 and C = 1 [38], which leads to the KAS equation (Eq. (5.4)).

Characterization of nanocomposites after cure: Nanocomposite samples were prepared by casting method in circular molds (diameter 35 mm, thickness 5 mm), and they were cured in oven at 50 °C for 24 h. Nanoindentation tests were performed using a NanoTest Platform instrument (Micro Materials Ltd., Wrexham, UK) with several indentations (6 for each point) in random positions on each specimen. Experiments were performed with a spherical tip, under different applied loads (0.5 mN and 1 mN) with a

loading rate of 0.5 mN/s and holding the maximum load for 20 s. Hardness and reduced elastic modulus were calculated from the load-displacement curves [55]. Contact angles were measured by the sessile drop method using a DataPhysics OCA15Pro analyzer (DataPhysics Instruments, Filderstadt, Germany) with degassed ultrapure water as testing liquid. A minimum of ten drops (volume 3 μl) on different areas of the substrate were analyzed for each nanocomposite sample. The determination of the water contact angle (WCA) values was performed according to the Young-Laplace fitting method using the DataPhysics SCA20 image analysis software.

5.5 References

[1] S. Michel, B.T. Chu, S. Grimm, et al., Self-healing electrodes for dielectric elastomer actuators, J. Mater. Chem., 22 (2012) 20736-20741.

[2] Y.-Q. Li, W.-B. Zhu, X.-G. Yu, et al., Multifunctional Wearable Device Based on Flexible and Conductive Carbon Sponge/Polydimethylsiloxane Composite, ACS Appl. Mater. Interfaces, 8 (2016) 33189-33196.

[3] Y. Zhu, S. Murali, W. Cai, et al., Graphene and graphene oxide: synthesis, properties, and applications, Adv. Mater., 22 (2010) 3906-3924.

[4] H. Kim, A.A. Abdala, C.W. Macosko, Graphene/Polymer Nanocomposites, Macromolecules, 43 (2010) 6515-6530.

[5] C. Yan, W. Kang, J. Wang, et al., Stretchable and Wearable Electrochromic Devices, ACS Nano, 8 (2014) 316-322.

[6] S. Gong, W. Schwalb, Y. Wang, et al., A wearable and highly sensitive pressure sensor with ultrathin gold nanowires, Nat. Commun., 5 (2014) 3132.

[7] M.G. Santonicola, M.G. Coscia, M. Sirilli, et al., Nanomaterial-based biosensors for a real-time detection of biological damage by UV light, Proceedings of 37th Annual International Conference of the IEEE Engineering in Medicine and Biology Society (EMBC), IEEE, 2015, pp. 4391-4394.

[8] E. Toto, M.G. Santonicola, M.C. Mancini, et al., Ultraviolet-sensing surfaces based on hybrid nanocomposites for radiation monitoring systems, Proceedings of IEEE International Workshop on Metrology for AeroSpace (MetroAeroSpace), IEEE, 2017, pp. 369-373.

[9] J.-L. Ravanat, T. Douki, J. Cadet, Direct and indirect effects of UV radiation on DNA and its components, J. Photochem. Photobiol., B, 63 (2001) 88-102.

[10] T. Matsunaga, K. Hieda, O. Nikaido, Wavelength dependent formation of thymine dimers and (6-4) photoproducts in DNA by monochromatic ultraviolet light ranging from 150 to 365 nm, Photochem. Photobiol., 54 (1991) 403-410.

[11] E. Toto, M. Palombi, S. Laurenzi, et al., Functional nanocomposites with graphene-DNA hybrid fillers: Synthesis and surface properties under UV irradiation, Ceram. Int., 45 (2019) 9631-9637.

[12] T.C. Hain, K. Kroeker, D.G. Stich, et al., Influence of DNA conformation on the dispersion of SWNTs: single-strand DNA vs. hairpin DNA, Soft Matter, 8 (2012) 2820-2823.

[13] A.J. Patil, J.L. Vickery, T.B. Scott, et al., Aqueous stabilization and self-assembly of graphene sheets into layered bio-nanocomposites using DNA, Adv. Mater., 21 (2009) 3159-3164.

[14] J. Solon, I. Levental, K. Sengupta, et al., Fibroblast adaptation and stiffness matching to soft elastic substrates, Biophys. J., 93 (2007) 4453-4461.

[15] M. Amjadi, K.-U. Kyung, I. Park, et al., Stretchable, Skin-Mountable, and Wearable Strain Sensors and Their Potential Applications: A Review, Adv. Funct. Mater., 26 (2016) 1678-1698.

[16] Y. Shu, H. Tian, Y. Yang, et al., Surface-modified piezoresistive nanocomposite flexible pressure sensors with high sensitivity and wide linearity, Nanoscale, 7 (2015) 8636-8644.

[17] M.G. Santonicola, Chapter 8 - Label-Free Biosensing Platforms Based on Graphene/DNA Interfaces, in: A. Tiwari (Ed.) Graphene Bioelectronics, Elsevier 2018, pp. 177-191.

[18] S. Botti, A. Rufoloni, S. Laurenzi, et al., DNA self-assembly on graphene surface studied by SERS mapping, Carbon, 109 (2016) 363-372.

[19] S.R. White, H. Hahn, Process modeling of composite materials: residual stress development during cure. Part II. Experimental validation, J. Compos. Mater., 26 (1992) 2423-2453.

[20] P. Mohan, A critical review: the modification, properties, and applications of epoxy resins, Polym.-Plast. Technol. Eng., 52 (2013) 107-125.

[21] R. Jain, P. Kukreja, A. Narula, et al., Studies of the curing kinetics and thermal stability of epoxy resins using a mixture of amines and anhydrides, J. Appl. Polym. Sci., 100 (2006) 3919-3925.

[22] O. Becker, Y.-B. Cheng, R.J. Varley, et al., Layered silicate nanocomposites based on various high-functionality epoxy resins: the influence of cure temperature on morphology, mechanical properties, and free volume, Macromolecules, 36 (2003) 1616-1625.

[23] P.-Y. Kuo, N. Yan, M. Sain, Influence of cellulose nanofibers on the curing behavior of epoxy/amine systems, Eur. Polym. J., 49 (2013) 3778-3787.

[24] M. Abdalla, D. Dean, P. Robinson, et al., Cure behavior of epoxy/MWCNT nanocomposites: The effect of nanotube surface modification, Polymer, 49 (2008) 3310-3317.

[25] S.S. Park, N. Bernet, S. de la Roche, et al., Processing of Iron Oxide-epoxy Vinyl Ester Nanocomposites, J. Compos. Mater., 37 (2003) 465-476.

[26] M. Ivankovic, I. Brnardic, H. Ivankovic, et al., DSC study of the cure kinetics during nanocomposite formation: Epoxy/poly(oxypropylene) diamine/organically modified montmorillonite system, J. Appl. Polym. Sci., 99 (2006) 550-557.

[27] T. Zhou, X. Wang, X. Liu, et al., Influence of multi-walled carbon nanotubes on the cure behavior of epoxy-imidazole system, Carbon, 47 (2009) 1112-1118.

[28] J.H. Yu, J.K. Duan, W.Y. Peng, et al., Influence of nano-AlN particles on thermal conductivity, thermal stability and cure behavior of cycloaliphatic epoxy/trimethacrylate system, Express Polym. Lett, 5 (2011) 132-141.

[29] J. Pérez, M. Oliet, M. Alonso, et al., Cure kinetics of lignin–novolac resins studied by isoconversional methods, Thermochim. Acta, 487 (2009) 39-42.

[30] M. Ghaemy, H. Behmadi, Study of cure kinetics of DGEBA with optically active curing agents, J. Therm. Anal. Calorim., 101 (2010) 1011-1017.

[31] J. Domínguez, J.-C. Grivel, B. Madsen, Study on the non-isothermal curing kinetics of a polyfurfuryl alcohol bioresin by DSC using different amounts of catalyst, Thermochim. Acta, 529 (2012) 29-35.

[32] S.K. Sahoo, S. Mohanty, S.K. Nayak, A study on effect of organo modified clay on curing behavior and thermo-physical properties of epoxy methyl ester based epoxy nanocomposite, Thermochim. Acta, 614 (2015) 163-170.

[33] C. Andronescu, S.A. Gârea, C. Deleanu, et al., Characterization and curing kinetics of new benzoxazine monomer based on aromatic diamines, Thermochim. Acta, 530 (2012) 42-51.

[34] H.E. Kissinger, Reaction kinetics in differential thermal analysis, Anal. Chem., 29 (1957) 1702-1706.

[35] M.G. Santonicola, M.G. Coscia, S. Botti, et al., Graphene/DNA nanostructured films for bioinspired sensing of UV radiation effects, Proceedings of the International Astronautical Congress, IAC, International Astronautical Federation, IAF, 2014, pp. 6313-6317.

[36] K. Yang, M. Gu, Y. Jin, Cure behavior and thermal stability analysis of multiwalled carbon nanotube/epoxy resin nanocomposites, J. Appl. Polym. Sci., 110 (2008) 2980-2988.

[37] S.H. Ryu, J. Sin, A. Shanmugharaj, Study on the effect of hexamethylene diamine functionalized graphene oxide on the curing kinetics of epoxy nanocomposites, Eur. Polym. J., 52 (2014) 88-97.

[38] S. Vyazovkin, A.K. Burnham, J.M. Criado, et al., ICTAC Kinetics Committee recommendations for performing kinetic computations on thermal analysis data, Thermochim. Acta, 520 (2011) 1-19.

[39] H.-m. Xiao, X.-q. Ma, Z.-y. Lai, Isoconversional kinetic analysis of co-combustion of sewage sludge with straw and coal, Appl. Energy, 86 (2009) 1741-1745.

[40] N. Sbirrazzuoli, L. Vincent, A. Mija, et al., Integral, differential and advanced isoconversional methods: complex mechanisms and isothermal predicted conversion–time curves, Chemom. Intell. Lab. Syst., 96 (2009) 219-226.

[41] Y. Xia, Y. Huang, Y. Li, et al., LaPO4: Ce, Tb, Yb phosphor—synthesis and kinetics study for thermal process of precursor by Vyazovkin, OFW, KAS, Starink, and Mastplosts methods, J. Therm. Anal. Calorim., 120 (2015) 1635-1643.

[42] M. Salehi, F. Clemens, T. Graule, et al., Kinetic analysis of the polymer burnout in ceramic thermoplastic processing of the YSZ thin electrolyte structures using model free method, Appl. Energy, 95 (2012) 147-155.

[43] N. Gabilondo, M. López, J.A. Ramos, et al., Curing kinetics of amine and sodium hydroxide catalyzed phenol-formaldehyde resins, J. Therm. Anal. Calorim., 90 (2007) 229-236.

[44] A. Yu, P. Ramesh, M.E. Itkis, et al., Graphite nanoplatelet− epoxy composite thermal interface materials, J. Phys. Chem. C, 111 (2007) 7565-7569.
[45] K.M. Shahil, A.A. Balandin, Graphene–multilayer graphene nanocomposites as highly efficient thermal interface materials, Nano Lett., 12 (2012) 861-867.
[46] A. Yu, P. Ramesh, X. Sun, et al., Enhanced thermal conductivity in a hybrid graphite nanoplatelet–carbon nanotube filler for epoxy composites, Adv. Mater., 20 (2008) 4740-4744.
[47] Y. Song, J. Yu, L. Yu, et al., Enhancing the thermal, electrical, and mechanical properties of silicone rubber by addition of graphene nanoplatelets, Mater. Des., 88 (2015) 950-957.
[48] I.D. Johnston, D.K. McCluskey, C.K.L. Tan, et al., Mechanical characterization of bulk Sylgard 184 for microfluidics and microengineering, Journal of Micromechanics and Microengineering, 24 (2014) 035017.
[49] S. Vyazovkin, Evaluation of activation energy of thermally stimulated solid-state reactions under arbitrary variation of temperature, Journal of Computational Chemistry, 18 (1997) 393-402.
[50] S. Vyazovkin, N. Sbirrazzuoli, Kinetic methods to study isothermal and nonisothermal epoxy-anhydride cure, Macromolecular Chemistry and Physics, 200 (1999) 2294-2303.
[51] T. Ozawa, A new method of analyzing thermogravimetric data, Bull. Chem. Soc. Jpn., 38 (1965) 1881-1886.
[52] J.H. Flynn, L.A. Wall, General treatment of the thermogravimetry of polymers, J Res Nat Bur Stand, 70 (1966) 487-523.
[53] T. Akahira, T. Sunose, Method of determining activation deterioration constant of electrical insulating materials, Res Rep Chiba Inst Technol (Sci Technol), 16 (1971) 22-31.
[54] C.D. Doyle, Estimating isothermal life from thermogravimetric data, J. Appl. Polym. Sci., 6 (1962) 639-642.
[55] X. Li, B. Bhushan, A review of nanoindentation continuous stiffness measurement technique and its applications, Mater. Charact., 48 (2002) 11-36.

Chapter 6

Functional nanocomposites with graphene-DNA hybrid fillers: synthesis and surface properties under UV irradiation*

This Chapter reports the fabrication of nanocomposite films made of graphene-DNA fillers incorporated in a polydimethylsiloxane (PDMS) matrix, and the analysis of their properties under UV-C exposure. In the previous Chapter, the effect of the GNP-DNA filler on the curing behavior of the PDMS matrix was investigated, showing that the presence of the filler progressively decreases the activation energy. Here, nanocomposites at higher filler loadings were prepared with the aim to improve the electrical properties of the nanocomposites for the UV sensing application. In the processing of these nanocomposites, a suitable solvent (isopropyl alcohol) was used in order to improve the dispersion of the high graphene-DNA loadings in the prepolymer matrix, as the sensing properties of the nanocomposite materials are highly affected by the amount and homogeneity of the filler dispersion. The electrical and thermal properties of the GNP-DNA/PDMS films, as well as their surface morphology and wettability, were investigated before and after exposure to UV-C radiation using complementary techniques. Results give information on the potential applications of these functional nanocomposites for radiation monitoring in environments that are characterized by high levels of biologically-damaging UV radiation.

---

*Parts of this Chapter have been published in: Toto E.; Palombi M.; Laurenzi S.; Santonicola M.G. *Ceramics International* **2019**, 45, 9631-9637

6.1 Introduction

Graphene-based nanocomposites possess functional properties that cannot be realized in conventional composites or other carbon nanocomposites [1-3]. Typical investigations of these materials are focused on developing novel devices for sensing [4-7] and EMI shielding [8], due to their enhanced thermal and electrical conductivities [9, 10]. In particular, nanocomposites with flexible polymer matrix offer interesting solutions for applications where the adaptability to a particular shape is one of the functional requirements [11-13]. Radiation sensing is another potential application of graphene-based nanocomposites [4, 14, 15], especially if they can be integrated in wearable devices, allowing for their use by astronauts during extra vehicular activities (EVA) or by operators exposed to radiation-contaminated environments on Earth.

Ultraviolet radiation is well-known to cause damage to materials [16-18] and biological systems [19, 20], and poses serious risks in all environments where radiations are needed for technical applications (e.g. sterilization and surface modifications facilities) and, most significantly, in space environment [21, 22]. Exposure to UV radiation can generate important physical and chemical changes altering the original structure and properties of materials. In particular, the high energy UV-C band, with wavelengths shorter than 280 nm, is associated with one of the most damaging radiation exposures. One hour of UV-C irradiation at 254 nm can damage DNA strands [23], breaking chemical bonds in the nucleic acid sequence and creating new intramolecular bonds that change the DNA native structure [24, 25].

In general, graphene nanoplatelets have many useful features for the design of multifunctional composite materials, including excellent electrical and thermal conductivities, considerable weight-saving lightness, and high mechanical strength [26]. Moreover, they are characterized by a high specific surface area, which allows for several types of functionalization using both covalent and non-covalent approaches [27, 28]. However, the integration of graphene nanomaterials with a polymer matrix is not a trivial task, and the overall functional properties of the materials are highly affected by the amount and homogeneity of the filler dispersion [29-31].

In this study, the fabrication process of graphene-based nanocomposite films containing UV-sensitive GNP-DNA fillers integrated with a flexible PDMS matrix was investigated, and their sensing properties were characterized under UV-C irradiation.

Besides having specific UV sensitivity, DNA also acts as efficient solubilizing agent for the graphene nanomaterial. In fact, graphene nanoplatelets can be functionalized with DNA molecules by non-covalent interactions, such as base-graphene π stacking and interactions between the DNA amines and the carboxyl groups of the nanoplatelets [32-34]. The dispersion of the GNP-DNA filler in the PDMS matrix was improved using isopropyl alcohol (IPA), which enabled the preparation of nanocomposite samples with sufficiently homogenous properties. On the other hand, PDMS is well known for its chemical inertia, biocompatibility and flexibility, which make it an excellent candidate for wearable sensors. More relevantly, PDMS exhibits high optical transparency to UV radiation, and is one of few polymers with good transmittance in the UV-C band (above 240 nm) [35]. For these reasons, PDMS was chosen as polymer matrix for embedding the GNP-DNA fillers and allowing for characterization of their response upon exposure of the nanocomposites to UV-C radiation. A full investigation of the GNP-DNA/PDMS surfaces before and after UV-C irradiation, using several complementary techniques, is presented in order to understand the mechanisms of material-radiation interactions that cause changes of the nanocomposite properties.

6.2 Results and discussion

UV-sensitive nanocomposite films were prepared by integration of GNP-DNA fillers, dispersed in isopropyl alcohol (IPA), with a PDMS matrix made of Sylgard 184. Different filler concentrations from 20 wt% to 40 wt% were considered. The use of IPA was found to be beneficial, among several organic solvents that were investigated, in order to obtain pre-polymer mixtures that were sufficiently homogeneous at high filler fractions and that could be successfully cured in oven at 75 °C for 24 h. Higher curing temperatures were not selected to avoid the formation of porosity in the nanocomposite structure at temperatures near the boiling point of IPA. Sylgard 184 PDMS was selected as matrix for the nanocomposites due to its biocompatibility and flexible nature, allowing for the fabrication of conformable and wearable sensors, and because it is transparent to UV radiation also in the UV-C region (200–280 nm). PDMS has a transmittance value of about 50% at 254 nm, which is the wavelength at which the UV-C irradiation tests were performed, as compared to other flexible polymers, such as polystyrene and styrene

elastomers, for which the UV transmittance drops to values around 10% at wavelengths below 280 nm [35]. A sufficient degree of UV-C transparency by the polymer matrix is necessary to test the interaction of UV radiation with the embedded GNP-DNA fillers without having relevant shielding effects coming from the matrix.

6.2.1 Analysis of the properties of GNP-DNA/PDMS films and their modifications under UV-C exposure

Figure 6.1 shows optical microscopy images of the nanocomposite surfaces at increasing concentration of GNP-DNA filler, indicating a clear improvement of the surface homogeneity at higher loading. Larger aggregates are present in the nanocomposite with 20 wt% of GNP-DNA with brighter and darker regions alternating in the polymer matrix (Figure 6.1a). On the other hand, a smoother composite morphology with smaller white-reflecting regions was obtained at 40 wt% of GNP-DNA (Figure 6.1d). The relatively homogeneous filler distribution on the macroscale has effects on the surface electrical properties of the nanocomposite films.

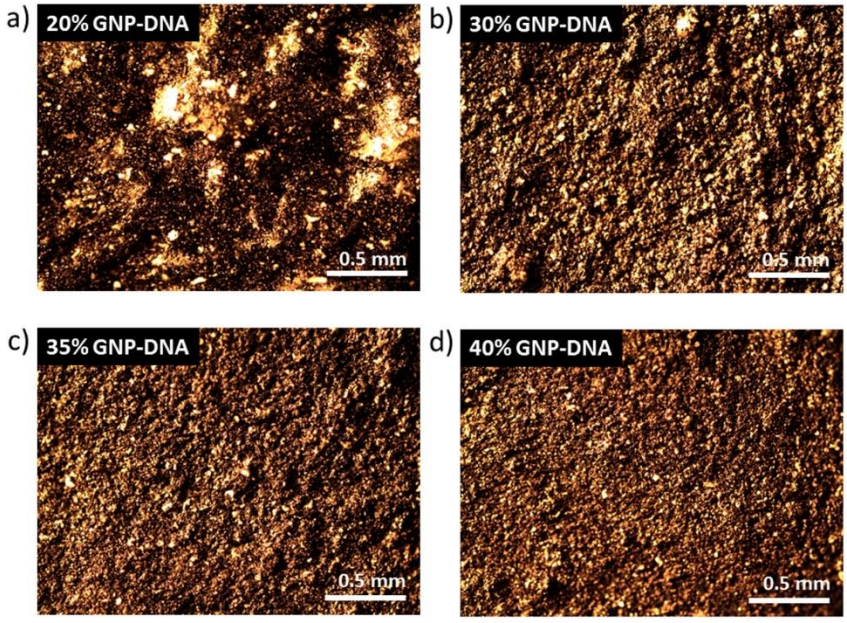

Figure 6.1. *Optical microscope images of the surface of GNP-DNA/PDMS films with different filler concentration (wt%): (a) 20% GNP-DNA, (b) 30% GNP-DNA, (c) 35% GNP-DNA, (d) 40% GNP-DNA. Images taken under reflected light (magnification 5X).*

Nanocomposite films with a GNP-DNA filler concentration of 20 wt%, 30 wt%, and 40 wt% were investigated by electrical impedance spectroscopy before and after UV-C irradiation (Figure 6.2). EIS data were fitted to a RC-circuit model and surface resistivity values were calculated from the fitted resistance values. Each value in Figure 6.2 was calculated averaging the results from ten EIS measurements for each sample. The relative standard deviations are in the range of 15-20%. Such high values of deviations were a consequence of the inherent variability of the electrical measurements on a nanocomposite surface with partially homogeneous filler dispersion and flexible polymer matrix. Nevertheless, results from the EIS analysis revealed that a significant decrease of surface resistivity is achieved when increasing the content of GNP-DNA to the value of 40 wt%. After exposure to UV-C radiation for 8 days, all GNP-DNA/PDMS surfaces showed an increase of their surface electrical resistivity (Figure 6.2), and therefore a decrease of surface conductivity, which is reported in Table 6.1.

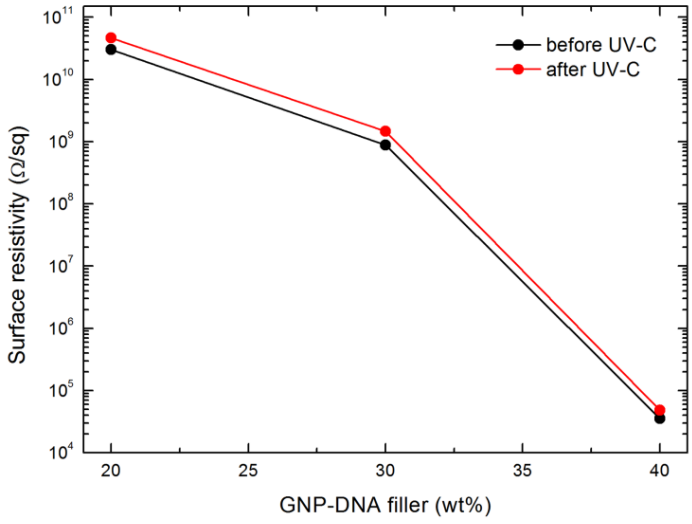

Figure 6.2. *Surface electrical resistivity as a function of the concentration of GNP-DNA filler in the PDMS matrix, before and after exposure to UV-C radiation (6.3 W/m^2, 8 days).*

Table 6.1. *Mean values and standard deviations of surface electrical conductivities (σ_s) of nanocomposites with different concentrations of GNP-DNA filler (wt%) before and after UV-C irradiation (6.3 W/m^2, 8 days). Conductivity values obtained after fitting the EIS data with a RC equivalent circuit model and converting the resistance values using Eq. (6.1).*

Sample	σ_s (μS/sq)	
	before UV-C	after UV-C
20% GNP-DNA/PDMS	$3.47\times10^{-5} \pm 0.80\times10^{-5}$	$2.94\times10^{-5} \pm 1.88\times10^{-5}$
30% GNP-DNA/PDMS	$1.60\times10^{-3} \pm 0.18\times10^{-3}$	$0.72\times10^{-3} \pm 0.19\times10^{-3}$
40% GNP-DNA/PDMS	34.81 ± 11.32	24.89 ± 8.78

The decrease of surface conductivity after radiation exposure was less evident in the 20% GNP-DNA/PDMS samples (-15%) than in the nanocomposites at higher concentrations of GNP-DNA. The largest variation of surface conductivity values after the 8-day UV-C exposure was observed for the 30% GNP-DNA/PDMS samples (-38%). These changes in the surface electrical properties are due to the lower degree of interconnections among the conductive carbon nanoparticles following irradiation by UV-C. Indeed, as previously demonstrated in the literature [36], UV-C radiation causes significant changes in the morphology of exposed graphene nanoplatelets with a clear smoothing of the particle edges after irradiation, and a consequent reduction of the electrical conductivity of the network. In this work, the 30% GNP-DNA/PDMS samples are more electrically conductive than the nanocomposites with less carbon fillers (20% GNP-DNA/PDMS), due to the higher degree of interconnections between the fillers, and they are also those showing a larger irradiation effect at the level of the conductive carbon network.

On the other hand, upon increasing the GNP-DNA filler content to 40 wt%, an additional effect was involved in the response of the nanocomposite sensors. In this case, the UV-C interaction with the DNA biological component became predominant over the UV absorption by the graphene network, thus limiting the decrease of electrical conductivity. This effect was elucidated by the DSC results, which indicated that the largest variations at the level of the DNA molecule due to the UV-induced crosslinking was maximum for the samples with 40 wt% of GNP-DNA filler (see discussion below and Table 6.3).

The analysis of the surface wettability by static contact angle revealed a good grade of hydrophobicity of the non-irradiated nanocomposites, which are characterized by water contact angles (WCA) above 110° (Figure 6.3). The WCA values strongly increase with the GNP-DNA content, reaching 134.9° ± 6.2° for the nanocomposites with 40 wt% of filler. Ten replicate measurements on different spots of the nanocomposite surfaces were performed, and the relative standard deviations were found to be below 5% (Table 6.2). After exposure to UV-C light for 8 days (λ = 254 nm, radiation dose 4.4×10^6 J/m^2), the WCA values of all nanocomposites and that of pure PDMS decreased. In particular, the surface hydrophobicity of the nanocomposites was reduced in proportion to the GNP-DNA content, with the smallest WCA decrease (2.7%) for the 20% GNP-DNA/PDMS surfaces and the largest (11.0%) for the 40% of GNP-DNA/PDMS samples. It is noted that the WCA values following UV-C exposure were measured after few days from the irradiation tests, to ensure that potential surface recovery phenomena were completed. The decrease of surface hydrophobicity of pure PDMS under UV-C irradiation at ambient conditions is in agreement with reports in the literature [37, 38] and can be ascribed to an oxidation phenomenon, which results in the formation of carboxylic acid moieties on the polymer chains [38, 39]. To further investigate the decrease of WCA values occurring under UV irradiation, a surface free energy analysis following the Owens-Wendt method [40] was carried out with two different testing liquids (water and diiodomethane). Results in terms of SFE and its dispersive and polar components for the GNP-DNA/PDMS nanocomposite films and for neat PDMS are reported in Table 6.2. For both irradiated and non-irradiated samples, the SFE decreases at increasing GNP-DNA content. This result indicates that the interactions of the nanocomposites with water and with diiodomethane are less favored at higher GNP-DNA content. The dispersive component (γ^d), which is due to the dispersive interactions among non-polar molecules, is

predominant over the polar one (γ^p) for all investigated sample, but decrease from PDMS to the nanocomposites and upon increase of the GNP-DNA concentration. After UV-C irradiation, the SFE and its dispersive component show a marked increase in the nanocomposite samples, whereas it is almost unvaried for the neat PDMS, indicating that the irradiation mainly affects the GNP-DNA filler and less the polymer matrix. For the neat PDMS sample, an increase of the polar component is observed after irradiation, which is consistent with an oxidation phenomenon generating carboxylic acids on the polymer surface.

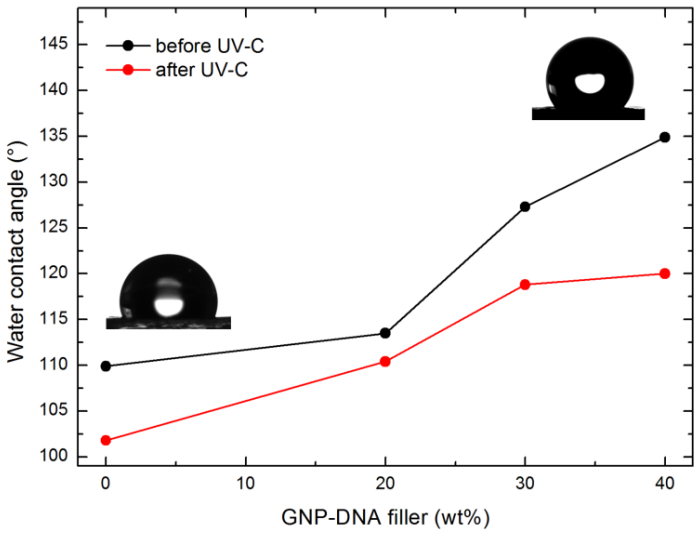

Figure 6.3. *Water contact angles as a function of the concentration of GNP-DNA filler in the PDMS matrix, before and after UV-C irradiation (6.3 W/m^2, 8 days). WCA values are the means of ten replicates on different areas of the nanocomposite surface (relative standard deviations < 5%).*

Table 6.2. *Water contact angles (WCA) and surface free energies (SFE) with dispersive and polar components for GNP-DNA/PDMS nanocomposites with different concentrations of GNP-DNA filler (wt%) before and after UV-C exposure (6.3 W/m^2, 8 days).*

Sample	before UV-C				after UV-C			
	WCA	SFE	γ^d	γ^p	WCA	SFE	γ^d	γ^p
	(degree)	(mJ/m^2)			(degree)	(mJ/m^2)		
PDMS	109.9 ± 4.6	21.98	21.81	0.17	101.8 ± 3.6	21.39	19.92	1.47
20% GNP-DNA/ PDMS	113.5 ± 3.5	16.18	15.90	0.28	110.4 ± 2.7	18.53	18.14	0.38
30% GNP-DNA/ PDMS	127.3 ± 4.5	10.70	10.70	0.00	118.8 ± 6.0	14.42	14.36	0.06
40% GNP-DNA/ PDMS	134.9 ± 6.2	9.18	9.03	0.15	120.0 ± 7.4	11.80	11.65	0.15

The thermal behavior of the UV-sensitive nanocomposites was investigated by DSC before and after irradiation in an extended temperature range (from -40 °C to 250 °C). Figure 6.4a shows the thermograms of the non-irradiated GNP-DNA/PDMS nanocomposites in comparison with a neat PDMS sample. The filler-loaded samples show a significant endothermal peak at about 146 °C, which is slightly shifted to higher temperatures after UV-C exposure (Figure 6.4b), whereas PDMS is thermally stable over the entire temperature range considered for this study. To understand the nature of the endothermal peak, pure DNA samples were measured by DSC at the same conditions (Figure 6.5). A similar shift of the endothermal peak to higher temperatures after UV-C irradiation was observed. Therefore, the presence of the peak in the nanocomposites was ascribed to denaturation of the double-stranded DNA component.

The shift of the denaturation peak after irradiation can be explained with the occurrence of a UV-induced crosslinking of the DNA chains, which increases the thermal stability of the biological component. The DSC measurements were analyzed in terms of peak temperature and enthalpy change (ΔH) associated with the endothermic events (Table 6.3). The relation between the endothermic peak and the DNA component of the nanocomposites is also supported by the fact that the ΔH values increase when the concentration of the GNP-DNA filler, and so the amount of DNA, is larger. After UV-C irradiation, all samples containing DNA show a shift of the denaturation peak and a corresponding increase of the enthalpy change, which is an additional indication of the higher crosslinked nature of DNA and its chemical surrounding.

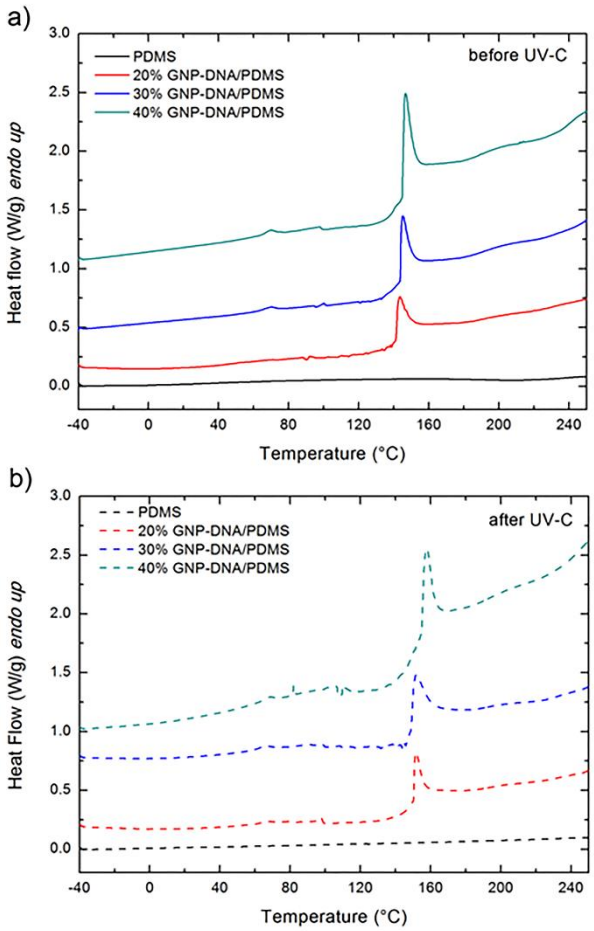

Figure 6.4. *DSC thermograms of GNP-DNA/PDMS nanocomposites with different concentrations of GNP-DNA filler, (a) before and (b) after UV-C irradiation (6.3 W/m^2, 8 days). Heating rate: 10 °C/min.*

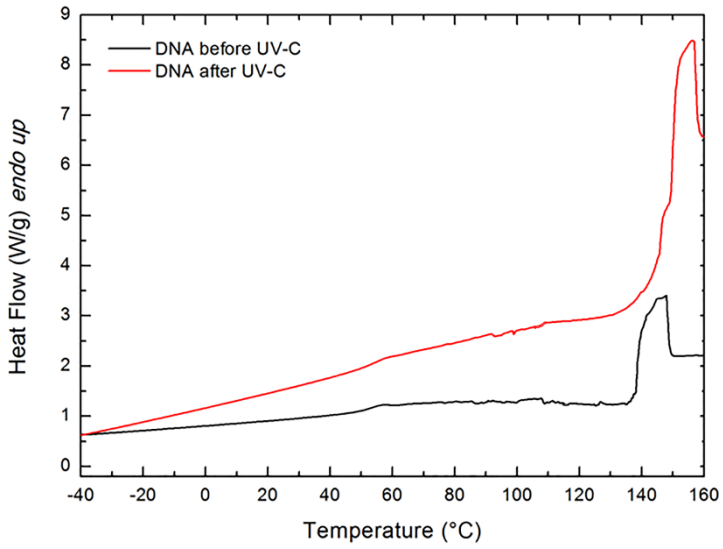

Figure 6.5. *DSC thermograms of pure DNA (powder form) before and after UV-C irradiation (6.3 W/m^2, 8 days). Heating rate: 10 °C/min.*

Table 6.3. *Endothermic peak temperatures (T_{peak}) and enthalpy changes (ΔH) determined from DSC thermograms of DNA and GNP-DNA/PDMS nanocomposites before and after UV-C exposure (6.3 W/m^2, 8 days).*

Sample	T_{peak} (°C)		ΔH (mJ/mg)	
	before UV-C	after UV-C	before UV-C	after UV-C
DNA	146.5 ± 1.5	159.5 ± 3.9	49.80 ± 25.56	80.63 ± 12.98
20% GNP-DNA/ PDMS	147.2 ± 2.6	152.2 ± 2.8	24.56 ± 3.82	31.42 ± 2.32
30% GNP-DNA/ PDMS	146.1 ± 0.9	151.9 ± 3.3	32.33 ± 3.26	63.43 ± 22.14
40% GNP-DNA/ PDMS	146.3 ± 1.1	156.1 ± 3.7	50.28 ± 7.05	85.90 ± 19.15

The surface morphology of the GNP-DNA/PDMS nanocomposites with higher filler content (40 wt%) was investigated by SEM before and after UV-C exposure for 8 days (Figure 6.6a and 6.6c).

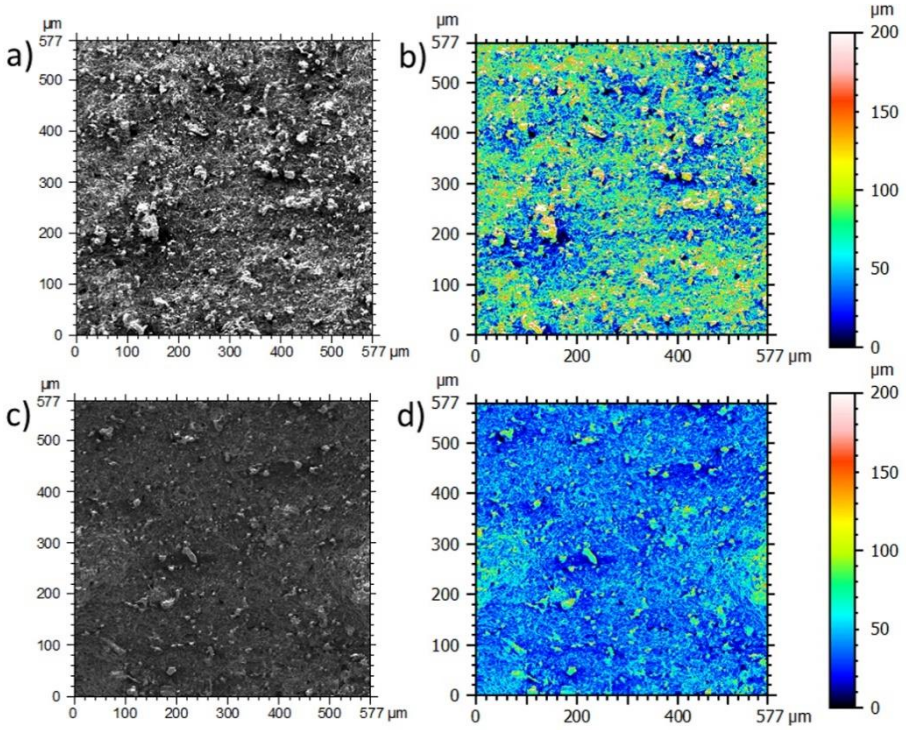

Figure 6.6. *SEM images (magnification 500X) of 40% GNP-DNA/PDMS nanocomposite (left) and its 3D surface morphology reconstruction (right), (a, b) before and (c, d) after UV-C exposure (6.3 W/m^2, 8 days).*

SEM images unveiled a markedly different surface morphology in the irradiated nanocomposite samples. In particular, after UV-C irradiation the nanocomposite surfaces appear smoother. To quantify the UV-induced changes at the level of surface roughness, a three-dimensional reconstruction of the profiles was performed with the MountainsMap software starting from two SEM images acquired at two different tilt angles (0° and 5°). The surface roughness values were calculated considering a minimum of ten profiles extracted across the reconstructed surfaces of the non-irradiated and irradiated 40% GNP-DNA/PDMS samples (Figure 6.6b and 6.6c, respectively). Mean values of the surface roughness were 25.9 ± 3 µm and 15.4 ± 2.4 µm before and after UV-C irradiation, respectively, with a decrease of 40.5% that is consistent with the observed surface erosion.

6.3 Conclusions

UV-sensitive nanocomposite films based on GNP-DNA hybrid fillers embedded in a PDMS polymer matrix were synthesized. The surfaces of the nanocomposites were investigated before and after UV-C irradiation in order to determine changes of their multifunctional properties. Results by differential scanning calorimetry revealed that, upon exposure to UV-C light, the thermal behavior of the GNP-DNA/PDMS nanocomposites is affected at the level of the DNA component, as its denaturation peak (at approximately 150 °C) exhibits an increase of both peak temperature and enthalpy change. These variations are consistent with a higher cross-linked nature of the biological element. At the same time, DSC thermograms showed that such nanocomposites are thermally stable in a wide range of temperature, from –40 °C to 140 °C, and so they are potentially useful in technological applications characterized by large temperature gradients, such as those in space environment. In addition, the GNP-DNA/PDMS nanocomposites exhibit a high degree of hydrophobicity that does not change significantly after UV-C exposure (water contact angles > 100°), and therefore they maintain a low tendency to adsorb humidity from the surrounding environment. The morphology analysis by SEM including 3D profile reconstruction was useful to assess and quantify the UV-C exposure effects on the nanocomposite surface, revealing a decrease of roughness after irradiation. Lastly, results by electrical impedance spectroscopy showed a surface conductivity variation after UV-C exposure for all concentrations of GNP-DNA filler investigated. In particular, the nanocomposite with filler content of 30 wt% revealed the maximum conductivity change after 8 days of irradiation (38%). The electrical response to UV light combined with the results from the other investigations are useful to guide the design and optimization of the GNP-DNA/PDMS nanocomposites towards the detection of the damaging effects of UV-C exposure in relevant environments.

6.4 Experimental section

Materials: Graphene nanopowder grade AO-4 (specific surface area ≤ 40 m^2/g, purity 98.5%, average flake thickness 60 nm, particle lateral size ≤ 7 μm) was purchased from Graphene Supermarket (Calverton, NY, USA). Double-stranded DNA and isopropyl

alcohol (IPA) were obtained from Sigma-Aldrich (Milan, Italy). Two-component PDMS Sylgard 184 was purchased from Dow Corning (Midland, MI, USA) and prepared using a mixing ratio of base to curing agent of 10:1 (w/w). Microscope glass slides from Menzel-Glaser (Braunschweig, Germany) were cut in square shape (25 mm × 25 mm) and used as substrates for the nanocomposite film deposition.

Preparation of nanocomposite films: Graphene nanopowder AO-4 and DNA were weighted and mixed at a mass ratio of 1:1 in isopropyl alcohol (4 mL). The PDMS elastomer base was added to the dispersion in a polymer-to-solvent ratio of 3:4 (w/v), and the mixture was sonicated for 1 h in a cold water bath (Elmasonic P30H, Elma, Singen, Germany). After sonication, the curing agent was gently mixed into the mixture using a ratio of base to curing agent of 10:1 (w/w). Fixed aliquots (0.5 mL) of the GNP-DNA/PDMS mixture were deposited on the glass substrates by drop casting and dried in oven at 75 °C for 24 h. The cure temperature was chosen below the boiling point of IPA (82.6 °C), so to avoid the formation of large voids in the nanocomposite structure due to rapid solvent evaporation. Different types of films were realized varying the fraction of GNP-DNA filler in the nanocomposite mixture (from 20 wt% to 40 wt%). The average thickness of the nanocomposite coating was measured with a digital caliper (resolution 0.01 mm) and found to be in the range from 0.45 to 0.70 mm, depending on the content of the GNP-DNA filler.

UV-C irradiation tests: The graphene-based nanocomposite films deposited on glass substrates were irradiated in a closed chamber under a low-pressure UV lamp (3UV-38, 8 W, UVP LLC, Upland, CA, USA) set at the wavelength of 254 nm. The UV energy flux was measured using a HD 2302.0 radiometer (Delta Ohm, Padova, Italy) fitted with a LP 471 UVC probe (spectral range 200–280 nm). Nanocomposite samples were kept at a distance of 11 cm from the lamp, and were exposed to a UV-C irradiance of 6.3 W/m^2. The irradiation tests were carried out over several days (up to 8 days), with a maximum radiation dose of 4.4×10^6 J/m^2.

Characterization methods: The morphology of the nanocomposite films before and after UV-C irradiation was investigated using a VEGA II LSH scanning electron microscope (TESCAN, Brno, Czech Republic) operated at an accelerating voltage of 5

kV and 500X magnification. SEM images taken at different tilt angles were processed using the MountainsMap Software (Digital Surf, Besançon, France) allowing three-dimensional morphology reconstruction of the surfaces and extrapolation of surface roughness values from the reconstructed profiles. A Leica DMLP polarized light microscope equipped with a N Plan 5X/0.12 objective and a EC3 digital camera (Leica Microsystems, Wetzlar, Germany) was used to image the nanocomposite surfaces.

Electrical impedance spectroscopy (EIS) was performed with a Reference 600 Potentiostat/Galvanostat/ZRA instrument (Gamry Instruments, Warminster, PA, USA) in the frequency range 10 Hz–1MHz. Measurements (10 replicates for each sample) were carried out using a configuration with two parallel electrodes (1-cm-wide copper strips) that were fixed in a custom-made cell fabricated in ABS material. The particular design of the measurement cell allowed for a reliable positioning of the sample and the electrodes. The cell was placed in a Faraday cage (Gamry Instruments) to shield the measurements from undesired noise. Impedance data were fitted to an equivalent circuit model using the Gamry Echem Analyst software package. The electrical resistance values (R_s) obtained from the fitting procedure were converted to conductivities using the following equation:

$$\sigma_S = \frac{1}{\rho_S} = \left(R_S \frac{D}{L}\right)^{-1} \tag{6.1}$$

where σ_s is the surface electrical conductivity, ρ_s is the surface resistivity, L is the distance between the electrodes, and D is the length of the electrodes in contact with the sample surface.

Thermal analysis was carried out with a DSC Pyris 1 instrument (Perkin-Elmer, Waltham, MA, USA). Experiments were performed under nitrogen flow in the temperature range from –40 °C to 250 °C at heating rate of 10 °C/min. A baseline was measured using an empty pan at the same experimental conditions and was subtracted from the sample data. Peak temperatures (T_{peak}) and enthalpy changes (ΔH) were determined from the DSC thermograms using the Perkin-Elmer Thermal Analysis Software provided with the instrument. Several samples were analyzed for each type of nanocomposite (between three and six) to ensure reproducibility of results.

Surface wettability tests were performed measuring the contact angles of water droplets on the sample surface using an optical analyzer (OCA15Pro, DataPhysics

Instruments, Filderstadt, Germany). The static sessile method (droplet volume 3 μL) was selected, and ultrapure water (Milli-Q, 18.2 MΩ·cm) and diiodomethane were used as testing liquids. A minimum of ten droplets localized on different areas of the nanocomposite sample were analyzed. Contact angle values were determined by drop shape analysis using the DataPhysics SCA 20 software module. The surface free energies (SFE) were calculated using the contact angle values measured with water and diiodomethane, following the Owens-Wendt method [40]:

$$\gamma_l(1+\cos\theta) = 2\left[(\gamma_s^d\gamma_l^d)^{1/2} + (\gamma_s^p\gamma_l^p)^{1/2}\right] \quad (6.2)$$

where γ_s is the SFE of the investigated sample, γ_l is the SFE of the measuring liquid, the apexes *d* and *p* indicate the dispersive and polar components respectively, and θ is the contact angle between the sample and the testing liquid.

6.5 References

[1] T. Kuilla, S. Bhadra, D. Yao, et al., Recent advances in graphene-based polymer composites, Prog. Polym. Sci. 35(11) (2010) 1350-1375.

[2] J.R. Potts, D.R. Dreyer, C.W. Bielawski, et al., Graphene-based polymer nanocomposites, Polymer 52(1) (2011) 5-25.

[3] D.G. Papageorgiou, I.A. Kinloch, R.J. Young, Graphene/elastomer nanocomposites, Carbon 95 (2015) 460-484.

[4] E. Toto, M.G. Santonicola, M.C. Mancini, et al., Ultraviolet-sensing surfaces based on hybrid nanocomposites for radiation monitoring systems, in: 4th IEEE International Workshop on Metrology for AeroSpace, MetroAeroSpace 2017 – Proceedings, 7999599 (2017) 369-373

[5] J. Xu, Y. Wang, S. Hu, Nanocomposites of graphene and graphene oxides: synthesis, molecular functionalization and application in electrochemical sensors and biosensors. A review, Microchim. Acta 184(1) (2017) 1-44.

[6] L. Shabnam, S.N. Faisal, A.K. Roy, et al., Doped graphene/Cu nanocomposite: a high sensitivity non-enzymatic glucose sensor for food, Food Chem. 221 (2017) 751-759.

[7] A. Rinaldi, A. Tamburrano, M.S. Sarto, Graphene nanoplatelets-based smart textile for kinesthetic monitoring, Proc. IEEE Sens. (2017) 1-3.

[8] Y.-J. Wan, P.-L. Zhu, S.-H. Yu, et al., Graphene paper for exceptional EMI shielding performance using large-sized graphene oxide sheets and doping strategy, Carbon 122 (2017) 74-81.

[9] M.-S. Cao, X.-X. Wang, W.-Q. Cao, et al., Ultrathin graphene: electrical properties and highly efficient electromagnetic interference shielding, J. Mater. Chem. C 3(26) (2015) 6589-6599.

[10] S. Bin, Z. Wentao, Z. Wenge, Ultrathin Flexible Graphene Film: An Excellent Thermal Conducting Material with Efficient EMI Shielding, Adv. Funct. Mater. 24(28) (2014) 4542-4548.

[11] J. Houk, P.Y. Ju, C. Xiang, et al., A. Jong-Hyun, Graphene-Based Flexible and Stretchable Electronics, Adv. Mater. 28(22) (2016) 4184-4202.

[12] B. Zhu, Z. Niu, H. Wang, et al., Artificial Skin: Microstructured Graphene Arrays for Highly Sensitive Flexible Tactile Sensors, Small 10(18) (2014) 3594-3594.

[13] W. Yan, W. Li, Y. Tingting, et al., Wearable and Highly Sensitive Graphene Strain Sensors for Human Motion Monitoring, Adv. Funct. Mater. 24(29) (2014) 4666-4670.

[14] M.G. Santonicola, M.G. Coscia, S. Botti, et al., Graphene/DNA nanostructured films for bioinspired sensing of UV radiation effects, Proceedings of the International Astronautical Congress, IAC 9 (2014) 6313-6317.

[15] M.G. Santonicola, M.G. Coscia, M. Sirilli, et al., Nanomaterial-based biosensors for a real-time detection of biological damage by UV light, Proceedings of the Annual International Conference of the IEEE Engineering in Medicine and Biology Society, EMBS 7319368 (2015) 4391-4394.

[16] A.L. Andrady, S. Hamid, X. Hu, et al., Effects of increased solar ultraviolet radiation on materials, J. Photochem. Photobiol. B: Biol. 46(1-3) (1998) 96-103.

[17] A. Charlesby, Atomic radiation and polymers: international series of monographs on radiation effects in materials, Elsevier, 2016.

[18] A. Swallow, Radiation Chemistry of Organic Compounds: International Series of Monographs on Radiation Effects in Materials, Vol. 2, Elsevier, 2016.

[19] B. Diffey, Solar ultraviolet radiation effects on biological systems, Phys. Med. Biol. 36(3) (1991) 299.

[20] W. Harm, Biological effects of ultraviolet radiation, Cambridge University Press, 1980.

[21] E. Grossman, I. Gouzman, Space environment effects on polymers in low earth orbit, Nucl. Instrum. Methods Phys. Res. Sect. B: Beam Interact. Mater. At. 208 (2003) 48-57.
[22] M. Maalouf, M. Durante, N. Foray, Biological effects of space radiation on human cells: history, advances and outcomes, J. Radiat. Res. 52(2) (2011) 126-146.
[23] D. Paunescu, C.A. Mora, M. Puddu, et al., DNA protection against ultraviolet irradiation by encapsulation in a multilayered SiO 2/TiO 2 assembly, J. Mater. Chem. B 2(48) (2014) 8504-8509.
[24] J.-L. Ravanat, T. Douki, J. Cadet, Direct and indirect effects of UV radiation on DNA and its components, J. Photochem. Photobiol. B: Biol. 63(13) (2001) 88-102.
[25] T. Matsunaga, K. Hieda, O. Nikaido, Wavelength dependent formation of thymine dimers and (6-4) photoproducts in DNA by monochromatic ultraviolet light ranging from 150 to 365 nm, Photochem. Photobiol. 54(3) (1991) 403-410.
[26] M.-Y. Shen, T.-Y. Chang, T.-H. Hsieh, et al., Mechanical properties and tensile fatigue of graphene nanoplatelets reinforced polymer nanocomposites, J. Nanomater. 2013 (2013) 1-9.
[27] V. Georgakilas, M. Otyepka, A.B. Bourlinos, et al., Functionalization of graphene: covalent and non-covalent approaches, derivatives and applications, Chem. Rev. 112(11) (2012) 6156-6214.
[28] M.G. Santonicola, Label-Free Biosensing Platforms Based on Graphene/DNA Interfaces, in: A. Tiwari (Ed.) Graphene Bioelectronics, Elsevier, 2018, pp. 177-191.
[29] Y.S. Song, J.R. Youn, Influence of dispersion states of carbon nanotubes on physical properties of epoxy nanocomposites, Carbon 43(7) (2005) 1378-1385.
[30] G.-M. Vallet, M. Dunand, J.-F. Silvain, Influence of Carbon Nanotubes Dispersion on Thermal Properties of Copper-Carbon Nanotubes (CNTs) Composite Materials, Univers. J. Mater. Sci. 3(4) (2015) 55-61.
[31] P. Martins, R. Gonçalves, S. Lanceros-Mendez, et al., Effect of filler dispersion and dispersion method on the piezoelectric and magnetoelectric response of CoFe2O4/P (VDF-TrFE) nanocomposites, Appl. Surf. Sci. 313 (2014) 215-219.
[32] T.C. Hain, K. Kroeker, D.G. Stich, et al., Influence of DNA conformation on the dispersion of SWNTs: single-strand DNA vs. hairpin DNA, Soft Matter 8(10) (2012) 2820-2823.

[33] A.J. Patil, J.L. Vickery, T.B. Scott, et al., Aqueous stabilization and self-assembly of graphene sheets into layered bio-nanocomposites using DNA, Adv. Mater. 21(31) (2009) 3159-3164.

[34] S. Botti, A. Rufoloni, S. Laurenzi, et al., DNA self-assembly on graphene surface studied by SERS mapping, Carbon 109 (2016) 363-372.

[35] M.D. Borysiak, K.S. Bielawski, N.J. Sniadecki, et al., Simple replica micromolding of biocompatible styrenic elastomers, Lab Chip 13(14) (2013) 2773-2784.

[36] M. Clausi, S. Laurenzi, V. La Saponara, et al., Multifunctional sensors for UV and mechanical damage detection of aerospace structures, in: 67th International Astronautical Congress, IAC 2016

[37] E.A. Waddell, S. Shreeves, H. Carrell, et al., Surface modification of Sylgard 184 polydimethylsiloxane by 254nm excimer radiation and characterization by contact angle goniometry, infrared spectroscopy, atomic force and scanning electron microscopy, Appl. Surf. Sci. 254(17) (2008) 5314-5318.

[38] C. Lin, R. Jicun, B. Rui, et al., Ultraviolet sealing and poly(dimethylacrylamide) modification for poly(dimethylsiloxane)/glass microchips, Electrophoresis 25(6) (2004) 914-921.

[39] H. Hillborg, U.W. Gedde, Hydrophobicity changes in silicone rubbers, IEEE Trans. Dielectr. Electr. Insul. 6(5) (1999) 703-717.

[40] O.D. K., W.R. C., Estimation of the surface free energy of polymers, Journal of Appl. Polym. Sci. 13(8) (1969) 1741-1747.

Chapter 7

Experimental study of solar radiation effects on carbon nanocomposite sensors in simulated space environment*

Solar radiation, generally referred to the electromagnetic radiation emitted by the Sun, constitutes one of the most critical risks for human exploration in space. As mentioned in Chapter 2, whereas on Earth such radiation is filtered for the shorter and highly hazardous wavelengths by the atmosphere and its ozone layer, in space solar radiation has profound and adverse effects on the structural and electronic components of spacecrafts, as well as on biological systems, if they are not properly shielded. In this context, research on innovative radiation sensing materials and devices to measure the internal radiation environment of spacecrafts or to monitor the radiation exposure experienced by astronauts during extra-vehicular activities is constantly growing. This Chapter reports the fabrication process of functional nanocomposites based on graphene nanoplatelets and DNA-decorated graphene nanoplatelets embedded in a flexible and UV-transparent polymer matrix. The properties of the nanocomposites were investigated before and after testing in a thermo-vacuum chamber equipped with a solar lamp, in terms of morphology, electrical conductivity, wettability and thermal behavior. Results show the potential applications of these nanocomposites as sensing materials for radiation monitoring in extreme environments characterized by high levels of biologically-damaging ionizing radiation, such as the space environment.

---

*Parts of this Chapter have been published in: Santonicola M.G.; Toto E.; Palombi M.; Paris C.; Laurenzi S. *Proceedings of 69th International Astronautical Congress, IAC* **2018**, 1-8

7.1 Introduction

The human exploration of space poses the significant problem to monitor and limit the effects of the highly damaging solar radiation. The destructive impact of this radiation on spacecraft structures [1, 2] and on biological systems [3, 4] is largely investigated and new solutions to prevent and reduce the associated risks are continuously researched.

In particular, one of the well-known radiation effects on human health is the acute radiation syndrome (ARS), a state of illness with different symptoms caused by the exposure to a high dose of penetrating, ionizing radiation over a short period of time [5, 6]. Several studies have focused on the relation between radiation exposure and the probability to develop diseases as cancer and cataract [7-9]. In 2012, the International Commission of Radiological Protection (ICRP) has presented a review of early and late effects of radiation in normal tissues and organs in reference to the degenerative tissue risks, circulatory diseases and cataracts, providing the threshold doses for tissue reactions [10]. The damaging effect of solar radiation on the DNA structure was also demonstrated by a large number of studies [11-14]. In particular, the ultraviolet photons damage the nucleic acid bases inducing the formation of pyrimidine dimers and altering the DNA chain [11, 15]. The connection between doses and DNA changes led to the development of biological dosimetry, which typically exploits resistant microorganisms, such as bacteriophages and spores [16-19].

The other relevant aspect affecting space exploration is represented by the changes and degradations of spacecraft materials caused by the combination of multiple factors such as solar radiation, atomic oxygen, thermal changes and high vacuum condition [20]. For this reason, several projects have been planned to test the effects of space conditions on spacecraft materials, from Skylab, America's first experimental space station that carried out 300 experiments on human adaptability and on materials exposure in space environment, to the Materials International Space Station Experiment (MISSE) consisting in a series of experiments mounted externally to the International Space Station (ISS) that investigated the effects of long-term exposure of materials to the space environment [21].

In this work, nanocomposite materials based on graphene nanoplatelets (GNPs) were developed and their properties and solar radiation sensitivity were tested in a simulated space environment. GNPs were selected for their advantageous characteristics such as the excellent electrical and thermal conductivity, lightweight and high mechanical strength

[22]. These nanoparticles were embedded into a polydimethylsiloxane (PDMS) matrix that is well-known for its flexibility, chemical inertia and good transparency to highly energetic ultraviolet radiation [23]. Isopropyl alcohol (IPA) was used as solvent to enhance the filler integration into the polymer matrix.

The intent to realize a material suitable to monitor solar radiation exposure during space missions suggested to experiment the use of a UV-sensitive biological component, such as DNA, integrated with the GNP element. The assembly of the GNP-DNA complexes and their electrical properties under UV-C irradiation were previously studied and results are reported in Chapters 3, 4 and 6. Here, PDMS-based nanocomposites with GNP-DNA fillers were fabricated exploiting the character of DNA as solar radiation target and, at the same time, as efficient solubilizing agent for the graphene nanoplatelets [24-26]. The properties of the GNP/PDMS and GNP-DNA/PDMS nanocomposites were investigated before and after testing in simulated space environment using several complementary techniques. The behavior of these nanocomposite materials is discussed in relation to their potential use in the space mission context.

7.2 Results and discussion

GNP/PDMS and GNP-DNA/PDMS nanocomposite samples were primarily investigated in terms of surface morphology. This characterization gives information about the surface changes caused by the solar radiation exposure and also about the different structure of the surface in presence of the DNA biological component. Figure 7.1 and Figure 7.2 show the nanocomposites morphology before the irradiation (Figure 7.1a, Figure 7.2a) and the related 3D reconstructions (Figure 7.1b, Figure 7.2b). The post processing of SEM images with MountainsMap software permits to examine the characteristics of the surfaces in depth. In fact, although from SEM images acquired at 0 tilt angle the GNP/PDMS surface appears flatter than the GNP-DNA/PDMS one, the 3D surface reconstruction (performed from pair of images in plane and tilted of 5°) revealed a larger difference between the maximum and the minimum z-axis value in the GNP/PDMS surface profiles than in the GNP-DNA/PDMS sample.

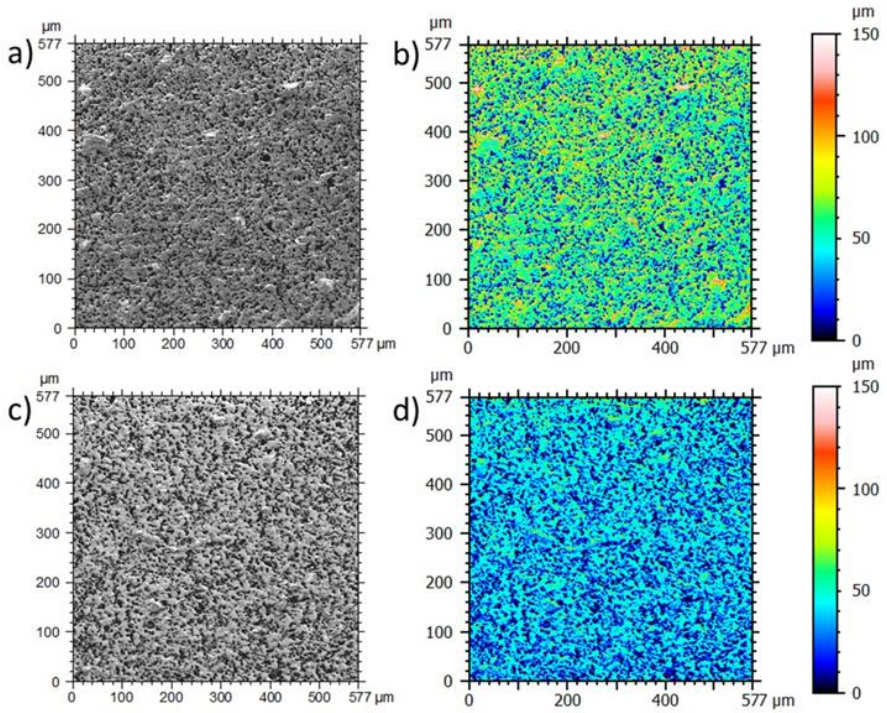

Figure 7.1. *SEM images (magnification 500X) of 15% GNP/PDMS nanocomposite (left) and its 3D surface morphology reconstruction (right), before (a, b) and after (c, d) the test in thermo-vacuum chamber.*

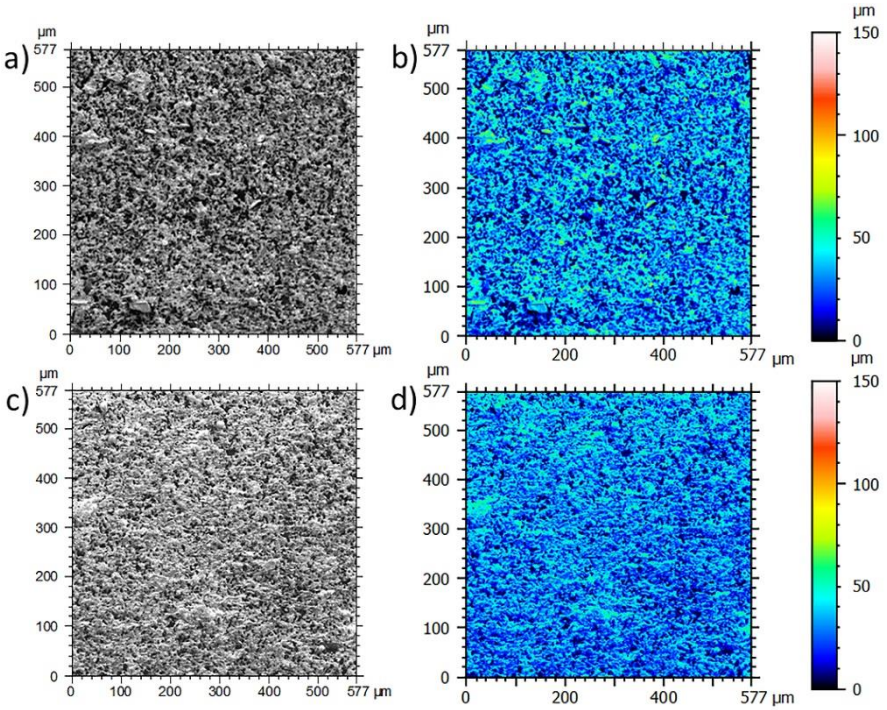

Figure 7.2. *SEM images (magnification 500X) of 30% GNP-DNA/PDMS nanocomposite (left) and its 3D surface morphology reconstruction (right), before (a, b) and after (c, d) the test in thermo-vacuum chamber.*

The roughness value, which was calculated from profiles extracted in different regions of the reconstructed surface, is higher in the absence of DNA (Table 7.1). After the solar irradiation test in the simulated space environment, the surfaces result smoother (Figure 7.1c, 7.1d and Figure 7.2c, 7.2d) and the roughness value decreases for the both types of nanocomposites (Table 7.1). In particular, for the GNP/PDMS sample, the decrease was of the order of 30%.

Table 7.1. *Roughness values of 15% GNP/PDMS and 30% GNP-DNA/PDMS nanocomposite surfaces, calculated after 3D reconstruction, before and after test in thermo-vacuum chamber.*

Sample	Roughness, Ra (μm)		
	Before test	**After test**	**ΔRa/Ra**
GNP/PDMS	18.83±1.67	13.14±0.91	-30.2%
GNP-DNA/PDMS	11.56±0.87	9.87±0.64	-14.6%

Electrical impedance spectroscopy performed before the solar radiation exposure revealed a good grade of electrical conductivity, in particular for the 15% GNP/PDMS nanocomposite. The conductivity values calculated by Eq. (7.1) starting from the EIS data fitted with a RC-circuit model are presented in Table 7.2. The results highlight a lower electrical conductivity in presence of DNA, in fact the 30% GNP-DNA/PDMS nanocomposite results less conductive than the nanocomposite with only 15% of GNP as filler. After the solar irradiation test, the conductivity values for both nanocomposites decrease and mostly for the GNP/PDMS one, for which the loss is of 98.6% (Table 7.2). These changes in electrical properties are likely due to the partial breaking of the interconnections among the carbon nanoparticles induced by the solar radiation exposure.

Table 7.2. *Conductivity values of 15% GNP/PDMS and 30% GNP-DNA/PDMS nanocomposites, calculated by Eq. (7.1) before and after test in thermo-vacuum chamber.*

Sample	Conductivity, σ (S/cm)		
	Before test	After test	Δσ/σ
GNP/PDMS	$1.6\times10^{-6} \pm 0.1\times10^{-6}$	$2.2\times10^{-8} \pm 0.3\times10^{-8}$	-98.6%
GNP-DNA/PDMS	$4.8\times10^{-9} \pm 0.9\times10^{-9}$	$1.2\times10^{-9} \pm 0.2\times10^{-9}$	-75.0%

The investigation of the surface wettability revealed a good grade of hydrophobicity of the samples analyzed, starting from the value of 116.4° for the pure PDMS to the highest value of 121.3° for the GNP-DNA/PDMS nanocomposite, as summarized in Table 7.3.

Table 7.3. *Water contact angles of pure PDMS, 15% GNP/PDMS and 30% GNP-DNA/PDMS samples, evaluated before and after test in thermo-vacuum chamber.*

Sample	Water contact angle (°)	
	Before test	After test
PDMS	116.4 ± 3.3	116.1 ± 1.4
GNP/PDMS	117.3 ± 2.6	113.3 ± 0.7
GNP-DNA/PDMS	121.3 ± 0.9	106.6 ± 2.0

After irradiation, the WCA values of all samples investigated decrease, and in particular for the nanocomposite containing DNA, which reaches a value of 106.6°. A surface free energy (SFE) analysis was carried out to complete the wettability study, following the Owens-Wendt method [27]. Results are reported in Table 7.4. Before the irradiation test, the SFE value decreases with the filler content, showing a maximum for the sample without filler (pure PDMS) and the minimum for the GNP-DNA/PDMS nanocomposite with 30 wt% of filler. The differences in terms of type of filler emerge analysing the SFE values determined after the solar irradiation test. In this case, the SFE decreases for the pure PDMS, remains similar for the GNP/PDMS nanocomposite and increases for the sample with the GNP-DNA filler. The dispersive component (γ^d), which is related to the

dispersive interactions among non-polar molecules, is prevalent over the polar one (γ^p) in all cases. After irradiation, the polar component increases for both nanocomposite samples, but mostly for the type with the GNP-DNA filler. These results indicate that the solar radiation alters the wettability properties of the nanocomposites acting on the filler, particularly on the one with the DNA component, without involving the GNP and the PDMS matrix.

Table 7.4. *Surface free energy values with dispersive and polar components of pure PDMS, 15% GNP/PDMS and 30% GNP-DNA/PDMS nanocomposites, determined by Eq. (7.2) before and after test in thermo-vacuum chamber.*

Sample	Surface free energy (mJ/m^2)					
	Before test			After test		
	SFE	**γ^d**	**γ^p**	**SFE**	**γ^d**	**γ^p**
PDMS	21.7	21.7	0.0	20.6	20.6	0.0
GNP/PDMS	19.2	19.2	0.0	19.9	19.8	0.1
GNP-DNA/PDMS	15.3	15.3	0.0	20.8	20.2	0.6

The thermal behavior of the nanocomposites was examined in a large temperature range, from -40 °C to 250 °C, which is of interest for space applications of materials. Analysis by DSC was carried out before and after the solar irradiation test. The related thermograms are shown in Figure 7.3. DSC results reveal the presence of thermal phenomenon only for the sample containing the DNA component. In particular, an endothermal peak occurs at 148.3 °C (Figure 7.3a), which can be attribute to the denaturation of the double-stranded DNA. After irradiation, the peak appears shifted at higher temperature (167.1 °C) and the enthalpy change decreases with respect to the pre-irradiation value, from 38.7 J/g to 22.4 J/g (Figure 7.3b). The shift of the denaturation peak after irradiation can be related to a DNA crosslinking promoted by the ultraviolet radiation, which makes the sample more thermally stable. Pure PDMS and GNP/PDMS samples show a good thermal stability over the entire range of temperature, without variations after the solar radiation exposure.

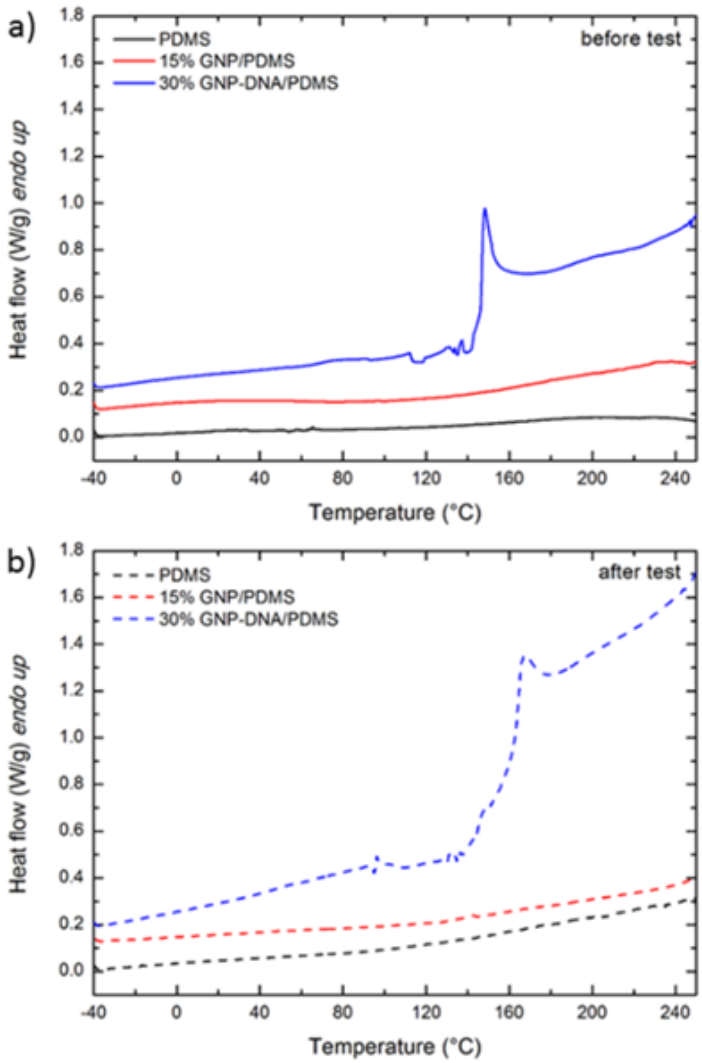

Figure 7.3. *DSC thermograms for neat PDMS, 15% GNP/PDMS and 30% GNP-DNA/PDMS nanocomposites before (a) and after (b) test.*

Table 7.5 summarizes the results of the TML% and WVR% values calculated for each sample after the solar radiation test in the simulated space environment. The GNP/PDMS nanocomposite shows a TML% value that is acceptable for space applications (less than 1%), in accordance with the ECSS-Q-70-02A standard. On the other hand, the sample with the GNP-DNA filler is characterized by a TML% value that exceeds the limit of 0.95%. Data collected on the pure PDMS sample reveals that the nanocomposite outgassing is mostly determined by the filler and to a lower extent by the polymer matrix (TML% = 0.14).

Table 7.5. *Percentage values of total mass loss (TML%) and water vapor regained (WVR%) for pure PDMS, 15% GNP/PDMS and 30% GNP-DNA/PDMS nanocomposite.*

Sample	TML%	WVR%
PDMS	0.14	0.04
GNP/PDMS	0.49	0.06
GNP-DNA/PDMS	1.95	0.01

The low values of WVR% confirm the hydrophobic nature of the nanocomposites, and so the low tendency to absorb humidity from the surrounding environment, as already established in the surface wettability experiments.

Further, data about the temperature reached by the samples during the tests were registered. Figure 7.4 shows the placement of the 15% GNP/PDMS sample into the thermo-vacuum chamber and the report of its temperature values during the test, with a peak of 98 °C reached after 4 hours of solar irradiation. The temperature at the walls was also detected and reported in Figure 7.4b. The same data were acquired for each sample revealing a peak temperature of 94 °C for the nanocomposite with the GNP-DNA filler, in comparison with the value of 74 °C reached by the neat PDMS sample.

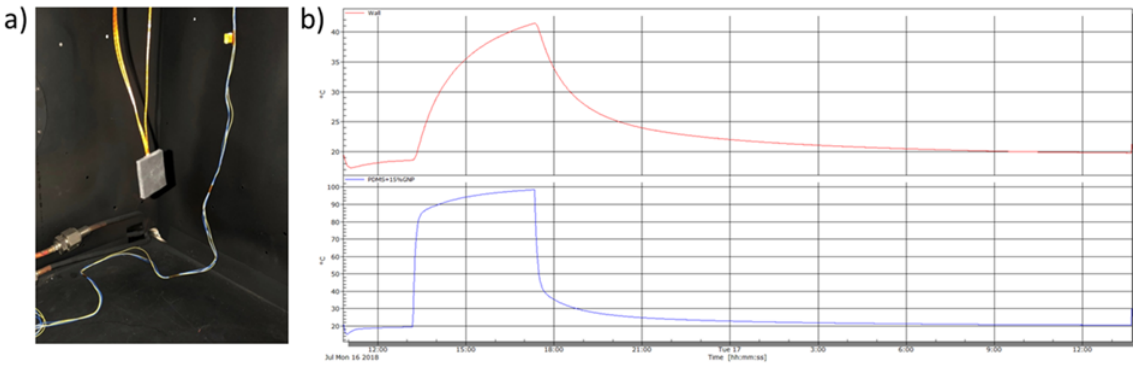

Figure 7.4. *a) Placement of 15% GNP/PDMS sample into the thermo-vacuum chamber and b) report of the temperature values reached by the chamber walls (top chart) and by the sample (bottom chart) during the test (irradiation time 4 h).*

7.3 Conclusions

Nanocomposite materials with GNP and GNP-DNA fillers integrate with a PDMS matrix were prepared, and their solar radiation sensitivity tested in simulated space environment. The properties of the nanocomposites were investigated before and after the test in order to assess the irradiation effects on the materials. Results by differential scanning calorimetry revealed that the nanocomposites are thermally stable in a wide temperature range, from -40 °C to 140 °C. Solar radiation exposure affected the thermal behavior of the GNP-DNA/PDMS nanocomposite at the level of the DNA denaturation peak determining an increase of peak temperature and a decrease of enthalpy change. The nanocomposites show a low tendency to adsorb the humidity, which is not significantly affected by the irradiation (water contact angles > 100°). This was confirmed by the low values of WVR% calculated after the tests. The 3D surface morphology reconstruction starting from SEM images permitted to appreciate the exposure effects on the different nanocomposite surfaces, highlighting a larger decrease of roughness for the GNP/PDMS nanocomposite. Results from electrical impedance spectroscopy showed a decrease of the nanocomposites conductivity after the test, mostly for the GNP/PDMS type, for which the variation reached 99%. Lastly, the values of TML% revealed the low outgassing features of the GNP/PDMS nanocomposite, which makes it suitable for applications in space. In the case of the GNP-DNA/PDMS nanocomposites, high values of TML% were obtained, suggesting this material would need to be encapsulated in a suitable enclosure such as quartz. Both types of nanocomposites exhibited a good stability in terms of thermal and wettability properties, showing a considerable electrical response to irradiation. The large variation of electrical conductivity could make these materials good candidates for monitoring solar radiation exposure in space environment.

7.4 Experimental section

Materials: Graphene nanoplatelets with a lateral size less than 7 μm and an average thickness of about 60 nm (grade AO-4) were purchased from Graphene Supermarket (Calverton, NY, USA). Double-stranded DNA and isopropyl alcohol (IPA) were obtained from Sigma-Aldrich (Milan, Italy). PDMS Sylgard 184 from Dow Corning (Midland, MI,

USA) was available as two components and prepared using a mixing ratio of base to curing agent of 10:1 (w/w).

Preparation of nanocomposite samples: Two types of nanocomposite materials were realized: the first using pristine GNP as filler at concentration of 15 wt%, and the second type using GNP functionalized with double-stranded DNA (mass ratio of 1:1) at a final concentration of GNP-DNA equal to 30 wt%. The nanocomposite mixtures were prepared following the same procedure for both types of nanofiller. GNP and DNA were weighted and dispersed into isopropyl alcohol (6.7 mL). Next, the PDMS elastomer base was added to the dispersion in a polymer-to-solvent ratio of 3:4 (w/v). The mixtures were sonicated for 1 hour in a cold-water bath (Elmasonic P30H from Elma, Singen, Germany). Next, the sonication was extended for additional 5 hours in association with the vacuum generated by a pump (Vacuubrand MZ 1C), in order to extract the IPA solvent from the mixtures. The curing agent was then added and gently mixed into the preparations using a ratio of base to curing agent of 10:1 (w/w). Finally, the GNP/PDMS and GNP-DNA/PDMS mixtures were deposited into apposite molds and dried in oven at 50 °C for 72 hours. This temperature was chosen to assure a slow process of cure avoiding the formation of microvoids in the nanocomposites structure due to the rapid evaporation of small residues of solvent. Nanocomposite samples with size of 25 mm × 30 mm and average thickness of 4 mm were prepared for the irradiation tests.

Solar irradiation in simulated space environment: facility and tests. The solar radiation sensitivity of the GNP/PDMS and GNP-DNA/PDMS nanocomposites was tested using the LARES-lab experimental set-up. This facility was created to test the components of LARES satellite in a simulated space environment [28] according to the standard requirements of ESA (ECSS, 2012; ECSS, 2002), and actually used for testing payloads and components for space applications. The equipment is characterized by a cubic vacuum chamber with an internal volume of 60×60×60 cm^3 in which the nanocomposite sample was positioned, in contact with a thermocouple (Figure 7.5a). The chamber is characterized by five walls entirely covered by a copper shroud painted with Aeroglaze Z306, a vacuum compatible black paint with high absorptivity and emissivity ($\varepsilon = 0.89$, $\alpha = 0.97$) [29]. The pressure was maintained below 10^{-6} mbar using two pumps: a dry scroll pump (Edwards XDS5) and a turbomolecular pump (Edwards EXT255DX).

The first type brings the pressure below 2 mbar, the limit required to start the second pump that brings the pressure to the operational value. The turbomolecular pump and the pressure gauge communicate with a controller (Edwards TIC Instrument Controller) connected to a personal computer and a software (Edwards TIC PC Program) to monitor the pressure and the pump parameters. A cooling shroud is composed of five copper plates cooled by an open circuit liquid nitrogen coil. Solar radiation is simulated by a SpectroSun XT-10 (Spectrolab) provided by a lamp (OSRAM XBO 1000 W) that projects a beam (AM0 spectrum) with a constant irradiance (1366 W/m^2) over a 12×12 cm^2 surface. The lamp is mounted outside the chamber and the access of light is permitted by a fused silica window that is transparent to UV radiation for wavelengths longer than 280 nm. The temperatures are recorded by platinum resistance thermometers PT100, and two monitoring systems allow to record data from up to 12 PT100 sensors. The nanocomposite samples were tested one at a time, and a neat PDMS polymer sample was also realized and tested as control. Each nanocomposite was weighted immediately before the test and positioned in the chamber, setting a starting temperature of 22 °C. The vacuum was applied and the solar radiation simulator was started when the turbomolecular pump assured the minimum pressure ($\leq 10^{-6}$ mbar). The solar irradiation was set for 4 hours and for the remaining time only vacuum was maintained. The entire duration of the test was 24 hours. At the end of the test, the vacuum was switched off, and the sample was brought to the initial room temperature (22 °C) and immediately weighted after removal from the chamber. The percentages of total mass loss (TML%) and of water vapor regained (WVR%) after the test were calculated as indicated by the ASTM E595 standard.

Characterization methods: The properties of each nanocomposite sample were examined before and after the solar irradiation test in the simulated space environment. The surface morphology was investigated using a VEGA II LSH scanning electron microscope (TESCAN, Brno, Czech Republic), with an accelerating voltage of 5 kV and a magnification of 500X. A 3D morphology reconstruction of the surfaces was realized, and roughness values were calculated using the MountainsMap Software (Digital Surf, Besançon, France) starting from the SEM images acquired at two different tilt angles.

Electrical impedance spectroscopy (EIS) was performed in the frequency range 10 Hz – 1 MHz using a Gamry Reference 600 Potentiostat instrument (Gamry Instruments,

Warminster, PA, USA). Measurements were repeated 10 times for each sample, and were carried out using a custom-made cell realized in plexiglass with two parallel copper electrodes fixed on the support. Each sample was placed in the cell with the opposite faces in contact with the parallel electrodes and the cell locked with screws. Impedance data were fitted by a suitable equivalent circuit model using the Gamry Echem Analyst software. The electrical resistance values (*R*) obtained from the fitting were converted to conductivity values using the following equation:

$$\sigma = \frac{1}{\rho} = \left(R\ \frac{A}{L}\right)^{-1} \tag{7.1}$$

where σ is the electrical conductivity, ρ is the resistivity, A is the area of each face of the sample in contact with the electrode, and L is the distance between the two electrodes, equal to the thickness of the sample.

The thermal behavior of the nanocomposites was investigated using a Perkin-Elmer Pyris 1 instrument (Waltham, MA, USA) in the temperature range from −40 °C to 250 °C, with a heating rate of 10 °C/min and under a nitrogen flow. The same heating cycle was previously applied to an empty pan obtaining the baseline that was subtracted from the sample data. For each nanocomposite, the analysis was repeated six times to validate the results. The values of peak temperature and enthalpy change (ΔH) were calculated using the Perkin-Elmer Thermal Analysis software.

Surface wettability investigations were carried out with a OCA 15 Pro optical analyzer (DataPhysics Instruments, Filderstadt, Germany). Ultrapure MilliQ water and diiodomethane were used as testing liquids and contact angles on the samples surface were measured. Tests were performed at room temperature, using the static sessile drop method and choosing a droplet volume of 3 μL. Ten droplets were examined for each sample, and the contact angle values were calculated with the DataPhysics SCA 20 software, choosing the ellipse fitting of the drops. The surface free energy (SFE) of the nanocomposites was determined according to the Owens-Wendt method [27]. The contact angle values obtained by two testing liquids (water and diiodomethane) were used in the following relationship:

$$\gamma_l(1 + \cos\theta) = 2\left[(\gamma_s^d \gamma_l^d)^{1/2} + (\gamma_s^p \gamma_l^p)^{1/2}\right] \tag{7.2}$$

where γ_s is the SFE of the solid that is analyzed, γ_l is the SFE of the measuring liquid, the apexes *d* and *p* indicate the dispersive and polar components respectively, θ the contact angle between the solid and the testing liquid.

7.5 References

[1] A. Swallow, Radiation Chemistry of Organic Compounds: International Series of Monographs on Radiation Effects in Materials, Elsevier2016.

[2] A.L. Andrady, S. Hamid, X. Hu, et al., Effects of increased solar ultraviolet radiation on materials, Journal of Photochemistry and Photobiology B: Biology, 46 (1998) 96-103.

[3] B. Diffey, Solar ultraviolet radiation effects on biological systems, Physics in medicine & biology, 36 (1991) 299.

[4] W. Harm, Biological effects of ultraviolet radiation, (1980).

[5] L. Carnell, S. Blattnig, S. Hu, et al., Evidence Report: Risk of Acute Radiation Syndromes Due to Solar Particle Events, (2016).

[6] E.H. Donnelly, J.B. Nemhauser, J.M. Smith, et al., Acute radiation syndrome: assessment and management, Southern medical journal, 103 (2010) 541-546.

[7] F.A. Cucinotta, M. Durante, Cancer risk from exposure to galactic cosmic rays: implications for space exploration by human beings, The lancet oncology, 7 (2006) 431-435.

[8] F. Cucinotta, F. Manuel, J. Jones, et al., Space radiation and cataracts in astronauts, Radiation research, 156 (2001) 460-466.

[9] L.T. Chylack Jr, L.E. Peterson, A.H. Feiveson, et al., NASA study of cataract in astronauts (NASCA). Report 1: Cross-sectional study of the relationship of exposure to space radiation and risk of lens opacity, Radiation research, 172 (2009) 10-20.

[10] F. Stewart, A. Akleyev, M. Hauer-Jensen, et al., ICRP publication 118: ICRP statement on tissue reactions and early and late effects of radiation in normal tissues and organs–threshold doses for tissue reactions in a radiation protection context, Annals of the ICRP, 41 (2012) 1-322.

[11] J.-L. Ravanat, T. Douki, J. Cadet, Direct and indirect effects of UV radiation on DNA and its components, Journal of Photochemistry and Photobiology B: Biology, 63 (2001) 88-102.

[12] J. Cadet, J.R. Wagner, DNA base damage by reactive oxygen species, oxidizing agents, and UV radiation, Cold Spring Harbor perspectives in biology, 5 (2013) a012559.
[13] M. Vorlíčková, E. Paleček, Changes in properties of DNA caused by gamma and ultraviolet radiation. Dependence of conformational changes on the chemical nature of the damage, Biochimica et Biophysica Acta (BBA)-Nucleic Acids and Protein Synthesis, 517 (1978) 308-318.
[14] H. Lang, G. Luck, Ultraviolet-light-induced conformational changes in DNA, Photochemistry and photobiology, 17 (1973) 387-393.
[15] T. Matsunaga, K. Hieda, O. Nikaido, Wavelength dependent formation of thymine dimers and (6-4) photoproducts in DNA by monochromatic ultraviolet light ranging from 150 to 365 nm, Photochemistry and photobiology, 54 (1991) 403-410.
[16] N. Munakata, Biologically effective dose of solar ultraviolet radiation estimated by spore dosimetry in Tokyo since 1980, Photochemistry and photobiology, 58 (1993) 386-392.
[17] N. Munakata, K. Makita, D. Bolsée, et al., Spore dosimetry of solar UV radiation: applications to monitoring of daily irradiance and personal exposure, Advances in Space Research, 26 (2000) 1995-2003.
[18] W.L. Nicholson, A.C. Schuerger, P. Setlow, The solar UV environment and bacterial spore UV resistance: considerations for Earth-to-Mars transport by natural processes and human spaceflight, Mutation Research/Fundamental and Molecular Mechanisms of Mutagenesis, 571 (2005) 249-264.
[19] A. Berces, M. Egyeki, A. Fekete, et al., Biological ultraviolet Dosimetry in Low Earth's Orbit, Astrobiol Outreach, 1 (2013) 2.
[20] M. Kutz, Handbook of environmental degradation of materials, William Andrew2018.
[21] https://materialsinspace.nasa.gov/background.html.
[22] M.-Y. Shen, T.-Y. Chang, T.-H. Hsieh, et al., Mechanical properties and tensile fatigue of graphene nanoplatelets reinforced polymer nanocomposites, Journal of Nanomaterials, 2013 (2013) 1.
[23] M.D. Borysiak, K.S. Bielawski, N.J. Sniadecki, et al., Simple replica micromolding of biocompatible styrenic elastomers, Lab on a Chip, 13 (2013) 2773-2784.

[24] T.C. Hain, K. Kroeker, D.G. Stich, et al., Influence of DNA conformation on the dispersion of SWNTs: single-strand DNA vs. hairpin DNA, Soft Matter, 8 (2012) 2820-2823.
[25] A.J. Patil, J.L. Vickery, T.B. Scott, et al., Aqueous stabilization and self-assembly of graphene sheets into layered bio-nanocomposites using DNA, Advanced Materials, 21 (2009) 3159-3164.
[26] S. Botti, A. Rufoloni, S. Laurenzi, et al., DNA self-assembly on graphene surface studied by SERS mapping, Carbon, 109 (2016) 363-372.
[27] D.K. Owens, R. Wendt, Estimation of the surface free energy of polymers, Journal of applied polymer science, 13 (1969) 1741-1747.
[28] C. Paris, G. Sindoni, LARES-Lab: a facility for environmental testing of satellite components and micro satellites, Proceedings of the 2nd IAA conference on dynamics and control of space systems, DyCoSS, 2014.
[29] M. Persky, Review of black surfaces for space-borne infrared systems, Review of Scientific Instruments, 70 (1999) 2193-2217.

Chapter 8

Conclusions

This Thesis reports the experimental approach towards the design, fabrication and testing of bio-inspired UV sensitive nanocomposites based on graphene/DNA interface. The literature background proposed in **Chapter 2** elucidated the starting points of this work, from the field of composite materials to the UV radiation effects on human health and on organic materials that are most degraded by such radiation, in the perspective of the application of these concepts for a bio-inspired UV sensing.

The first experimental work, which is described in **Chapter 3**, focused on the fabrication of GNP-DNA/PEDOT:PSS films and their testing under different doses of UV-C radiation. The surface wettability, the electrical and morphological properties of these films were analyzed before and after irradiation, and compared with the properties of GNP/PEDOT:PSS and of neat PEDOT:PSS films, with the aim to discriminate the role of each component of the overall nanocomposite material on the UV response. Results revealed that for the GNP-DNA/PEDOT:PSS films, after a cumulative radiation dose of 150 J/cm^2, a region can be detected in which the electrical conductivity variation is linearly proportional to the UV-C dose. Moreover, GNP-DNA/PEDOT:PSS films exhibited a good homogeneity that can be ascribed to the DNA component, which acts as exfoliating agent for the GNPs. Next, Raman investigations highlighted that the UV-C sensitivity of the GNP-DNA/PEDOT:PSS nanocomposites are prevalently due to their PEDOT:PSS and DNA components.

In the following experimental study, as reported in **Chapter 4**, the technique of electrical resistance tomography (ERT) applied to GNP-DNA/PEDOT:PSS coatings was proposed as possible method for the health monitoring of UV-exposed materials. In particular, the ERT technique was optimized in terms of current patterns and injection values in order to detect damage induced by UV irradiation. The nanocomposite area exposed and affected by the UV-C radiation was localized in the ERT maps with good agreement. Different levels of conductivity changes were detected by the technique when

exposing the surfaces to different intensities of UV-C radiation. The ERT experimental results were supported by SEM morphology and Raman spectroscopy analyses, highlighting that the combination of the UV sensitive GNP-DNA/PEDOT:PSS coatings and ERT could be used as a real-time health monitoring method for materials and structures that are subjected to UV-C degradation.

The UV-sensitive graphene/DNA filler was then incorporated in a different matrix, in order to obtain flexible free-standing films or 3D materials suitable to use as wearable UV sensitive parts of a radiation monitoring system. PDMS-based polymers were tested as matrix due to their flexibility, biocompatibility, and chemical inertia. Moreover, the good optical transmittance of PDMS matrix, for wavelengths above 240 nm, favors a major exposure of the incorporated UV-sensitive filler during the irradiation, without interfering with its sensing process.

The curing kinetics of different PDMS-based mixtures were examined and discussed in **Chapter 5**. This study was performed with the aim to collect useful information for the materials processing and to unveil eventual limitations in the nanocomposite fabrication due to the presence of the filler. In particular, the different curing behavior and the effect of the GNP-DNA loadings on the silicone matrices (standard PDMS and PDMS/PDMS-OH blend) were analyzed starting from dynamic calorimetric measurements. The Kissinger method and two isoconversional models (OFW and KAS) were applied, showing that the first method underestimates the presence of the filler, whereas the OFW and KAS models are able to follow the complex trend of the curing behavior of the nanocomposites as a function of the filler content. Results from this study highlighted that PDMS/PDMS-OH matrix is negatively affected by the modified graphene filler. In addition, the related nanocomposites showed higher levels of flexibility than the PDMS-based ones, as revealed by nanoindentation tests. Conversely, the curing reaction of PDMS was favored by the presence of the GNP-DNA filler, and PDMS-based nanocomposites exhibited mechanical properties that can assure their self-standing and, at the same time, sufficient flexibility to allow for their use as wearable UV sensitive materials.

Results reported in **Chapter 5** revealed the effect of GNP-DNA on the curing behavior of the PDMS matrix, showing that the presence of this filler progressively decreases the activation energy. Next, GNP-DNA/PDMS films at higher filler loadings

were prepared with the aim to improve the electrical properties of the nanocomposites for the UV sensing application. **Chapter 6** reported the fabrication process of these nanocomposites, which involves the use of a suitable solvent (isopropyl alcohol) in order to improve the dispersion of large amounts of graphene/DNA in the prepolymer matrix. The nanocomposite properties were characterized before and after UV-C irradiation, and the UV response of the films containing different concentrations of the sensitive filler was evaluated. DSC results revealed that the nanocomposites are thermally stable in a wide range of temperature, from –40 °C to 140 °C, and so they are potentially useful in technological applications characterized by large temperature gradients, such as those in space environment. Moreover, the surface wettability analysis highlighted a high degree of hydrophobicity that does not change significantly after UV-C exposure, maintaining a low tendency to adsorb humidity from the surrounding environment. Lastly, changes in the electrical conductivity were measured after UV-C exposure. The detected changes are larger for the nanocomposite with a GNP-DNA content of 30 wt%, and therefore this nanocomposite can be considered a good candidate material for the measurement of the UV-adsorbed dose.

Finally, GNP-DNA/PDMS nanocomposites with larger thickness (4 mm) were fabricated for testing in simulated space environment in a thermo-vacuum chamber. Procedures and results were described and discussed in **Chapter 7**. Specifically, GNP-DNA/PDMS and GNP/PDMS were prepared, in order to evaluate their response to solar irradiation also in the absence of the biological DNA component. The nanocomposites were irradiated in ultrahigh vacuum (~10^{-6} mbar) in the solar irradiation spectrum, and their properties analyzed before and after exposure. Results from these tests highlighted that both types of nanocomposite exhibited a good stability in terms of thermal and wettability properties, while showing a significant electrical response to irradiation. Moreover, the measured values of total mass loss (TML%) revealed low outgassing properties for the GNP/PDMS nanocomposites, whereas for the GNP-DNA/PDMS type, higher values of TML% were obtained. Nevertheless, by encapsulating the GNP-DNA/PDMS nanocomposites in a suitable UV-transparent enclosure, such as quartz, the outgassing could be limited allowing for the potential use of these materials for monitoring solar radiation exposure in space environment.

Overall, the results found in the experimental studies of this Thesis revealed that the bio-inspired nanocomposites with GNP-DNA filler have a specific UV response, in particular in terms of electrical conductivity variations, and therefore these materials have the potential to be applied in UV monitoring systems, with the additional advantages of real-time response, low weight/mass and reduced size. As future work, the analysis of the UV-induced damage on the GNP-DNA nanocomposites at the level of the DNA fragments would be useful, in order to correlate the UV sensitivity of these materials to both electrical and biological-weighted outputs. In this perspective, these bio-inspired materials would be beneficial to detect the extent of biological damage occurring under UV exposure in real time.

List of Publications

Articles

1. Toto E., Laurenzi S., Santonicola M.G., "Curing reactions of silicone nanocomposites filled with DNA-functionalized graphene investigated by differential scanning calorimetry", *Composites Part A*, under review

2. Toto E., Botti S., Laurenzi S., Santonicola M.G., "UV-induced modification of PEDOT:PSS-based nanocomposite films investigated by Raman microscopy mapping", *Applied Surface Science*, vol. 513, article number 145839, 2020. (DOI:10.1016/j.apsusc.2020.145839)

3. Clausi M.[†], Toto E.[†], Botti S., Laurenzi S., La Saponara V., Santonicola M.G., "Direct effects of UV irradiation on graphene-based nanocomposite films revealed by electrical resistance tomography", *Composites Science and Technology*, vol. 183, article number 107823, 2019. (DOI:10.1016/j.compscitech.2019.107823)
   [†]equal contribution

4. Toto E., Palombi M., Laurenzi S., Santonicola M.G., "Functional nanocomposites with graphene-DNA hybrid complexes: synthesis and surface properties under UV irradiation", *Ceramics International*, vol. 45(7), pp. 9631-9637, 2019. (DOI:10.1016/j.ceramint.2018.10.236)

Conference Papers

1. Santonicola M.G., Toto E., Palombi M., Paris C., Laurenzi S., "Experimental study of solar radiation effects on carbon nanocomposite sensors in simulated space environment", *Proceedings of the International Astronautical Congress, IAC*, vol. 2018-October, pp. 1-8, 2018

2. Santonicola M.G., Toto E., Laurenzi S., "Polymer composites filled with DNA-functionalized graphene nanoplatelets: effects of DNA modification on the curing behavior and properties of PDMS-based matrices", *ECCM 2018 - 18th European Conference on Composite Materials*, pp. 1-8, 2019

3. Toto E., Laurenzi S., Santonicola M.G., "Novel graphene-based nanocomposite films for monitoring UV radiation effects on space structures", *XIV AIMAT National Congress July 12-15, 2017, Journal of Applied Biomaterials & Functional Materials*, vol. 15(4), pp. e421-e422, 2018. (DOI:10.5301/jabfm.5000369; WOS:000415072200013)

4. Toto E., Mancini M.C., Laurenzi S., Santonicola M.G., "Ultraviolet-sensing surfaces based on hybrid nanocomposites for radiation monitoring systems", *4th IEEE International Workshop on Metrology for AeroSpace, MetroAeroSpace 2017 - Proceedings*, article number 7999599, pp. 369- 373, 2017. (DOI: 10.1109/MetroAeroSpace.2017.7999599)

Abstracts in Conference Proceedings

(First author is the presenting author)

1. Bartolo D., Rastogi S., Toto E., Zaccardi F., Santonicola M.G., Laurenzi S., La Saponara V., "Electrical resistance tomography for structural health monitoring of nanocomposite materials for spacesuit and crew surface mobility applications", *NASA Exploration science forum (NESF 2019)*, Mountain View, California, United States, July 23-25, 2019

2. Toto E., Botti S., Laurenzi S., Santonicola M.G., "UV-induced modification of graphene-based sensor surfaces investigated by Raman microscopy mapping", *3rd International Conference on Applied Surface Science (ICASS 2019)*, Pisa, Italy, June 17-20, 2019

3. Santonicola M.G., Toto E., Laurenzi S., "Engineering functional coatings for UV damage detection based on graphene/DNA interface", *E-MRS Spring Meeting 2019*, Nice, France, May 27-31, 2019

4. Toto E., Laurenzi S., Santonicola M.G., "Curing reactions and thermal stability of nanocomposites with DNA/graphene nanoplatelets by differential scanning calorimetry", *XL National Congress on Calorimetry - Thermal Analysis and Applied Thermodynamics (AICAT/GICAT 2018),* Pisa, Italy, December 17-19, 2018

5. Toto E., Botti S., Laurenzi S., Santonicola M.G., "Raman microscopy analysis of graphene-based nanocomposite materials under UV-C exposure", *Materials.it 2018,* Bologna, Italy, October 22-26, 2018

6. Toto E., Palombi M., Laurenzi S, Santonicola M.G., "Graphene-based nanocomposite materials for applications in space radiation environment", *NanoInnovation Conference & Exhibition 2018,* Rome, Italy, September 11-14, 2018

7. Toto E., Palombi M., Laurenzi S, Santonicola M.G., "Functional Nanocomposites with Graphene-DNA Hybrid Complexes: Fabrication and Surface Properties under UV Irradiation", *CIMTEC 2018 – 8th Forum on New Materials,* Perugia, Italy, June 10-14, 2018

8. Toto E., Clausi M., Laurenzi S., Santonicola M.G., "Smart nanomaterial-based hybrid films for sensing UV radiation damage in space environment", *NanoInnovation Conference & Exhibition 2017,* Rome, Italy, September 26-29, 2017

9. Santonicola M.G., Toto E., Coscia M.G., "Biocompatible nanocomposites with multifunctional properties: integrating DNA-decorated graphene with PDMS-based matrices", *25th Annual International Conference on Composites and Nano Engineering (ICCE-25),* Rome, Italy, July 16-22, 2017

10. Toto E., Laurenzi S., Simone A., Santonicola M.G., "Flexible nanostructured composites with graphene/DNA hybrids as multifunctional substrates for biomedical applications", *International Conference on Graphene and related Materials,* Paestum, Italy, May 23-27, 2016

11. Toto E., Coscia M.G., Santonicola M.G., "Conductive and flexible materials containing graphene-DNA hybrids for cell culture applications", *6th International Conference on Advanced Nanomaterials*, Aveiro, Portugal, July 20-22, 2015

Acknowledgments

The first person I would like to thank is my advisor, Prof. Mariagabriella Santonicola, for giving me the opportunity to carry out my PhD path in her group and for all the support that she gave me during the research work. She made her knowledge available to me, giving me the encouragement for always doing better and for improving myself. I am very grateful also to my co-advisor, Prof. Susanna Laurenzi, who guided and supported me in all phases of my PhD course, enriching my path with her knowledge, concreteness and way to approach the research work. I want to thank Dr. Sabina Botti (ENEA Research Centre, Frascati) for her scientific support on Raman spectroscopy, for her kindness and contribution in improving my research work. I would like to thank all colleagues and all friends that made this path more pleasant, and the people who stayed by my side both in the beautiful and the most difficult moments. Last, I want to thank my family for always believing in me, and in particular my parents, who allowed me to get here, showing me their love and their support at all times.